

Universität für Baukunst und Metropolenentwicklung
Geodäsie und Geoinformatik

Title:

**BATHYMETRIC SURVEY FOR ASSESSING AND
FORECASTING THE RATE OF SEDIMENT DEPOSITS IN
KAINJI RESERVOIR ACROSS RIVER NIGER IN NIGERIA**

IBRAHIM Pius Onoja Matr.-Nr.: 6063601

Supervisor: Prof. Dr.-Ing. Harald Sternberg

Second Supervisor: Prof. Dr. Lazarus M. Ojigi

A thesis submitted in fulfilment of the
requirements for the award of the degree of
Doktor der Ingenieurwissenschaften (Dr.-Ing.)

Submission:

Hamburg, 22nd April 2022

DECLARATION

I declare that this thesis entitled “*Bathymetric Survey for Assessing and Forecasting the Rate of Sediment Deposits in Kainji Reservoir Across River Niger in Nigeria*” is the result of my research except as cited in the references. The thesis has not been accepted for any degree and is not concurrently submitted in the candidature of any other degree.

Signature:.....

Name:.....

Date:.....

DEDICATION

With the humility of the heart and mercy of God Almighty, this study is dedicated to my father, CPL. ONOJA Ibrahim.

ACKNOWLEDGEMENTS

All glory to God Almighty for the privilege granted unto me to come to this beautiful country to pursue my PhD programme.

I sincerely thank my supervisor Prof. Dr. Ing. Harald Sternberg, for accepting to supervise me and to learn under his watch; it is indeed a great honour. Thank you for your mentorship. I appreciate Mrs. Ahrend Meike Kröger for her kind understanding and prompt response anytime I need information on a particular issue; she has indeed engraved her name in my heart. Additionally, thanks go to the department staff for their support throughout my study period, “especially for Miss Tanya and Miss Mona”, at HafenCity University, Hamburg, Germany.

I thank the Government of Germany (DAAD) and Nigeria (PTDF) for their cooperation to sponsor those who are financially handicapped to further their study, of which I am one of them. In addition, thanks go to the management of Federal University of Technology (FUT) Minna for giving me this great opportunity by releasing me for the study at Hafen City University, Hamburg, Germany.

My gratitude goes to Prof. I.J. Nwadiakor, Dr. Y.D. Opaluwa, Dr. O.G. Ajayi, Dr. J.O. Odumosu, Surv. A. Daniel, Miss. Stella Egbo and others for their support in diverse ways during the PhD programme. I deeply appreciate Late Mr. James S. Ibrahim for his support at various points of need.

My parents (Mr. Ibrahim Onoja and Miss Lydia Idoko), I can never thank you enough for all you have done for me. My sister, Roseline Onoja, thank you for always being there for me right from when I took the decision to go further academically. Mr. Boyi Armful and his wife, and every other relation, I thank you all greatly.

Last, my gratitude goes to my wife Dorcas Pius and My son Harald Power Pius for their support and calmness throughout the PhD pursuit.

ENGLISH ABSTRACT

Sedimentation and siltation are gradual and continuous processes that fill up water bodies, especially reservoirs. The menace of sediment deposits can cause flooding or dam failure if left unchecked. This will be pronounced globally “especially in developing countries” due to the rising sea levels caused by climate emergencies, which will further exacerbate the destructive power of flooding. Therefore, science, international cooperation, preparedness and early action must be pivotal to safer people and communities (Antonio, 2021). To this end, accurately determining or estimating the amount of sediment deposits in a reservoir and possibly forecasting the future reservoir depth surface has been a global challenge if the activities of sedimentation remain the same. To ensure proper monitoring and management of reservoir, sounding operations to determine the amount of deposited lacustrine material to be dredged should be conducted regularly. Hence, bathymetric and sedimentation surveys were conducted in 2020 using a dual-frequency (20/200 kHz) echo sounder system in the Kainji Reservoir in New Bussa, Niger State, Nigeria. A Hi-Target V30 dual-frequency Differential Global Positioning System (DGPS) was used to delineate the reservoir shoreline at some strategic locations, including tidal measurement. The data were merged to provide detailed visualization and analyses of current depth distribution and thickness and to estimate the volume of lacustrine sediment, time average sediment accumulation rates, long-term average annual sediment flux, and water storage capacity. A recent day reservoir stand-alone information system was generated from 200 kHz sounding data. Linear regression of the reservoir depths was assessed from 1990 bathymetric datasets and 2020 datasets using profiles and cross-sections. The results show that the maximum observed depth is 71.2 m, indicating a 7.53% loss in depth from the 1990 archived data and a 16.24% depth loss to sedimentation from 1968 to 2020. The calculated long-term average sediment accumulation rates were used to model sediment infilling and the projected lifetime of the reservoir. The outcome from the echo sounder datasets suggests that the basin has a projected lifetime of 85.65 years due to sediment load. Furthermore, Markov chain and cellular automata (MC – CA) were used to forecast the future bathymetric surface of 2050, but the final surface generated some artefacts but well-predicted depths were achieved. Hence, Cellular Automata and Gradient Boosting Regression (CA – GBR) were specifically integrated for this research to model future bathymetric surfaces to evaluate the outcome of CA – Markov chains. The results show that CA – GBR effectively forecasted the future bathymetric surface of 2050 without any artefacts at a 95.7% accuracy rate. Furthermore, to investigate the scientific reasons for the high sedimentation rate in the study area, first, land use land cover classification was conducted to assess the land-use changes using Landsat data from 1990, 2005, and 2020 with five classification schemes: water, vegetation, built-up, forest, and bare-ground. The results suggested that forest and vegetation have lost a greater percentage of their area to bare ground, giving rise to erosion because the soil loses its resistivity over time without adequate vegetation cover. Second, drainage network and catchment area analyses were conducted. The results show that the catchment has 1 to 6 stream orders and 28 subbasins, again indicating a mass movement of sediment from the catchment area to the central basin. Third, the Universal Soil Loss Equation (USLE) model was employed to estimate the soil loss in ton/acre/year via rill and sheet erosion into the reservoir. The results show a high rate of soil loss of calculated annual sediment loss from USLE of 5.6% greater than the estimated yearly sediment flux using a low-frequency echo sounder. The small change between USLE and low-frequency sediment estimation suggests that USLE can be used to validate low-frequency lacustrine sediment measurements. Finally, the flood impact

vulnerability map was modelled with a maximum elevation of 137 m above mean sea level. The results indicated that all the communities within 1500 km from the river centre are in great danger of flooding, while others are either medium- or low-risk and safe zones.

GERMAN ABSTRACT

Sedimentation und Verschlammung sind allmähliche und kontinuierliche Prozesse, die Gewässer, insbesondere Stauseen, auffüllen. Die Bedrohung durch Sedimentablagerungen kann zu Überschwemmungen oder zum Versagen von Dämmen führen, wenn sie nicht eingedämmt wird. Dies wird sich aufgrund des durch den Klimawandel verursachten Anstiegs des Meeresspiegels, der die zerstörerische Kraft von Überschwemmungen noch verstärken wird, weltweit und "insbesondere in den Entwicklungsländern" bemerkbar machen. Daher müssen Wissenschaft, internationale Zusammenarbeit, Vorsorge und frühzeitiges Handeln von zentraler Bedeutung sein, um Menschen und Gemeinschaften in Sicherheit zu bringen (Antonio, 2021). Zu diesem Zweck ist es eine globale Herausforderung, die Menge der Sedimentablagerungen in einem Stausee genau zu bestimmen oder abzuschätzen und möglicherweise die künftige Tiefe des Stausees vorherzusagen, wenn die Sedimentationsaktivitäten gleich bleiben. Um eine ordnungsgemäße Überwachung und Bewirtschaftung des Stausees zu gewährleisten, sollten regelmäßig Sondierungen durchgeführt werden, um die Menge des abgelagerten und auszubaggernden Seematerials zu bestimmen. Daher wurden im Jahr 2020 im Kainji-Stausee in New Bussa, Niger State, Nigeria, mit einem Zweifrequenz-Echolotsystem (20/200 kHz) bathymetrische und Sedimentationsmessungen durchgeführt. Ein Hi-Target V30-Doppelfrequenz-Differential-Global-Positionierungssystem (DGPS) wurde verwendet, um die Uferlinie des Stausees an einigen strategischen Stellen abzugrenzen, einschließlich Gezeitenmessungen. Die Daten wurden zusammengeführt, um eine detaillierte Visualisierung und Analyse der aktuellen Tiefenverteilung und Mächtigkeit sowie eine Schätzung des Volumens des Seesediments, der zeitlichen durchschnittlichen Sedimentakkumulationsraten, des langfristigen durchschnittlichen jährlichen Sedimentflusses und der Wasserspeicherkapazität zu ermöglichen. Aus 200-kHz-Sondierungsdaten wurde ein eigenständiges Informationssystem für den Stausee erstellt. Die lineare Regression der Tiefen des Stausees wurde anhand der bathymetrischen Daten von 1990 und der Daten von 2020 mit Hilfe von Profilen und Querschnitten bewertet. Die Ergebnisse zeigen, dass die maximale beobachtete Tiefe 71,2 m beträgt, was auf einen Tiefenverlust von 7,53 % aus den archivierten Daten von 1990 und einen Tiefenverlust von 16,24 % durch Sedimentation von 1968 bis 2020 hindeutet. Die berechneten langfristigen durchschnittlichen Sedimentakkumulationsraten wurden zur Modellierung der Sedimentverfüllung und der voraussichtlichen Lebensdauer des Stausees verwendet. Die Ergebnisse der Echolotdatensätze deuten darauf hin, dass das Becken aufgrund der Sedimentbelastung eine voraussichtliche Lebensdauer von 85,65 Jahren hat. Darüber hinaus wurden Markov-Ketten und zelluläre Automaten (MC - CA) verwendet, um die künftige bathymetrische Oberfläche für das Jahr 2050 zu prognostizieren, wobei die endgültige Oberfläche zwar einige Artefakte aufwies, aber gut vorhergesagte Tiefen erreicht wurden. Daher wurden Zelluläre Automaten und Gradient Boosting Regression (CA - GBR) speziell für diese Forschung integriert, um zukünftige bathymetrische Oberflächen zu modellieren und das Ergebnis von CA - Markov-Ketten zu bewerten. Die Ergebnisse zeigen, dass CA - GBR die zukünftige bathymetrische Oberfläche des Jahres

2050 ohne Artefakte mit einer Genauigkeit von 95,7 % vorhersagen konnte. Um die wissenschaftlichen Gründe für die hohe Sedimentationsrate im Untersuchungsgebiet zu untersuchen, wurde zunächst eine Landnutzungsklassifizierung durchgeführt, um die Landnutzungsänderungen anhand von Landsat-Daten aus den Jahren 1990, 2005 und 2020 mit fünf Klassifizierungsschemata zu bewerten: Wasser, Vegetation, bebauter Boden, Wald und un bebauter Boden. Die Ergebnisse deuten darauf hin, dass Wald und Vegetation einen größeren Prozentsatz ihrer Fläche an nackten Boden verloren haben, was zu Erosion führt, da der Boden ohne angemessene Vegetationsdecke mit der Zeit seinen Widerstand verliert. Zweitens wurden Analysen des Entwässerungsnetzes und des Einzugsgebiets durchgeführt. Die Ergebnisse zeigen, dass das Einzugsgebiet 1 bis 6 Bachordnungen und 28 Teileinzugsgebiete aufweist, was wiederum auf eine Massenbewegung von Sedimenten aus dem Einzugsgebiet in das zentrale Einzugsgebiet hindeutet. Drittens wurde das Modell Universal Soil Loss Equation (USLE) verwendet, um den Bodenverlust in Tonnen pro Hektar und Jahr durch Rill- und Flächenerosion in den Stausee zu schätzen. Die Ergebnisse zeigen, dass der mit der USLE berechnete jährliche Sedimentverlust um 5,6 % höher ist als der mit einem Niederfrequenz-Echolot geschätzte jährliche Sedimentfluss. Die geringe Abweichung zwischen der USLE und der Niederfrequenz-Sedimentschätzung deutet darauf hin, dass die USLE zur Validierung von Niederfrequenz-Sedimentmessungen in Seen verwendet werden kann. Schließlich wurde die Karte der Hochwassergefährdung mit einer maximalen Höhe von 137 m über dem mittleren Meeresspiegel modelliert. Die Ergebnisse zeigen, dass alle Gemeinden im Umkreis von 1500 km um das Flusszentrum stark überschwemmungsgefährdet sind, während andere entweder ein mittleres oder ein geringes Risiko aufweisen und als sichere Zonen gelten.

TABLE OF CONTENTS

Declaration..... i

Dedication ii

Acknowledgements iii

Abstract in English iv

Abstract in German v

1 CHAPTER ONE: Introduction..... 1

1.1 Background to the Study..... 1

1.2 River Niger and Nigeria..... 1

1.3 Statement of Problem..... 3

1.4 Aim and Objectives of the Study 5

1.5 Scope and Limitations of the Study 5

1.6 Contributions and Significance of the Study 6

2 CHAPTER TWO: Sounding and Hydrographic Surveying..... 7

2.1 Introduction..... 7

2.2 Description of Sound and Frequency..... 7

2.3 Echo Sounding: Principles and Operating Systems..... 11

2.3.1 Operating Principles of Sonar..... 12

2.3.2 Passive Sonar 12

2.3.3 Active Sonar 13

2.3.4 Limitations of Active and Passive Sonar..... 14

2.3.5 Transducer 15

2.3.6 Sonar Equation 16

2.3.7 Determination of Sounding Resolution 18

2.3.8 Signal to Noise Ratio (SNR) and Directivity 19

2.3.9 Bathymetry Systems of Operation on Waterbody 19

2.3.10 Single Beam System..... 20

2.3.11 Maximum Operating Range Calibration of a Single Beam Echosounder..... 24

2.3.12 Swath System (Sweep Sounders) Echosounder 24

2.3.13 Multibeam Echosounder..... 25

2.3.14 Side-Scan SONAR 27

2.3.15 Description of Projector Arrays and Beam Forming..... 28

2.3.16 Description of Hydrophone Arrays 31

2.3.17	Mills Cross Arrays.....	32
2.3.18	Array Gain (AG).....	33
2.3.19	Enhancing Array Gain.....	34
2.3.20	Beam Steering.....	34
2.3.21	Doppler Shift and Ship Speed Measurement.....	37
2.3.22	Sound Velocity Profiler.....	39
2.3.23	Conductivity Temperature Depth (CTD)	41
2.3.24	Motion Sensors.....	41
2.3.25	Latency	44
2.3.26	Tide and Positioning.....	44
2.3.27	Vertical Datum and Chart Datum.....	46
2.4	Positioning	47
2.4.1	Global Positioning System (GPS)	49
2.4.2	Dilution of Precision (DOP).....	50
2.4.3	Fixing the Position of a Ship Using a GPS Receiver	51
2.4.4	Differential GPS (DGPS)	52
2.5	Sedimentation	53
2.5.1	Measuring Sedimentation in Dams or Rivers.....	55
2.5.2	Sediment Yield Computation	56
2.5.3	Sediment Determination from Bathymetric Volume.....	57
2.5.4	Reservoir Half-life Computation.....	57
2.6	Application of Bathymetry Systems.....	58
2.6.1	Application of Single Beam Echosounder.....	58
2.6.2	Application of MBES (summer school experience).....	60
2.6.3	Summer School Experience.....	61
2.7	Markov Chain Model, Gradient Boosting Regression, and Cellular Automata ...	65
2.7.1	Markov Chain Model.....	66
2.7.2	Discrete-Time Markov Chain.....	66
2.7.3	Continuous – Time Markov chain.....	67
2.7.4	Practical Application of Markov Chain Model	69
2.7.5	Gradient Boosting Regression.....	70
2.7.6	Loss Functions.....	71
2.7.7	GBR Algorithm	72
2.7.8	Discussion of the Mathematical GBR Algorithm.....	72

2.7.9	Practical Application of GBR.....	75
2.7.10	Cellular Automata.....	75
2.7.11	Cellular Automata Mathematical Model	76
2.7.12	Practical Application of CA in Spatial Data Analysis.....	78
2.7.13	Practical Application of CA in Land use Modelling	79
2.7.14	Practical Application of CA to Flood Modelling	80
2.8	Abridge Gap Description.....	82
3	CHAPTER THREE: Methodology.....	83
3.1	Introduction.....	83
3.2	Datasets for the Study	84
3.3	Bathymetric Survey of Kainji Reservoir and Control Establishment.....	84
3.3.1	Establishment of Temporary Control	87
3.3.2	Calibration Test of HD-380 Digital Echo Sounder	89
3.3.3	The Bar Check Calibration.....	89
3.3.4	Bathymetry Surveys	92
3.3.5	Reservoir Shoreline Delineation.....	94
3.4	Reservoir Bathymetric Stand Alone System, Profiling, Cross-Sections, Volume Determination and Sediment Deposite Analysis, Digital Depth Modeling.....	95
3.4.1	Procedure for Developing a Bathymetric Stand-Alone Reservoir System....	95
3.4.2	Profile and Cross Sections.....	96
3.4.3	Volume Determination and Sediment Deposite Analysis	98
3.4.4	Digital Depth Modelling.....	100
3.4.5	Digital Depth Accuracy Evaluation.....	100
3.5	Markov Chain and Cellular Automata to Assess and Forecast Sediment Deposits	103
3.5.1	Initial Dataset and Preprocessing	104
3.5.2	Cellular Automata Application.....	105
3.5.3	Markov Chains Procedures.....	106
3.5.4	Final CA-Markov Forecasting.....	107
3.6	Cellular Automata-Gradient Boosting Regression (CA-GBR).....	107
3.7	Quality or Accuracy evaluation of Forecasted Surfaces.....	109
3.8	Investigating the Scientific Contribution to Sedimentation in the Kainji Reservoir.	110
3.8.1	Landuse Land Cover Classification, Catchment Area and Drainage Network of Kainji Reservoir and Environs.....	111

3.8.2	Land Use Land Cover Classification Procedure.....	111
3.8.3	Drainage Network and Catchment Area Delineation	112
3.8.4	Predicting Soil Loss Via Universal Soil Loss Equation Model (USLEM) .	114
4	CHAPTER FOUR: Result and Analysis.....	118
4.1	Result and Analysis (Objective One):.....	118
4.1.1	Introduction	118
4.1.2	Reservoir Bathymetric Information System (RBIS)	118
4.1.3	Cross Section and Profile	121
4.1.4	Sediment Deposit and Volume Determination Analysis.....	125
4.1.5	Digital Depth Model of Kainji Reservoir	131
4.2	Result and Analysis (Objective Two): CA-Markov Sediment Effect Forecasting	134
4.3	Result and Analysis (Objective Three): CA-GBR Sediment Effect Forecasting	137
4.4	Summary	139
5	CHAPTER FIVE: Result and Analysis (Objective Four)	141
5.1	Introduction.....	141
5.1.1	Land Use Land Cover Classification Scheme of Kainji Reservoir and Environs.....	141
5.1.2	Drainage Network and Catchment Area Analysis of Kainji Reservoir.....	145
5.1.3	Linear Aspects of Kainji Reservoir Catchment.....	147
5.1.4	Aerial Aspect of Kainji Reservoir Catchment.....	148
5.1.5	Drainage Texture of Kainji Reservoir Catchment.....	149
5.1.6	Relief Aspect of Kainji Reservoir Catchment	150
5.2	Universal Soil Loss Equation Model of the Kainji Reservoir Catchment.....	151
5.3	Flood Vulnerability Impact Assessment.....	153
5.4	Summary	156
6	CHAPTER SIX: Conclusion and Future Outlook of the Research.....	158
6.1	Conclusion	158
6.2	Future Outlook of the Study	160
7	LIST OF REFERENCES	161
8	Appendix 1: Python script of CA – MC	183
9	Appendix 2: Python script of CA – GBR.....	187
10	Appendix 3: Journal Publications	190

LIST OF TABLES

Table 2:1 Nominal speed of sound and medium (Source: Urick, 2013)	10
Table 2:2 Comparison between wider beam and narrow beam echo sounders (http://www.acousticsunpacked.org)	22
Table 2:3 Motion parameters required for Hydrographic Surveys (Source: Reproduced in the lab from Lekkerkerk and Theijs, 2017)	43
Table 2:4 GNSS and differences in parameters. (Source: Kai-Wei et al., 2010)	48
Table 2:5 Group of Loss functions	71
Table 3:1 Datasets for the study	84
Table 3:2 Descriptions and specifications HD380 Digital Echo Sounder.....	85
Table 3:3 Descriptions and specifications of the Hi-Target HD-Lite Echo Sounder	85
Table 3:4 List of some equipment used (Source: Research book)	86
Table 3:5 Established Controls at the Reservoir corridor (Unit: Metre).	88
Table 3:6 Sample result of a Barcheck calibration of 24 th March 2020. Time: 0902 hrs (Source: Field record book).	90
Table 3:7 Daily reservoir water level below datum	92
Table 3:8 Sounding operation schedule (Source: Research lab)	93
Table 3:9 Cross-validation/split – sample technique outcome (Source: Research lab)....	102
Table 3:10 Depth classified according to Markov states.....	106
Table 3:11 Quality and accuracy evaluation of forecasted bathymetric surfaces. The change is the difference between CA – Markov and CA – GBR, neglecting the negative signs. The measurement is meter (m).	110
Table 3:12 Description of data used for classification and drainage network analysis. Source: https://earthexplorer.usgs.gov/	111
Table 3:13 Some morphometric parameter determination equations from the DEM. The parameters in the equations are computed directly except for the Kirpich equation with a constant $K = 0.01947$. Source: Research lab from the literature as cited.....	113
Table 3:14 NN value based on terrain slope (Source: Robert and Hilborn, 2012).....	116
Table 4:1 Kainji Reservoir depth volume comparison. The volume is in billion cubic metres (BCM) with a contour interval of 4 m. Source: Research lab	128
Table 4:2 Sediment yield from different models. Source: Research lab	130
Table 4:3 Transition probability matrix of the Markov chain states in percentage.....	136
Table 5:1 Area statistics of LULCC conversions (1990 – 2005, 2005 – 2020). This shows the land use land cover area changes over the period under investigation. The dash sign (–) indicates the transition from one class to another e.g. Bare ground to built up or water to water etc. Source: Research lab	142

Table 5:2 Linear Aspects of the Kainji Reservoir catchment (Source: Research lab) 146
Table 5:3 Aerial aspect of the Kainji reservoir catchment (Source: Research lab)..... 146
Table 5:4 Drainage texture of the Kainji reservoir catchment (Source: Research lab) 146
Table 5:5 Relief aspect of the Kainji reservoir catchment (Source: Research lab) 147
Table 5:6 USLE model results of the Kainji reservoir and catchment 152
Table 5:7 Flood risk vulnerability class and towns. Source: Research lab. 154

LIST OF FIGURES

Figure 1:1 The Source and Discharge of River Niger 2

Figure 1:2 Map of the Study Area- Kainji Dam. Source: The map was produced using QGIS software and Google Earth Engine in the research lab. 3

Figure 2:1 The relationship between sound and waves in water (Source: Research lab.) ... 8

Figure 2:2 Longitudinal and transverse waves (Source: Silvia, 2015)..... 9

Figure 2:3 Frequency with common hydrographic and seismic systems. Source: The idea was obtained from (Lekkerkerk and Theijs, 2017) and replicated in the research lab. 10

Figure 2:4 Acoustic depth measurement (Source: USASC, 2002) 11

Figure 2:5 Passive Sonar Tow Array in Action..... 12

Figure 2:6 Schematic Active sonar installed in a sonar dome below the ship 13

Figure 2:7 Major components and basic principles of echosounders. This is based on the sequence of single beam echosounder schematic operations. Source: Lubis and Pujiyati, 2016 16

Figure 2:8 Showing the derivation process of Target Strength (Source: Replicated in the research lap. The ideal is from Urick, 2013) 17

Figure 2:9 Working principles of Single Beam Echo Sounder 20

Figure 2:10 Wide beam and a long pulse (Source: Research Lap) 21

Figure 2:11 Narrow beam and short pulse (Source: Research lab) 21

Figure 2:12 Illustration of depth measurement using a single narrow and wide beam (Source: IHO: C-13, 2010) 23

Figure 2:13 Echo sounders footpath (a) Single-beam (b) Multibeam 23

Figure 2:14 Schematic representation of Sweep Echosounder in action for 25

Figure 2:15 MBES in action mapping the seafloor 26

Figure 2:16 Theory of side-scan sonar data collection during one sound transmission..... 28

Figure 2:17 Power patterns from a two-element array: (a) Broadside, (b) end-fire, 29

Figure 2:18 Example of radiation power patterns 30

Figure 2:19 Constructive and destructive dipole projection of 31

Figure 2:20 Hydrophone Array with a Perpendicular 32

Figure 2:21 Description of each ensonified strip and ensonified area at the mills cross (Source: Donghwan et al., 2017). 33

Figure 2:22 A plane acoustic wave of wavelength (λ) incident under angle θ on a vertical array of N discrete transducer sensors (source: Bjorno, 2017). The wavelength (λ) in the figure is presented by the parallel lines incident under angle θ 35

Figure 2:23 Wavefronts Striking a Hydrophone Array from a Source at Angle θ . Source: L-3 communication seabeam instrument, 2000.....	36
Figure 2:24 Main Lobe Shifted to Angle θ by Introducing a Time Delay.....	37
Figure 2:25 Two acoustic beams of a Doppler sonar in a Janus configuration.....	39
Figure 2:26 SVP – Hy1201AB series (Source: Hydrate.en.made)	40
Figure 2:27 Sound speed, salinity, and sound profiles in the	41
Figure 2:28 The Cartesian right-handed coordinate system of a vessel.....	42
Figure 2:29 A resolved Cartesian coordinate system of a vessel	43
Figure 2:30 Ideal sinusoids of both spring and neap tides	45
Figure 2:31 Description of the three types of tides (Source: sailingissues.com).	45
Figure 2:32 Chart Datum establishment (Source: dragons8mycat.com).....	47
Figure 2:33 Description of GPS segments (Source: owaysonline.come).....	49
Figure 2:34 (a) Good DOP and (b) Poor DOP (Source: tstarmet.com and modified in the research lab).....	50
Figure 2:35 Position fixing using GPS (Source: owaysonline.com).....	51
Figure 2:36 Description of the principle of DGPS real-time measurement of the survey vessel. Real-time position determination allows the position of points below the waterbody to be fixed. (Source: fao.org).....	53
Figure 2:37 A typical 3D reservoir sediment profile.....	56
Figure 2:38 One-dimensional arrays of CA. In which the label black.....	76
Figure 2:39 (a) Von Neumann neighbourhood, (b) Moore neighbourhood.	77
Figure 2:40 Voronoi based on the spatial CA model (a), Regular CA with regular arrays	78
Figure 3:1 The composite framework of the research methodology. Source: Research lab	83
Figure 3:2 Description of the schematic approach used to determine bathymetry and sediment thickness from dual-frequency (100/10 kHz) echo sounding data.....	87
Figure 3:3 Jacksonville district calibration method (Source: USACE, 2002).....	91
Figure 3:4 Kainji Reservoir daily water level below datum: It shows the tidal pattern within the sounding period. The range is 0.9 m within the echo sounding period, while the highest tide was 0.88 m. Source: Research lab.....	92
Figure 3:5 Point cloud bathymetry data (Source: Field observation/research lab as for the 2020 data and the 1990 that was provided by Mean Stream Dam: Managers of Kainji Dam, Nigeria. The 1990 bathymetric data was capture using SBES at 200kHz)	94
Figure 3:6 QGIS interface during reservoir bathymetric information development.....	95

Figure 3:7 Design of cross-sections and profiles (Source: The image was downloaded on 14. February 2021 and processed in the research lab). P indicates profile while CS stands for cross section. Source: Google Earth Pro, 2020..... 96

Figure 3:8 Neighbourhood algorithm on cell 5 (Source: Research lab)..... 97

Figure 3:9 Flow diagram of sediment thickness and long-term average accumulation rate and storage capacity determination (Source: Research lab)..... 99

Figure 3:10 Description of the split-sample technique for assessing and quantifying interpolation errors. Source: Replicated in the research lab from the idea of Hare et al. (2011)..... 101

Figure 3:11 Flow diagram of the CA-Markov model for predicting future depth changes due to sediment deposits in the Kainji reservoir (Source: Research lab). 103

Figure 3:12 Generated contours from linear interpolation. According to these plots, it is clear that the limiting depth decreases with time due to sedimentation and siltation from 104

Figure 3:13 CA significant neighbourhood template. The cell to be defined is highlighted in red, significant neighbours are highlighted in white, and insignificant neighbours are black. Source: Research lab..... 105

Figure 3:14 Flow chart for conducting the CA-GBR model for predicting future depth changes due to sediment deposits in the Kainji reservoir. Source: Research lab..... 108

Figure 3:15 Flow diagram of land use/land cover methodology (Source: Research lab). 111

Figure 3:16 Methodology flow diagram of drainage and catchment area delineation (Source: http://webhelp.esri.com/arcgisdesktop/9.3/printBooks_topics.cfm?pid=6050 and modified in the Research lab)..... 113

Figure 3:17 Conceptual framework of general flood assessment (Source: Merz et al., as cited by de-Moel et al., 2015)..... 117

Figure 3:18 Downloaded contour data (a) and superimposed bathymetric contours on downloaded contour data (b) for interpolation to generate a digital elevation model (DEM) for flood hazard assessment..... 117

Figure 4:1 RBIS of Kainji Reservoir and Lake superimposed on the OSM standard. The map was generated at a scale of 1 in 150,000 on a paper size of A2 (Source: Research lab) 120

Figure 4:2 Cross sections of lines 1 to 4. The scale of the graph is $0.01 m = 1 km$ “i.e., $0.02 m = 2 km$ ” and $0.01 m = 10 m$ on the X and Y axes, respectively..... 121

Figure 4:3 Cross-sections of lines 5 to 8. The scale of CS5 is the same as that of Figure 4.1. Additionally, they all have equal horizontal scales, but the vertical scale differs at some points where the depth values increase. The vertical scale of CS6 to CS8 is $0.01 m = 20 m$. Source: Research lab. 122

Figure 4:4 Percentage slope from CS1 to CS4 (Source: Research lab) 123

Figure 4:5 Percentage slope from CS5 to CS8 (Source: Research lab) 124

Figure 4:6 Longitudinal profile and slope from upstream to the embankment..... 125

Figure 4:7 Maps of Kainji Reservoir describing (a) sediment thickness (contour intervals of 0.5 m) and (b) long-term average sediment accumulation rates (contour intervals of 0.01 m/y). Source: Research lab..... 126

Figure 4:8 Elevation capacity curve of the Kainji reservoir. The volume presented is computed from the LF and HF of 2020 acquired bathymetric data and the received HF_1990 bathymetric data. Source: Research lab..... 127

Figure 4:9 100% stacked column chart of 1990 and 2020 computed volume. The graph shows the relative loss in volume to depth between the two epochs of data. Mainly, it compares the percentage that each depth range value contributes from each dataset to the computed volume of that section. Source: Research lab. 129

Figure 4:10 Reservoir capacity curve from 1990 and 2020_200 kHz data 130

Figure 4:11 Digital depth model relief of Kainji Reservoir generated using a TIN technique from datasets of 1990 and 2020 high-frequency pulses (Source: Research lab) 131

Figure 4:12 3-D display of the Kainji reservoir of 1990 (a) and 2020 (b). The 3-dimensional models describe the reservoir from the water level to the reservoir bed, and the colour scale shows the difference and loss in storage capacity. The content of the basin at each moment indicates its storage capacity and can be determined at every depth range (see Table 4.1). (Source: Research lab). 132

Figure 4:13 Residual plots from the split-sample evaluation method employed using TIN DD modelling. The error outcome is dominated with an error range of -1 m to 1 m on the residual of 1990 and -0.5 m to 0.5 m on the 2020 residual as computed. Hence, the residual maps are encompassed by one colour scale (source: Research lab)..... 133

Figure 4:14 3-D model of residual 1990 data (a) and 2020 data (b). The three-dimensional model shows the maximum pecks caused by the steep slopes created by some points that are deeper than neighbouring points. The flatness of some regions is within the value of -1 m and 1 m. However, zero is the most dominant (Source: Research lab)..... 134

Figure 4:15 Contour plots for depth states based on historical data. Horizontal and vertical scale readings are in metres (m). The plots present the Markov chain depth states based on the transformation conducted on the historical datasets of 1990 and the measured datasets of 2020. Source: Research lab. 135

Figure 4:16 CA-Markov historical and forecasted plots. The vertical scale is the Markov states in all plots. The predicted plot (Markov 2050) contains artifacts caused by the uncertainty of the modeled Markov states. However, this assertion is subject to future investigation. Source: Research lab..... 137

Figure 4:17 CA-GBR historical, measured and forecasted plots. The vertical scale is in meter (m). The projected surface is without artifacts, indicating that CA-GBR is most suitable for predicting future bathymetric data that are affected by sedimentation and siltation. Source: Research lab..... 138

Figure 5:1 Land use land cover (LULC) maps of Kainji Reservoir and environs from three epoch datasets “1990, 2005, and 2020”. Source: Research lab 142

Figure 5:2 Stream network superimposed on the elevation map (a) and aspect in degree of Kainji reservoir. Source: Research lap 145

Figure 5:3 Flow accumulation superimposed on drainage basins (a), stream junctions and 2020 bathymetric map (b). Source: Research lab..... 146

Figure 5:4 Slope steepness in degree (a) and slope steepness in percent (b). 152

Figure 5:5 Flood impact map of potential Kainji dam failure. The broad spectrum predicted flood map indicates the spatial extents that are expected to inundate in the event of dam failure..... 154

LIST OF PLATES

Plate 2:1 Oceanograf Gdynia at the dock at the Hel marine station with one of the summer school students standing in position. Source: Photographed by one of the students after returning from field exercise. 61

Plate 2:2 Deployment of SVP for sound velocity measurement. (a) SVP with its compartment before launching. (b) Launching of the SVP in the Poland region of the Baltic Sea. (c) Downloading and uploading the SVP data from the SVP to the computer system with real-time bathymetric processing Quincy software. Source: Ecomap summer school 2019 62

Plate 2:3 (a) Modified Van Vee grab before Lowering down the sea, 63

Plate 2:4 (a) Bathymetric backscatter data without settings for corrections, 64

Plate 2:5 (a) Bathymetric image of a boat wreck with a vertical impact value of 10,..... 64

Plate 2:6 (a) Showing the Ship image location and passing on the scan at the bottom, 65

Plate 3:1 Base station (a), Rover in static mode (b). Source: Research field book 89

ACRONYMS

A – Basin Area
 AG – Array Gain
 AUV – Autonomous Unman Vehicle
 BCM – Billion Cubic Meters
 BS - Backscattering Strength
 CA – Cellular Automata
 CA – Coarse Access code
 CA-ffe – Cellular Automata Fast Flood Evaluation
 Cc – Compactness coefficient
 CS – Cross Section
 CTD – Conductivity Temperature Depth
 CTMC – Continuous time Markov chain
 dBs – Decibels
 Dd – Drainage Density
 DDM – Digital Depth Model
 DGPS – Differential Global Positioning System
 DI – Receiving Directivity Index
 DNA – Deoxyribonucleic acid
 DOP – Dilution of Precision
 DP – Dynamic Positioning
 Dpi – Dots per inch
 DT – Detection Threshold
 DTM – Digital Terrain Model
 DTMC – Discrete-time Markov chain
 EEZ – Exclusive Economic Zones
 EL – Echo Level
 GBR – Gradient Boosting Regression
 GDOP – Geometric Dilution of Precision
 GIS – Geographical Information System
 GNSS – Global Navigation Satellite System
 GPS – Global Positioning System
 HAT – Highest Astronomical Tide
 HF – High Frequency
 Hz - Hertz
 IHO – International Hydrography Organization
 INS – Inertial Navigation System
 ISI – International Sediment Initiative
 kHz – Kilo Hertz
 LAT – Lowest Astronomical Tide or Mean Low Water
 Lb – Basin Length
 LBL – Long Baseline system

LF – Low Frequency
Lg – Length of overland flow
LHDA – Lesotho Highlands Development Authority
LR – Logistic Regression
Lu – Stream Length
LULC – Land Use Land Cover
LW – Low Water
MBES – Multi Beam Echo Sounder
MC – Markov Chain
MHz – Million Hertz
MLLW – Mean Lower Low Water
MLLWS – Mean Lower Low Water Springs
MLW – Mean Low Water
MRn – Melton Ruggedness
NL – Ambient Noise Level
NL – Noise Level
NL – Self-Noise Level
NOAA – National Oceanic and Atmospheric Administration
Nu – Stream Order and Stream Number
OpenDEM – Open Digital Elevation Model
OSM – Open Street Maps
P – Basin Perimeter
PCA – Principal Component Analysis
P-code – Precision code
Pr – Relative perimeter
QGIS – Quantum Geographical Information System
R – Basin Relief
Rb – Bifurcation Ratio
RBIS – Reservoir Bathymetric Information System
Rc – Circularity Ratio
Re – Elongation ratio
Rf – Factor Ratio
Rf – Fitness ratio
RL – Reverberation Level
RMSE – Root Mean Square Error
Rn – Ruggedness number
R_r – Relief ratio
SBES – Single Beam Echo Sounder
SBL – Short Baseline systems
SE – Signal Excess
Sf – Shape factor ratio
Sf – Stream Frequency
SL – Source Level

SL – Target Source Level
SNR - Signal to Noise Ratio
SSBL – Super-Short Baseline
SVP – Sound Velocity Profile
T – Drainage Texture
TA – Target Area
TASS – Towed Array Sonar System
 T_{ch} - Concentration Time
TIN – Triangulation Irregular Network
TL – Transmission Loss
TS - Target Strength
USACE – US Army Corps of Engineers
USBL – Ultra-Short baseline systems
USLE – Universal Soil Loss Equation
UTM – Universal Transverse Mercator
WGS84 – World Geodetic System 84
WQI - Water Quality Index

LIST OF SYMBOLS

c – Speed of sound/ velocity
 f – Frequency
 λ – Wavelength
 T – Period
 Ψ - long pulse regime
 T - Short pulse regime
 θ – Angular view
 δ – Relative phase between two emitters
 G – power spectrum function
 f_d – doppler shift
 T – Temperature
 Δt – Change in time
 ppt – parts per thousand
 ϕ – latitude
 R – satellite range from user
 PR – pseudo range
 Y – sediment yield
 V_0 – original reservoir capacity
 V_r – reservoir capacity at the most recent bathymetric survey
 t_0 – beginning of the reservoir operation
 t_r – date of the most recent bathymetric survey
 V_i – initial reservoir volume
 V_f – final reservoir volume
 $t_{1/2}$ – half-life of a reservoir
 Pr – conditional probabilities
 δ_{ij} – Kronecker delta
 Q – nonnegative matrix
 $.L(y_i, f(x))$ – differentiable loss function
 $.S_{t+1}$ – Markov transition state
 k – system index constant
 dr – transducer drift
 P_{ij} – transition probability matrix
 K – soil erodibili

1 CHAPTER ONE: Introduction

1.1 Background to the Study

A more significant percentage of the earth is covered with water, and effectively mapping out these areas is possible via a hydrography survey. The data obtained through the hydrographic survey are known as bathymetric data. Bathymetric data are components that adequately present information about a given water body, showing depths and underwater configurations (David, 2000; Amante and Easkin, 2016; Stefan, 2017). The presentation of the waterbody bed's nature is synonymous with a topographic map of land areas (Ingham, 1984; Hare *et al.*, 2011; Smith and Marks, 2014;). Similarly, the information acquired from the activities of hydrography aids in a better understanding and interpretation of marine navigation, dredging, offshore oil and gas exploration drilling, marine construction and other related operations within and outside the water body environment (Ingham, 1984; Ojigi *et al.*, 2010; Hell *et al.*, 2012; IHO, 2018). The numerous advantages offered by humanity by global oceans and other waterbodies make the study of water bodies a vital field of research to humans (Chukwu and Badejo, 2015). The roles played by these natural and artificial gifts of nature call for continuous investigation and management (Ibrahim and Sternberg, 2021).

Similarly, reservoirs are constructed perpendicular to a river to collect water flowing from the upper region for hydroelectric power generation, water supply for domestic use, irrigation, and possible fishing. However, the geomorphometric characteristics affect the catchment stream flow patterns by influencing the concentration-time (Jones, 1999; Mentzafou *et al.*, 2021).

1.2 River Niger and Nigeria

The four principal rivers of Africa are the Nile (4,160 miles), the Congo (2,900 miles), the Niger (2,590 miles) and Zambezi (1,700 miles). Additionally, River Niger is the principal river of western Africa, with a drainage basin area of approximately 2,117,700 km². The River Niger passes through four countries: Guinea (Source), Mali, Niger Republic, Benin, and Nigeria. (Welcomme, 1986; Gleick, 2000). Its primary source is the Tembi River, and other tributaries join and replenish the Niger River. The significant sources lie within the Guinea Highlands in southeastern Guinea, and other branches also join as it flow through

countries. The blue line in Figure 1:1 describes the Niger River from its source to where it is empty.



Figure 1:1 The Source and Discharge of River Niger
 (Source: <https://geography.name/niger-river/>)

Similarly, the length of River Niger in Nigeria is approximately 710 miles, with an average width of 1.24 miles. The Niger flows through eleven Nigerian states and joins the Benue River to form a vital confluence. The Niger heads southward, empties into the Niger delta, and finally discharges into the Gulf of Guinea or the Atlantic Ocean (Inger et al., 2005).

Consequently, the Kainji dam was constructed perpendicular to the River Niger in 1968, and it is the largest dam on the Niger River. Kainji has a main concrete dam with rockfill embankments and a saddle dam. The saddle dam protects the main dam during flooding. There are four spillways with hydraulic operated gates of 15.2×15.2 m, which are used to control flooding and supply water to the Jebba dam downstream. The dam has a maximum depth of 85.5 m and 4.971 miles in length before joining the lake upstream. The lake and the dam are wholly joined together; the total length is approximately 59.03 miles, as shown in Figure 1:2. Figure 1:2 is the map of the study area describing Kainji Dam. The Kainji dam is located in Niger State, while the lake, which serves as a supporting reservoir, is bordered by Kwara, Kebbi and Niger states. The geographical extent of the entire reservoir is $10^{\circ}36'40.16''$ N, $4^{\circ}31'08.11''$ E; $9^{\circ}51'17.55''$ N, $4^{\circ}36'03.48''$ E; $10^{\circ}21'24.46''$ N, $4^{\circ}40'46.59''$ E; and $10^{\circ}22'53.66''$ N, $4^{\circ}17'13.64''$ E.

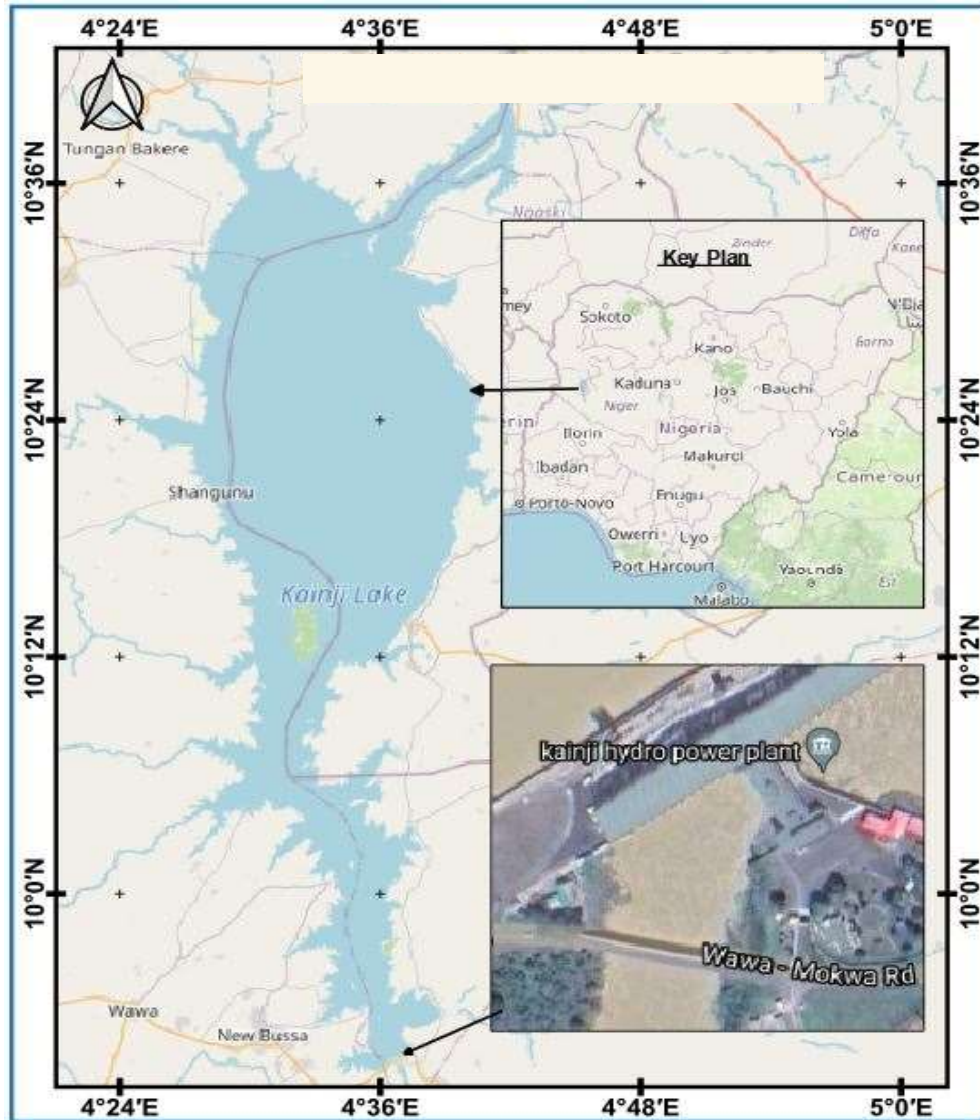


Figure 1:2 Map of the Study Area- Kainji Dam. Source: The map was produced using QGIS software and Google Earth Engine in the research lab. The dots per inch (dpi) were 55 with a height pixels of values of 448 and 640, respectively. Additionally, the image in the lower right part of Figure 1:2 shows the location of the hydropower plant, major and minor access road, and other vital structures, such as offices and security checkpoints.

1.3 Statement of Problem

There has been a renewed interest of the Nigerian governments in water transport and navigation to boost and enhance its industrial, international maritime and socioeconomic services, which led to an award of the dredging contract of the Niger River from Baro to Warri in September 2009 (Ojigi et al., 2010). However, this has not yielded any good

result, as the project has been abandoned. It follows that reservoirs play an essential role in the water resource development and the economic development of any region. Sedimentation is the gradual and continuous transportation of eroded particles, “both gravel and sand”, that accompany the flow of a river or any moving water body ([Cui et al., 2006](#)). Damming a river also entails trapping the sediment and silt, which in turn affects the effective life of any reservoir by reducing the functionality of hydropower generation, poor irrigation, and risk of early flooding over time ([Cui 2007](#); [Girish et al., 2014](#)).

Kainji Reservoir was constructed across Niger River in 1968 to store water for economic development to the region, country and other nations. The hydroelectric power being generated is supplied to the Ghana and Benin republic. The sediment load carried by Niger from upstream is trapped in the basin, primarily at the reservoir axis. If not investigated, this is a continuous process that may cause devastating damage to the infrastructure and neighbouring environment. Interestingly, recent improvements utilize the daily and yearly discharge record to compute and predict the accumulated sediment over time. This approach does not accurately account for the spatial loss in depth. Another method being used is the utilization of a dual-frequency echosounder, where the difference is the loss in depth. This method also only accounts for the loss at present.

Naturally, a better approach to effectively account for the spatial loss in open channel depth due to sedimentation and siltation will be adequate using multiple epoch bathymetric charts. Equally, having a series of bathymetric datasets and considering the trend, a projection can be made for better and accurate future planning. Thus, it will be remarkable to map out the Kainji dam of the river Niger axis and possible forecast what the reservoir depth will represent in the future based on the present phenomenon.

Therefore, this research attempts to address these challenges by utilizing existing and present bathymetric datasets to model the change and forecast the spatial depth depending on the current trend. However, the following questions need to be addressed:

- i) Is there any recent bathymetric chart of the Kainji dam?
- ii) What is the maximum and average depth and width of the Kainji dam in the river Niger axis?
- iii) What is the state of the dam compared to when it was constructed?

- iv) How can the data be modelled to form information that will aid sediment deposit analysis and forecasting?
- v) Which method of predicting will be the best based on the data?
- vi) What are the major scientific contribution to sedimentation?

1.4 Aim and Objectives of the Study

This research aims at employing bathymetric survey data for assessing and forecasting the rate of sediment deposits in Kainji Reservoir across the Niger River in Nigeria. The following objectives were implemented to achieve the aim of this research to:

- i) design and execute an underwater topographic profile survey, produce a bathymetric chart and 3-D models of the dam for ease of assessment.
- ii) carry out sediment deposit analysis of the study area and forecast by the use of Cellular Automata - Markov chain.
- iii) employ cellular automata and gradient boosting regression models to measure the accuracy of objective (ii) above.
- iv) investigate the scientific contribution to sediment deposits from river catchment analysis and model flood scenarios.

1.5 Scope and Limitations of the Study

This study focuses mainly on developing a reservoir bathymetry information system and investigating the rate of sediment deposition in the Kainji dam from sounding observations using cellular automata – Markov chain (CA–MC) and cellular automata – gradient boosting regression (CA – GBR) models to project the trend of the reservoir in the future. In addition, data from OpenDem were used to assess the scientific contribution to sediment load deposits in the study area.

Furthermore, a hydrography survey was conducted over Kainji Lake of the river Niger axis using Single Beam Echo Sounder (SBES – dual frequency) and its accessories. Hi-Target V30 Differential Global Positioning System (DGPS) – GNSS receivers were used to establish control points at the dam corridor to orient the observations. The bathymetry data of 1990 of the study area were collected from the Power Holding Company of Nigeria, Kainji branch, Niger State.

Finally, the datasets were processed using software such as Quantum Geographical Information System (QGIS 3.16), Microsoft Excel, and Python programming language to write the scripts for the CA – MC and CA – GBR to analyse and forecast the change in spatial depth. The scientific contribution to sediment deposits in the study area was assessed from OpenDEM data using catchment area analysis tools in QGIS and Universal soil loss equation (USLE). However, the major limitation encountered is the non-availability of historical or time series bathymetric data over the study area within an epoch interval of maximum of ten (10) years: a best practice approach. The research as therefore provided a justification for alternative or surrogate bathymetric datasets which is not as perfect as the conventional time series bathymetric datasets over the study area.

1.6 Contributions and Significance of the Study

This research has developed upto-date reservoir information systems for Kainji reservoirs. The underwater profile maps of the study area were modelled and can be used as a national database for decision making.

A new approach for sediment deposit analysis and forecasting was realized in this study. These are the Cellular Automata – Markov Chain and Cellular Automata – Gradient Boosting Regression. These are new innovations in the field of hydrography because bathymetric data were directly used to assess sediment load deposits, and projections were made. Both models were used to forecast the reservoir spatial trend in the future if the sediment inflow pattern continued with the same characteristics. However, the environmental and soil erosion factors will only become aggravated due to the negative effect of climate change. Meanwhile, the forecasting was carried out using a Python programming language, a new development.

Another significant contribution of this study is that the knowledge can be replicated in the fields of hydrography, geodesy, meteorology/atmospheric science, hydrology, and other aspects of environmental science applications. In the field of geodesy, the gravity value is the major component for the determination of geoids, but this value is not readily available in most parts of the world, especially Africa. Thus, this approach can be employed to predict the gravity of other points because of its applications to both discrete and continuous dataset.

2 CHAPTER TWO: Sounding and Hydrographic Surveying

2.1 Introduction

Studies have shown that the mapping of Earth's water bodies is increasing considerably. This is because it is a well-known fact that 71% of the earth is covered with water ([Matt, 2014](#)). Meanwhile, the purpose of surveying the water's is not limited to: resource exploitation – fishing, minerals; environmental protection and management; national marine spatial data infrastructures; maritime boundary delimitation; maritime defence security; recreating boating; coastal zone management; tsunami flood and inundation modelling coastal zone management; tourism; and marine science ([Ingham 1984](#); [IHO, 2021](#)). Thus, “branch of applied sciences which deals with the measurement and description of the physical features of oceans, seas, coastal areas, lakes and rivers, as well as with the prediction of their change over time, for the primary purpose of safety of navigation and in support of all other marine activities, including economic development, security and defence, scientific research, and environmental protection is known as Hydrography, ([IHO, 2021](#))”. However, the role of sound, especially in hydrography acquisition systems, is worth mentioning. This is because they operate on the basis of acoustic energy ([Lekkerkerk and Theijs, 2017](#)). Additionally, acoustics is the process of transmitting and receiving energy periodically, accompanied by waves in or from a body, and an object with such characteristics is the sound wave, which happens to be a longitudinal wave in nature ([Xavier, 2010](#); [Urlick, 2013](#)).

2.2 Description of Sound and Frequency

The ability of sound to travel a longer distance in water and with great clarity compared to when it travels in air resulted in its broad application to study and monitor waterbodies. When a sound ping is released in water, it forms a circular wave spread from the centre, and the energy reduces as the wave continues to travel from the centre equipotential, i.e., spread from the centre with equal distances, and in all directions ([Nieukirk, 2015](#)). A better example of this phenomenon is when a ball-shaped object is thrown into the water, as described in Figure 2.1. This explained how the waves spread with equal pressure in all directions. The compressions and decompressions associated with it change with a definite pattern.

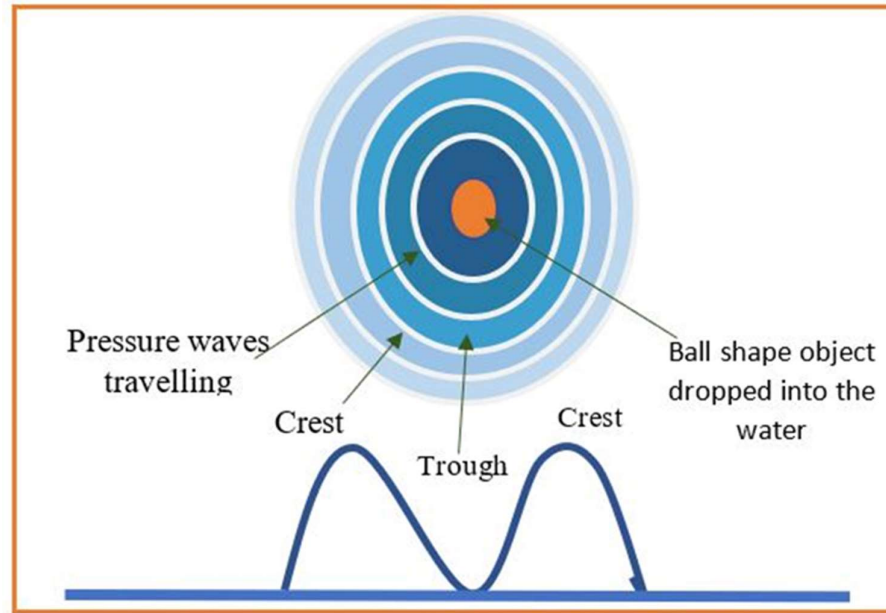


Figure 2:1 The relationship between sound and waves in water (Source: Research lab.)

The reduction in energy per unit area is called the spreading loss. Attenuation and absorption also affect the pings. If a ping experiences both spread loss and absorption loss at the same time, it will be referred to as transmission loss, and this depends on the distance travelled. The longer the distance propagates, the wicker it will get, and at a point, it will eventually die, as shown in Figure 2.1.

In particular, the instrument that uses sound to acquire information is known as sonar, and they are classified based on their frequency of operation, which also determines their accuracy. Sound travels in water with an actual speed and with a compressional wavefront, and it can be affected by the constituent of the waterbody, e.g., salinity, temperature and pressure. The well-described speed of sound in water is an average of 1500 meters per second (1500 m/s). The distance covered by the wavefronts is known as the wavelength, while the number of successive pressure fronts (wavefronts) in the water per unit time is the frequency; the former is measured in meters (m), while the latter is measured in Hertz (Hz) and always in a cycle (L-3 Communication Sea-Beam Instruments, 2000; Richard, 2010).

However, the propagation of waves is either transverse or longitudinal depending on the medium of propagation, as described in Figure 2.2. When a sound experiences a change in direction, the wavelength changes, but the frequency remains the same; this is why it is described by its frequency and not the wavelength. The size of the oscillation is the

amplitude of the wave. The amplitude is related to the acoustic energy. “Acoustic energy is the energy carried by a sound wave and can be detected by a device known as hydrophone” being transmitted in the wave. A higher amplitude carries higher energy, and the vertical distance between one successive wavefront (crest and trough) is the amplitude (Ingham, 1984, L-3 Sea-Beam Instruments, 2000; Silvia, 2015).

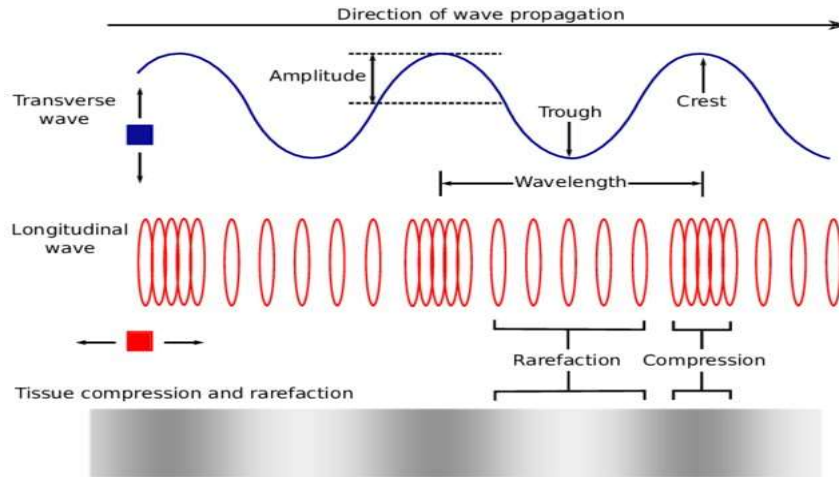


Figure 2:2 Longitudinal and transverse waves (Source: Silvia, 2015)

The relationship that exists between the three parameters is presented as:

$$c = f \times \lambda \tag{2.1}$$

where c is the speed of sound or the medium propagation velocity (s), f is the frequency (Hz), and λ is the wavelength (m). The time it takes to complete one vibration cycle is related to the frequency by $T = 1/f$. Therefore, the overall relationship will be;

$$\lambda = cT = \frac{c}{f} \tag{2.2}$$

Underwater acoustic systems are usually made of frequencies ranging from $10Hz$ to $1 MHz$ depending on the application (Xavier, 2010); see Figure 2.2. For an average sound velocity of $1500m/s$, the underwater acoustic wavelength will be $100 m$ at $15Hz$, $1 m$ at $1.5kHz$, and $0.001 m$ at $1.5 MHz$. Figure 2.3 describes the frequency of common hydrographic and seismic systems.

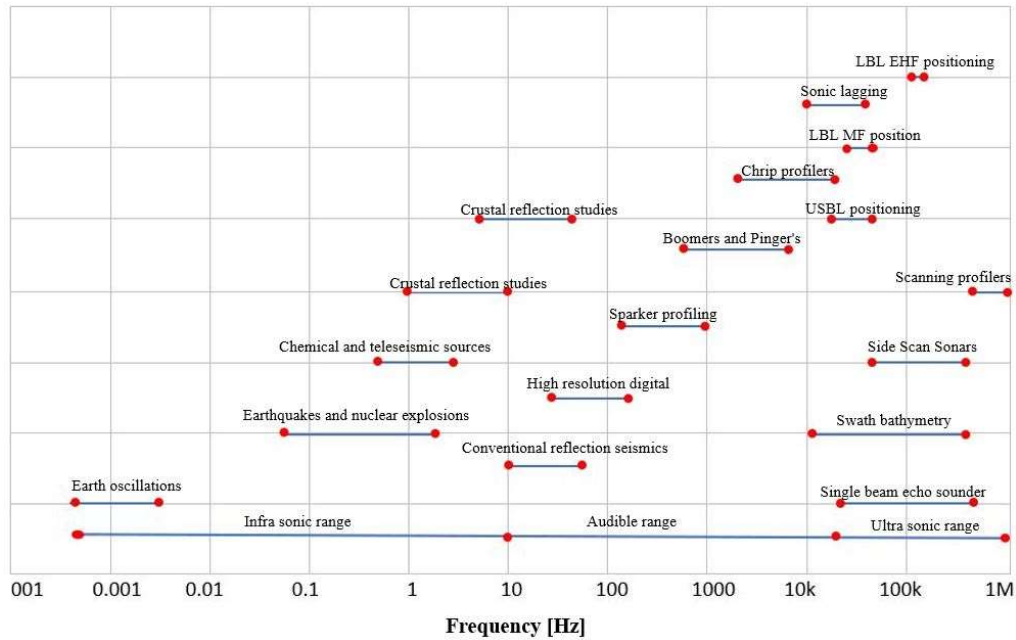


Figure 2:3 Frequency with common hydrographic and seismic systems. Source: The idea was obtained from (Lekkerkerk and Theijs, 2017) and replicated in the research lab.

The main setback to frequencies depending on a specific deployment is sound wave attenuation in water, the dimensions of the sound sources, the spatial selectivity, and the target acoustic response. These factors affect the operation of hydrographic systems; thus, they must be considered when designing a sonar system for a particular application (Xavier, 2010). In general, the principle of echo is undoubtedly the bedrock on which all sonar systems work for adequate transmitting and receiving signals from the transmitter to the target and from the target to the receiver and then to the display unit for interpretation. The table below shows the nominal speed of sound according to their material conductivity.

Table 2:1 Nominal speed of sound and medium (Source: Urick, 2013)

	Material	Speed of Sound (m/s)	Density (g/cm ³)
1	Aluminium (rolled)	6420	2.7
2	Stainless steel	5790	7.9
3	Rubber, Gum	1550	0.95
4	Fresh water (25 ⁰ C)	1498	0.998
5	Seawater (25 ⁰)	1531	1.025
6	Air	331	0.002
7	Seawater	1430 to 1530	

Meanwhile, the denser the medium, the quicker sound travels within that medium. This is because the molecules are closer together; therefore, it is faster for the particles to transmit vibrations to a neighboring molecule.

2.3 Echo Sounding: Principles and Operating Systems

Echo sounding is a process of determining the depths of the waterbody from the water surface to the bottom by transmitting the acoustic signal and the reflection of the signal back to the medium of transmission. This process is termed echo and has enabled hydrographers and other disciplines to understand the happenings on and beneath the waterbody. The depth information obtained is used to produce navigational charts of most rivers, seas and oceans, which in addition aid ship navigation. The depth must be accurately determined based on the registered hydrography standards established by the International Hydrographic Organization and other recognized organizations. To effectively measure depth, an acoustic wave is transmitted and received by the acoustic sounder by the two-way travel time at the instant of observation. The depth is determined by the utilization of a basic principle of echo formulae given as:

$$\text{depth} = c \times \frac{\Delta T}{2} \quad 2.3$$

where c is the speed of sound in water, whose value is given as 1500 m/s on average (Xavier, 2010), and ΔT is the change in transmitting time to the object and the returning time of the signal after interacting with the object. Figure 2.4 shows how depth is measured from the principles of echo (acoustic pulse), where d is the depth relative to the water surface.

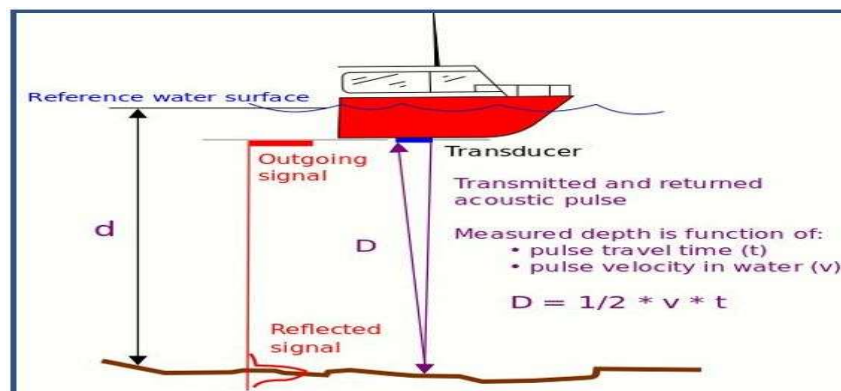


Figure 2:4 Acoustic depth measurement (Source: USASC, 2002)

Usually, the space between the transducer and the reference water surface is the drift and should be accounted for during the actual observation process.

2.3.1 Operating Principles of Sonar

Sonar “sound navigation and ranging” is a device that is usually attached or mounted on a vessel and is being used for detecting and locating objects and mapping the seafloor with the aid of sound. There are primarily two types of sonar sensors, namely, passive and active sonars, and they are distinguished based on their sensitivity and application.

2.3.2 Passive Sonar

Passive Sonar is sonar that is designed to receive signals from external sources and record and interpret the emitted sounds from an object in the water. In recent times, it has found tremendous applications in marine activities, e.g., seismic activities, ship communication, submarine monitoring, military and aquatic habitant investigations. The mode of operation in water is based on towing hydrophones, “a system called TASS (Towed Array Sonar System)”, which records sound waves using a hydrophone, and by processing these signals, we can detect, locate, and classify different targets (Xavier, 2010; Hamed and Farsi, 2018). They are usually enclosed with well-fabricated molds to prevent water from having access to the hose (see Figure 2. 5).

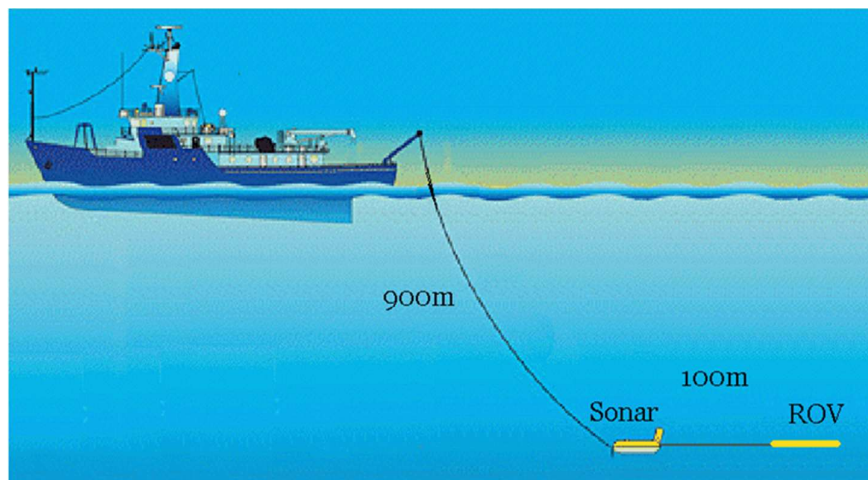


Figure 2:5 Passive Sonar Tow Array in Action
(Source: <https://cellcode.us/quotes/finder-scan-lowrance-fish>)

They are launched using specific hoisting machines on vessels or submarines. The length of the towed arrays is so long that they are efficient enough both in terms of signal-to-noise ratio (SNR) gain and angular resolution. Precisely, these kinds of systems are basically for other professional field-based applications and not for accurate waterbed mapping.

2.3.3 Active Sonar

These are sonars that emit signals and receive the reflected signals from the object and then send the signals received to the display unit. The unique aspect of these sets of devices is their ability to produce sound waves of definitely controlled frequencies and receive the signals via echoes from the remote object in the water. Active sonar systems involve the transmission and reception of one or more probing sequences, which provide a basis for the extraction of target information in a region of interest (Jun and Jian, 2011). Because of its unique operating technique, it has found wide application in-depth determination. For this reason, all waterbody instruments are active sonar. Figure 2.6 is a schematic representation of a hull-mounted active sonar system that describes how the active sonar works by sending pulses down to the target or seafloor. The returned signal called echo is used to analyse, dictate, and locate the object.

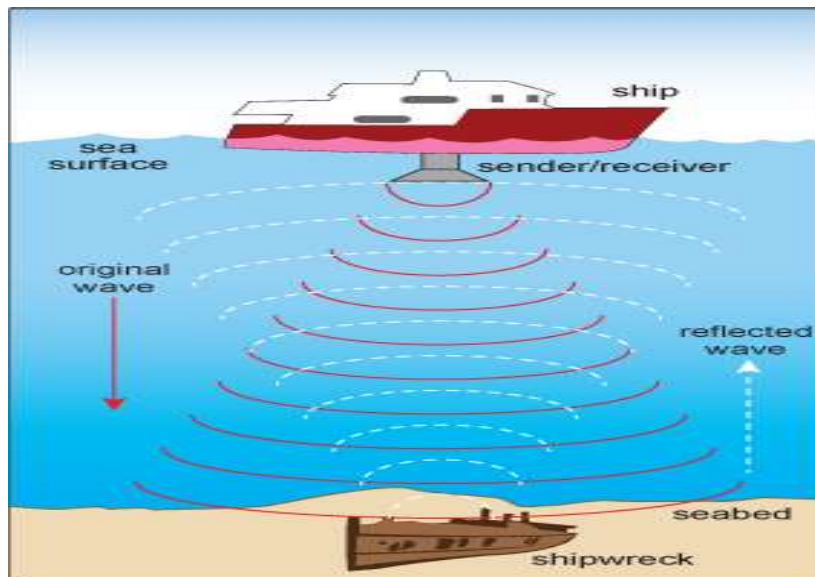


Figure 2:6 Schematic Active sonar installed in a sonar dome below the ship
(Source: <https://www.open.edu/openlearn>)

The geometry of this device that has flourished is a cylindrical shape, which has made it possible to produce horizontal beams and a few vertical beams. Other geometrical shapes are possible, e.g., spherical shapes, but one challenge with this shape is that mechanical design and array processing are too demanding but provide better 3-D scanning of the water column. The ship's speed determines the efficiency of the hull-mounted array due to the noise level increase and is occasionally masked as a result of a local increase in noise and absorption caused by the propeller and wake (Tellez et al., 2017).

2.3.4 Limitations of Active and Passive Sonar

Several limitations are confronting both active and passive sonar, which are not limited to background noise, changes in water density, murky water and time delays; these setbacks affect the overall performance of sonar devices. An abridge explanation according to [Justin, 2004](#); [Maranda, 2008](#); [Xavier, 2010](#); [Urlick, 2013](#); and [NOAA, 2021](#) as:

- i) **Background noise:** ideally, sonar must transmit and receive signals (active or passive sonar); an object makes for effective communication to the display unit. Background noise or ambient noise and supporting vessel speed, marine habitats and tectonic/volcanic or machinery activities all generate noise that affects sonar performance. The deeper the object is from the surface of the sea, the greater the probability that the background noise will overshadow it. To effectively counter these challenges is to use louder signals, but this may have a negative effect on aquatic animals.
- ii) **Changes in water density** are the constituents of the water column affecting the efficiency of both active and passive sonar; these constituents are the temperature, salinity and pressure. Warm water is lighter than cold water; as the surface of the water is heated by the heat of the sun, the surface becomes warmer while the bottom becomes colder. This often causes reverberation, and to control this, is by enhancing the spatial selectivity of the signal used (wide band, very narrow directivity lobes in reception or by using through narrow-band frequency filtering “the differences in the doppler shifts of the target and reverberation echoes”).
- iii) **Murky water:** the foggy nature of some water body because of swarm be suspended on/in the water, the suspended particles can be of mud, air bubbles, crystals, plankton any other materials that reflect signals in so doing gives a poor or wrong interpretation and presentation of the seafloor. They can be a result of seabed explorations, military activities or a situation where rivers carrying silts meet the ocean. Passive sonars are not left out of these challenges.
- iv) **Time delay:** The average speed of sound in water is within the neighbourhood of 1450 to 1500 metres per second but 343 metres per second in the air at

room temperature and pressure. It is expected that sound travels through denser water faster and slower in warmer or pure water (sound travels faster in liquid, solid and slower in gases). This explained why most bathymetry sonars process data using the time and amplitude method for better resolution and accuracy instead of the phase comparison method.

2.3.5 Transducer

The term transducer refers to both hydrophone and projector devices ([L-3 communication sea-beam instrument, 2000](#)). Transducers can be classified basically on transduction “material made off” or by function “purpose and area of application” ([Lekkerkerk and Theijs, 2017](#)). A transducer that converts sound into electricity is called a receiver or hydrophone; a transducer that converts electric energy into sound is called a projector ([Richard, 2010](#); [Urlick, 2010](#)). These two devices are responsible for transmitting and receiving energy from the base to the targeted object back to the base but can be in different locations. The energy that is incident back to the instrument from the bottom of the ocean is referred to as the backscattering strength of the bottom, while the noise level is the magnitude of unwanted signals, limiting the range of any sonar instrument ([Richard, 2010](#); [Lekkerkerk and Theijs, 2017](#)). In general, the function of the transducer can be classified as:

- i) To convert electrical power into acoustic power.
- ii) To send the acoustic signal into the water and
- iii) To receive the echo of the acoustic signal

In addition, a ping and its echo have a transmission loss that makes them weaker and weaker but never gets to zero, but it will get to a situation where it will be difficult to differentiate them from the noise level. The signal-to-noise ratio is the ratio of the signal strength to that of the noise level. It determines the device signal capability to detect an object. Figure 2.7 illustrates the schematic working principles of the transducer.

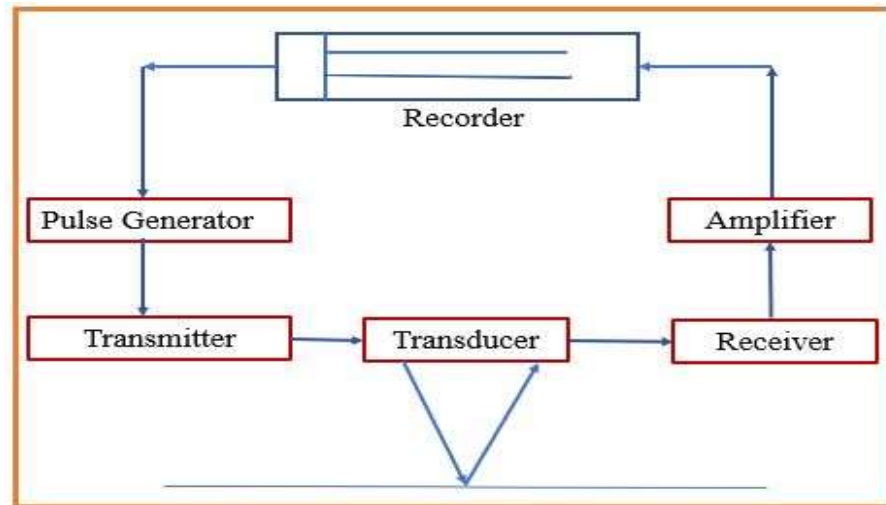


Figure 2:7 Major components and basic principles of echosounders. This is based on the sequence of single beam echosounder schematic operations. Source: [Lubis and Pujiyati, 2016](#); <https://marinegyaan.com/>. However, the idea was replicated in the research lap using the Microsoft PowerPoint application.

2.3.6 Sonar Equation

During sonar operation, some basic challenges are experienced as a result of desired and undesired phenomena. The desired signal can be referred to as the signal, and the undesired signal can also be referred to as the background noise. In the calibration state of the sensor, the challenges of propagation noise, reverberation, signal processing and others are being considered. These considerations can be grouped into three sets of parameters:

- i. The parameters were determined by the equipment: Projector Source Level (SL), Self-Noise Level (NL), Receiving Directivity Index (DI), and Detection Threshold (DT).
- ii. The parameters determined by the medium are transmission loss (TL), reverberation level (RL), and ambient noise level (NL).
- iii. The parameters determined by the target are the target strength (TS) and target source level (SL).

All these factors are considered to enhance the functionality response of the sensor and limit the response from the sensor to the background and, in a simple term, “enhance the signal-to-noise ratio” ([Urick, 2010](#); [Xavier, 2010](#) and [Ying et al., 2018](#)). The detection threshold (DT) measures the return signal required for an operator using installed equipment to detect a target 50% of the time. Consequently, the formulae for the sonar

equation are divided into the active sonar equation and the passive sonar equation (Henry, 1999; IHO: C-13, 2010; Urick, 2010; Xavier 2010) and are expressed as follows:

The Active sonar equation in a simplified way is:

$$\text{Signal} - \text{Noise} + \text{Gain} > \text{Threshold}$$

$$SE = SL - 2TL + BS - NL + TA \quad 2.4$$

Or

$$RT = SL - 2TL + TS - NL + DI + PG \quad 2.5$$

where SE is signal excess, SL is the transmission source level, TL is the two-way transmission loss, BS is the backscattering strength, NL is the noise level, TA is the target area, TS is the target strength; quantifying its capacity to reflect the acoustic energy received, DI is the directivity index associated with the directivity pattern of the receiving signal, PG is the processing gain of the signal and the receiver used, and RT is the reception threshold corresponding to the desired level of performance.

Passive sonar equation is given as;

$$RT = RNT - TL - NL + DI + PG \quad 2.6$$

All other parameters in the equation are as defined above except for RNT, which is the noise level that is radiated by the target, and TL is the transmission loss in one way only. Target strength and reverberation disappear. Usually, all units are measured in decibels (*dBs*). Figure 2.8 below indicates the expression for deriving the target strength.

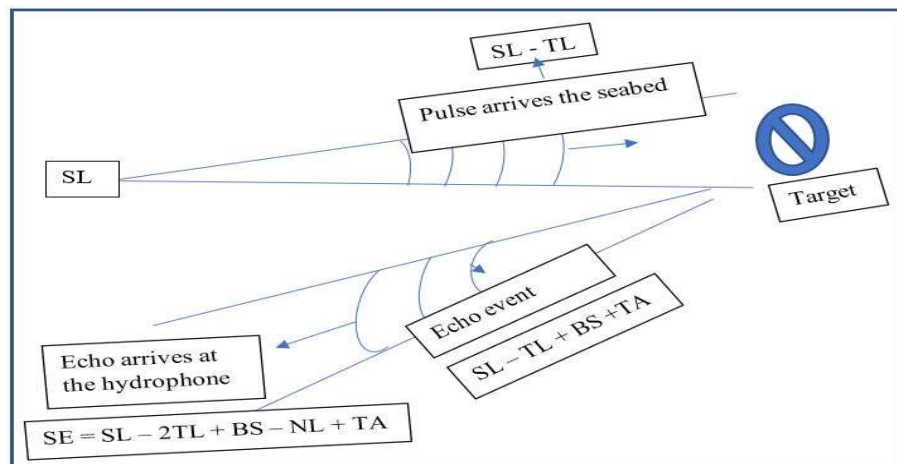


Figure 2:8 Showing the derivation process of Target Strength (Source: Replicated in the research lap. The ideal is from Urick, 2013)

The reception threshold is defined as the minimum signal-to-noise ratio (SNR) value at the receiver output that is capable of detecting an object (Henry, 1999). This makes it possible for a given level of performance to determine the limit, function and application for a given system (Gomes et al., 2004; Xavier, 2010). The reception threshold (RT) is connected to the output SNR r by

$$RT = 10 \log r \text{ (amplitude, or linear receiver) and} \quad 2.7$$

$$RT = 5 \log r \text{ (square law, or power receiver)} \quad 2.8$$

The different form for the square-law receiver ensures the homogeneity of dimensions between the input and output SNR. It is the minimum SNR at the output, while the directivity index is included inside the SNR at the receiver input. Additionally, the detection threshold (DT) is also determined at the input of the receiver; therefore, it produces both the processing gain and the detection index. Although this explanation is weighted on its own, it will be accommodating to consider the separation in the sonar equation analysis distinctly.

The performance of most systems is not tied to detection; instead, it is somewhat tied to the measurement or parameter estimation or transmission quality; therefore, the word detection threshold is sometimes misleading in an application. This demonstrates why the detection threshold is widely referred to as a minimum quality for the signal (all receiver gains considered) practically in all sense. Thus, DT is given as;

$$DT = 10 \log \frac{S}{N} \quad 2.9$$

The designer, at a point, is left with the probability of either a true or false decision. At the receiver input, when the signal is present, the decision will be either absent or present. When a signal is, in fact, present, the same two decisions can be made (Urlick, 2010).

2.3.7 Determination of Sounding Resolution

Detecting the range difference between sonar and targets is a significant criterion for determining object resolution, and it is advisable to apply spatial resolution instead of time resolution. At the time resolution, it is difficult to differentiate between close targets because the signals will be randomly spread. The sonar can only receive one wavefront at

time except if the time lag increases. This is only possible when it is defined in the rectangular envelope “which is the duration of signal in this case”. The spatial resolution is the minimal distance between two targets separated by the time resolution T of the signal (Henry, 1999; Gomez et al., 2004; Xavier, 2010).

2.3.8 Signal to Noise Ratio (SNR) and Directivity

The directivity index is the measure of the directionality of projectors and hydrophones. For instance, the projector indicates the distribution of acoustic energy. At the same time, the hydrophone lies in its ability to differentiate against an omnidirectional noise level (NL) when listening to a signal from a distinct direction. The purpose is to enhance the signal-to-noise ratio and is given as (Robert et al., 2005; <http://www.acousticsunpacked.org>):

$$SNR = PL - NL + DI \quad 2.10$$

The signal-to-noise ratio is the ratio of signal power to noise power (Xavier, 2010). It is also the desired signal's ratio to the background signal's ratio (noise), often expressed in decibels (dB). A ratio higher than one or greater than zero decibels indicates more signal than noise. The mathematical expression of SNR is given as;

$$SNR = 10 \log \left(\frac{P_{signal}}{P_{noise}} \right) dB \quad 2.11$$

The signal must be greater than the noise for the system to function effectively. If the signal in the sonar system is less than noise, there will be an incorrect interpretation and presentation of the output, which will affect the final analysis of the object in context (Nieukirk, 2015).

2.3.9 Bathymetry Systems of Operation on Waterbody

Bathymetry systems of operation depend on the techniques or method and type of sonar used for data acquisition. Basically, it is classified as a single beam system, swath beam system, multibeam system and side-scan sonar system. These systems are described based on their data acquisition methods, processes and accuracy associated with them. Meanwhile, in an application, it depends on the purpose of the survey and available resources. The Sonar system uses a projector and hydrophone to produce sound for two-

way communications (L-3 communication seabed instrument, 2000). These devices acted as transmitters and receivers and formed an integral part of any sonar system.

Furthermore, bathymetry sonars need projectors that have the capability to continuously produce acoustic pings with precise, controllable and repeatable characteristics. They are mostly made of piezoelectric ceramic, a material with the ability to change its size frequently when a voltage is applied to it (De-jong, 2009; Chris, 2010). Consequently, a brief design and operating mechanism of each of the systems will be worth looking into before reviewing their applications to date.

2.3.10 Single Beam System

Some components are incorporated together, which make up a single beam echo sounder. These components are the control and display unit, transmitter, transducer, and receiver. Figure 2.9 shows the systematic diagram of operation from a wider beam angle. The single-beam echo system determines depth by transmitting a single pulse or ping with a wide beam angle system that is unstable and measures a single depth at a time. This limits the capability to accurately depict seafloor information for safe navigation, as illustrated in Figure 2.10 for a wide beam and long pulse.

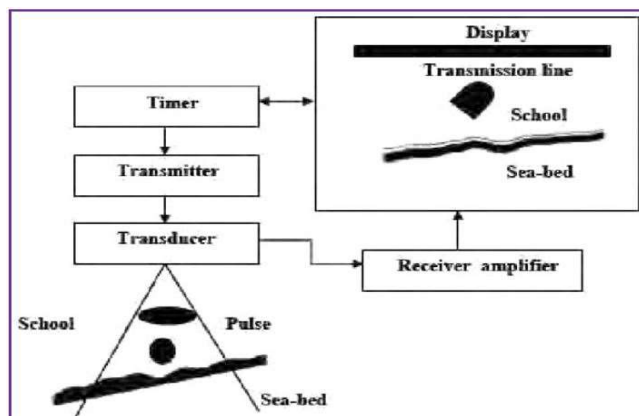


Figure 2:9 Working principles of Single Beam Echo Sounder
(Source: Lubis and Pujiyati, 2016)

However, the wider beam has a greater sampling volume in terms of searching for a school of fish. However, they are sensitive to omnidirectional background noise compared to narrow beams (Simmonds and MacLennan, 2005) “see Figure 2.9, Figure 2.10, and Figure 2.11”, which makes the narrow beam adaptable in noise environments.

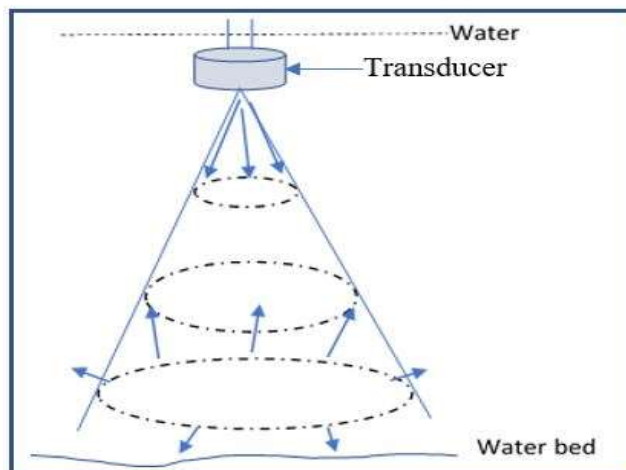


Figure 2:10 Wide beam and a long pulse (Source: Research Lap)

Improvement has been made to reduce the wide beam angle, and it has attained stability due to the narrow beam, which provides high spatial resolution with the small solid angle covered by the beam (Figure 2.11). In a situation where the waterbed is flat, this would not be a problem, but the challenge is where the seafloor is undulating; thus, to mitigate the error of the wide beam to an extent, a narrow beam was developed, as demonstrated in Figure 2.11 of the narrow beam and short pulse.

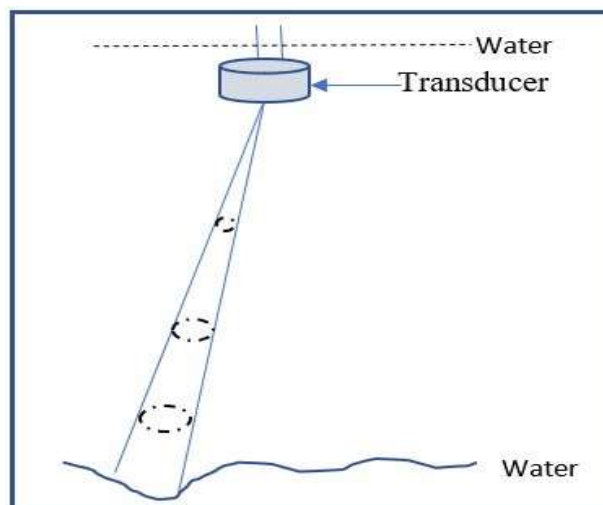


Figure 2:11 Narrow beam and short pulse (Source: Research lab)

The challenge is that it can only cover a small area at a time (one ping at a time), limiting the potential to provide broader information for ship navigation within the shortest possible space. However, the wide beam is deficient in special resolution. The introduction of narrow beam stability does not take care of the problem entirely due to several factors; for example, a transducer attached to the hull of the ship is affected by wave motion, giving

rise to beam scattering in the whole area of the seafloor: “this is known as an unstable beam which also depends on the weather condition of the environment at the instant of the survey” (L-3 communication seabeam instrument, 2000; Wilbers & Brinke, 2003; Xavier, 2010). The beam is made narrow by making the transducer face wider; for instance, a circular 12 kHz transducer with a 30° beamwidth has a diameter of approximately 25 cm. Meanwhile, it requires approximately 295 cm for a 2.5° beam (L-3 communication seabeam Instrument, 2000). The solid beam angle is the significant determinant of the transducer resolution of the seafloor, which means that the beam angle determines the accuracy of the underwater mapping in terms of depth measurement. The mathematical expression is given as:

$$area = (solid\ angle) * depth^2 \quad 2.12$$

In the ping cycle during operation, the transmitted ping must return to the receiver before the subsequent transmission can occur, which totally removes the ping control from the operator but depends on the depth and speed of the ship. Table 2.1 describes the setbacks between wider and narrow beam echo sounders.

Table 2:2 Comparison between wider beam and narrow beam echo sounders
(<http://www.acousticsunpacked.org>)

Consideration	Wider Beam	Narrow Beam
Depth penetration	Lower	Higher
Horizontal extent	Higher	Lower
Horizontal resolution at depth	Lower	Higher
Near-field	Lower	Higher
Dead zone	Higher	Lower
Ambient noise levels	Higher	Lower

In addition, for better resolution mapping, 2° to 5° narrow beam systems are required. Figure 2.12 describes the single narrow beam and wide beam simulation in mapping the waterbed. The echogram shows that the narrow beam has a greater percentage of mapping the seabed than its counterpart wider beam effectively.

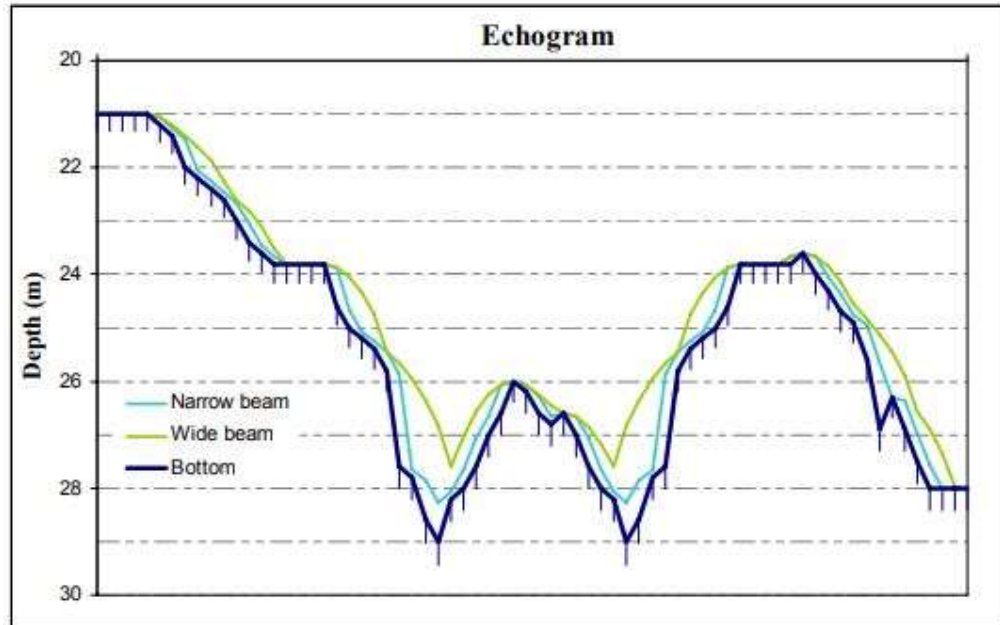


Figure 2:12 Illustration of depth measurement using a single narrow and wide beam
(Source: IHO: C-13, 2010)

The fact that a single beam echo sounder has experienced a wide range of acceptability in the surveying industries since its inception still has much setback. The setbacks also affect its application in various areas, such as limitations in large-scale hydrography work, object detection and location, as illustrated in Figure 2.12 (a) for a single beam footpath. Figure 2.13 describes the paths followed by single beam and multibeam echo sounders. Consequently, because of the numerous challenges faced by the single beam giving birth to a multibeam sounder, it has replaced the single beam echosounder but has found setback in cost and maintenance (L-3 communication seabeam Instrument, 2000; Wilbers & Brinke, 2003; Hansen, 2007; Marian et al., 2012).

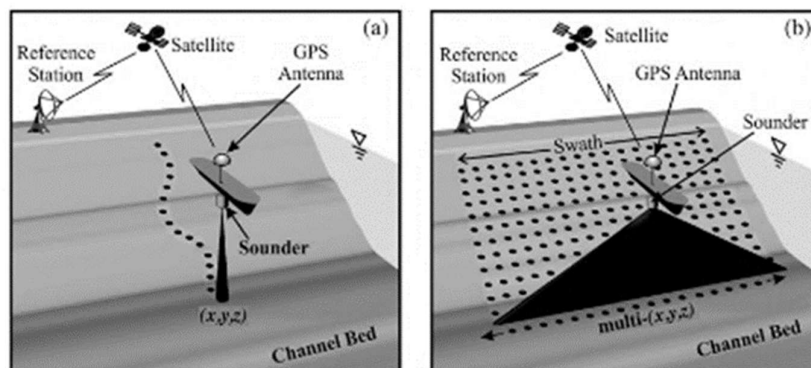


Figure 2:13 Echo sounders footpath (a) Single-beam (b) Multibeam
(Source: Marian et al., 2012).

Multibeam echosounders have significantly mitigated the challenges faced in large-scale seabed mapping in terms of time and accuracy for better navigational chart production, waterbed presentation, and precise volume of material before and after dredging can be determined, pipeline laying accurate information and other maritime activities.

2.3.11 Maximum Operating Range Calibration of a Single Beam Echosounder

According to [Xavier \(2010\)](#), the optimal performance of the single beam system is tied to the sonar equation, as given in Equations 2.4 and 2.5. The focus is the seafloor “the target”, with a performance setback of the exposure centre ψ (long pulse regime) or by the pulse period T (short pulse regime). Where the seafloor backscattering is approximated, it is maximized by its vertical and signal footprint area values and is given as:

- a) For the long pulse regime, the received echo level is:

$$EL = SL - 20\log R - 2\alpha R + 10\log\psi + BS_B \quad 2.13$$

The sonar equation is transformed as;

$$SL - 20\log R - 2\alpha R + 10\log\psi + BS_B - NL + PG + DI > RT \quad 2.14$$

- b) For the short pulse regime, the echo level is:

$$EL = SL - 30\log R - 2\alpha R + 10\log(\pi cT) + BS_B \quad 2.15$$

The sonar equation is transformed as;

$$SL - 30\log R - 2\alpha R + 10\log(\pi cT) + BS_B - NL + PG + DI > RT \quad 2.16$$

Finally, to determine the maximum range calibration of SBES (R_{max}), the first short pulse regime that is in connection with the longest ranges: the equation will now be

$$30\log R_{max} - 2\alpha R_{max} = EL + 10\log(\pi cT) + BS_B - NL + PG + DI - RT \quad 2.17$$

where R is the range, EL is the echo level, SL is the transmission source level.

2.3.12 Swath System (Sweep Sounders) Echosounder

The act of connecting several single beam transducers to map the seafloor is called the sweep or swath sounding system. This technique is also called the Atlas BOMA system. According to Stenborg (1987) in [Grant and Schreiber \(1990\)](#), it involves using multiple transducers attached to booms at equal distances on the sailing ship. This method of bathymetry survey is usually applied in rivers, dams, and harbours because of its capability

of increasing the number of points with some advantage compared to multibeam echosounders 'the challenges experience with multibeam in terms of sound velocity profile (SVP) variation, which are corrected for are avoided in this system. This is because vertical sounding is not responsive to sound velocity variations due to the equidistant sounding points irrespective of the water depth (Grant and Schreiber, 1990; Xavier, 2010). Figure 2.14 is a representation of the system according to Jones et al. (2017).

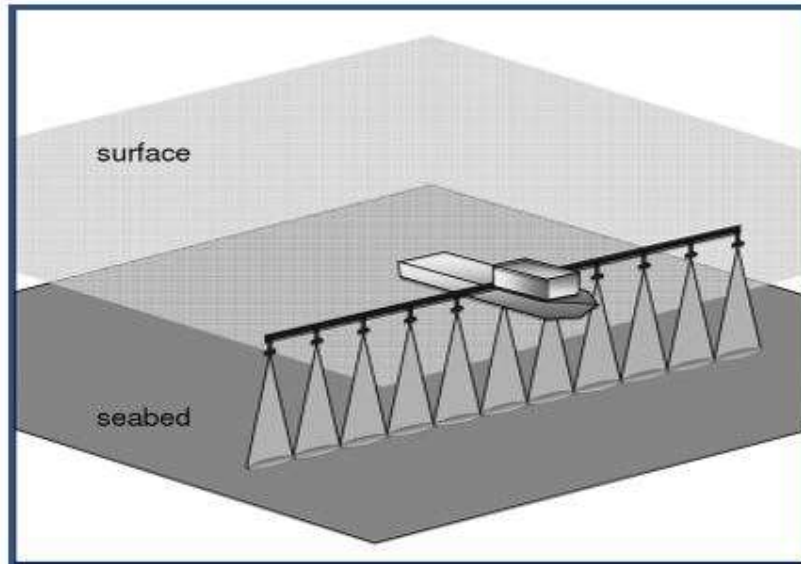


Figure 2:14 Schematic representation of Sweep Echosounder in action for hydrography survey (Source: Jones et al., 2017).

The merit of this system is that vertical measurement is better than oblique measurement, as in the case of multibeam echo sounders, and that the multibeam echosounder is very expensive both in purchasing and maintenance. Another merit is that accuracy and resolution are homogeneous throughout the swath, but the setback is in the practical application of the system, which is why implementation is recommended in rivers, dams, and harbours or small areas, better off for local application for which high vertical accuracy is demanded (Xavier, 2010; Jones et al., 2017).

2.3.13 Multibeam Echosounder

Multibeam echosounder (MBES) instruments are used to survey considerable areas during the bathymetric survey when compared with the single beam counterpart and with a greater horizontal resolution or accuracy. The principle is like sweeping, wherein one large ping area can be mapped, which will take several sweeps to accomplish using the single beam.

The transducers are attached at the bottom hull of the ship in such a way that it maps a neighbouring area with one strip and in the direction perpendicular to the direction of the vessel; this is known as swath bathymetric sounding (de Moustier, 1988; Wentzell and Ziese, 1988 according to Grant and Schreiber, 1990'; L-3 communication seabeam instrument, 2000; Xavier, 2010). The horizontal area (across-track) covered during sounding is called the swath width. The swath width is not a fixed pattern; it changes with depth, i.e., the smaller the swath width is, the shallower the waterbody and vice visa. The survey coverage width is three-quarters of the water depth (Hunzendorf, 1986). This is where the multibeam echo sounder has found a greater advantage. Figure 2.15 describes the operations of multibeam sonar in action mapping of the seafloor topography. It has the capacity to map a large area in one focus before the next pulse is returned in no distance time.

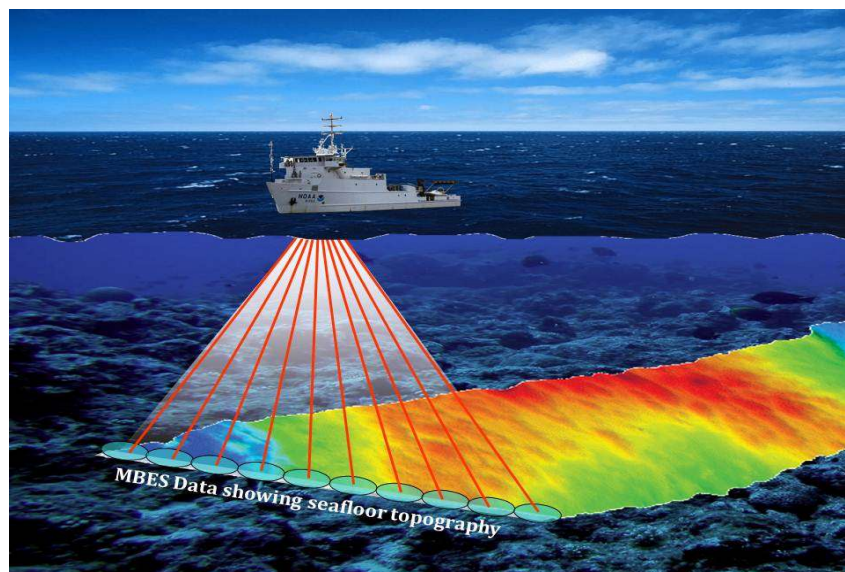


Figure 2:15 MBES in action mapping the seafloor
(Source: NOAA Photo Library - fis01334)

Additionally, other merits include enhanced bottom coverage, new methods of sound velocity measurement and compensation for refraction, new methods of calibration, flexible adaptation to the sediment, and a new method to improve spatial resolution and signal processing (Volberg and Meurling, 2007). This system operates in a specialized technique from the design to the final field applications. Some specific area of discussion is the projector, hydrophone, and how the beams are being formed. The beamforming is oriented in a definite direction to extract information from the reflected soundwaves.

2.3.14 Side-Scan SONAR

Multibeam echo sounders are undeniably unique and adequate for mapping exclusive economic zones (EEZs), and their processing is well standardized depending on high standards of calibration and accuracy (IHO-S44 for bathymetry). Meanwhile, the choice for high-resolution seabed mapping remains side-scan sonar. This system covers a much larger area of the seabed at a distance from the survey vessel, from a few tens of meters to 60 km or more ([Andreatos and Leros, 2021](#)). The area coverage is achieved by emitting a beam on each side (broad in the vertical plane and narrow in the horizontal plane). Using different frequencies (6.5 kHz to 1 MHz). Side-scan sonars achieve resolutions of 60 m to 1 cm ([Philippe, 2009](#)). The side-scan sonar works like the camera, but in this case, photographing the seabed. This tool is used for several purposes, such as creating nautical charts, detecting and identifying underwater objects, bathymetric features, and detecting debris and obstructions to navigation that are hazardous to vessels. Additionally, it is also for laying, inspections, and monitoring pipelines ([Yong and Qiang, 2019](#)).

Side-scan sonar transmits conical or fan-shaped pulses over a wide angle perpendicular to the path of their towed sensors. The returned signals create a detailed image of the reflectivity of the seafloor and its anomalies within the beam. The reflectivity of the seafloor depends on its roughness and the nature of the overlying material because coarse-grained sediments reflect higher than fine-grained sediments and rocky outcrops reflect higher than sediments and so on ([Bates et al., 2011](#)). Figure 2.16 describes tow-fish mapping of the seafloor. The seabed line in a side-scan waterfall image is a set of points, and each point indicates a position from which the first seabed echoes return during one pulse transmission.

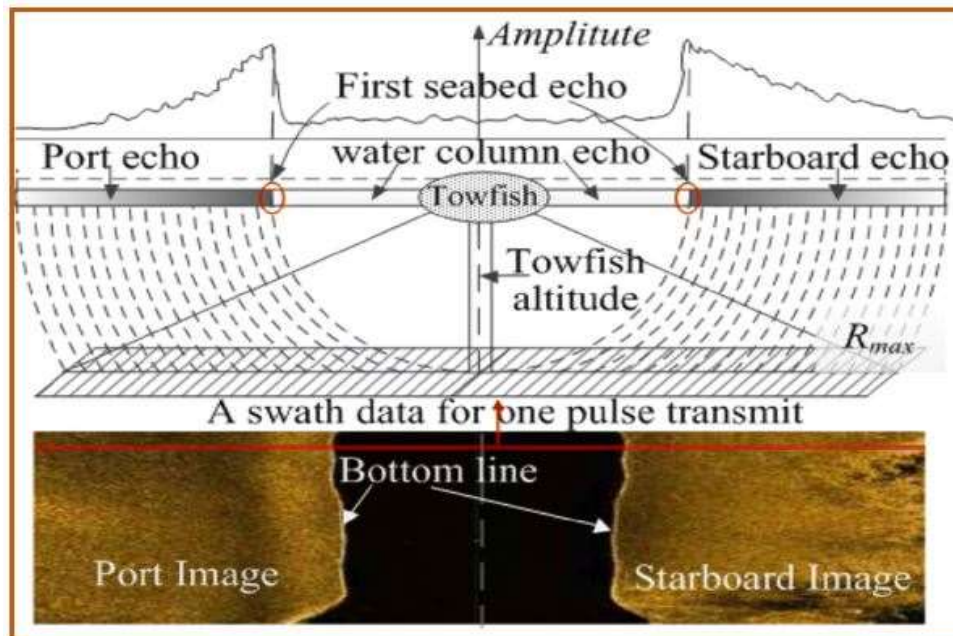


Figure 2:16 Theory of side-scan sonar data collection during one sound transmission. On both sides of the side-scan sonar waterfall image, these seabed points from which the first seabed echoes reflected formed a continuous bottom line with the slant range varying slowly with time sequences. (Source: Wang et al., 2020).

However, there are some limitations associated with this system, and they are not limited to: the period of quality survey data is tied to low wave energy, i.e., the summer months; major problems are experienced when the current is perpendicular to the path of the survey vessel; lack of contrast or excessive contrast between target and the surrounding bottom can influence error, and maintaining a constant speed and tow-fish elevation is needed for accurate results; and the presence of other ships can affect the stability of the vessel track.

2.3.15 Description of Projector Arrays and Beam Forming

A set of projectors and hydrophones are referred to as projector arrays and hydrophone arrays, respectively. They are used to create beam arrays for transmission and reception, a procedure known as beamforming (L-3 communication seabeam instrument, 2000). This is achieved by adding phases of the sensors considering constructive and destructive interference of waves at a definite angle (Donghwan et al., 2018). Beamforming is a process that involves sending and receiving beams from a set of arrays in a specific direction for the purpose of minimizing sound power in the target direction and to minimize sensitivity in a direction away from the target direction; as a result, enhancing the target signal-to-noise ratio for better resolution and accuracy in depicting objects (Curtis

and Ward, 1980; L-3 Communication Seabeam Instrument 2000; Shefeng and Yuanliang, 2004; Lisa and Daniel, 2012; Donghwan et al., 2018; Jie et al., 2018).

Charles (2000) gave a unique illustration of how beams are formed from 2 – projectors, assuming the devices are smaller than the wavelength of interest. Each broadcast isotropically with all measurements made in the far field. Thus, the power radiated at a given angular position is the square of the sum of the fields put by the two elements:

$$E(\theta) = \exp(i\pi \frac{d}{\lambda} \cos\theta + \delta) + \exp(-i\pi \frac{d}{\lambda} \cos\theta + \delta) \quad 2.18$$

$$I(\theta) = E(\theta)^2 = \cos(\pi \frac{d}{\lambda} \cos\theta + \delta)^2 \quad 2.19$$

where θ is the angular view, d is the distance between the two arrays, and δ is the relative phase of the two emitters. Equation 2.18 will generate an intensity pattern with two lobes, i.e., the main lobe and the back lobe. Thus, a few interesting beam patterns can be formed by varying the separation and phase of the elements, as seen in Figure 2.17. The values of $n, \delta,$ and d are applied to form the beam patterns for the two-element arrays in consideration.

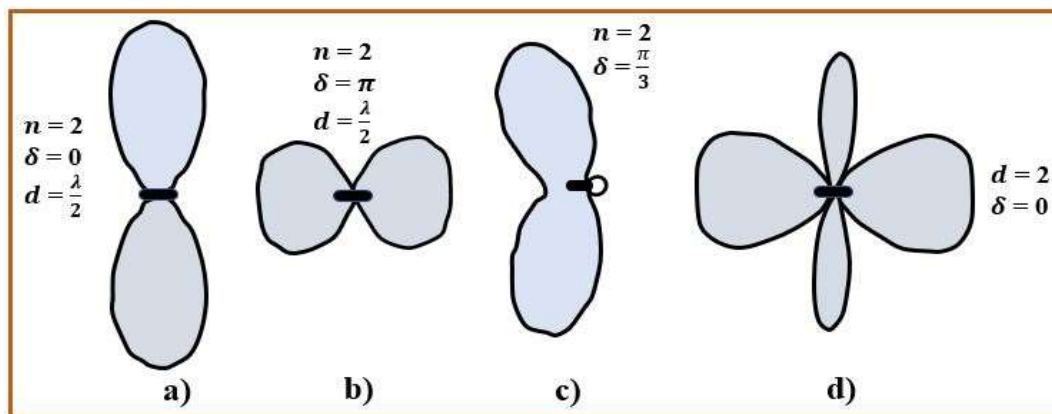


Figure 2:17 Power patterns from a two-element array: (a) Broadside, (b) end-fire, (c) Arbitrary phase, (d) full-wavelength spacing (Source: Reproduced in the research lab according to Charles, 2000)

In addition, there exist N projectors with a separation of d/λ apart, which can be quantified as a series of 2-elements of arrays say $(1, 2), + (1, 3), + \dots + (1, N)$, and the sum output will be:

$$E(\theta) = \sum_{n=0}^{N-1} \exp(in \frac{2\pi d}{\lambda} \cos\theta + in \delta) \quad 2.20$$

When $N = 2$ equation 2.20 becomes equation 2.18. In addition, the more projectors that are used, the sharper the main beam and back lobe will be, as illustrated in Figure 2.18.

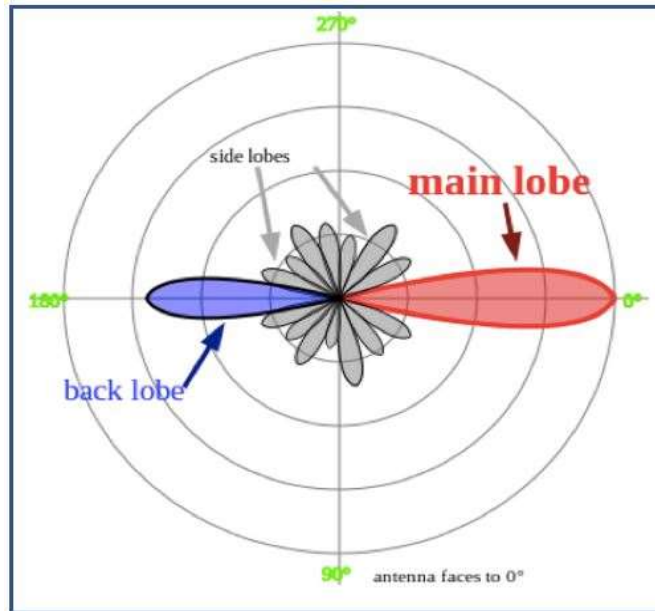


Figure 2:18 Example of radiation power patterns
 (Source: <https://www.nutaq.com/blog/introduction-beamforming>)

In any instance where the main lobe extends perpendicular in alignment with the line between the projectors is called broadside, and the one that is on-axis is called end-fire, as demonstrated in Figure 2.17 (a) and (b) above.

Furthermore, constructive or destructive interference is experienced if the waves overlap. This is usually experienced when two projectors emit signals at the same frequency (Von Ramm and Smith, 1983). Constructive interference occurs when a trough of a source wave P_1 intercepts with that of P_2 , thereby creating a steep trough, while destructive interference is experienced when they both repel each other, as seen in Figure 2.19. It usually occurs when the projectors are separated by equal distance or at the distance where the difference between successive wavelength is an integer number ($0, \lambda, 2\lambda, 3\lambda, \dots$), and the destructive occurred at a point where the discrepancies between the projector's distance between each other are half the wavelength or half the wavelength plus an integer ($\lambda/2, 3\lambda/2, 5\lambda/2\dots$), (L-3 communication seabeam instruments, 2000).

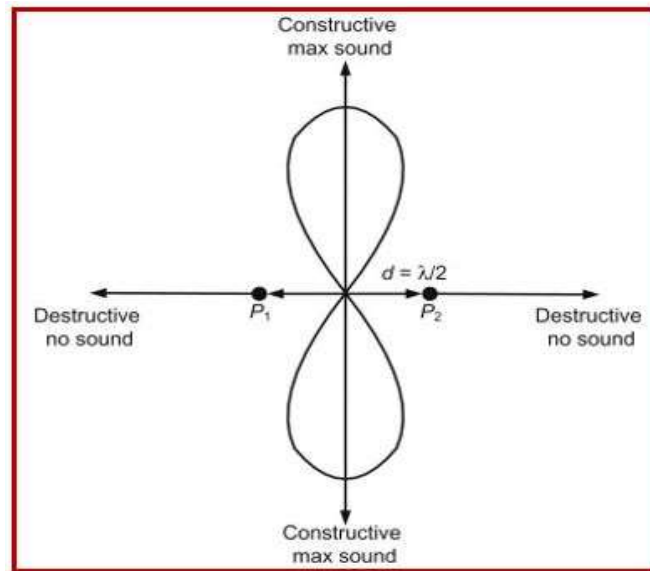


Figure 2:19 Constructive and destructive dipole projection of sound along a beam axis (Source: [Robert and Robert, 2014](#)).

The positions of the hydrophones determine whether constructive or destructive will be measured or not. Suppose the hydrophones are placed in the position of constructive interference; in that case, a combined wave will be measured with an amplitude twice that of the signals emitted by each projector, and at the position of destructive interference, nothing will be measured.

2.3.16 Description of Hydrophone Arrays

Hydrophone arrays act as the reception mechanism just the way projector arrays transmit the signal to the target, but in this case, the hydrophone serves as the receiver of such reflected pings from external sources. It has the capability to differentiate signals based on design. The most modern systems, especially radar and sonar systems, rely on hydrophones for optimal performance ([Harry, 2004](#)). In this case, the sound source (projector) is separated from the hydrophone, i.e., they are not in the same plane, which makes the hydrophone case significantly complicated but interesting to handle ([Whitlow and Mardi, 2008](#)). Consider three hydrophones as described in Figure 2.20, where each measured reflected signal from a far field of sound at an individual wave. These signals measured can be graphed based on time in what is called the signal trace. If the three plots are identical and in phase adding the three signals trace plot together with the same frequency, the amplitude will increase three times because the hydrophone will add up constructively,

and the sound will be highly sensitive in this direction (L-3 communication seabeam instruments, 2000)

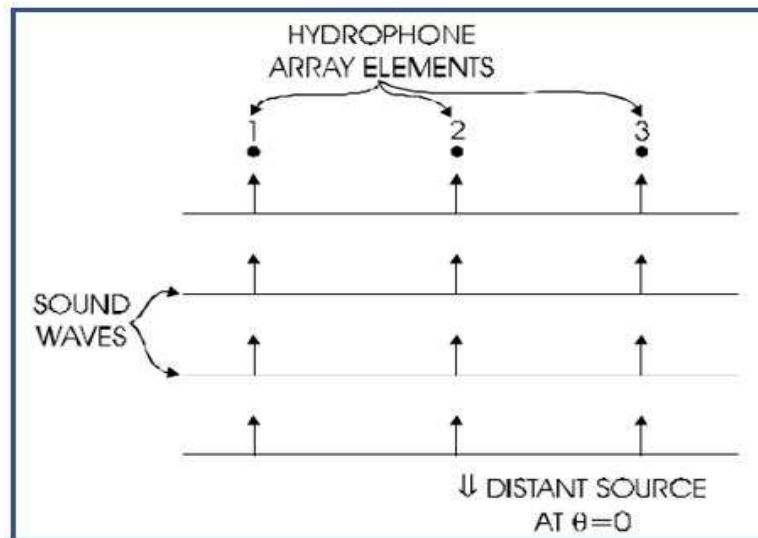


Figure 2:20 Hydrophone Array with a Perpendicular
(Source: L-3 communication seabeam instruments, 2000).

Typically, the four major array geometries are linear, planar, circular, and mill cross array geometries. As discussed in the subsequent section, the array geometry that has found wider application apart from the linear array geometry is the mill cross array because of its narrow beam signal tracking or reception capability.

2.3.17 Mills Cross Arrays

The method explores directors designed to project signals at some distinct path to transmit and receive the reflected signal from the ensonified surface or seafloor to the display unit for processing and interpretation. The main advantage of this system is that it is economical in array elements and thus reduces construction costs (Hassan, 1964). The mills cross method was introduced by Mills at Fleurs in Australia in 1953; for this reason, the system of hydrophone arrays of beam steering and utilization is called the Mills cross (Wohlleben et al., 1991). The principle of operation is that sonar arrays are placed perpendicular to each other in a cross-like manner, where the receiver (hydrophone) array is arranged horizontally relative to the projector array, and then the hydrophone receives the reflected signals from the direction of the strip from the seafloor, as described in Figure 2.21.

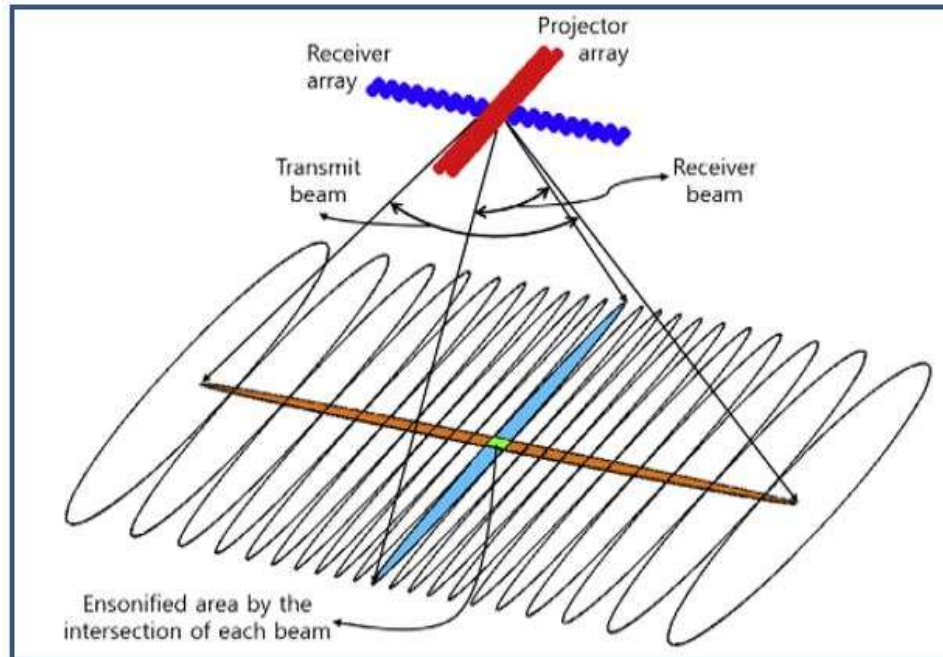


Figure 2:21 Description of each ensonified strip and ensonified area at the mills cross (Source: [Donghwan et al., 2017](#)).

The correlation between the mills cross and the rectangular array system is that, if they both make use of the same number of elements; the beam pattern will be of the same value, e.g., for two-line array elements of mills cross and rectangular arrays, the value will be $2n$ and n^2 respectively, and that the challenge with the mills cross array apart from being economical and of lighter weight it has the deficiency of poor array gain and low sensitivity. Nevertheless, it has a high resolution signal-to-noise ratio where array gain is immaterial ([Urick, 2010](#)).

2.3.18 Array Gain (AG)

The effectiveness of both the projector and hydrophone arrays in sea mapping and target identification cannot be overemphasized. The resolution, accuracy, and signal-to-noise ratio calibrations are made possible due to the array gain. Array gain is undoubtedly one of the highly difficult aspects of the sonar equation to be calculated precisely. Meanwhile, this is not a challenge since it can be approximated by replacing it with the directivity index (DI), equal to array gain in certain idealized circumstances ([Michael, 2010](#)).

To determine the degree to which a directional hydrophone or projector will improve the signal-to-noise ratio (SNR) over an omnidirectional antenna and enhance a weak signal is

defined by a quantity called array gain. The capability to amplify a weak signal buried in noise is array gain (Robert, 2008). Mathematically, it is the ratio of the output SNR of a directional array to the output SNR of an omnidirectional projector in the same signal plus noise field (Ronald, 1992):

$$AG = \frac{(SNR)_{directional}}{(SNG)_{omnidirectional}} \quad 2.21$$

In terms of beam patterns, the computing units are in decibels (dB) by computing $10 \log_{10}(AG)$. Additionally, it is usual to define a receiving array gain as:

$$AG = SG - NG \quad 2.22$$

where SG is the signal gain and NG is the noise gain in the sonar equation.

2.3.19 Enhancing Array Gain

Array gain is a major factor to be considered for adequate function of the sonar; a determinant of this gain is the coherence nature of the sensors. Basically, to increase the array gain, it is necessary to have high signal coherence but low noise coherence. This is because array gain depends on the coherence of the signal and noise between the sensors of the array and that coherence loss can be attributed to ocean motion, object motion, multipath, and reverberation or scattering. The coherence function has many applications, e.g., measurement of array gain or signal-to-noise ratio, system identification and determination of time delays (Clifford et al., 2001). coherence is a normalized cross-spectral density function “that is, it is a measure of the similarity of received signals and noise between any sensors of array”. Mathematically, the coherence function between two wide sensors at stationary processes x and y is determined by:

$$\gamma_{xy}(f) = \frac{G_{xy}(f)}{\sqrt{G_{xx}(f)G_{yy}(f)}} \quad 2.22$$

where f is the frequency and G is the power spectrum function.

2.3.20 Beam Steering

The process of intentionally focusing the main lobe array on receiving signals from a specific direction of choice is called beam steering (Xavier, 2010). The main difference between beamforming and beam steering is that the former involves shaping the beam to some required angular range, while the latter is all about pointing the beam to some

specified direction of interest. In other words, beam steering is all about the array direction ‘directing a strong beam signal in an arbitrary direction’ (Donghwan, 2018). However, to prevent signal loss, beam steering can be employed to face forward and backward directions for better reception to receive incoming pulses that would have been missed by a monodirectional side facing beam (Woon, 2012). Figure 2.22 describes a vertical receiving array of hydrophones separated by equal distance d of the N number of sensors or elements. N can be of any number, but basically, it depends on the depth of the sea or on the purpose of the design and usually ranges to 100 or less. The vertical array plane has a wavelength λ with an incident angle of θ , and the distance perpendicular to the first and second sensors will be $d \sin \theta$. Thus, the distance from the first sensor to the N sensor will be $(n - 1) d \sin \theta$.

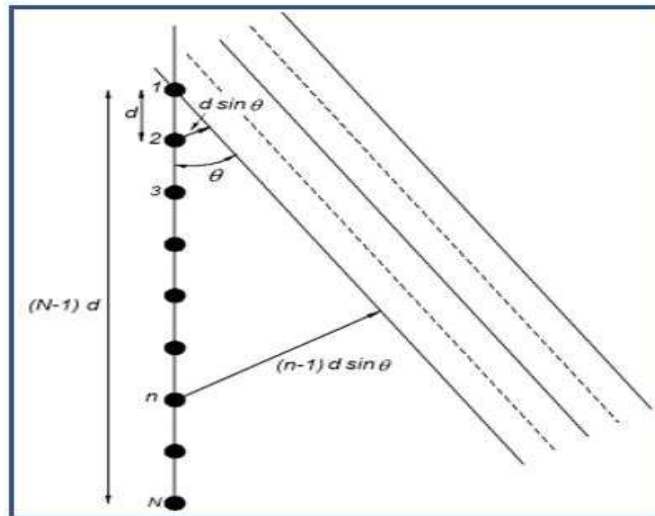


Figure 2:22 A plane acoustic wave of wavelength (λ) incident under angle θ on a vertical array of N discrete transducer sensors (source: Bjorno, 2017). The wavelength (λ) in the figure is presented by the parallel lines incident under angle θ .

Assume that they are of the same weight, i.e., the total output signal will be the summation of each sensor, and the pressure directivity function $DF(\theta)$, is also referred to as the standardized directivity pattern ‘which is the essence of beam steering’. Therefore,

$$DF(\theta) = [\sin(Nkd2\sin\theta) N \sin(kd2\sin\theta)] \quad 2.23$$

where $k = 2\pi/\lambda$, which is the number of acoustic waves formed, and this equation is for the discrete sensor line array directional sensitivity.

In a situation where $N = 1$, then $DF(\theta) = 1$, which is the attribute of a single omnidirectional element, and at $N = 2$, it will not produce the classical dipole directivity function except the two sensors are transmitting at 180° out of phase and the distance d is less than λ . The directivity factor of such a discrete element line array with N sensors is:

$$D = N \left\{ 1 + \left(\frac{2}{N} \right) \sum_{n=1}^{N-1} n(N-n) \sin(nkd) \right\} \quad 2.24$$

If N is greater than 1 and $d = \lambda/2$, it will result in $D = N$. It is worth noting that directivity changes as frequency changes (Bjorno, 2017).

Another consideration described by (L-3 communication seabeam instrument, 2000) is the array of hydrophones setup perpendicular to each other and each receiving reflected signal randomly from angle θ , as illustrated in Figure 2.23 below.

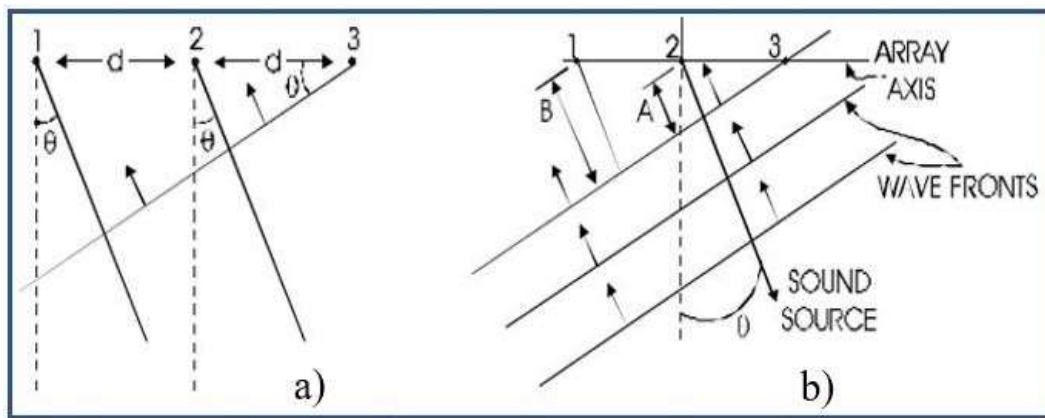


Figure 2:23 Wavefronts Striking a Hydrophone Array from a Source at Angle θ . Source: L-3 communication seabeam instrument, 2000.

The signal must travel the space marked A between the wavefront and hydrophone 2 for hydrophone 2 to sense the signal, and the same thing applies to hydrophone 1, but at this point, they differ with the time of arrival. The expressions hold for A and B

$$A = d \sin \theta \quad 2.25$$

$$B = 2d \sin \theta \quad 2.26$$

The additional time needed for each signal to propagate to each hydrophone with acoustic speed c is expressed as:

$$T_2 \text{ (time to hydrophone 2)} = \frac{A}{c} = (d \sin \theta) / c \quad 2.27$$

$$T_1 \text{ (time to hydrophone 1)} = \frac{B}{c} = (2d \sin \theta) / c \quad 2.28$$

By knowing these time differences t , the maximum directivity sensitivity at angle θ can be achieved by adding up all the readings from each hydrophone such that the wave pattern constructively interferes; applying the time lapses principles is known as introducing time delay as described in Figure 2.24.

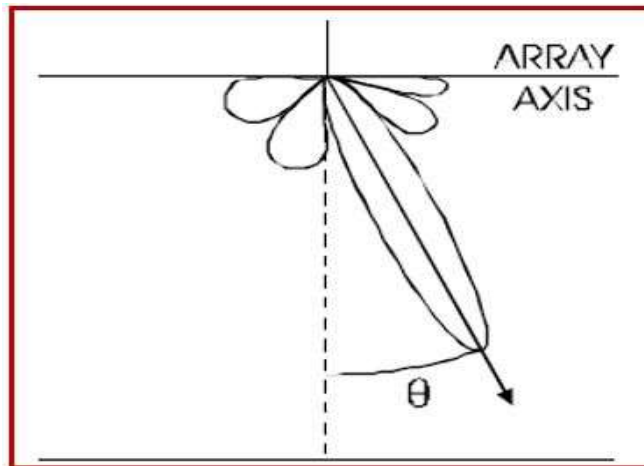


Figure 2:24 Main Lobe Shifted to Angle θ by Introducing a Time Delay.
Source: [L-3 communication seabeam instrument, 2000](#)

Additionally, Figure 2.24 describes a steered beam at angle θ using the time delay principles, and this can be done from any of the angles. The steering of the hydrophone does not affect the hydrophone itself, but only the interpretation of the data to determine that is affected.

2.3.21 Doppler Shift and Ship Speed Measurement

Christian Doppler introduced the idea of the Doppler shift in 1842. The phenomenon involves studying the change in frequency or wavelength regarding the observer moving relative to the sound source. This phenomenon has found acceptable application since the introduction of computers, even in modern navigation technology. The three most important areas of application in navigation studies are as follows:

- i) Determine the ship's position with the aid of a signal received from the polar-orbiting satellite.

- ii) Determine the sailing speed of a ship and Autonomous Unman Vehicle (AUV) with the aid of Doppler acoustic transducers. Determine the aircraft flight speed using microwave Doppler radars.

More emphasis will be placed on the area of Doppler shift application to determine the sailing speed of a ship and autonomous unman vehicle (AUV) with the aid of Doppler acoustic transducers. This area has found a specific application in the study of the seabed and other water body-related investigations in terms of vessel speed and sonar operation during hydrography and marine surveys ([Antony, 2000](#); [Urlick, 2010](#)).

The interest in knowing the speed of vessels in water is as old as when it was invented. This has resulted in various conventional methods of measuring the speed of a vessel, such as throwing a log in water; in this case, a wooden log is dropped in the water, and the time taken by the ship to move from the wooden log is recorded and estimated. Chip and log method; this is an improvised method of the wooden method, but there is an additional attachment of a logline knotted at an almost equal distance, and the displacement of the ship from point A to B is measured on the chip log. Others are the Pitometer device, electromagnetically induced voltage across electrodes, etc. These methods are adequate but are limited to the vicinity of the water body but relative to the seabed, which is a fixed reference. It has been established that all these methods are grossly affected by the dynamic nature of the water body, e.g., ocean currents and waves, which in turn affect the accuracy of vessel speed. Such a setback in ship speed estimation can be accommodated by cargo or passenger vessels, but unfortunately, this cannot be adopted for more scientific and precise survey applications where the vessel speed plays a significant role in the accuracy to be obtained ([Antony, 2000](#)). Hence, the shipping speed needs to be monitored against ocean currents and waves to achieve good survey data.

The current technique is used to measure ship speed relative to the seafloor with better and reliable accuracy is the two-way Doppler shift of acoustic signals backscattered from the seafloor. However, this depends on the induced frequency change, which is a function of the vessel speed, transmitted frequency and sonar orientation ([Antony, 2000](#); [Xavier, 2010](#)). Figure 2.25 describes two acoustic transducers mounted at the vessel's bottom in the opposite direction of the Janus configuration.

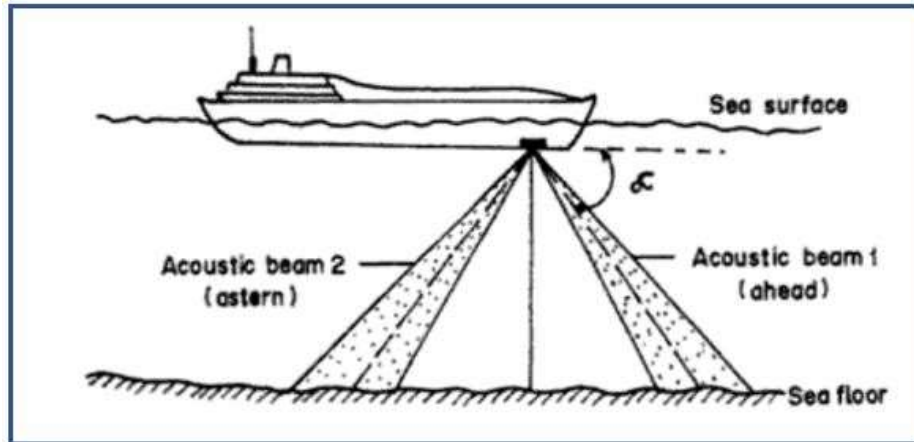


Figure 2:25 Two acoustic beams of a Doppler sonar in a Janus configuration
(Source: [Anon, 1973](#))

In application, the narrow acoustic signal transmitted from the projector at a defined angle on the horizontal platform in such a way that the reflected echo is the Doppler shift ([Antony, 2000](#); [Urlick, 2010](#)) and is given as:

$$f_d = \frac{2f_t v}{c} \cos\theta \quad 2.29$$

where f_d is the Doppler shift, f_t is the transmitted frequency, v is the speed of the vessel, c is the speed of sound in water, and θ is the transmission angle relative to the horizontal platform. The merit of this technique is that shipping speed can be measured at its least sailing speed. Meanwhile, accurate determination of the vessel's speed depends on the speed of sound in water, the emitting angle, and the accuracy at which the Doppler shift f_d is calculated. The speed of sound c (m/s) in water is expressed as:

$$c = 1449.3 + 4.572t - 0.0445t^2 + 0.016d + 1.398(s - 35) \quad 2.30$$

where t is the water temperature ($^{\circ}\text{C}$), d is the water depth (m), and s is the salinity of the water. However, the determination of sound speed from the measurements of temperature and salinity affects the overall performance of Doppler sonar ([Jorgensen et al., 1994](#)).

2.3.22 Sound Velocity Profiler

Sound velocity is one of the major parameters needed for accurate depth range determination using sounders, such as single beam and multibeam echo sounders. The sound velocity profiler (SVP) is an instrument used to measure the sound velocity through

the water column before averaging for the sonar used. This device has one pressure sensor to measure depth, a transducer and a reflector at a certain distance d apart. It uses the basic equation of $c = 2d/\Delta t$, where the change in time Δt is the two-way travel time of the pulse between the transducer and the reflector. The SVP principles of operation are similar to those of echosounders (IHO – C-13). Figure 2.26 is an example of the SVP – HY1200AB series with a design frequency of 10.7 kHz, a maximum depth of 100 m and a maximum temperature of 40 °C.



Figure 2:26 SVP – Hy1201AB series (Source: Hydrate.en.made)

Figure 2.27 describes the profile plots of temperature, salinity, and speed of sound in the western North Atlantic. This shows that temperature and salinity decrease with depth and affect sound speed mainly at the points where these hindrances are predominant.

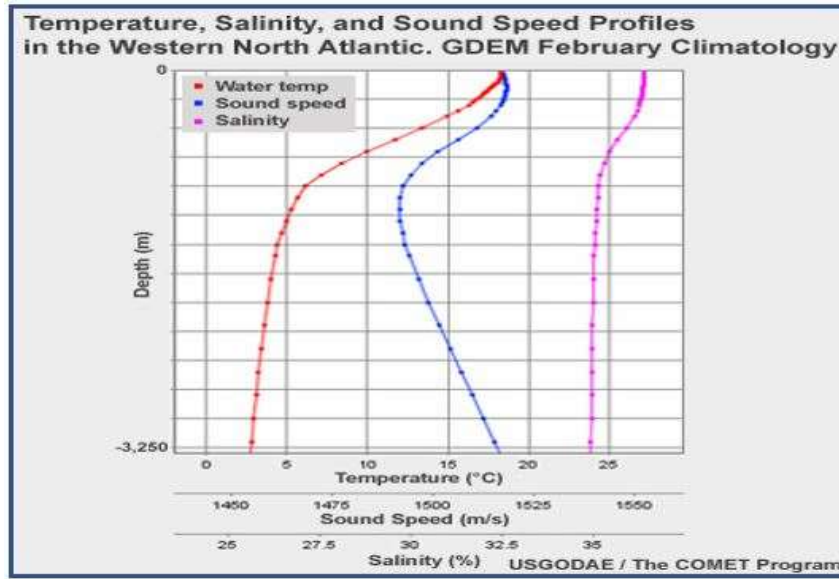


Figure 2:27 Sound speed, salinity, and sound profiles in the Western North Atlantic (Source: COMET, 2021).

2.3.23 Conductivity Temperature Depth (CTD)

CTD is an electronic device attached to sensors for the determination of seawater conductivity, temperature, and depth. It operates by directly recording the salinity from the measurement of the seawater electrical conductivity. Additionally, sound velocity can be computed from the information (salinity, temperature, and pressure) recorded by CTD using empirical equations such as the given by Kinsler et al., 1982:

$$C(Z, T, S) = 1449.05 + T[4.57 - T(0.0521 - 0.00023 * T)] + [1.333 - T(0.0126 - 0.00009 * T)](S - 35) + \Delta(Z) \quad 2.31$$

where T is the temperature measurement in degrees Celsius ($^{\circ}\text{C}$), S is salinity in parts per thousand (ppt), Z is the depth in km, and $\Delta(Z) \approx 16.3 * Z + 0.18 * Z^2$. However, this equation is valid for a latitude of 45° ; for different latitudes, Z should be replaced by:

$$Z[1 - 0.0026 * \cos(2\phi)] \quad 2.32$$

Where ϕ is the latitude.

2.3.24 Motion Sensors

Among others, depth measurement is one of the basic components of hydrography. The sonar for depth determination is usually attached at a location of the vessel away from the

artificial noise of the ship. A global positioning system (GPS) is typically used to determine the position with the antenna located on the ship's mast. The vessel geometry, i.e., altitude (roll, pitch, and heading) and heave, must be known for better results. Thus, inertial sensors with a heading sensor (gyro or fluxgate compass) or the integration of inertial sensors and GPS information are employed to determine the altitude and heave of the hydrography vessel.

Furthermore, a central reference point (CRP) has to be selected and defined by the Cartesian right-handed coordinate system. The CRP is the centre of origin, as shown in Figure 2.28. The location of CRP has no physical significance: "it can be anywhere of the survey vessel". However, some points should be avoided, such as the echo sounder transducer; this is because when the transducer is changed, the point is lost. Additionally, the vessel's centre of gravity is not recommended because it is not apparent and deviates from the weight of the load in the vessel. Meanwhile, the positions of the various sonars must be identified with forwarding, starboard, and downward coordinates in the chosen coordinate system.

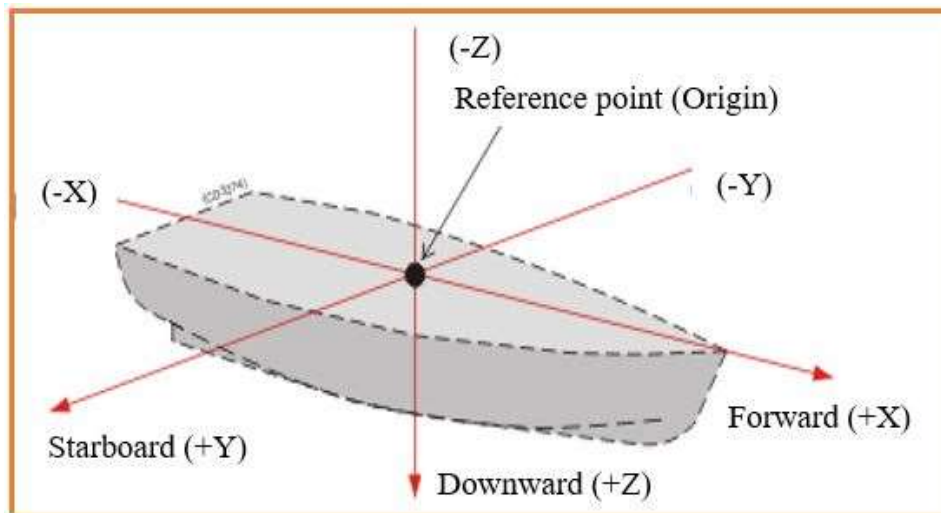


Figure 2:28 The Cartesian right-handed coordinate system of a vessel
(Source: Replicated in the research lap from [Lekkerkerk and Theijs, 2017](#))

The forward axis (X) must be parallel to the vessel bow, keel, or rudder, and the downward axis (Z) must be vertical when the vessel is adjusted for sailing or trimmed normally. This will make the plane defined by the forward and starboard axes horizontal, and the altitude sensor should measure zero (0) roll and pitch with a normally trimmed vessel at rest. This

is only achievable when the attitude sensor is properly installed and calibrated. Hence, Figure 2.29 describes the resolved geometry of the survey vessel.

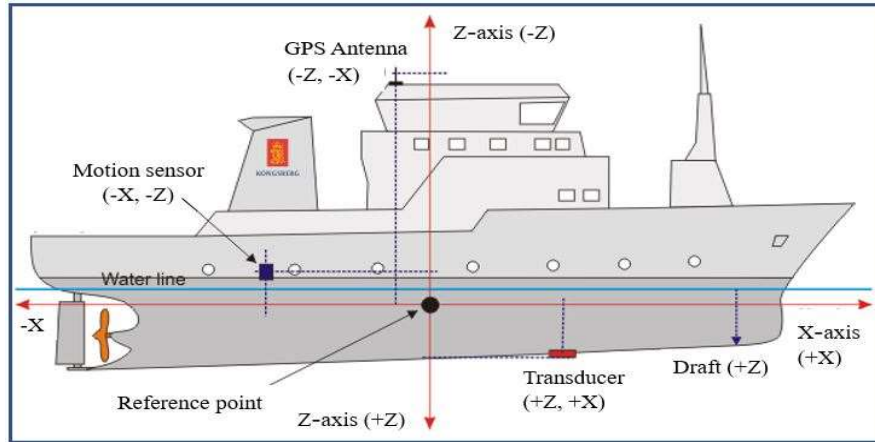


Figure 2:29 A resolved Cartesian coordinate system of a vessel
(Source: linux.geodatapub.com and modified in the lab).

From Figure 2.29, it can be deduced that the forward position (X) is defined on the X-axis and is positive further forward from the reference point and negative further backward from the reference point. The downward position (Z) defined on the Z-axis is positive below the reference and negative upward. Similarly, the starboard position (Y) will be positive if the sensor is on the starboard side of the reference point and otherwise negative. Inertial sensors integrating GPS information are now considered a very important component required for multibeam echosounders, and some automatic data record single beam sounders. The motions (Movement “Sway, Surge, Heave” and Rotation “Pitch, Roll, and yaw”) are relative to the vessel axis or frame. In practical hydrography operations, only the heave, roll, pitch, heading, yaw, and velocity, including sway and surge, are measured (Lekkerkerk and Theijs, 2017). Table 2.3 describes the parameters needed for each system of operation.

Table 2:3 Motion parameters required for Hydrographic Surveys (Source: Reproduced in the lab from Lekkerkerk and Theijs, 2017)

Parameters	Single beam low quality	Single beam high quality	Multibeam	ROV	Geophysical (SSS and SBP)
Heave	N/Y	Y	Y	N	Y
Roll	N	Y	Y	Y	N
Pitch	N	N	Y	Y	N
Heading	N/Y ²	Y	Y	Y	Y
Velocity	N	N/Y	N/Y	Y	N/Y ³

where **Y** stands for Used, **N** stands for not used, and **N/Y** is generally not used but, if available, is an addition to the system. ² Only used if offset calculation is required between GPS antenna and echo sounder transducer. ³ GPS derived velocity is generally used to perform scale correction of the Side Scan sonar record.

2.3.25 Latency

Latency is the time delay between the actual measurement of a certain sensor and the transmission or reception of the sensor reading to the acquisition system. It was measured using survey acquisition system software. The major factors that influence latency are time consumption by internal calculations (measurement delay) and transmission delay (this is the time delay during the transmission of measurement over the line, i.e., the delay between the communication port of the sensor and the communication port of the acquisition system). The time delay between the signal arriving at the sensor communication port and the acquisition system and the display or storage unit depends on the system, such as processor load and software efficiency. Similarly, the two major latencies in hydrography are latency between the attitude sensor and depth reading and latency between the positioning system and depth ([Lekkerkerk and Theijs, 2017](#)).

2.3.26 Tide and Positioning

Tides are the continuous rise and fall of water levels such as sea, ocean, or lake as a result of the forces of attraction of the moon and the sun. This is usually depicted as high water and low water levels on a tidal curve graph. Tidal readings must be tied above or below a reference level. The vertical axis is usually the water height, and the horizontal axis frequently represents the time. Additionally, the interaction of the moon and the sun in some instances results in spring tides and neap tides based on the geographical region. Spring tides have higher high tides and lower low tides, whereas neap tides have lower high tides and higher low tides, as described in Figure 2.30. The range is the difference in water level between high and low tide, and it is much more prominent in spring than in low tide.

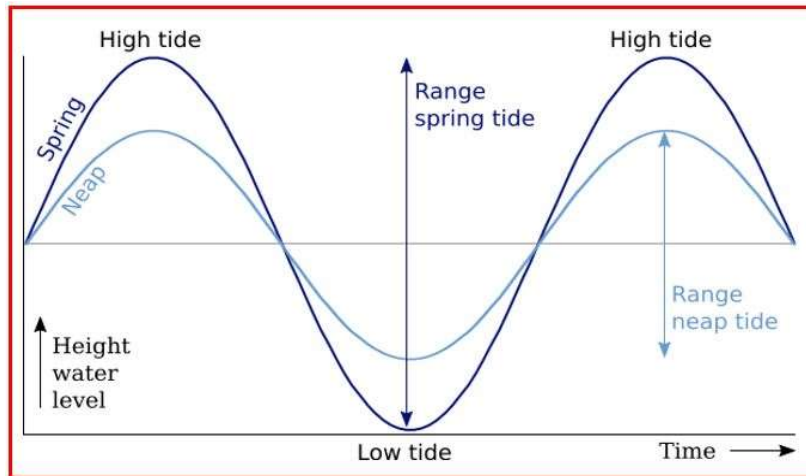


Figure 2:30 Ideal sinusoids of both spring and neap tides
(Source: sailingissues.com)

Furthermore, three types of tidal patterns (unlike the idealized sinusoid curve shown in Figure 2.30, with two equally proportioned high and low tides every lunar day) can be found on the Earth's surface since the planet is not a perfect square without vast continents. The three tidal cycles are semidiurnal (produces two equal high tides and two nearly equal low tides in each lunar day, and the total period is 24 hours 50 minutes, i.e., 24 hours 50 minutes). 12 hours 25 minutes from high tide to the next high tide); diurnal (this produces only one high and one low tide, and the tidal period is 24 hours and 50 minutes and it is twice as long as the semidiurnal cycle); and mixed semidiurnal (produces a cycle with two high and low tides with different sizes in each lunar day, and the difference between two successive high or low tides is known as diurnal inequality). Figure 2.31 below describes the primary types of tides and their regions of dominance.

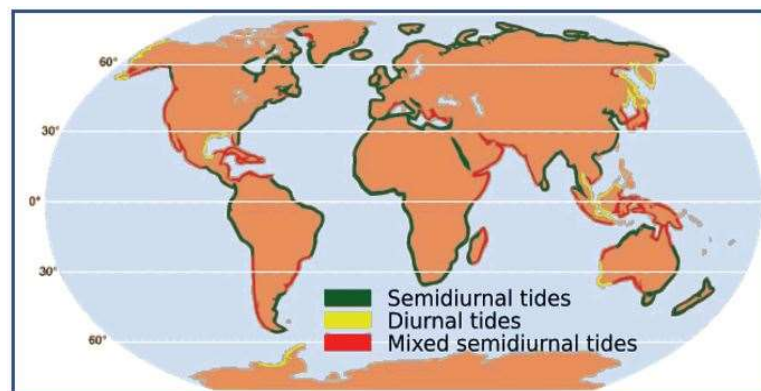


Figure 2:31 Description of the three types of tides (Source: sailingissues.com).

The regions not covered by water prevent the westward passage of the tidal bulges as the earth rotates. The same is true for different coastal shapes and differences in depth. Additionally, it is evident in Figure 2.31 that the African continent is predominantly semidiurnal tides. The fact that tides cannot move freely around the globe creates complex patterns within each ocean basin, and they differ based on region. Consequently, the menace of tide over depth measurements must be accounted for, and to resolve this drawback, all sounding observations must be referenced to vertical datum.

2.3.27 Vertical Datum and Chart Datum

Generally, vertical datums are necessary for all survey measurements for reference purposes. There are four different types of vertical datums in practice:

- i) The geoidal vertical datum is used in land surveying or geodesy. It is a surface of a specific zero point of constant gravity and is usually referred to as a geoid.
- ii) Depth-related vertical datum used in hydrography; in this field, a zero point is defined as a level that has meaning for the vertical measurement sure as LAT, GLWWS, etc.
- iii) The barometric datum used in oceanography and meteorology and with atmospheric pressure as zero are often represented as one thousand and twenty-three hectopascals (1023 hPa).
- iv) Other reference surfaces are used in engineering, such as the one used in drilling, where the upper or lower side of the geologically identifiable layer is used as a reference ([Lekkerkerk and Theijs, 2017](#)).

Additionally, hydrography surveys aim at water depth measurement; thus, all depths must be referenced to a vertical or chart datum. The reference frame is usually tied to the mean sea level (MSL), which is the mathematical mean of the observations of sea level height measured for a longer period, and the observations should be within a short time interval. “The observations are usually hourly measurements for the period of 19 ½ years” ([Igham, 1984](#)). The chart datum value is always indicated on navigation charts to give navigators an ideal water body depth range for safety in navigation. The variation in tide based on region mandated countries to establish their chart datum. Typical chart datums are Mean Lower Low Water Springs (MLLWS), Mean Lower Low Water (MLLW), Mean Low Water

(MLW), Low Water (LW), Highest Astronomical Tide (HAT), Lowest Astronomical Tide (LAT) or Mean Low Water Springs. Figure 2.32 describes some of the chart datums and their establishment.

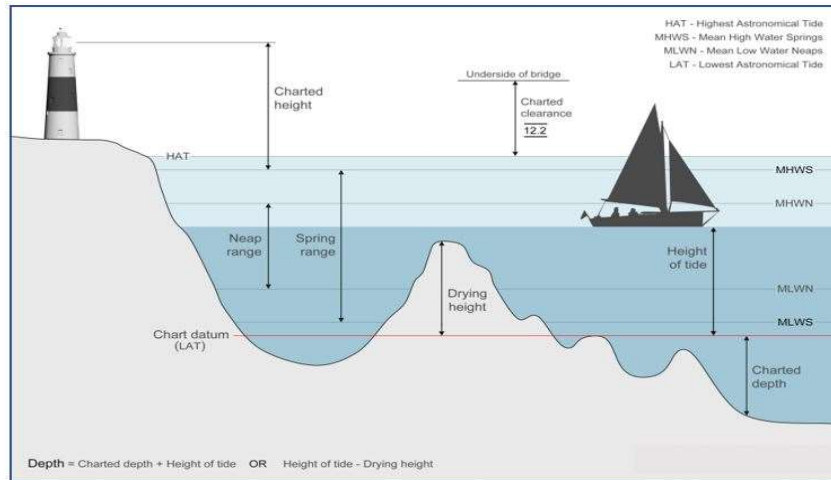


Figure 2:32 Chart Datum establishment (Source: dragons8mycat.com)

Meanwhile, the mean low low water spring (MLLWS) is the mean of the measured lowest spring tides taken every month for the period of five (5) years. Charts tied to MLLWS will provide 99.5% navigation safety for mariners. In Holland, MLLWS has been replaced with Lowest Astronomical Tides (LAT). LAT is the lowest water tide that will be experienced based on astronomical arguments from astronomical bodies and local geographical circumstances (Externe et al., 2007; Lekkerkerk and Theijs, 2017).

2.4 Positioning

Surface and underwater positioning have metamorphosed since introducing the differential global positioning system (DGPS). However, underwater positioning is where underwater acoustic waves play a major role because of the inability of radio waves to penetrate the water column to a reasonable depth, and it is not suitable for underwater positioning. Surface positioning, also called dynamic positioning (DP), entails fixing or determining the positions of floating platforms for exploration and exploitation, e.g., drilling rigs. Similarly, the other set of positioning is the underwater vehicle positioning needed for detailed soundings, search and rescue missions, an inspection of structures and pipelines, etc. Some of these platforms can be in hundreds to thousands of metres below the water level, and they are either permanent, flexible or mobile and temporally (de-Jong, 2010; GPS.gov). Global navigation satellite systems (GPS, GLONASS, Beidou, and Galileo) are

combined with other independent underwater positioning systems to attain a high degree of redundancy and reliability. In these systems, correction messages are transmitted to vessels via a robust fault-tolerant broadcast infrastructure providing precise, reliable, real-time satellite positioning that is accurate worldwide, to just a few centimeters (Fugro.com).

Furthermore, there are diverse methods of position fixing techniques with different degrees of accuracy based on the area of applications. Generally, marine position fixing is grouped into two groups: first, dead reckoning positioning systems, such as distance lines, trailing wheels, current metres, gyrocompasses, Doppler logs/gyrocompasses, and inertial navigation systems (INSs). Second, underwater acoustic position fixing systems can be integrated with DGPS, such as short baseline (SBL) systems and supershort baseline (SSBL) systems, also known as ultrashort baseline (USBL) systems, and long baseline (LBL) systems ([de-Jong, 2010](#)). It can also be the combination of any underwater acoustic position fixing system. The table below summarizes and describes the differences between the various GNSSs. However, the first three (3) compass satellites were launched between 2000 and 2003 ([Kai-Wei et al., 2010](#)).

Table 2:4 GNSS and differences in parameters. (Source: [Kai-Wei et al., 2010](#))

Parameter	GPS	GLONASS	Galileo	Compass
First launch	1978	1982	2005	2007
FOC	1995	1996	2012	2013
Services	Military civil	Military civil	Commercial open	Authorized Open/commercial
Number of SV	31	24	27	27
Number of orbital planes	6	3	3	3
Inclination	~55°	64.8°	56°	55°
Semimajor axis (km)	26560	25508	29601	27840
Period	11 h 58 m	11 h 15 m	14 h 05 m	12 h 50 m
Coordinate frame	WGS-84	PZ-90	GTRF	Beijing 1954
Time system	GPST	UTC(SU)	GST	China UTC
Coding	CDMA	FDMA	CDMA	CDMA
Frequencies	L1:1575.42 L2:1227.60 L5:1176.45	G1: 1602 G2: 1246 G3: TBD	E1: 1575.42 E5a: 1176.45 E5b:1207.14 E6: 1278.75	B1-2: 1589.74 (E1) B-1: 1561.1 (E2) B2:1207.14 (E5b) B3: 1268.52 (E6)

Similarly, from the various applications of satellite navigation systems, little emphasis will be placed on GPS/DGPS.

2.4.1 Global Positioning System (GPS)

The working principles of GPS in fixing positions are based on the principle of the trilateration mathematical model. GPS consists of satellites in space (space segment), ground reference station infrastructure (control segment), and user equipment (user segment); they are used to determine the positions and velocity of a specific vehicle. The parameters of this satellite navigation system are listed in Table 2.4, while Figure 2.33 describes the segments of the GPS. The minimum number of satellites required for positioning is four, although it depends on the purpose of the observation. Currently, the GPS uses two pseudorandom noises, which are the identification codes. The codes are coarse access (CA code) and precision code (P code).

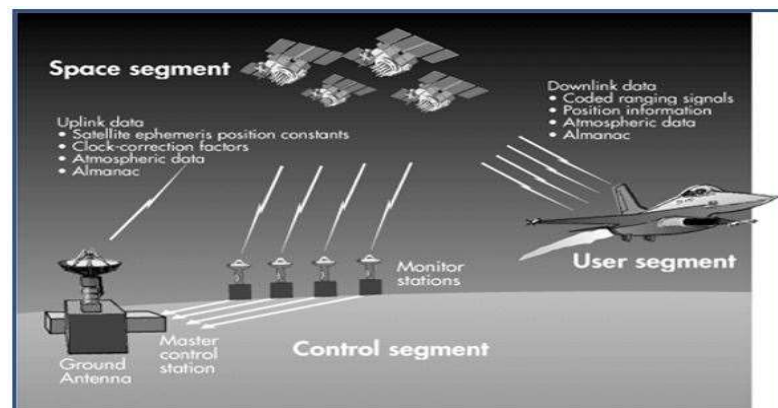


Figure 2:33 Description of GPS segments (Source: owaysonline.com)

The raw GPS data are based on the CA code or P-code, but the P-code data are better. The difference in accuracy between the CA and P-code is mainly caused by the difference in length of the code and the transmitted position data; the former is transmitted on the L1 frequency, while the latter is transmitted on frequencies of L1 and L2. In addition, the P-code also experiences some setbacks inaccuracy due to some error sources. The differential GPS method compensates for most of these errors. Some of these errors are errors in satellite clock and ephemeris, selective availability error, tropospheric error, multipath error, user errors, etc. (Kai-Wei et al., 2010; Emel'yantsev et al., 2017; Lekkerkerk and Theijs, 2017)

Additionally, to obtain a good GPS position using the receiver, some quality measure parameters are used. The quality parameters are but are not limited to dilution of precision,

line of position, mean error, root mean square, quality index, and W and F test. In practice, the quality assessment parameter readily available to the user is the DOP.

2.4.2 Dilution of Precision (DOP)

Dilution of precision (DOP) is the strength of the satellite configuration in space. It describes the spreading of individual satellites above the horizon. A good DOP is attained when the satellites are above the horizon and away from the local zenith. In the same way, poor DOP is a situation where the closest satellites are directly overhead or too low on the horizon, as described in Figure 2.34 (De Jong et al., 2010, tstarmet.com).

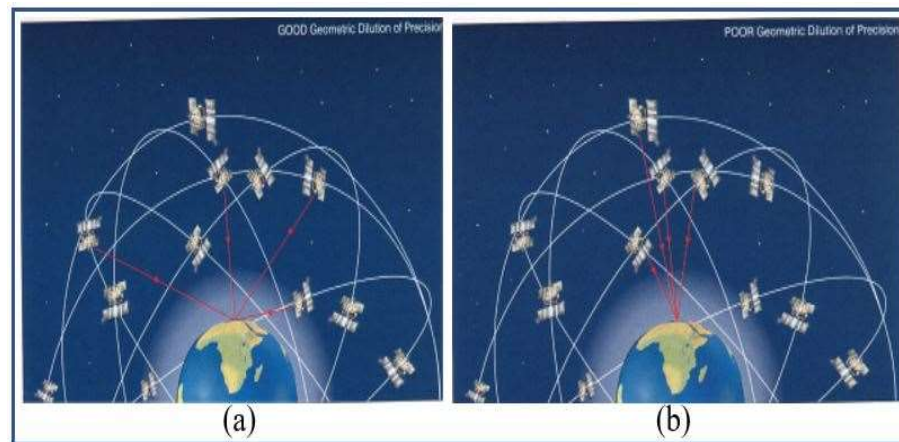


Figure 2:34 (a) Good DOP and (b) Poor DOP (Source: tstarmet.com and modified in the research lab)

Similarly, several DOP quality controls exist, but the most imperative is the geometric DOP. DOP can be presented as several separate measurements as:

- GDOP – 3D position plus clock offset in the solution
- HDOP – horizontal dilution of precision
- VDOP – vertical dilution of precision
- PDOP – position (3D) dilution of precision
- TDOP – time dilution of precision
- RDOP – relative (normalized to 60 seconds).

2.4.3 Fixing the Position of a Ship Using a GPS Receiver

In fixing the position of a ship using a GPS receiver as described in Figure 2.35, the following procedures take place:

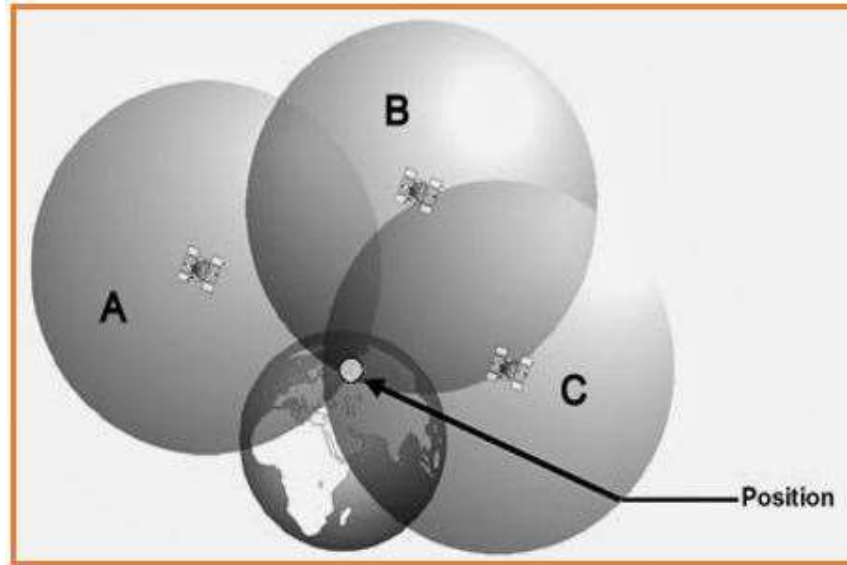


Figure 2:35 Position fixing using GPS (Source: owaysonline.com)

- i) The receiver locks on to one satellite, and from this satellite, it obtains the almanack of the other satellites and thereby selects the adequate satellites for position fixing.
- ii) The position obtained by the receiver basically determines the distances from the receiver to each of the selected satellites.
- iii) The range measurement is achieved by measuring the propagation time from the selected satellite to the receiver.
- iv) Thus, an additional satellite is used to obtain the true ranges, and the mathematical equation is given as:

$$R = CX(t - t^2) \quad 2.33$$

where R is the range of the satellite to the user, C is the velocity of the radio waves, and $(t - t^2)$ is the time difference (time taken for satellite signals to reach the receiver).

However, the inability of the satellite's clock and the receiver clock to be precisely synchronized in some instances may result in an error in the range measurement. This is

because an error of one microsecond between the two clock synchronizations will lead to an error of 300 meters), making the determined value pseudorange. Therefore, four unknowns are available: latitudes, longitudes, and altitudes (x, y, z coordinates) of the user, including the user's clock error relative to the satellite clock. Knowing the position of satellite $S_1(x_1, y_1, z_1)$ to the user by the 30-second navigation message, the following expression is established:

$$PR_1 - (C * \Delta t) = \sqrt{(x_1 - x)^2(y_1 - y)^2(z_1 - z)^2} \quad 2.34$$

where PR_1 is the pseudorange from satellite S_1 , $(C * \Delta t)$ is the error in the range measurement due to the error in the user's clock, and the remaining three unknown are expressed as:

$$PR_2 - (C * \Delta t) = \sqrt{(x_2 - x)^2(y_2 - y)^2(z_2 - z)^2} \quad 2.35$$

$$PR_3 - (C * \Delta t) = \sqrt{(x_3 - x)^2(y_3 - y)^2(z_3 - z)^2} \quad 2.36$$

$$PR_4 - (C * \Delta t) = \sqrt{(x_4 - x)^2(y_4 - y)^2(z_4 - z)^2} \quad 2.37$$

Meanwhile, utilizing these equations, the 3D fixation of a point can be computed. In the aspect of craft floating on water, a 2D fix, i.e., latitude and longitude, is needed, and 3 equations from 3 satellites will be sufficient to fix position.

2.4.4 Differential GPS (DGPS)

DGPS achieves enhanced accuracy since the reference and user receivers both experience common errors that the user position can remove; hence, errors are highly minimized in this position fixing technique. The basic operation of DGPS is that the position of a reference receiver at the monitor or reference station and its position are known accurately. The user receiver should not be more than 480 km or approximately 500 km in diameter (250 km radius) away from the reference station, making pseudorange measurements, just as any user receiver would (Jose et al., 2016). However, because the reference station knows its position accurately, it can determine (biases) in its pseudorange measurement for each satellite because of the reference receiver; these biases are computed by differencing the pseudorange measurement and the satellite from the reference receiver

geometric range. Figure 2.36 describes the principle of DGPS real-time measurement of survey vessel position fixing and depth determination.

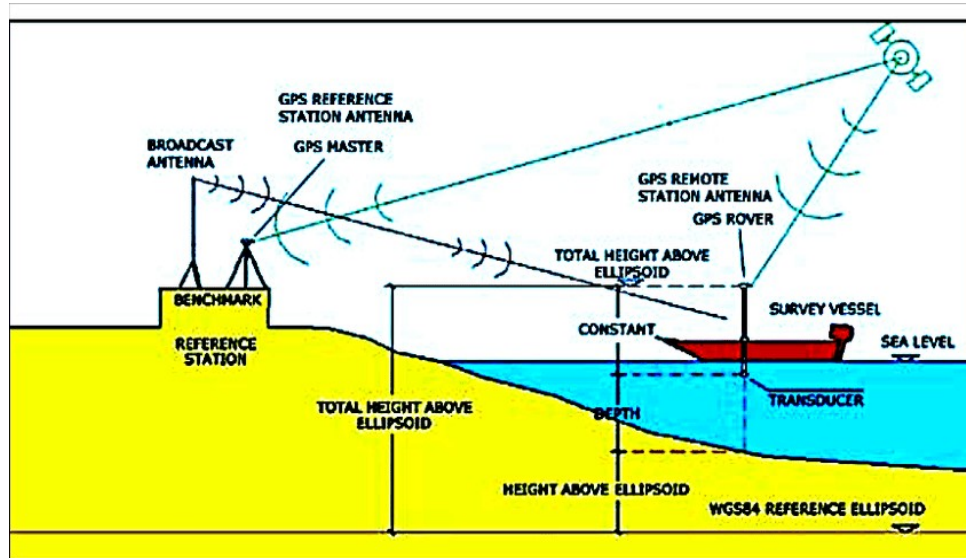


Figure 2:36 Description of the principle of DGPS real-time measurement of the survey vessel. Real-time position determination allows the position of points below the waterbody to be fixed. The fixed points will have the absolute spatial coordinates “Eastings, Northings, and depth.” The depth, if referenced to the existing height datum system, will result in the reduced height of the waterbody depicting the topography. (Source: fao.org)

These biases incurred in the pseudorange measurement process include errors arising from ionosphere delay, troposphere delay, and satellite clock offset of GPS time. For real-time applications, the reference station transmits these biases, called differential corrections, to all users in the coverage area of the reference station. Users incorporate these corrections to improve the accuracy of their position solution, and the accuracy of those closer to the reference station is higher than those far away from the reference station.

2.5 Sedimentation

The bottom of the alluvial watercourse, such as rivers and estuaries, is composed of granular materials that are transported as sediments. Variations in the velocity of the watercourse correspond to changes in the rate of sediment transport, which might result in soil erosion of any one section of the river and sedimentation at the other end of the river (Ingham, 1984). Sediment is one of the most common pollutants that impacts streams and rivers and is more visible in dams or lakes. The sand and gravel size sediments transit from the upper region following the topography watercourse and are deposited or come to rest

against a barrier within the plate of the waterbody. The fragments vary greatly in composition, shape and size and respond differently to the movement of water. The range of sizes present at one site determines the packing of the particles and defines the underwater topography when surveyed (Buller and McManus, 1979).

More than fifty percent (50%) of the original storage capacity of the world's reservoirs is likely to be lost within the next thirty years due to sedimentation (International sediment initiative (ISI), 2009). The menace of erosion and sedimentation is further exacerbated by global climate changes resulting from the rapidly growing population and human activities that increase soil erosion. Erosion, transport, and deposition of sediment are natural processes carrying a greater percentage of sediment load, which occur in arid and semiarid regions where the vegetation cover is low and experiences high-intensity rainfall.

When sediments are present in excess quantity, sediments can result in the following problems:

- i. A reduction in reservoir capacity and, in the case of dams, will result in a low water supply for domestic use, irrigation or hydroelectricity and, to some extent, dam collapse.
- ii. Reduction of channel capacity and results in flooding
- iii. Degradation of water quality
- iv. Sediments originating from the channel's water-land interface may cause instability of channel banks, resulting in the destruction of agriculture and other lands.

The rate of sediment transport can be computed from observed data, but the value obtained remains fairly inaccurate for the following reasons:

- i. The interaction between water movement and sediment transport is complex and difficult to describe mathematically accurately.
- ii. Sediment transport measurements are inaccurate. Therefore, sediment transport formulae cannot be accurately assessed.
- iii. The collection of sediment transport data using standard techniques is labour intensive and expensive.

Therefore, the prediction of suspended sediment load in a river is uncertain due to the dynamic nature of bulk load in the water column. However, that of reservoirs can be determined to some extent of accuracy because of their basin-like shape, and the barrier traps most materials.

2.5.1 Measuring Sedimentation in Dams or Rivers

The problem of sediment accumulation determination has been the major problem confronting water managers, water resource engineers and other water-related managers. This is because the negative impact of sediment deposits can cause severe damage to the storage facility and surrounding environment. Consequently, various researchers, such as [Estigoni et al., 2014](#); [Eakins and Grothe, 2014](#); [Khattab et al., 2017](#); [Ibrahim and Sternberg, 2021](#), etc. have worked in different capacities in an attempt to determine sediment accumulations in reservoirs around the world using repeated bathymetry survey approaches aimed at investigating and documenting the changes in the level of the reservoir bed in response to sediment deposition and distribution.

Furthermore, repeated bathymetry has become the most common and generally accepted technique for estimating long-term sediment accumulation in reservoirs. This involves using the data of different epochs, from obtaining the data when the dam started operation and the time when the bathymetric survey was done. These two datasets will show the volume lost to sedimentation and erosion. Additionally, the sediment accumulation rate can also be obtained by combining measurements of the sediment load entering the reservoir from upstream with an estimate of the trap efficiency of the waterbody ([Vulegbo et al., 2014](#); [Diego et al., 2017](#); [Greg et al., 2017](#)). The same approach can be used to determine the rate of sediment loss through the discharge gate. Figure 2.37 describes how sedimentation occurs in a reservoir as the finer materials gradually become trapped with the dam.

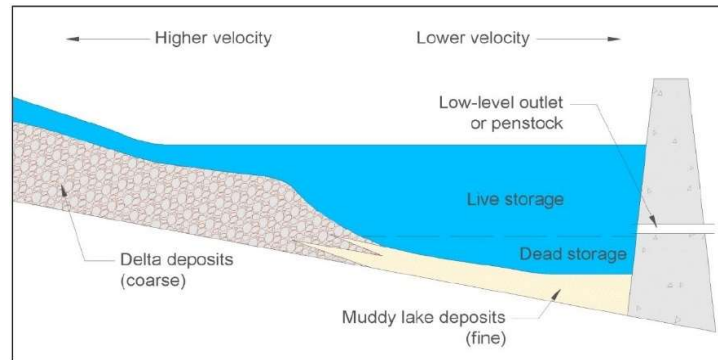


Figure 2:37 A typical 3D reservoir sediment profile
(Source: Moris and Fan, 1998 as cited in [Greg et al., 2017](#)).

According to [Mohammed et al. \(2018\)](#) and [Dutta \(2016\)](#), different soil erosion and sediment models are discussed in several studies, and they can be classified as empirical, physically based, and hybrid models. They are readily available for modelling soil loss due to water erosion and sediment transport in the river channel but cannot accurately account for the rate of sedimentation. [Psilovikos and Margoni \(2010\)](#) account that the empirical models are not limited to the Universal Soil Loss Equation (USLE), Modified Soil Loss equation (MUSLE), and Revised Universal Soil Loss Equation (RUSLE). Conceptual models integrate empirical and physically based models such as AGNPS, ANSWERS, CREAMS, WEPP, MIKE – 11, MIKE – SHE, OPUS, PRMS, REMM, SWAT, SWIM, and SEDNET. and researchers such as [Chen et al., 1978](#); [Soares et al., 1982](#); [Moris and Fan, 1998](#); [Martin \(2015\)](#); and [Mohammed et al., \(2018\)](#) have developed and employed some of these models to estimate sediment yield in rivers and reservoirs. Physically based methods include CREAM, ANSWER, EKWM, QSSE, and continuum mechanics. Conclusively, the hybrid soil erosion models are MMMF, USPED, AGWA, SPL, and AQUALM. An in-depth review of which technique accounts for the rate of sedimentation to some degree of accuracy was published by [Mohammed et al. \(2018\)](#) in the American Society of Engineers.

2.5.2 Sediment Yield Computation

Sediment yield determination using two different bathymetric datasets separated by time. The time difference between the two datasets should be a minimum of five years for an evident result. [Vahid et al. \(2018\)](#) presented a mathematical equation for computing

sediment yield but did not account for the trapped sediment in the portion of the reservoir flood pool considered to be above the conservation pool and those discharged via the spill gate. The equation is presented as:

$$Y = \left(\frac{V_0 - V_r}{t_0 - t_r} \right) \div W \quad 2.38$$

where Y is the sediment yield in ($m^3/km^2/year$), V_0 is the original reservoir capacity (m^3), V_r is the reservoir capacity at the most recent bathymetric survey, t_0 is the beginning of the reservoir operation, t_r is the date of the most recent bathymetric survey, and W refers to the drainage area (km^2).

2.5.3 Sediment Determination from Bathymetric Volume

This method of sediment accumulation (R) determination in a reservoir entails that the difference between the initial and present volumes of the period in consideration will constitute the space occupied by the sediment over time. In addition, this is achieved by subtracting the designed reservoir volume (V_i) from the present computed volume (V_f) from a bathymetric survey (Adediji, 2005; Alkali et al., 2016; Timothy and Jennifer, 2017). The mathematical expression is given as:

$$R_{annual} = \left(\frac{V_i - V_f}{T} \right) \quad 2.39$$

where R_{annual} is the annual mean reservoir sediment deposits in volume ($Mm^3/year$), V_i is the initial reservoir volume in (Mm^3), V_f refers to the final reservoir volume (Mm^3), and T is the number of years that the dam was in operation before the bathymetric survey.

2.5.4 Reservoir Half-life Computation

The maximum functioning period for a concrete dam varies from 100 to 200 years, but this relies on the rate of sedimentation (Yang, 2015). The determination of reservoir half-life aids in determining the effective and economic life span of any reservoir during a particular period. The effective life suggests that the dam is functioning to its maximum or certain capacity based on the purposed construction and that it is not affected by the collected or trapped sediment in the basin. According to Veli et al. (2019), the equation for computing the reservoir half-life is given as:

$$t_{1/2} = t_0 = \left(\frac{V_0}{Y*W} \right) \div 2 \quad 2.40$$

where $t_{1/2}$ is the half-life of the reservoir considering the negative effects of sedimentation over time. Other parameters are as defined in equation 2.38. Furthermore, a series of uncertainties arise when estimating the amount of sediment accumulation in a reservoir, such as the quantity of streamflow, sediment load, sediment particle size, specific weight, trap efficiency, and reservoir operation pattern (Dutta, 2016).

2.6 Application of Bathymetry Systems

This section reviewed and presented some of the applications of bathymetry systems. In addition, is the presentation of the field experience acquired by the researcher during the course of the PhD programme in the application of multibeam echosounder.

2.6.1 Application of Single Beam Echosounder

SBE is still one of the most commonly used systems in hydrographic depth measurement due to the cost implication of using a multibeam echosounder. Meanwhile, the purpose of the survey and the available resources determine which system to use. Hence, a series of researchers worldwide have employed single beam echo sounder bathymetric data to estimate the rate of sediment deposits in different water bodies, especially in reservoirs. However, the data are interpolated to align to equal geospatial distributions in the eastings and northings without serious distortions in the observed depth. Nevertheless, distortions in measured depth may arise depending on the interpolation model used. Below are some reviewed articles that used SBE bathymetric data to estimate sediment deposits in reservoirs.

[Odhiambo and Stephen \(2004\)](#) employed a dual-frequency single beam echosounder (28/200 kHz) and geographical information system (GIS) to study the rate of sedimentation and projected lifetime in two reservoirs (Lee Creek Reservoirs and Lake Shepherd Springs), both on the Ozark Plateau of northwestern Arkansas. Their results show that the former has a projected lifetime of 500 years and the latter has a projected lifetime of 3000 years. The estimated differences in the projected lifetimes of these reservoirs reflected the differences in the initial reservoir volume and long-term average annual sediment flux

from the respective watersheds related to the watershed area, physiography, land cover, and land use.

[El-Hattab \(2014\)](#) used SBES bathymetric data obtained from the Port Said Port maintenance project and employed twelve interpolation models to generate a digital terrain model (DTM) to determine the most accurate and fastest models that can be applied during maintenance dredging projects to mitigate the challenges that may arise at possible extra cost due to unpaid overdredging. The researcher results showed that a triangulated irregular network and natural neighbor interpolation techniques were optimal because they produced the best root mean square error (RMSE). However, other researchers, such as [Parente and Vallario \(2019\)](#) and [Ibrahim and Sternberg \(2021\)](#), concluded that there is no one best interpolation method. The technique to adopt depends on the nature of the data, purpose and analyst. [Estigoni et al. \(2015\)](#) carried out a study assessing reservoir volume and sedimentation based on bathymetric surveys in the Peruvian Andes region Peru. The bathymetry was acquired using an SBES Raytheon 90 Hz in combination with a Pentax total station for horizontal positioning. The bathymetric data and topographic data of the reservoir before impounding were compared, and the sedimentation rate was estimated. The dataset is interpolated using TIN, and the volume determined of TIN and by Insertion of Mesh Points. The authors' results show that the reservoir has a yearly sedimentation rate of 2.90%.

Furthermore, research was conducted by [Ajith \(2016\)](#) using bathymetric data acquired using SBES NS-415 dual-frequency (33/200 kHz) to study the rate of sediment deposition in the reservoir of the Peechi dam with the combination of GPS Leica Mx 420 (mobile station) for horizontal position fixing. The research indicated that the reservoir had experienced a reduction in the capacity of approximately 14.027% from the original over the past 56 years, and the rate of sedimentation was 0.25% per year. Similarly, [Khaba and Griffiths \(2017\)](#) researched the calculation of reservoir capacity loss due to sediment deposition in the Muela reservoir in northern Lesotho. The authors used four bathymetric datasets acquired using SBES from the Lesotho Highlands Development Authority (LHDA) between 1985 and January 2015. They employed four interpolation techniques to interpolate each dataset to create DTMs for better analysis. The researchers' results suggested that there is high interannual variability in the rate of reservoir capacity

reduction, and the reservoir volume reduction varies between 11,400 m³/year and 18,200 m³/year.

Likewise, [Temitope and Kehide \(2019\)](#) researched bathymetric surveys and topography change investigations of parts of Badagry Creek and the Yewa River in Lagos state, Southwest Nigeria. The authors used the bathymetric datasets of 2008 and 2015 acquired using digital echo sounder SDE28 in collaboration with Handheld real-time kinematic GPS for spatial coordinate position fixing. Their results show that there were no adequate change in depth between 2008 and 2015 despite the rate of dredging within the study area. They concluded that the increase in the volume of sediment deposits could result from the adjoining Yewa River flowing into the larger river tributaries of Badagry Creek; however, this is subject to further studies. [Ibrahim and Sternberg \(2021\)](#) recently researched bathymetric surveys to enhance the volumetric capacity of the Tagwai dam in Nigeria via a leapfrogging approach. The authors used bathymetric data collected using SBES and Hi-Target V30 Differential Global Positioning System (DGPS). The data were interpolated using the ordinary kriging technique, and thereafter, four scenarios were set using the leapfrogging technique to increase the reservoir volume. The researchers' results suggested that scenario D demonstrated an adequate increase in the storage capacity, and it is a win-win situation. They concluded that the decision on which leapfrogging approach to employ depends on the government's willingness to enhance the reservoir's capacity and the available resources.

2.6.2 Application of MBES (summer school experience)

Multibeam echo sounders (MBESs) have been applied for various underwater studies worldwide since their development. This includes the study of the sedimentation situation of a large reservoir after an earthquake, such as [Yan et al., 2018](#). Similarly, it has been used for other sediment deposit investigations, such as [Amiri-Simkooei et al., 2008](#); [Schneider et al., 2013](#); [Chun et al., 2016](#); [Trung, 2018](#); [Zakariya et al., 2018](#); [Amiri-Simkooei et al., 2019](#) and others. In addition, it has been employed for the study of biological monitoring and other related research, such as [Che Hasan et al., 2011](#); [Montereale-Gavazzi et al., 2018](#); [Annalisa et al., 2020](#); and [Benjamin et al., 2021](#).

2.6.3 Summer School Experience

The 2nd Bonus Ecomap summer school was from 27th to 31st August 2019 at the University of Gdansk, Institute of Oceanography, Hel Marine Station Poland. The course focused on optoacoustic methods currently emerging as valuable tools for geospatial and environmental analysis and habitat mapping. The course also provided an overview of gas in sediments and the acoustic classification of the seabed. Furthermore, Oceanograf Gdynia is the survey vessel of the hosting institution, as illustrated in Plate 2.1. It is equipped with all the necessary equipment for adequate, efficient, and effective underwater research. It is equipped with equipment such as the DGPS for real-time differential positioning, MBES for depth measurement and underwater habitat investigation, initial motion sensors, complete sets of computer systems, SVP, complete platform for ocean geological exploration, etc. to crown it all, the vessel is completely equipped for research purposes.



Plate 2:1 Oceanograf Gdynia at the dock at the Hel marine station with one of the summer school students standing in position. Source: Photographed by one of the students after returning from field exercise.

The MBES is mounted on the hull at the bottom around the vessel's centre. The operators had done all necessary settings and calibrations before the students boarded the vehicle for typical field experience. In the course of the exercise, the information gathered from the organizers was that the average depth of the Baltic Sea is approximately 58 m. The deepest point within the Poland region of the sea is approximately 112 m. In contrast, the deepest

part of the entire Baltic is approximately 460 m, and that area is found in the Sweden region of the Baltic Sea.

Basically, three hydrographic field exercises were conducted during the summer school programme and are explained below.

First, at a point during sailing on the Baltic Sea, the vessel was adjacent to the launch of SVP. The SVP was deployed at a depth of approximately 69 m, and it recorded the velocity of sound in the water column. Immediately, it touched the seabed, stopped working and came up for withdrawal. Plate 2.2 (a) describes the SVP with its compartment at rest, (b) demonstrates the launching of the SVP in the water column for sound velocity measurement, and (c) shows the sound velocity downloaded and uploaded into the computer system with the necessary Qinsy bathymetry software for accurate real-time depth determination during the sounding operations.

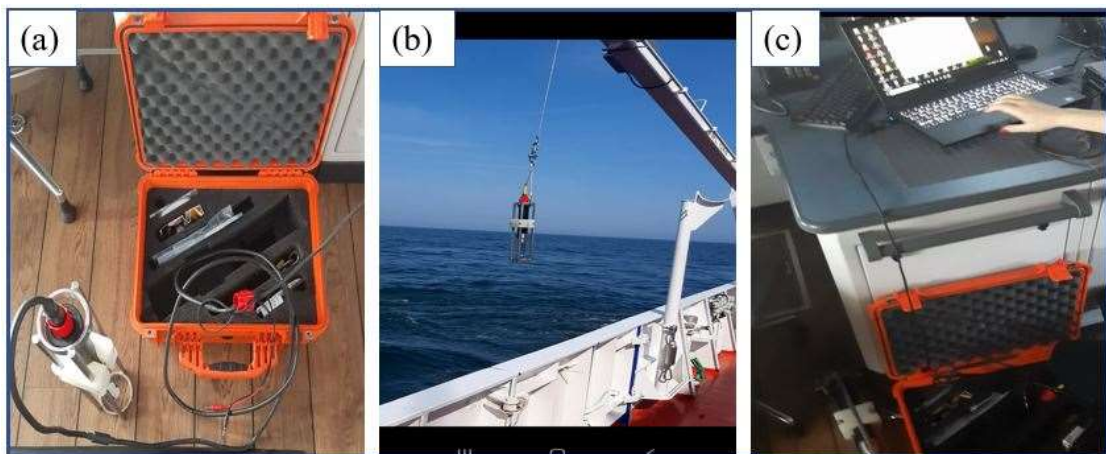


Plate 2:2 Deployment of SVP for sound velocity measurement. (a) SVP with its compartment before launching. (b) Launching of the SVP in the Poland region of the Baltic Sea. (c) Downloading and uploading the SVP data from the SVP to the computer system with real-time bathymetric processing Quincy software. Source: Ecomap summer school 2019

These processes were repeated as the vessel kept sailing, especially when the depths changed at some particular distances to accurately account for variations in salinity, temperature, and pressure.

Second, the modified Van Veen grab was lowered at a depth reading of 69 m to take sediment samples, as shown in Plate 2.3 (b). This is being done at intervals as the vessel

sails for the purpose of knowing how soft, dip or reflected the layers may be or grassy; most importantly, the sample taken is used to compare with what the acoustic map produced for accurate and precise data analysis. Plate 2.3 (a) describes the modified Van Vee grab, with the added teeth and the observation ports.

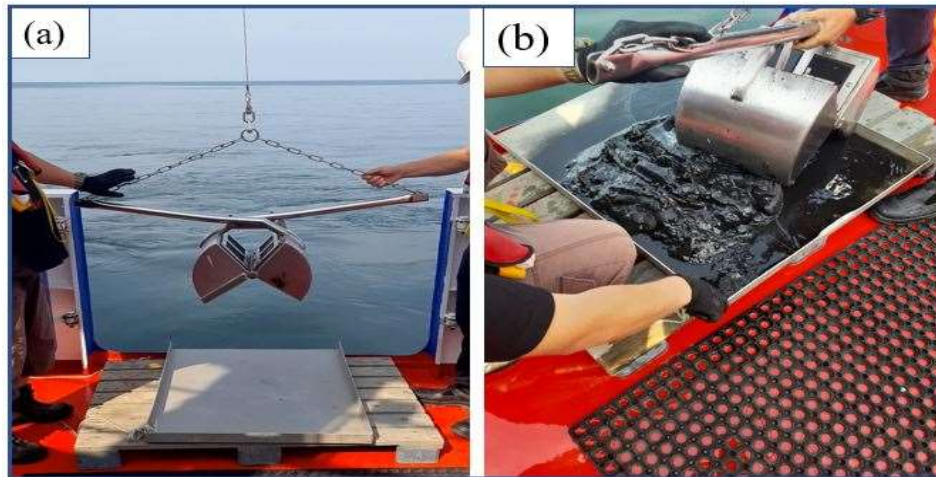


Plate 2:3 (a) Modified Van Vee grab before Lowering down the sea, (b) Sediment sample being removed from the Van Vee grab for further investigation.

Source: Ecomap summer school 2019

The jaws of the grab are held together firmly during withdrawal because the lifting cable is attached to the ends of the arms, which protrude past the axis and exert a strong clamping action. This type of equipment usually has inspection hatches on the flat side of the sampler bucket, which enable inspection of sediment surface structures or withdrawal of small cores before the release of the sample (Buller and McManus, 1979).

Third, the real-time bathymetric survey and ship or boat wreck search were carried out using the MBES, which is made up of 512 beams with complete positioning systems. The depth resolution is 1 cm, and the angular resolution is 0.5 by 1 cm in both directions. The MBES was set on equidistance. However, for an accurate survey, equiangular is far better because the precision is higher than equidistance, which is also called beam focus. Plate 2.4 (a) describes the bathymetric backscatter data in the water column without settings and transmitting for correction. Plate 2.4 (b) shows the bathymetric backscatter data in the water column being transmitted for postprocessing software correction. The nadir and the beam are higher than the fan, as shown on the scan of monitor two (2) at the plate.

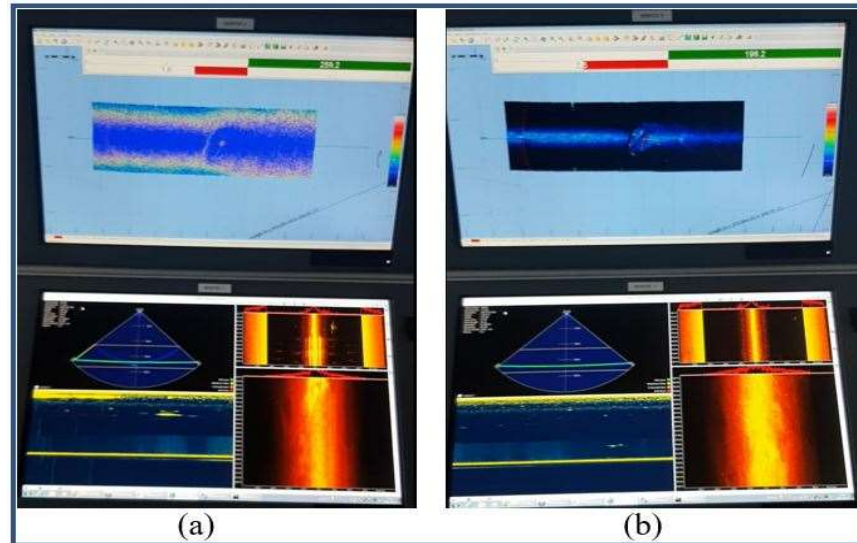


Plate 2:4 (a) Bathymetric backscatter data without settings for corrections, (b) Bathymetric backscatter data with settings for postprocessing software corrections. Source: Ecomap summer school 2019.

Plate 2.5(a) describes the boat wreck location with a vertical impact presentation of settings with a value of 10. Nevertheless, the bottom bathymetric image is very rough and visually poor. At the same time, Plate 2.5(b) shows the bathymetric image of vertical impact presentation of settings 1, and it is evident that with a vertical impact value of 1, the image is sharper and more apparent.

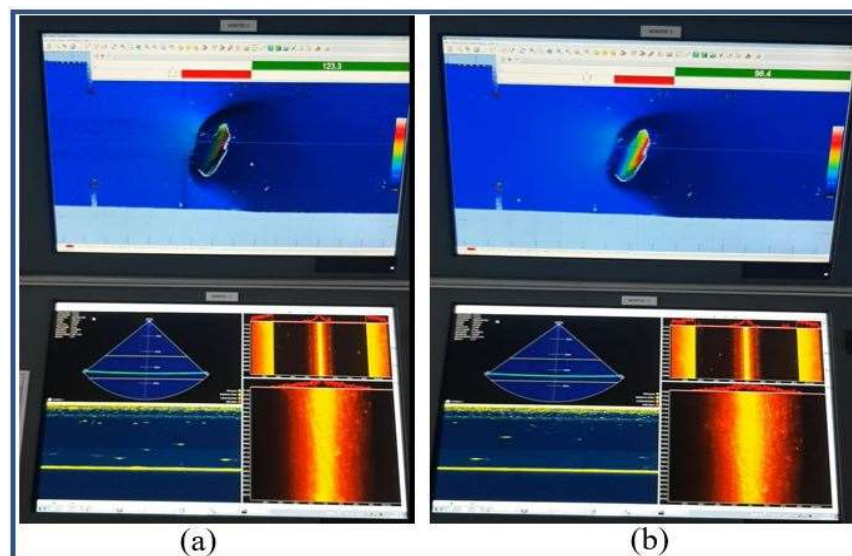


Plate 2:5 (a) Bathymetric image of a boat wreck with a vertical impact value of 10, (b) Bathymetric image boat wreck with a vertical impact value of 1. Source: Ecomap summer school 2019.

Furthermore, a marine ship that was sunk during World War II was found. However, the ship was previously located by the research team of the Institute of Gdansk. We were told that discussion is ongoing on how to retrieve the ship because it was discovered that it still has the full loaded tank of oil. The vessel is equipped with a crane and other valuable objects, as shown in Plates 2.6 (a) and (b), respectively.

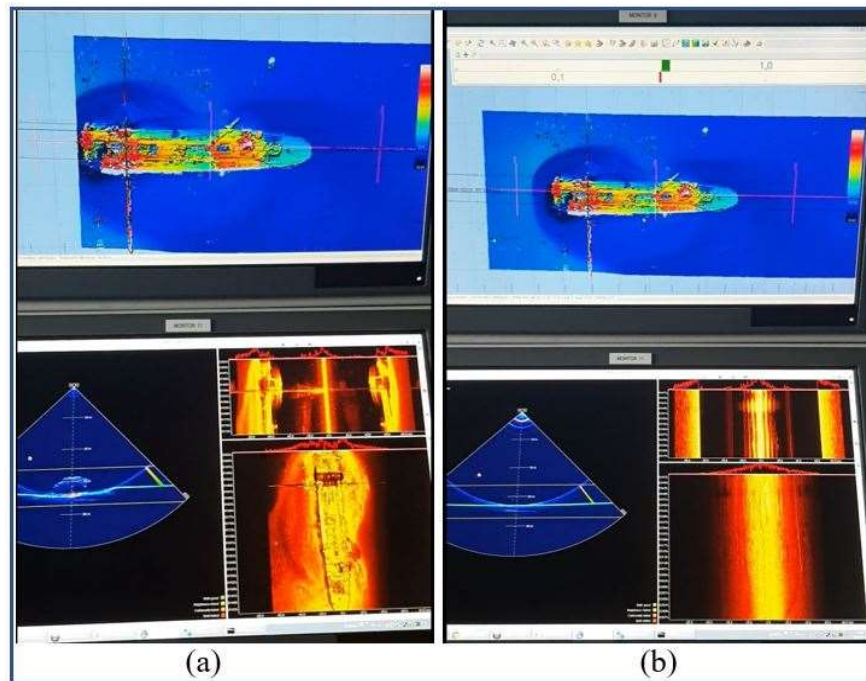


Plate 2:6 (a) Showing the Ship image location and passing on the scan at the bottom,
(b) Describing the ship image and location at full pass.
Source: Ecomap summer school 2019.

In addition, the width and length of the ship as measured in real time were 25 m and 130 m, respectively. Meanwhile, the original length of the ship before it was sunk was 160 m. The presentation of a shipwreck in Plate 2.6 describes the superiority of MBES over SBES. It will take multiples of sweeps for an SBES to give a representation of such, and the resolution will be poor and rough.

2.7 Markov Chain Model, Gradient Boosting Regression, and Cellular Automata

The Markov chain model and gradient boosting regression are models for predicting feature occurrences with the aid of cellular automata for effective classification and projection.

However, their application and best fit depend on the data structure and care taken during model technique implementation.

2.7.1 Markov Chain Model

This section introduces the Markov chains or Markov process and its applications. The Markov process is a stochastic model describing a sequence of possible events in which the probability of each event depends only on the state attained in the previous event (Gagniuc, 2017). Markov chains are exceptionally useful to model a discrete-time, discrete space or continuous-time stochastic process/random process of various domains, such as environmental sciences (land use and land cover classification), meteorology (weather forecasting), finance (stock price movement), and engineering physics (Brownian motion). A discrete-time Markov chain (DTMC) is a countably infinite series in which the chain state changes at discrete time steps, while a continuous-time Markov chain is called a continuous-time Markov chain (CTMC) (Pankin, 2007; Serfozo, 2009). A stochastic process that satisfies the Markov property is the term Markovian.

2.7.2 Discrete-Time Markov Chain

For a series of random variables $X_0, X_1, X_2 \dots$ with values in a countable set S is a Markov chain if at any time n , the future states $X_{n+1}, X_{n+2}, X_{n+3} \dots$ depend on the history X_0, \dots, X_n only through the present state X_n with Markov property, that is the probability of moving to the next state depends only on the present state and not on the previous states (Seneta, 1996; Serfozo, 2009; Rocca, 2019):

$$\Pr(X_{n+1} = x | X_1 = x_1, X_2 = x_2, \dots, X_n = x_n) = \Pr(X_{n+1} = x | X_n = x_n) \quad 2.41$$

If both conditional probabilities are well defined and satisfied, that is if

$$\Pr(X_1 = x_1, \dots, X_n = x_n) > 0. \quad 2.42$$

Therefore, the possible values of X_i from a countable set S are called the state of the chain. Moreover, knowledge of the previous state is required and necessary to determine the probability distribution of the current state.

There are variations depending on the discrete-time Markov chain process; these variations are summed as:

- 1) *Time-homogeneous Markov chains*: the process where the probability of the transition is independent of n for all values of n , that is:

$$\Pr(X_{n+1} = x | X_n = y) = \Pr(X_n = x | X_{n-1} = y) \quad 2.43$$

- 2) *The stationary Markov chain* involves the processes where

$$\Pr(X_0 = x_0, X_1 = x_1, \dots, X_k = x_k) = \Pr(X_n = x_0, X_{n+1} = x_1, \dots, X_{n+k} = x_k) \quad 2.44$$

For all n and k , Baye's rule can act as an agent to show that every stationary Markov chain can be transformed to be a time-homogeneous Markov chain. When the distribution of X_0 is a stationary distribution of the Markov chain, it has satisfied all conditions for a time homogeneity to be stationary.

- 3) *Markov chain memory or a Markov chain of order m* : a Markovian process where m is finite and satisfies the condition;

$$\Pr(X_n = x_n | X_{n-1} = x_{n-1}, X_{n-2} = x_{n-2}, \dots, X_1 = x_1) = \Pr(X_n = x_n | X_{n-1} = x_{n-1}, X_{n-2} = x_{n-2}, \dots, X_{n-m} = x_{n-m}) \text{ for } n > m \quad 2.45$$

This implies that the future state depends on the past m states. A chain of (Y_n) can be constructed from (X_n) , which is the 'main' Markov property, by taking state-ordered m -tuples of X values, that is $Y_n = (X_n, X_{n-1}, \dots, X_{n-m+1})$.

2.7.3 Continuous – Time Markov chain

A continuous-time Markov chain of the order $(X_t)_{t \geq 0}$ is said to be a finite or countably state space (δ) , with a transition rate matrix Q with dimensions equal to that of the state space (S) and formal probability distribution defined on the state space (S) . For $i = j$, the q_{ij} elements are nonnegative and describe the speed of the transition from state i to j . The q_{ij} elements are chosen so that each row of the transformation rate matrix sums to one, where the row sum of the probability transformation matrix on the Markov series is equal

to one (William, 2012; Norris, 1997). The continuous Markov chain can be summarized in 3 parts.

- 1) *Infinitesimal*: Take X_t to be the random variable that describes the state of the process at time t , with a presumed process state i at time t . Therefore, knowing that $X_t = i, X_{t+h} = j$ is independent of previous values ($X_s: S < t$), and as $h \rightarrow 0$ for all j and t .

$$\Pr(X(t+h) = j | X(t) = i) = \delta_{ij} + q_{ij}h + o(h) \quad 2.46$$

where δ_{ij} is the Kronecker delta, using the little - 0 notation. q_{ij} is a factor that measures how speedy the transformation from i to j will occur.

- 2) *Jumpchain or holding time*: This is a discrete-time Markov chain of Y_n that describes the n^{th} jump of the process and variables, say S_1, S_2, S_3, \dots , to describe holding times in each of the states where S_i follows the exponential distribution with rate parameter $-q_{Y_i Y_j}$

- 3) *The transition probability*: the transition probability q_{ij} specifies the probability of going from state i to j in one step. The transition matrix of the chain is the $M * M$ matrix $Q = q_{ij}$. We hold that Q is a nonnegative matrix in which each row sums to 1. Considering the value $n = 0, 1, 2, 3, \dots$ and times indexed up to this value of $n: t_0, t_1, t_2, \dots$ and all states recorded at these times i_0, i_1, i_2, i_3 , it refers to

$$\Pr(X_{t_{n+1}} = i_{n+1} | X_{t_0} = i_0, X_{t_1} = i_1, \dots, X_{t_n} = i_n) = P_{i_n i_{n+1}}(t_{n+1} - t_n) \quad 2.47$$

where P_{ij} is the solution of the forward equation (a first-order differential equation) and $P^t_{(t)} = P(t)Q$ with the initial condition $P(0)$ is the identity matrix.

Furthermore, in *finite state space* for a stochastic process of natural numbers in a state space, the transition probability distribution can be represented by a matrix, known as the transition matrix with the notation $(i, j)th$ element of P equal to

$$p_{ij} = \Pr(X_{n+1} = j | X_n = i) \quad 2.48$$

P will be a good stochastic matrix when each row is added up to one and all the elements of P are nonnegative.

2.7.4 Practical Application of Markov Chain Model

Markov chains (MCs) have found greater application in land use land cover (LULC) classification since their implementation in the field of geographic science by Andrey Markov. While the model can be processed individually, many researchers have integrated Markov chain and cellular automata (CA and MC). [Iacono et al. \(2012\)](#) used the concept of the Markov chain model to introduce an alternative to land-use modelling. The model concept assumes that land use at any given time, which is viewed as a discrete state, can be considered a function of only its previous state. The transition probability between each pair of states is recorded as an element of a transition probability matrix. Assuming that this matrix is stationary over time, it can be used to predict future land use distributions from current data. They used the historical epoch data of 1958 and 2005 of the Twin Cities of the Minneapolis-St. Paul, MN, USA. The authors' results presented land use patterns and predicted future land use distribution patterns and other special land reservations, such as transportation facilities and major highways. Their research proved the capability of MC to describe and model complex and long-term processes of land-use conversion.

[Nurmiaty et al. \(2014\)](#) analysed land-use change using the integration method of CA and MC in remote sensing and GIS. The researchers applied all the necessary image corrections before finally processing the data using the combined models. The research produced a predicted land use pattern for the next 29 years, i.e., 2029. The results showed an increase in built-up area and a reduction in agricultural land use. Similarly, [Kumar et al. \(2016\)](#) combined MC- and CA-based models to predict the urban growth of Vijayawada city, the new capital of Andhra Pradesh state, India. The MC and CA chain analysis is embedded in a geographic information system called the land change model (LCM) module of the Terrset software. The data epoch used is for 1977, 1996, and 2015. Hence, the data after processin MC and CA were used to predict LULC in the future (2053). The author's research was able to show the capability of MC and CA to demonstrate the urban transition from past to present and to the future with supporting results (images). Furthermore, other authors have also combined MC and CA to simulate and forecast land use patterns for the present and the future, but in a different study area. Some of these authors are [Thomas and Laurence \(2006\)](#); [Al-shar et al., 2021](#); [Francina et al., \(2021\)](#); [Ebrahimpour et al., \(2020\)](#); [Tadese et al. \(2021\)](#); [Zouiten et a., \(2021\)](#).

2.7.5 Gradient Boosting Regression

Gradient boosting regression (GBR) is an analytical method that is designed to explore the connection between two or more variables (X , and Y). Its analytical output establishes important factors (X_i) impacting the dependent variable (Y) and the nature of the connection between each of these factors and the dependent variable (Friedman, 2001; Terence and Jeremy, 2021). Gradient boosting is one of the most powerful methods for constructing predictive models (Dietterich et al., 1995; Elith et al., 2008; Friedman, 2001). Forecasting future events is essential in many fields to support decision making, as it contributes to reducing future uncertainty. A gradient boosting algorithm can be employed to train models for both regression and classification problems. A gradient boosting regression algorithm is used to fit the model that predicts the continuous value. In addition, regression models depend on building a connection between independent variables, e.g., features such as previous observations, and dependent variables, e.g., target outcomes (Elith et al., 2008; Igor et al., 2020).

Furthermore, the idea of boosting was born out of the idea of whether a weak learner can be modified to become better. A weak learner hypothesis or weak learner is said to be one whose performance is at least slightly better than random chance. This technique constructs an additive mode by using multiple decision trees of fixed size as weak learners or weak predictive models (Kumar, 2020). More precisely, the GBR trees fit a decision tree on the residuals obtained from the fitted prediction model (or base learner) and aim to improve the prediction model by adding new decision trees to update the base prediction. The predicted residuals are used to update the base prediction after being multiplied by a learning rate at each iteration. This implies that GBR trees use all the rules to update the prediction with a fixed learning rate.

The parameter estimators support the arguments to control the fitting behaviour; these arguments are often called hyperparameters. The relevant ones for the GBR technique are the number of regression trees (`n_estimators`), the depth of each individual tree (`max_depth`), loss functions (`loss`), and the learning rate (`learning_rate`).

2.7.6 Loss Functions

There are different loss functions $L(y_i, f(x))$ to use depending on the particular learning task; however, the choice is usually motivated by the demand of unique characteristics of the conditional distribution. One of the important observations is to check the robustness to outliers, but other factors can be considered (Natekin and Knoll, 2013). Many loss functions have been developed for implementation in the gradient boosting machine algorithm (Friedman, 2001; Schmid and Hothorn, 2008; Schmid et al., 2011). Additionally, loss functions can be grouped based on the type of response variable y . Special boosting algorithms have been developed for various response groups, including the regression, classification and time to event analysis tasks. Relying on the response variable y , the often employed loss function can be summarized as described in Table 2.5 (Natekin and Knoll, 2013; Grover, 2018).

Table 2:5 Group of Loss functions
(Source: Natekin and Knoll, 2013 and modified in the research lab)

Group of Loss functions	Loss functions
Continuous response ($Y \in \mathbf{R}$)	Gaussian L_2 loss function
	Laplace L_1 loss function
	Huber loss function, δ specified
	Quantile loss function, α specified
Categorical response, $Y \in \{0, 1\}$	Binomial loss function
	Adaboost loss function
Other group of response variable	Loss functions for survival models
	Loss functions counts data
	Custom loss functions

Specifically, the commonly used loss function practises the basic squared error L_2 the loss function of the continuous response:

$$\psi(y, f)L_2 = 1/2 (y - f)^2 \quad 2.49$$

This implies that the derivative of equation 2.49 is the residual $y - f$, meaning that the GBR algorithm simply performs residual refitting. The main goal of this loss function is to minimize large derivatives from the target outputs while neglecting small residuals. Meanwhile, the loss function (L_1) is more robust to outliers, but its derivatives are not

continuous. So it is incapable of finding a solution. In contrast, the loss function (L_2) is sensitive to outliers but gives a more stable and closed-form solution by setting its derivative to zero (0) (Friedman, 2001; Grover, 2018). Details of the loss function can be found in Friedman, 2001; Natekin and Knoll, 2013, Grover, 2018).

2.7.7 GBR Algorithm

The gradient boosting regression (GBR) algorithm is a gradient boosted algorithm for numerical prediction. There are three basic steps of the mathematical representation, with other subsidiary steps within each of those three steps. The GBR algorithm can be presented as follows:

The input data $\{(x_i, y_i)\}_{i=1}^n$ and a differentiable loss function $L(y_i, F(x))$

Step (1): Initiate the model with a constant value: $F_0(x) = \underset{\gamma}{\operatorname{argmin}} \sum_{i=1}^n L(y_i, \gamma)$

2.50

Step (2): For $m = 1$ to M :

A. Compute $r_{im} = - \left[\frac{\partial L(y_i, F(x_i))}{\partial F(x_i)} \right]_{F(x)=F_{m-1}(x)}$ 2.51

B. Fit a regression tree to the r_{im} values and create terminal regions $R_{j,m}$, for $j = 1 \dots$

J_m

C. For $j = 1 \dots J_m$ compute $\gamma_{im} = \underset{\gamma}{\operatorname{argmin}} \sum_{x_i \in R_{ij}} L(y_i, F_{m-1}(x_i) + \gamma)$

2.52

D. Update $F_m(x) = F_{m-1}(x) + v \sum_{j=1}^{J_m} \gamma_{jm} I(x \in R_{j,m})$ 2.53

Step (3): Output $F_m(x)$

2.7.8 Discussion of the Mathematical GBR Algorithm

The input data and the loss function describe the training dataset and how well the method adopted best fit the training dataset. Where x_i refers to the rows of each coordinate (position) in this case and y_i refers to the depth measures at each position. $i=1$ is the i_s in X_i and y_i and goes from 1 to n , where n is the number of points in the entire dataset. The

loss function ($L(y_i, F(x))$) is a factor that evaluates how well we can predict the depth. The loss function that is usually used when performing regression with GB is $\frac{1}{2} (\text{observed} - \text{predicted})^2$. If $\frac{1}{2}$ is removed, we have the loss function we use for linear regression. Thus, the loss function is just the square of the residuals $(\text{observed} - \text{predicted})^2$. However, $\frac{1}{2} (\text{observed} - \text{predicted})^2$ the loss function is best adopted for GB because when it is differentiated with respect to the predicted value, we have “ $-(\text{observed} - \text{predicted})$ ”, that is:

$$\frac{\partial}{\partial \text{predicted}} \frac{1}{2} (\text{observed} - \text{predicted})^2 \quad 2.54$$

Using the chain rule

$$\begin{aligned} &= \frac{2}{2} (\text{observed} - \text{predicted}) \times (-1) \\ &= -(\text{observed} - \text{predicted}) \end{aligned} \quad 2.56$$

Hence, this makes the maths direct since GB uses the derivative frequently.

Step (1): Initialize the model with a constant value: $F_0(x) = \underset{\gamma}{\text{argm}} \sum_{i=1}^n L(y_i, \gamma)$, where y_i is the observed value, and gamma (γ) is the predicted value, while summation ($\sum_{i=1}^n$) is the summation of each of the loss functions. Argmin over gamma means that we need to find a predicted value that minimizes the sum of the loss functions.

Step (2): This is the loop where the trees are being constructed. For $m = 1$ to M , $m = M$ refers to the last tree, and M can be any number of trees. Little m refers to an individual tree.

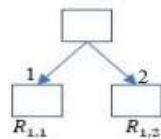
A. Compute $r_{im} = - \left[\frac{\partial L(y_i, F(x_i))}{\partial F(x_i)} \right]_{F(x)=F_{m-1}(x)}$ for $i = 1, \dots, n$

$- \left[\frac{\partial L(y_i, F(x_i))}{\partial F(x_i)} \right]_{F(x)=F_{m-1}(x)}$ is the derivative of the loss function with respect to the predicted value, i.e.,

$$\frac{\partial}{\partial \text{predicted}} \frac{1}{2} (\text{observed} - \text{predicted})^2 = (-)(-)(\text{observed} - \text{predicted})$$

Therefore, $(observed - F_{m-1}(x))$. When $m = 1$ we replace $F_{m-1}(x)$ with $F_0(x)$. Then, we have $(observed - F_0(x))$. To compute r_{im} where r is the residual, i is the sample number, and m is the tree that is to be built. For $i = 1, \dots, n$ means computing the residual for all the samples in the dataset. The derivative equation is what the gradient is named after. Consequently, step (2) equations are technically called pseudoresiduals. When we use this loss function $(\frac{1}{2}(observed - predicted)^2)$, we end up calculating normal residuals $(observed - predicted)$, but if we used another loss function not multiplied by $\frac{1}{2}$ that is $(observed - predicted)^2$, then we would end up with something similar to a residual, but not quite, that is $2(observed - predicted)$. In other words, we would end up with a pseudoresidual $2(observed - predicted)$, which is the reason r_{im} 's are called pseudoresiduals.

- B. Fit a regression tree to the r_{im} values and create terminal regions R_{im} , for $j = 1, \dots, J_m$, which refers to building a regression tree to predict the residuals instead of the weights. It should be noted that m is the index for the tree, and j is the index for each leaf in the tree.
- C. For $j = 1 \dots J_m$, compute $\gamma_{im} = \underset{\gamma}{argmin} \sum_{x_i \in R_{ij}} L(y_i, F_{m-1}(x_i) + \gamma)$; specifically, x_i in R_{ij} means that the value in x_i goes to leaf $R_{1,1}$, or x_1 and x_2 are used to calculate $R_{2,1}$, which is $\sum_{x_i \in R_{ij}}$, in summation. Having two leaves, that is:



since this is the first tree, which means $j = 1$, and $m = 1$

$$\gamma_{1,1} = \underset{\gamma}{argmin} \frac{1}{2} (y_n - F_{m-1}(x_n) + \gamma)^2$$

the derivative will yield the desired result.

Based on the loss function, the output values are always the average residuals that end up in the same leaf. Even if only one residual ends up in a leaf, the output value is still the average.

- D. In section D, “Update $F_m(x) = F_{m-1}(x) + v \sum_{j=1}^{J_m} \gamma_m I(x \in R_{j,m})$ ”, a new prediction is made for each sample and then updated. Then, $F_1(x) = F_0(x) +$ the tree that was made in C.

Note that the summation is there just in case a single sample ends up in multiple leaves. This is to add up all the output values $\gamma_m I(x \in R_{j,m})$ for all the leaves $R_{j,m}$ that sample X can be found in. while the Greek character (v) is the learning rate and lies between 0 and 1. In addition, a small learning rate (v) reduces the effect that each tree has on the final prediction; thus, this improves the accuracy in the long run.

Step (3) is the final output $F_M(x)$; if $M=2$, then $F_2(x)$ is the output from the gradient boost algorithm.

2.7.9 Practical Application of GBR

The practical application of GBR in hydrography, or hydrology is not readily available. However, [Saikat-Islam et al. \(2021\)](#) conducted research on water quality prediction and classification based on principal component regression and the gradient boosting classifier approach. The authors' three main approaches are as follows: first, they computed the water quality index (WQI) using the weighted arithmetic index method. Second, principal component analysis (PCA) was applied to the dataset, and the most dominant WQI parameters were extracted. Third, to predict the WQI, different regression algorithms were used to determine the PCA output. Finally, the gradient boosting classifier was used to classify the water quality status. The author's results showed 95% prediction accuracy for the principal component regression method and 100% classification accuracy for the GBR classifier method. The researchers concluded that their results demonstrated credible performance compared with the state-of-art models.

2.7.10 Cellular Automata

Cellular Automata (CA) is a sophisticated mathematical technique employed to manipulate data in rows and columns often represented in extended binary format, where neighbouring pixel information is paramount ([Neuman, 1966](#); [Heldlund, 1969](#); [Wolfram, 1994](#); [Wenzhong and Matthew, 2000](#); [Chih-Hung, 2014](#)). The arrays of the cell can either be 1D, 2D, or 3D, and each cell is an identically programmed automaton ([Agapie et al., 2014](#)). Over the years, the CA model has been employed to simulate complex systems or processes. The combination of the CA model with order models for effective data manipulation, processing and analysis, e.g., CA and Markov chains ([Agapie, 2014](#)), has

found extensive application in the field of geographic information systems to study geographic phenomena (Tobler, 1970; Batty et al., 1997; Torrens, 2007). It has also found greater application in several fields, such as biology, physics, chemistry, and economics, to investigate and analyse the growth of plants, DNA evolution and embryogenesis, consumer behaviour, and to study the spatial dimension of economic systems (Neumann, 2010). Above all, this technique was first promulgated by John Von Neumann in the 1940s to create and formalise a theoretical model for self-reproducing machines. Neumann’s ideal was propelled by his action to understand biological evolution and self-reproducing (Neumann, 2010). However, emphasis will be placed on the geographical point of view.

2.7.11 Cellular Automata Mathematical Model

This scheme works on stipulated rules based on neighbouring cells of which each cell has a finite state, such as 0 or 1, and is flipped or updated based on the set rules not neglecting the value of the centre cell “Figure 2.38 demonstrates 1D arrays of cells where the label black cells is 1, and the white cells are 0”. This is because CA is a nonlinear dynamical system in which space and time are discrete (Amir et al., 2013). CA is composed of several identical arrays (identical automata) that are physically arranged as 2-dimensional pixels of rectangular cells, where each cell is referred to as an automaton (A), with a set of rules (T) that obtains its inputs from its own state and from neighbouring cell states (V) (Amir et al., 2013):

$$A \sim (S, T, V) \tag{2.57}$$



Figure 2:38 One-dimensional arrays of CA. In which the label black cells is 1 and the white cells is 0. (Source: Research lap)

Torrens (2007), presented the basic computing automata equation as:

$$A \sim (S, R); S = \{S^1, S^2, S^3, \dots S^k\}; R: (S_t, I_t) \rightarrow S_{t+1} \tag{2.58}$$

where A is an automaton characterized by states S and a transition rule T. The transition rule functions to manage changes in state S from t to time t + 1, given input of other state information from outside the automaton at time t. In this case, the transition rule becomes the medium of exchange, and states become the raw material when many of such automata

are designed to cointeract. In addition, time is the final component of CA in which the cells interact based on specific rules assigned. Adding cells to the basic automaton structure gives the following expression:

$$CA \sim (S, T, N); S = \{S^1, S^2, S^3, \dots, S^k\}; R: (S_t, N_t) \rightarrow S_{t+1} \quad 2.59$$

CA is the cellular automaton, characterized by states S , a transition rule or (vector of rules) R , and a neighbourhood N .

Similarly, there are predominantly two types of neighbourhoods: Von Neumann neighbours and the Moore neighbourhood (Kier et al., 2005); see Figure 2.39.

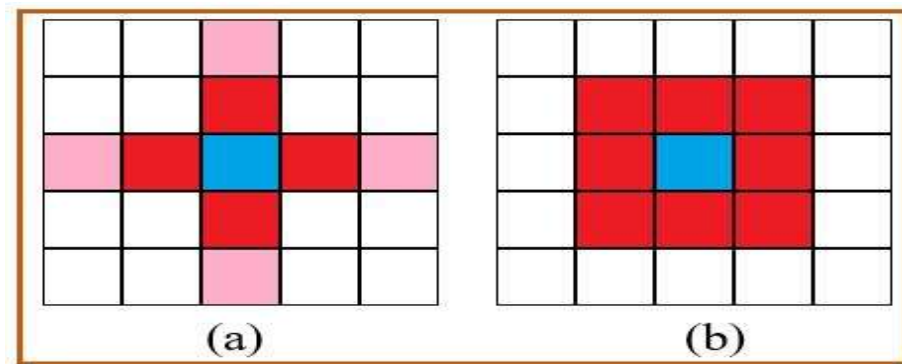


Figure 2:39 (a) Von Neumann neighbourhood, (b) Moore neighbourhood.

The red cells are the Von Neumann neighbourhood for the blue cell.

The range-2 "cross neighbourhood" also includes pink cells (a).

The red cells are the Moore neighbourhood for the blue cell (b).

(Source: Kier et al., 2005 and modified in the lap).

However, most geographical features are not regular in shape for adequate implementation of the CA model. This posed challenges that promulgated several researchers, e.g., Flache and Hegselmann, 2002; Amir et al., 2013; and others to extend the CA model to irregular cells. A successful approach in mitigating this challenge is using the Voronoi spatial model (Wenzhong and Matthew, 2000; Flache and Hegselmann, 2002). The Voronoi spatial model is a tessellation of space that is constructed by breaking down the entire space into a set of Voronoi regions around each spatial object. Figure 2.40 describes the Voronoi spatial CA model (a) and a regular spatial CA model (b).

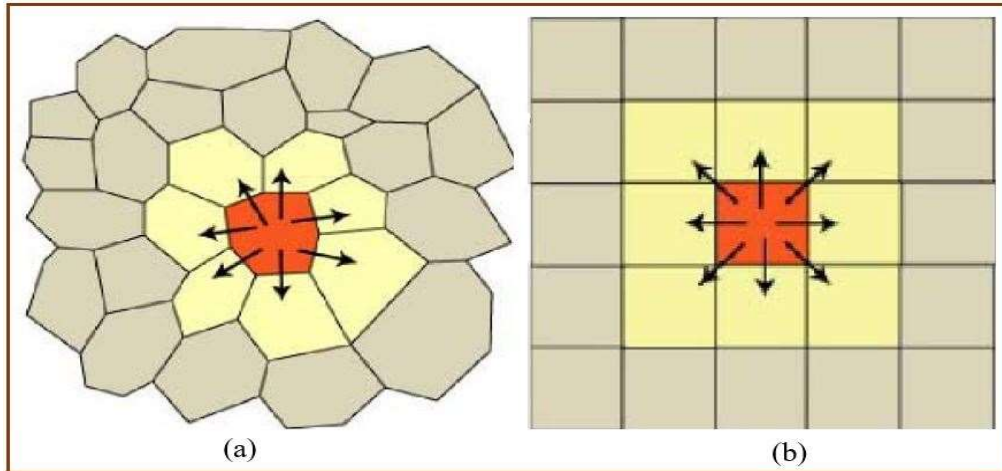


Figure 2:40 Voronoi based on the spatial CA model (a), Regular CA with regular arrays (Source: Amir et al., 2013 and modified in the lab).

The formation of Voronoi regions is in the form of expanding spatial objects at a definite pattern until these areas intersect one another (Carvalho et al., 2002). The mathematical equation of the Voronoi region is given as:

$$V(p_i) = \{p | d(p, p_i) \leq d(p, p_j), j \neq i, j = 1, \dots, n\} \quad 2.60$$

where p_i is the Voronoi region of the spatial object, $V(p_i)$ is the region defined by the set of locations p in space where the distance from p to the spatial object p_i , and $d(p, p_i)$ is less than or equal to the distance from p to any other spatial object p_j . Additionally, Voronoi regional boundaries are convex polygons in nature. The points along the common border between the Voronoi regions are equidistant from similar spatial objects, while the objects with common borders are neighbours in the Voronoi model (Klein and Aurenhammer, 2001; Carvalho et al., 2002; Wenzhong and Matthew, 2000).

2.7.12 Practical Application of CA in Spatial Data Analysis

Cellular automata has been applied in various fields of studies over the years. The focus will be on its application in the field of geographic sciences and environmental management. This is because of the enormous advantages of CA in geographic modelling, as it supports a vast parameter space for simulation. For instance, a 1-dimensional CA with a binary state set and 13 cells has 2^{13} possible configurations, and a 2-dimensional version of the same CA has 2^{169} possible configurations; in the same way, a 3-dimensional CA with the parameter has 2^{2197} . An example will be dividing the earth landmass by km^2

pixels and running a 2-dimensional CA over it with 50 states (this is possible, for instance, if we are to develop a simple global climate model); the space of possible state switches would be $25^{260,173,445,184,000,000}$. This figure is large and outrageous (Torrens, 2007). CA supports the implicit use of space and spatial complexity.

2.7.13 Practical Application of CA in Land use Modelling

Jose Andres et al. (1999) employed the cellular automata paradigm for remote sensing applications in multispectral, multitemporal and spatial data analysis. The authors show that the CA paradigm is relevant in remote sensing for detecting changes (burn scar land/use cover change detection) because it increases the flexibility and reliability of global information systems. They also presented a methodology to design CA for remote sensing applications. The researchers concluded that the technique is still in the progressive state because it has not been compared with Landsat-TM images at higher resolution, but the detected areas are regions where vegetation changes are occurring. Alkheder et al. (2006) employed the cellular automata technique to model historical urban growth over Indianapolis. The authors' objective was to design the model as a function of local neighbourhood structure to minimize the input data to the model. Their result shows that CA demonstrated a noticeable effect on producing a good spatial match between the real and simulated image data. Additionally, a genetic algorithm is introduced to enhance the CA calibration process.

Furthermore, Pratomoatmojo (2013) used LanduseSim as land use change modelling software, Cellular Automata, to predict future urban growth and land use change, particularly focusing on future-oriented development and scenario planning. The area of Pekalongan municipality was selected as the study area to model the land-use change modelling process. The author's work shows that LanduseSim is capable of dealing with trend-oriented prediction and shows high accuracy on spatial assessment. Nugroho (2013) and Gharbia et al. (2016) used the same CA modelling software and attained accuracies of 89% and 87-89%, respectively. However, Pratomoatmojo (2013) did not expressly state the percentage of accuracy obtained in his own research.

Additionally, Yongjiu (2017) developed a generalized pattern search (GPS)-based cellular automata (GPS-CA) model to simulate urban land-use change in a GIS environment. The

model is based on a fitness function that computes the difference between the observed results produced from the remote-sensing images and the simulated results produced by a general CA model. The GPS-CA model was applied to a study area of Kunshan city in the Yangtze River data from 2000-2015 to simulate the land-use change. The author results show that the GPS method had a smaller root mean square error of 0.2821 than the logistic regression (LR) method (0.5256) in fitting the CA transition rules. The GPS_CA model thus outperformed the LR-CA model, with an overall accuracy improvement of 4.7%. The researcher suggested that GPS-CA is superior to other models; therefore, it should be adopted for land use modelling and prediction.

2.7.14 Practical Application of CA to Flood Modelling

[Wu et al. \(2006\)](#) used the basic principle of a hydrological model and Cellular Automata to develop a watershed routing model based on GIS and cellular automata called HydroCA. The key was the local updating rule of HydroCA, which is the core of combining Cellular Automata with distributed hydrology models. The local rules are closely correlated to the model precision. The major inputs of the model are divided into two classes, namely, one of which includes the core variable of the lattice site, and the other consists of assistant variables such as the DEM, topographic index (TOPMODEL), water supply ratio, M, etc. core variables are computed using the runoff production model. The model was applied to a study area called LeAnhe. The authors' simulation results show that TOPMODEL was improved by using Hydro-CA from 64% to 71%. The researchers' outcomes show that the HydroCA model is feasible to simulate watershed runoff routing. [Juraj and Michal \(2013\)](#) described and implemented the process of using a CA for simulating the spreading of liquid using comparatively simple rules and conditions that include several factors affecting the spreading of water, such as slope, roughness, and infiltration. Their challenge was that CA is slower in the calculation process, which is strongly dependent on the size of the study area. However, the issue was handled by using three optimization methods to reduce the computation time. The authors' results show that a comparison of model output with real measurements showed good agreement, demonstrating that a CA approach can provide realistic results for a complex natural process such as liquid runoff despite the simplicity of the model.

[Michele et al. \(2016\)](#) developed a two-dimensional cellular automata for fast flood modelling. The model uses simple transition rules and a weighted-based system rather than complex shallow water equations. The authors model was tested using an analytical solution and four case studies, and the outputs were compared with other commercial physically based hydraulic models. The outcomes show that the model is capable of simulating water-depth and velocity variables with reasonably good agreement with the benchmark model, using only a fraction of the computation time and memory, and it is eight times faster than other models. Similarly, [Ghimire et al. \(2011\)](#) used the CA method to model 2D pluvial flood propagation. In this case, the local rules are applied in the Von Neumann neighbourhood for the spatial-temporal evolution of the flowing fluid. The result was compared with those of the physically 2D urban inundation model (UIM), and CA shows low computational cost and its ability to mimic realistic fluid movement.

Furthermore, [Jamali et al. \(2019\)](#) used the cellular automata approach to develop a new fast flood inundation model. The model is called Cellular Automata Fast Flood Evaluation (CA-ffe). Their model was able to predict the maximum inundation depth with reasonable accuracy in a matter of seconds to a few minutes for a single rainfall event simulation. The setback of their model, when compared with HEC-RAS or TUFLOW, was that it was not capable of accounting for floodwaters with higher momentum and velocity. The model was unable to represent the temporal evolution of flooding and flow velocities. However, CA-ffe shows a reasonable and remarkable accuracy in providing spatial flood extents and depths in a fraction of time compared to its hydrodynamic counterparts. [Goharian et al. \(2021\)](#) applied the cellular automata approach to optimize the hydropower reservoir operation of the Folsom Dam. The results of their research demonstrated that the CA approach provides more efficient solutions in comparison to the commonly used evolutionary optimization algorithms. Further results show that CA, although the annual average inflow to the reservoir during the dry period was approximately 30% less than that under normal conditions, offered an approximately 20% reduction in average hydropower generation. The final outcome shows that reservoir operation will be optimized when implemented.

2.8 Abridge Gap Description

Markov chain, cellular automata, and gradient boosting regression models are techniques for modelling and predicting future discrete and continuous data. While Markov chains and cellular automata have found greater and continuous application in land use change modelling and forecasting and flood modelling, both individually and integrated. The gradient boosting regression technique, on the other hand, has found no application because the system is an object position-based model. All three models have not been adequately implemented in the area of hydrography surveying, especially in the area of bathymetric data for reservoir monitoring and management, where they can be employed for sediment yield over time by investigating, predicting, and forecasting related to reductions in depth and possible poor functioning of reservoirs or waterbodies.

Consequently, employing the three models to process, model, and forecast bathymetric data of a reservoir will be a great stride in the field of hydrography surveying. The result can propagate to a new level of depth forecasting (if all necessary data are available) for adequate planning to mitigate future disasters

3 CHAPTER THREE: Methodology

3.1 Introduction

This section discusses the methods used for this research from the preliminary stage to the final presentation and discussion results. It encompasses the bathymetry survey of the study area, shoreline delineation, data processing and evaluation, profiling and cross-section. The datasets were prepared for Python coding and implementation of Markov Chain – Cellular Automata and Cellular Automata – Gradient Boosting Regression. The models were used to model the reservoir at present and forecast by predicting the depth distribution in the future because of the menace of sedimentation and siltation, which is a function of time. Figure 3.1 is a composite and comprehensive research methodology framework. Finally, the procedures of investigating the scientific contribution to sedimentation were also discussed.

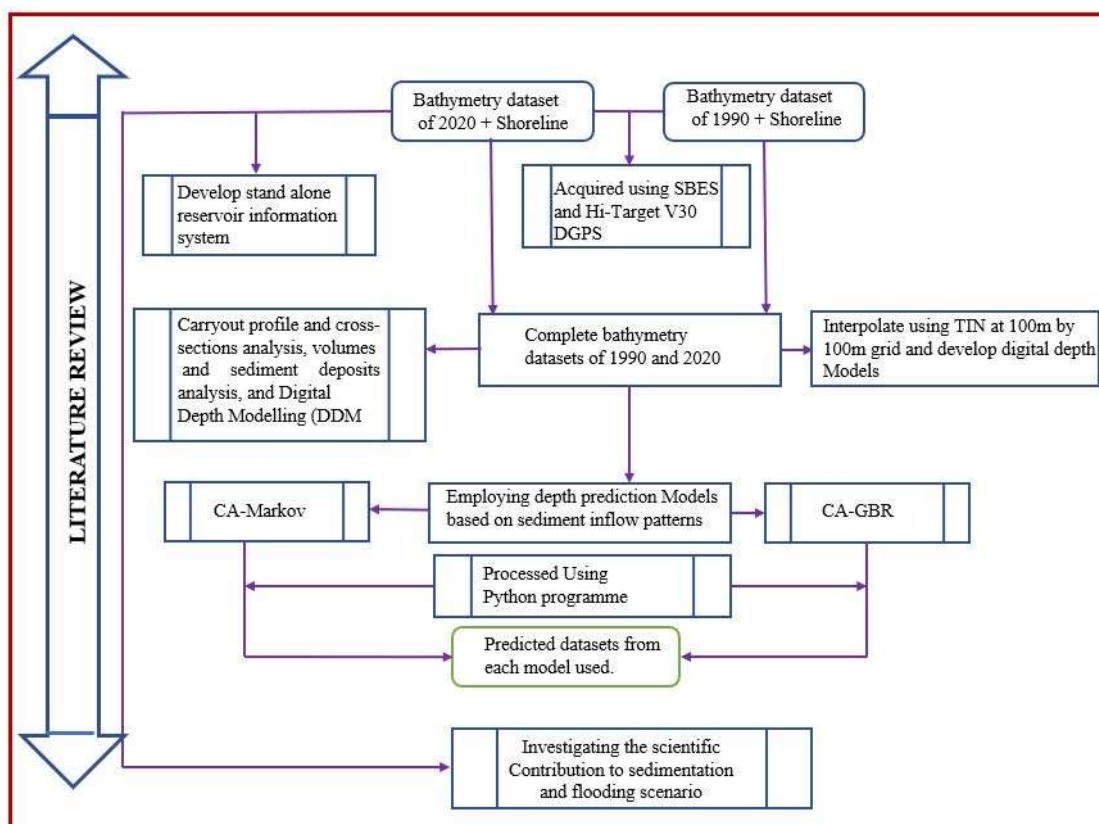


Figure 3:1 The composite framework of the research methodology. Source: Research lab

3.2 Datasets for the Study

The datasets used for this research are from primary and secondary sources. The datasets reference system is World Geodetic reference system 1984 (WGS84) to maintain global datum uniformity of the data used.

Table 3:1 Datasets for the study

Data	Data format	Period	Instrument type	Source
Bathymetric	N, E, D (coordinates)/ CSV	1990	SBES_200 kHz	Archive/Dam Management
Bathymetric	N, E, D (coordinates)/ CSV	2020	SBES_200 and 20 kHz respectively	Field observation
Landsat Imagery	Rows and Columns of 30m by 30m grid resolution (Pixel)	1990, 2005 and 2020		https://earthexplorer.usgs.gov/
SRTM-OpenDEM	Shape (contour lines) (25 m interval)	2020		https://www.openDEM.info/openDEM_client.html

3.3 Bathymetric Survey of Kainji Reservoir and Control Establishment

For this research, an HD380 digital echo sounder dual-frequency was hired for the execution of this project. In addition, a Hi-Target HD-Lite 620960 digital echo sounder (single frequency) from the Department of Surveying and Geoinformatics, Federal University of Technology, Minna, Niger State, Nigeria, was used with the HD380 during the bar check operation. A 5 m police security boat stationed at the reservoir for security purposes with a well-trained captain was used as vessel for the survey task. The HD380 echo sounder transmits acoustic energy at two different frequencies. 100 – 750 kHz (high frequency) and 10 – 50 kHz (low frequency) are all adjustable. Table 3.1 describes the digital echo sounder HD380, while Table 3.2 describes the Hi-Target HD-Lite 620960 single frequency digital echo sounder. The 100 - 750 kHz (high frequency) band has no sufficient energy to penetrate the top layer of the waterbody bed. Like the Low Frequency, it can penetrate through the sediment to a certain layer (Xavier, 2010). Most bathymetry maps of reservoirs are generated from this frequency (Odhiambo and Stephen, 2004).

Table 3:2 Descriptions and specifications HD380 Digital Echo Sounder
(Source: Operation manual)

Digital Echo Sounder	HD Dual frequency
Frequency	High: 100-750 kHz (adjustable) Low: 10-50 kHz (Adjustable)
Transmission power	500 W (200 kHz high-frequency band) 1000 (20 kHz low-frequency band)
Bathymetric range	0.3 m-600 m (high frequency) 0.3 m-2000 m (high frequency)
Depth resolution	0.1ft/0.01 m
Accuracy	+0.01 m +0.1% of h(depth value)
Ping rate	Up to 30 Hz
Draft range	0.0m~15 m
CPU	1.6 GHz
Memory and storage	1G DDR2 and 4G storage
LCD display	12 inches, 1024×768 resolution, 1000cd/m ²
I/O interface	2×RS-232 ports, 3×USB ports, 1×DC power port, 2×TX ports (for transducer)
Power supply	DC 9~36 V/AC 220 V
Operation temperature	-30 ⁰ C~60 ⁰ C, noncondensing
Dimension	44 mmL × 341 mmW × 164 mmH
Weight	9 kg

Table 3:3 Descriptions and specifications of the Hi-Target HD-Lite Echo Sounder

Measurement			
Frequency	200 kHz	Resolution	1 m/s
Range	0.15 m to 200 m	Ping rate	Max 30 Hz
Accuracy	0.01m±0.1%	Output data format	NMEA DBT, NMEA DBS, DESO 25, ODOM, Hi-Target
Draft	0 m to 15 m	Weight	5.8 kg
Beam angle	5 ⁰	Dimension	L 404 mm ×W 33 mm × H 110 mm
Sound velocity	1370 m/s to 1700 m/s	software	Hi-Max Sounder
Hardware Part			
CPU	1.92 GHz, 2 core	Interface	3*USB 2.0, 3*RS232, 1 Bluetooth, 1 VGA
RAM	2GB	Temperature	
Storage	32GB (Max 80GB)	Power	
Screen size	15 inch		

However, high- and low-frequency echo sounders have their pro and con in applications. Transducers with low frequencies (below 40 kHz) tend to have larger beam widths, resulting in distortion and smoothing of features on irregular bottoms or side slopes. Nevertheless, lower frequencies are less prone to attenuation, hence permitting greater depth measurements and penetration of lacustrine sediments. However, greater depth measurements are not needed for river and port projects; the capability to penetrate lacustrine sediment is a crucial benefit, especially when conducting dredging survey projects. The main limitation of a higher frequency transducer is that there is high attenuation of the signal with depth, and lacustrine sediments with low specific gravity or lower vegetation will easily reflect the signal. Similarly, high-frequency transducers are not recommended in areas where layers of lacustrine sediment are common or where the vegetation may mask the required grade of payment. Hence, frequencies ranging from 20 kHz to 50 kHz are commonly used for payment (USACE, 2002).

Additionally, Table 3.3 presents some of the equipment employed during the bathymetry survey and control establishment.

Table 3:4 List of some equipment used (Source: Research book)

S/N	Equipment	Make	Quantity
1	Echosounder	Hi-Target Multi-Frequency – HD 380	1
2	GNSS Receiver	Hi-Target V30	1 set
3	Boat	Yamaha Speed boat (Aluminium and Fibre)	1
4	Life Jacket		4
5	Laptop Computer	HP i3 Core processor	1
6	Handheld GPS receiver	Garmin 78 sc	1
7	Handheld GLONASS receiver	Etrex	2

Furthermore, Figure 3.2 describes the schematic approach used to determine bathymetry and sediment thickness from dual-frequency (100/10 kHz) echo sounding data. From Figure 3.2, it is evident that the low frequency has the capacity to penetrate the sediment (recent lacustrine) to some degree of thickness from the water surface. However, ping is reflected back from the pre-existing layer (compacted soil or rock) that has accumulated over the years.

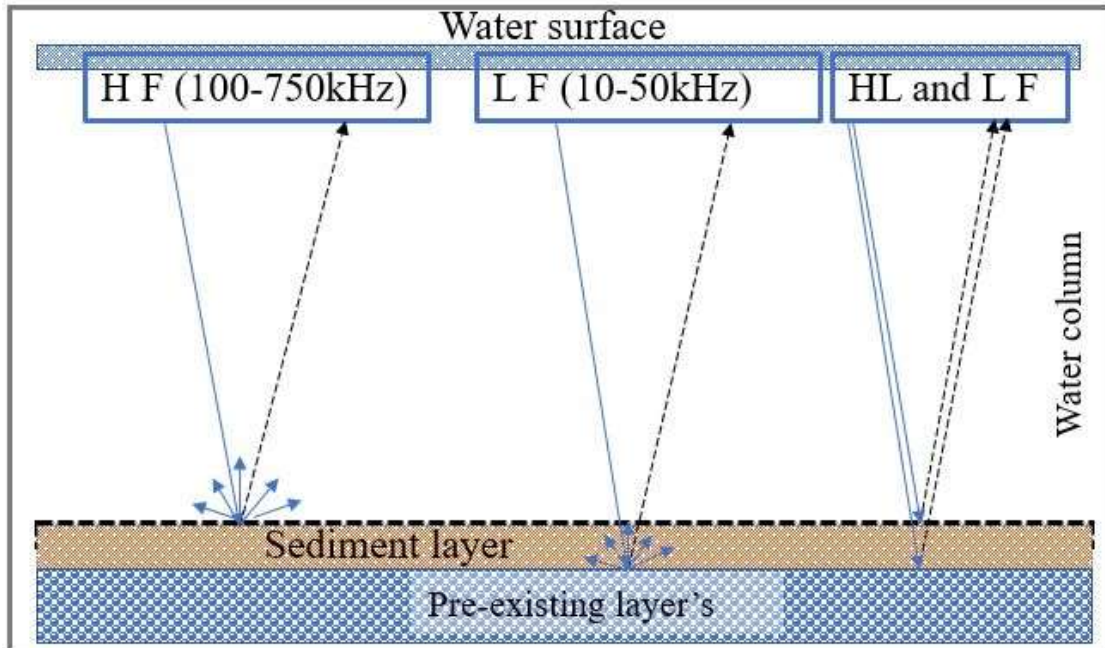


Figure 3:2 Description of the schematic approach used to determine bathymetry and sediment thickness from dual-frequency (100/10 kHz) echo sounding data.
(Source: Replicated in the research lab from the ideal of [Odhiambo and Stephen, 2004](#))

Similarly, the low frequency is used to generate maps showing the accumulated sediment over time after impounding the reservoir. Maps also show the reservoir bed topography before impound, i.e., the existing surface before storage. Thus, conducting a comparative analysis between the before and impounding data and some years after storage will result in knowing the amount of sediment deposited. In operation, the change in depth between the high and low frequencies yields the lacustrine sediment thickness of that particular area (see Figure 3.2).

3.3.1 Establishment of Temporary Control

Temporary controls were established at different locations of the reservoir corridor for continuous use during the echo sounding operation. They are called temporary controls because they were not monumented according to specifications. This is because the field observations received no external funding. The DGPS Hi-Target V30 and its accessories were used to fix the points in static mode. For each occupied point, one and half hours were utilized to fix the horizontal and vertical spatial attributes (X, Y, H). The spatial attributes of the control from which all others were established is GL01: 677578.839 mE, 1091372.684 mN, and 141.814 mH. All observations were performed from global datum

World Geodetic System 1984 (WGS84) to a targeted projection system of Minna-Universal Transverse Mercator Zone 31 (Minna-UTM zone 31). The Minna datum was established based on Clark 1880 ellipsoidal parameters. Table 3.4 presents the list of established coordinates on-site. Additionally, all observations were performed under the good satellites Geometric Dilution of Precision (GDOP) i.e 3 position coordinates plus clock offset in the solution. It shows the spreading of satellites above the horizon. When satellites are on one side according to the antenna, the DOP will be high which will result to poor observations. When it is spread around the antenna the DOP will be low and low DOP value gives good observation with high accuracy (Lekkerkerk and Theijs, 2017). Hence, the receivers were situated at an open space to avoid errors that might affects the observations such as multi-path error etc. The GDOP value was maintained and lies between 1 and 3. The baseline of the DGPS master station and the receiver or rovers varies depending on the suitability of the location. In general, the minimum and maximum horizontal distance between points lies between 1.8 km to 3.5 km.

Table 3:5 Established Controls at the Reservoir corridor (Unit: Metre).
Source: Research field work

Easting	Northing	Height	Easting	Northing	Height
675362.046	1089699.391	140.123	679289.405	1158375.673	139.279
677644.612	1091544.622	138.422	682665.012	1146285.557	137.634
671181.094	1099984.104	140.021	676989.756	1130884.408	140.123
669498.081	1110997.051	144.206	670528.155	1121127.902	140.346
664926.916	1126915.824	140.561	675584.270	1112532.511	141.653
659454.510	1146828.295	142.327	675836.223	1105777.246	143.452
661283.563	1158371.073	139.652	675929.111	1095753.157	137.653
666329.631	1173084.602	136.341	679877.443	1094898.701	138.823
676892.402	1093266.101	137.572			

Similarly, controlled establishment was conducted to delineate the major location of the shoreline. Plate 3.1 (a) is a presentation of a base station with a master receiver, and plate 3.1 (b) is the rover at the reservoir corridor during static mode observation.



Plate 3:1 Base station (a), Rover in static mode (b). Source: Research field book

3.3.2 Calibration Test of HD-380 Digital Echo Sounder

The calibration of acoustic sounding equipment is irrefutably mandatory to maintain the integration of all depth measurements. This is required primarily because of the variations in the water column, or to some extent, in the equipment. It is compulsory for all navigation and dredging surveys for project measurement and acceptance as a minimum standard. This is required to be carried out twice a day (at commencement and at the end of the project) at the project work site. There are basically three methods of calibrating SBES instruments: Bar check calibration, Ross ball check, and Velocity probe calibration (USACE, 2002). However, for this research, the Bar check approach was adopted.

3.3.3 The Bar Check Calibration

The major depth calibration procedure widely accepted is the bar check (IHO-C13). This is a depth measurement quality control measure and should not be mistaken for a quality assurance procedure. The Bar check is made of a flat bar or plate tie with two equally and precisely calibrated lines from both ends that are suspended in the waterbody to a known depth below the water surface and under the transducer. Consequently, this method was employed in this research. However, a calibrated pole with a flat bar was used in this case. The calibrated pole was deployed off the bow at the abeam of the transducer. The pole was held vertically as possible, and the depth recorder was simultaneously noted and annotated. Personal movement was controlled to avoid or minimize the effect of the boat's nominal (underway) trim. This test was conducted daily before the main sounding observation.

Table 3.5 describes the result of the Bar check undertaken on one of the sounding days (24 March, 2020). The differences between the Bar check depth and the recorded depth show both constant index and velocity errors on the recorded data.

Table 3:6 Sample result of a Barcheck calibration of 24th March 2020. Time: 0902 hrs (Source: Field record book).

Initial velocity set at 1498 m/s. Initial draft: 0.8 m. Maxproject depth: 71 m			
Depth of Bar (m)	Recorded depth (m)	Difference (m)	Notes
2	2.03	0.03	0.03 m index error was detected
4	4.03	0.03	
6	6.03	0.03	
8	8.03	0.03	
10	10.02	0.02	

If the differences after some readings vary greatly due to the variation in sound velocity in the water column, then equation 3.1 can be applied to compute the corrected depth.

$$d_c = [[(bar_i - bar_{i+1}) \div (rec_i - rec_{i+1})] * (d_o - rec_i)] + bar_i \quad 3.1$$

where d_c is the corrected depth, d_o is any observed/recorded depth to the corrected speed of sound and index error, bar_i is the bar depth at checkpoint i , bar_{i+1} is the bar depth recorded at $i + 1$, rec_i is the recorded depth at bar depth i , rec_{i+1} is the recorded depth at $i + 1$, while $i, i + 1$ is two successive calibration depth points and $rec_i > d_o < rec_{i+1}$.

Meanwhile, before the Barch check calibration test, the depth correction to the water surface was applied using equation 3.2. This is because if the velocity of sound propagation in the water column is known, along with the distance between the transducer and the reference water surface (draft), the corrected depth (d) can be determined by the measured travel time of the pulse.

$$d = 1/2 (v.t) + k + dr \quad 3.2$$

where d indicates the corrected depth from the reference water surface, v is the average velocity of sound in the water column, t denotes the measured elapsed time from the transducer to bottom and back to the transducer, k is the system index constant, and dr indicates the distance from the reference water surface to the transducer (drift); see Figure 2.4 for a description (USACE, 2002). In this case, the average velocity was set at 1498 m/s, which is the velocity of fresh water at 25^oC, t was 0.052 seconds, the k was 0.03 m, dr

was 0.8 m. This was done at some selected points, and the computed depth was compared to what the sounder measured, and the deviation was within 0.8 to 1% at depths of 25 m, 30 m, 41, and 52 m. However, this approach should not be used to compute the final reduced depth because the parameters v , t , and dr cannot be perfectly determined during the sounding process, k must be determined from periodic calibration of the equipment. The elapsed time t is also affected by the reflectivity of the bottom and related signal processing methods used to discern a valid return. The Jacksonville district calibration method presents a typical and graphical calibration process, as described in Figure 3.3 (USACE, 2002).

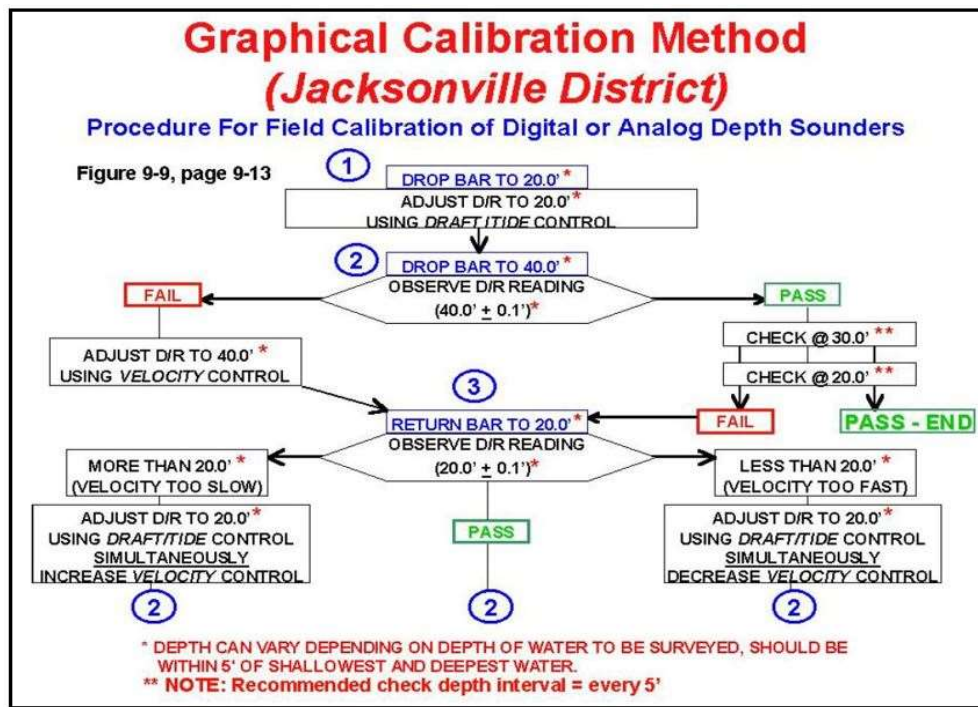


Figure 3:3 Jacksonville district calibration method (Source: USACE, 2002)

Finally, all depth measurements must be reduced to an established tidal gauge or a known sounding datum. The reduced level of each depth was computed by deducting the corrected depth values from the average water level of each day obtained from the tidal gauge. The average water level for the sounding period is presented in Table 3.6, while Figure 3.4 describes the tidal pattern of the reservoir between the period of the bathymetric survey.

Table 3:7 Daily reservoir water level below datum

Date	Water level (m)	Date	Water level (m)
24 th March, 2020	140.43	3 rd April, 2020	140.23
25 th March, 2020	140.44	4 th April, 2020	140.16
26 th March, 2020	140.36	5 th April, 2020	139.62
27 th March, 2020	140.34	6 th April, 2020	140.12
28 th March, 2020	140.38	7 th April, 2020	140.16
30 th March, 2020	140.39	9 th April, 2020	139.54
31 th March, 2020	140.29	10 th April, 2020	139.82
1 st April, 2020	140.20	11 th April, 2020	140.20
2 nd April, 2020	140.30	13 th April, 2020	140.17

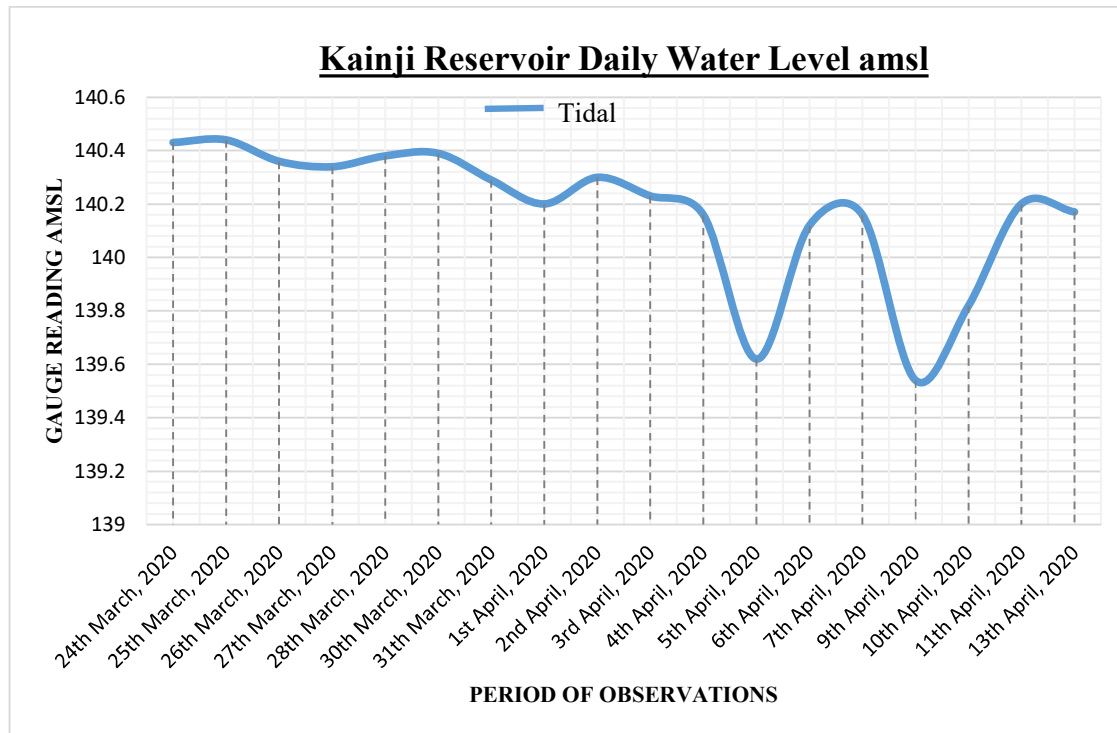


Figure 3:4 Kainji Reservoir daily water level below datum: It shows the tidal pattern within the sounding period. The range is 0.9 m within the echo sounding period, while the highest tide was 0.88 m. Source: Research lab

3.3.4 Bathymetry Surveys

Bathymetric observations of the Kainji Reservoir and Lake were carried out in March and April 2020. This period is termed the dry season in Nigeria and Subsahara, Africa. The observation schedule is as presented in Table 3.7. The HD-380 digital echo sounder was mounted on the boat's bow with all necessary connections, and calibration was ensured for better observations. The frequencies were adjusted to 200 kHz (high frequency) and 20

kHz (low frequency). The connection of the transducer to the echo sounder and at the same time, a GPS unit were attached to the echo sounder, which was used to obtain the positional (X, Y, Z) information about each point observed. The vessel was steered in an overlapping orthogonal grid survey pattern at a survey speed of approximately four nautical miles per hour (2.05 m/s). The survey lines consisted from west to east, as shown in Figure 3.5, with an average offset of 20 m along the course and 100 m off course (see Figure 3.5).

Table 3:8 Sounding operation schedule (Source: Research lab)

		March-April, Year 2020					
S/N	Activity	Duration	Week 1	Week 2	Week 3	Week 4	Week 5
1	Reconnaissance survey	3	■				
2	Establishment of Control	4		■			
3	Confirmation of gauge bench mark	3		■			
4	Water level observation	Each day of sounding			■	■	■
5	Equipment calibration/draft check	Each day of sounding			■	■	■
6	Sounding operation	Each day of sounding			■	■	■
7	Shoreline delineation	5		■			
8	Data compilation	All the period	■	■	■	■	■

Furthermore, the navigation data were acquired using DGPS Hi-Target V30 of a complete set (Base and Rover). The base was set up on one of the established controls at different locations within the river corridor. The automatic log time was set every five seconds (5 s) during the survey. The DGPS positional accuracy is 8 mm for the horizontal direction and 15 mm for the vertical direction based on the manufacturer’s claim. However, several factors determine the attainable accuracy, e.g., the availability of satellites (see section 2.4.9).

Consequently, after the field survey of each day, the bathymetry and the DGPS navigation data were merged using Microsoft spreadsheet software. The geographical coordinates were interpolated between five-second navigation fixes to give a database spatially combined with the echo profile data at one-second intervals of approximately every 2 m along the strip. The accuracy of the bathymetric data obtained and the DGPS data was evaluated by comparing the 200 kHz (low frequency) data with the survey data obtained in 1990. The examination shows that the echo data accurately depict the topography. Figure 3.5 presents the point cloud bathymetric data of 1990 and 2020.

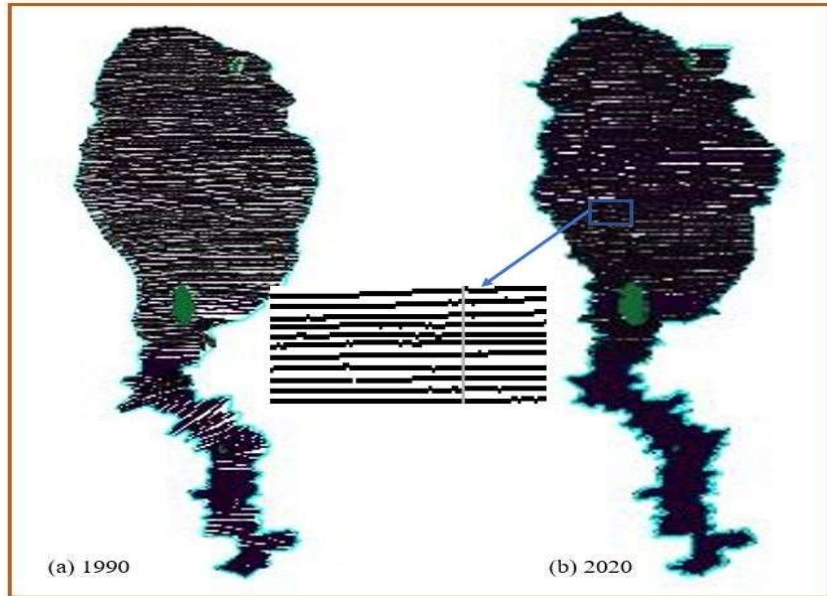


Figure 3:5 Point cloud bathymetry data (Source: Field observation/research lab as for the 2020 data and the 1990 that was provided by Mean Stream Dam: Managers of Kainji Dam, Nigeria. The 1990 bathymetric data was capture using SBES at 200kHz)

3.3.5 Reservoir Shoreline Delineation

The reservoir shoreline was delineated using interactive vectorization. Shoreline delineation using satellite imagery and GIS has received recognition over the years due to difficult terrain that is associated with waterbodies (Barman et al., 2014). The approach employed to delineate the Kainji reservoir was that the DGPS Hi-Target V30 was used to pick several points during the echo sounding survey. Spreadsheet software was used to process these points and saved them in CRV (comma delimited) data format. QGIS software was launched, and the Open Street Maps (OSM) standard was launched under the Web icon “this was accessed on 14th August 2020”. The OSM standard was set to the same coordinate system as the field data. The field data were plotted directly on OSM standards. The points were used as orientation and conformity for the interactive vectorization (converting raster data to vector via digitization). Thus, the spatial attributes were extracted and combined with the bathymetric data. Figure 3.5 describes the shoreline in cyan (light blue colour). The reservoir water line was assumed to be the zero point during data modeling analysis.

3.4 Reservoir Bathymetric Stand Alone System, Profiling, Cross-Sections, Volume Determination and Sediment Deposit Analysis, Digital Depth Modeling

This section discusses the procedures used to achieve objective one of this research.

3.4.1 Procedure for Developing a Bathymetric Stand-Alone Reservoir System

The present day reservoir bathymetric information system was developed using QGIS 3.16.4 software. The 2020 high-frequency data were used to generate a recent stand-alone bathymetric information system of the basin. This is because the high-frequency data defined the existing reservoir from the water surface to the reservoir bed. The data were first transformed using the TIN technique to bathymetric grids, which consist of an array containing the maximum and minimum reservoir depth values, with a pixel size of 100 m by 100 m and the measured and digitized shoreline as the boundary. Contours were derived at an interval of 2 m and an index contour at every 4 m using some basic programme in the attribute table interface, e.g., $\text{if}(\text{"depth"} \% 4 = 0, 1, \text{NULL})$ meaning “if the depth divided by 4 is = 0, then let it be 1, if not let it be NULL”, etc. After generating the basic component of the reservoir depth system, the raw data were used to check the accuracy of the depth generated from array data. The examination confirmed that the outcome was reliable and had high precision. Figure 3.6 is a QGIS interface describing some processes and manipulations carried out while developing the reservoir stand-alone system.

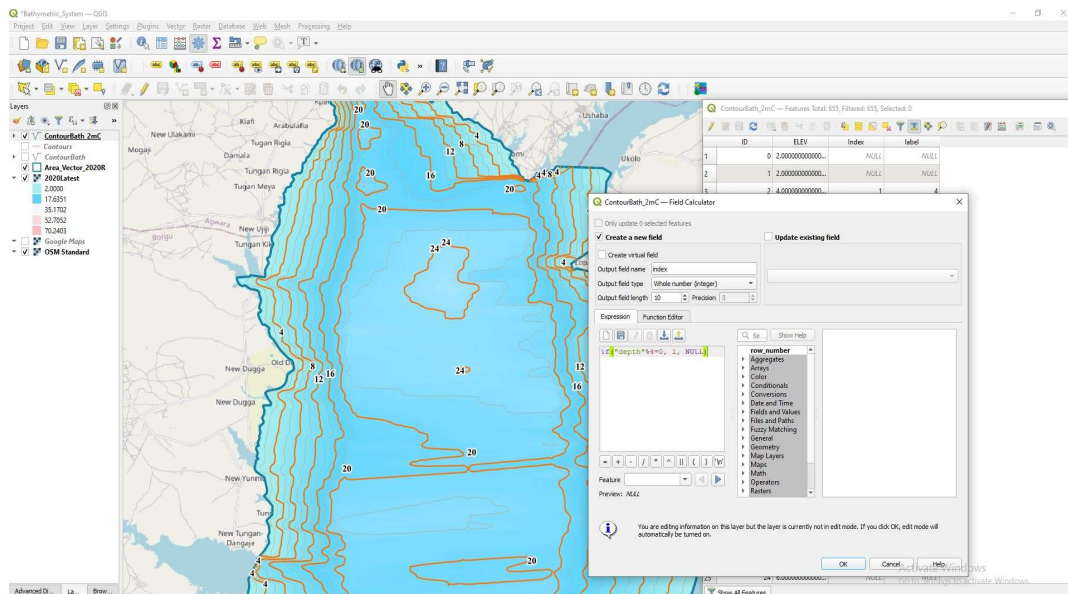


Figure 3:6 QGIS interface during reservoir bathymetric information development (Source: Research lab)

Meanwhile, there are different procedures and software to model bathymetric information systems. Hence, the focus should be on the source of data because poor data will lead to bad navigation information. Figure 4.1 describes the finished reservoir bathymetric information system (RBIS).

3.4.2 Profile and Cross Sections

Profiles and cross-sections were performed to analyse the relief of the reservoir bed at different sections. This will present the change in a two-dimensional pattern. Comparing the cross-sections of the two datasets (1990 – 200 kHz and 2020 – 200 kHz) will yield the change in depth due to accretion of sediment. Figure 3.7 describes the design for the cross-section and profile. In total, there are eight cross-section lines (CS_1 to CS_8) and three profile lines (P_1 to P_3). The relief lines were selected based on the nature of the data and the area perceived to be the region of concentration. Additionally, the slope percentage (%) was also plotted to show the rise and fall pattern of the reservoir bed.

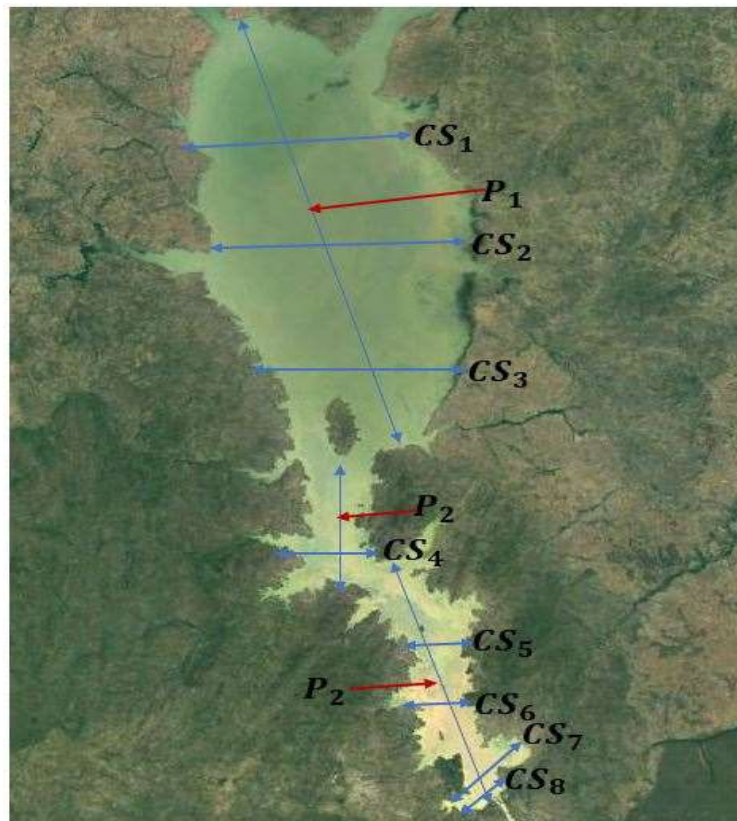


Figure 3:7 Design of cross-sections and profiles (Source: The image was downloaded on 14. February 2021 and processed in the research lab). P indicates profile while CS stands for cross section. Source: Google Earth Pro, 2020

The percentage slope was computed from the grided data using the neighbourhood algorithm. The algorithm calculates the slope for every cell in the elevation grid by analysing each 3 x 3 neighbourhood pixel. This approach computes the slope at one grid point by comparing the depths of the eight grid points that surround it. Figure 3.8 describes 3 x 3 pixels where the slope at d_5 is determined from neighboring pixels.

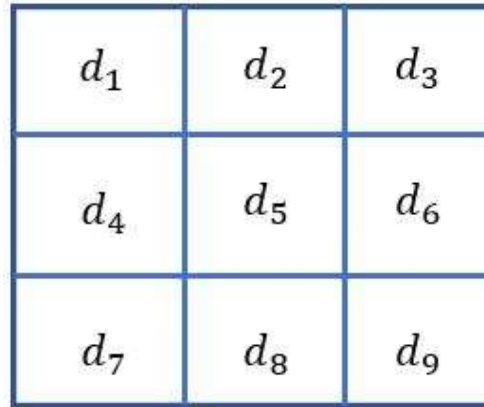


Figure 3:8 Neighbourhood algorithm on cell 5 (Source: Research lab)

The neighbourhood model estimates the percentage slope at grid cell 5 (d_5) as the summation of the absolute values of the east – west and north – south slopes and multiplies the sum by 100. Equation 3. 3 describes the mathematical expression of the neighbourhood algorithm (Burrough and McDonnell, 1998).

$$S_5 = (\sqrt{S_{e-w}^2 + S_{n-s}^2}) * 100 \tag{3.3}$$

By extension equation 3.3 can be rewritten as:

$$d_5 = \sqrt{\left[\frac{dz}{dx}\right]^2 + \left[\frac{dz}{dy}\right]^2} \tag{3.4}$$

$$\left[\frac{dz}{dx}\right] = \left[\frac{((d_3+2d_6+d_9)-(d_1+2+d_7))}{8 \times grid\ width}\right] \tag{3.5}$$

$$\left[\frac{dz}{dy}\right] = \left[\frac{((d_7+2d_8+d_9)-(d_1+2d_2+d_3))}{8 \times grid\ width}\right] \tag{3.6}$$

where dz is the depth, dx is the horizontal distance, and dy is the vertical distance.

This yields east to the west slopes and north to south slopes in computing the S_{e-w} difference between the sum of the depths in the first and third columns of the 3 x 3 matrix. Additionally, S_{n-s} is the difference between the sum of the depth in the first and third rows. Additionally, in each instance, the middle value is weighted by a factor of two (Guth, 1992; Etzelmuller, 2000; Guth, 2006). Additionally, the cross-sections and profiles were successfully implemented in QGIS software in the environment. Thus, the results are presented in Figure 4.2 to Figure 4.6.

3.4.3 Volume Determination and Sediment Deposit Analysis

The sounding data for 1990 were confirmed to have been that of high frequency (200 kHz). This was stated on the one-page note received from the reservoir managers. In addition, some points were compared with the 2020 high-frequency (200 kHz) echo sounding dataset using the point trace method. The point trace method involves selecting some points at random with their locations and then matching their spatial attributes to evaluate their differences. In all, three datasets were available for processing and analysis. First, the 200 kHz bathymetric data of 1990; second, the data obtained from 200 kHz in 2020; and third, the low frequency (20 kHz) data of 2020. The difference between these two datasets (200 and 20 kHz) of 2020 values will yield the lacustrine sediment thickness deposited since the time the reservoir was impounded. The difference was calculated to develop a map showing sediment thickness (see Figure 4.6(a)). After determining the sediment thickness from the dataset, the sediment volume was calculated using a standard method for volumetric estimation (Chapra, 1997). The area and volume were calculated at each level, and finally, the sediment volume was estimated. Additionally, the volume and area at each depth value were computed from the high-frequency datasets of 1990 and 2020. Software such as Civil 3D Metric - 2020, QGIS 3.16.4, Surfer 2020, and Spreadsheet was used to process the data to achieve the desired results. This result will give the estimated reservoir water storage capacity at present at each water column. Figure 3.9 describes the procedures used to determine the change in storage capacity, sediment thickness, and long-term average sediment accumulation (m/y)

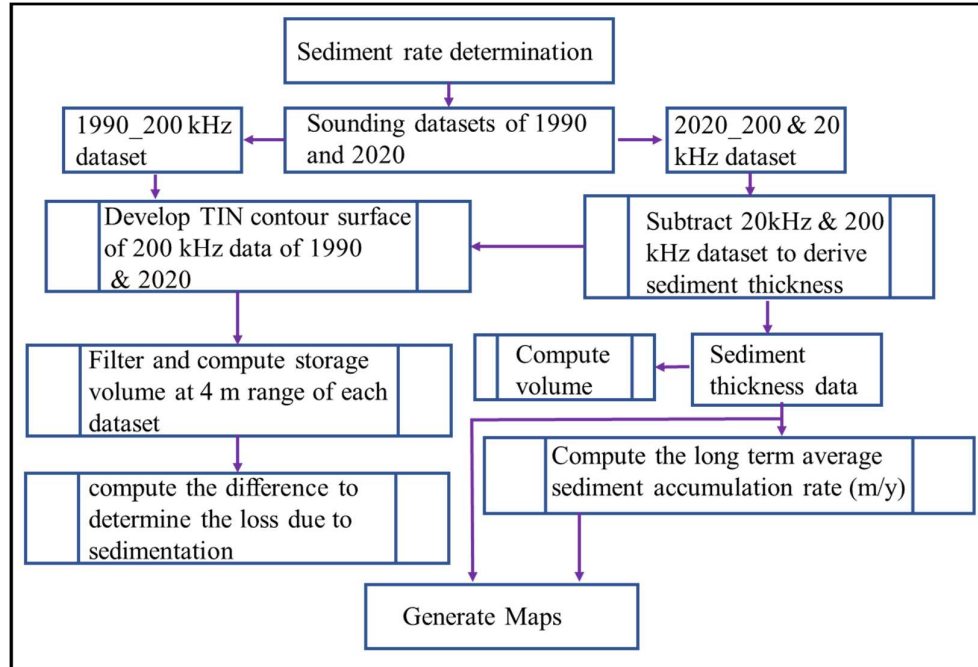


Figure 3:9 Flow diagram of sediment thickness and long-term average accumulation rate and storage capacity determination (Source: Research lap).

Furthermore, the long-term average sediment accumulation rate (m/y) was calculated basically by dividing the observed sediment thickness (m) at each sounding by the age of the lake. Knowing the age of the lake/reservoir, it is then possible to determine a long-term average annual flux (m^3/y) by dividing the observed sediment volume by the age of the reservoir (Chapra, 1997). That is:

$$\frac{dQ_s}{dt} = \frac{V_s}{t} \quad 3.7$$

where $\frac{dQ_s}{dt}$ is the long-term average annual sediment flux (m^3/y), V_s is the observed sediment volume (m^3), and t is the age of reservoir (y). Thus, the age of Kainji Dam and lake is 52 years. Figure 4.6 (b) describes the long-term average sediment accumulation rate (m/y) of the Kainji reservoir. Additionally, the storage capacity of the reservoir from the bathymetric data (200 kHz) of 1990 and 2020 using Simpson's 3/8 technique as described by Ibrahim and Sternberg (2021) was executed in a Civil 3D software environment. Table 4.1 describes the computed volume in billion cubic metres at a range of 4 m and the area in kilometres squared. Additionally, equations 2.38, 2.39, 2.40 and 3.7 were used to determine the sediment yield and the half-life of the reservoir, as presented in Table 4.2.

3.4.4 Digital Depth Modelling

The digital depth model (DDM) represents the nature of the waterbed topographic surface, which is an integral part of seafloor assessment (Liu et al., 2006; Hare et al., 2011). Building DDM requires interpolation of data, especially where the data were acquired using SBES. However, building DDM from sparse data is an approximation of the actual seafloor topography (Aguilar et al., 2005). Thus, employing any of the interpolators to model bathymetric data generates an error in the process, which can be quantified using descriptive statistical models. Additionally, the DDM of the Kainji reservoir was built using the exact Delaunay triangulation interpolation technique. The purpose of interpolating the data were to account for areas that were deliberately or conditionally neglected during sounding. This enables each cell to have a depth value (Hare et al., 2011). The goal of modelling the reservoir digital depth model is to present the basin topography surface in three dimensions for precise surface analysis. In addition, the interpolation error surface was generated by subtracting the measured data from the interpolated data.

3.4.5 Digital Depth Accuracy Evaluation

The modelling of waterbeds or topographic surfaces via interpolation requires that each pixel has at least one depth or elevation value to avoid modelling instability (Hare et al., 2011). During the process of interpolation, errors may originate from different phases, such as the source measurement or the gridding process. There is a diverse approach to investigate the degree of errors in interpolated depths employing known measurements, such as the split – sample also refers to cross-validation, jackknifing, and bootstrapping (Paquet, 2020). The split sample entails that some points are deliberately omitted from the dataset, interpolation is conducted, and the difference between the interpolated depths and the measured omitted depths is computed. Figure 3.10 describes the procedures involved in conducting split–sample techniques of interpolated surface evaluation. Figure 3.10 A is the stage where each pixel's measured data are averaged to have one depth value. Afterwards, they are randomly split by specifying the number or percentage of points to use in the control data and data subset. B, at the level, the interpolation technique is identified and employed to generate the DDM. At C, the interpolated DDM and the control data are compared to assess the interpolation errors. Stages A to C can be repeated with different

control data and data subsets to determine each pixel's interpolation error to account for the bathymetric stability.

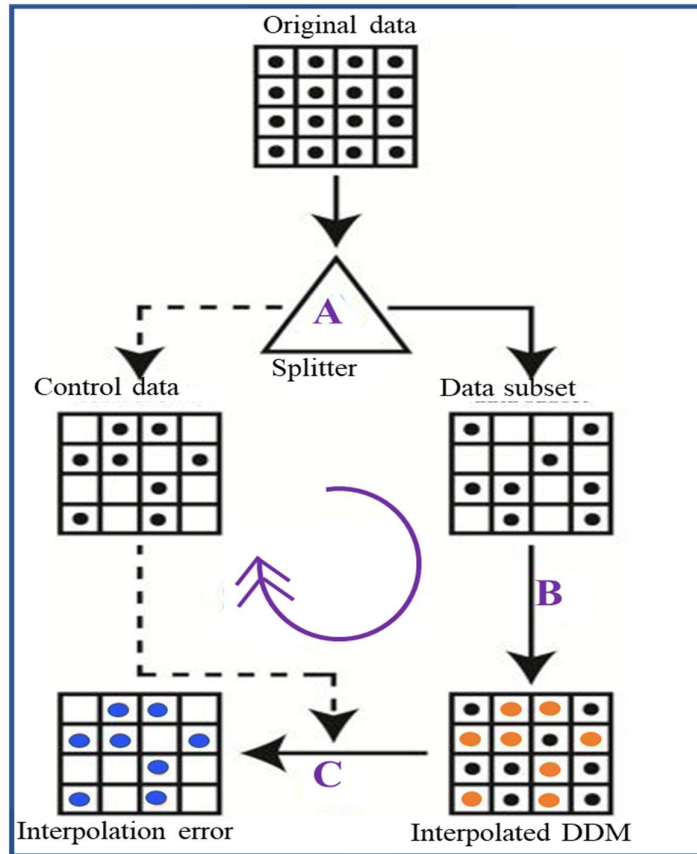


Figure 3:10 Description of the split-sample technique for assessing and quantifying interpolation errors. Source: Replicated in the research lab from the idea of [Hare et al. \(2011\)](#).

Similarly, to quantify the errors generated in the interpolation technique at each data point, the procedure is repeated, and the differences between the measured omitted depths and the interpolation are added up. Descriptive statistics are mostly employed to quantitatively assess interpolation errors such as the minimum, maximum, mean, root mean square error (RMSE), mean error (ME), R – square, and standard deviation ([Burrough and McDonnell, 1998](#); [Hu et al., 2004](#); [Ibrahim and Sternberg, 2021](#)). The mathematical expressions for the descriptive statistics are:

$$MSE = \frac{1}{n} \sum_{i=1}^n (\hat{Z}_i - Z_i)^2 \quad 3.8$$

$$RMSE = \sqrt{\frac{\sum_{i=1}^n (\hat{Z}_i - Z_i)^2}{n}} \quad 3.9$$

where Z_i = is the observed value, \hat{Z}_i = is the predicted value, and n = is the total number of points.

While the mean error can be computed as:

$$ME = \frac{\sum_{i=1}^n (Z_i^{PRED} - Z_i^{OBS})}{n} \quad 3.10$$

where Z_i^{PRED} and Z_i^{OBS} represent the predicted and observed depths, respectively, and n is the total number of samples. The statistical models are used to test the experiment's performance; when they tend to zero, it represents the reliability of the interpolation technique.

Furthermore, the split-sample technique was used to evaluate the dependency of the generated digital depth model surface of the Kainji reservoir from the two epoch datasets. In each case, the data were partitioned into a series of 10000, 30000, 50000, etc., the mean varied from 0.018 to 0.016, and the root mean square (RMS) varied from 0.429 to 0.434 for the 1990 dataset. The 2020 dataset presented a mean of 0.00127 to 0.0092, and the RMS was within the neighbourhood of 0.477 to 0.516. Similarly, the final cross-validation was conducted, and the result is presented in Table 3.8.

Table 3:9 Cross-validation/split – sample technique outcome (Source: Research lab)

Final Split – sample technique		
Statistical model	1990 data	2020 data
<i>ME</i>	0.003	0.00009
<i>MSE</i>	0.012	0.029
<i>RMSE</i>	0.108	0.169
<i>R²</i>	0.702	1.003

From Table 3.8, as the mean error (ME) tends to zero in both datasets, the mean square errors (MSE) also drive toward the same direction, supporting the central limit theorem, which says that as the sample size n increases, the variance of the quantity $\frac{1}{n} \sum_{i=1}^n (\hat{Z}_i - Z_i)^2 = \sum_i (\varepsilon_i)^2 / n$ should converge to zero. At the same time, the standard way to measure the error of the model of the predicting quantitative data (RMSE) suggested that the model error is 0.108 and 0.169 in both cases. The cross-validation outcome clearly indicated that the generated DDMs are replicated of the reservoir bed based on the data used.

Additionally, this is collaborated by the coefficient of multiple determination (R^2), which shows how well the predicted model best fits the observed data. The predicted model is a complete replicate of the original when R – squared tends to one (Devore, 2011). Consequently, Figure 4.11 describes the colour relief maps of the generated DDM, while Figure 4.12 shows the reservoir's 3-dimensional surface model. Figure 4.13 shows the generated error maps, and Figure 4.14 shows the 3 D surface error maps.

3.5 Markov Chain and Cellular Automata to Assess and Forecast Sediment Deposits

Researchers have used CA-Markov technology in various works on modeling and analysing spatial data. For example, Samat, 2009; Lingling et al., 2011; Jamal et al., 2011; Aqil and Shu, 2020. This model has proven to be effective in transients in various data that can be divided into categories. For instance, the type of land use and land cover classification changes in the ratio of variation in development. Hence, this section discusses the methodology employed to achieve objective two: “*To evaluate sediment deposit analysis of the study area and forecast by using Cellular Automata - Markov chain*”. Figure 3.11 describes the procedures used to execute CA-Markov to forecast sediment deposits of the Kainji reservoir. This was carried out using the Python programming language.

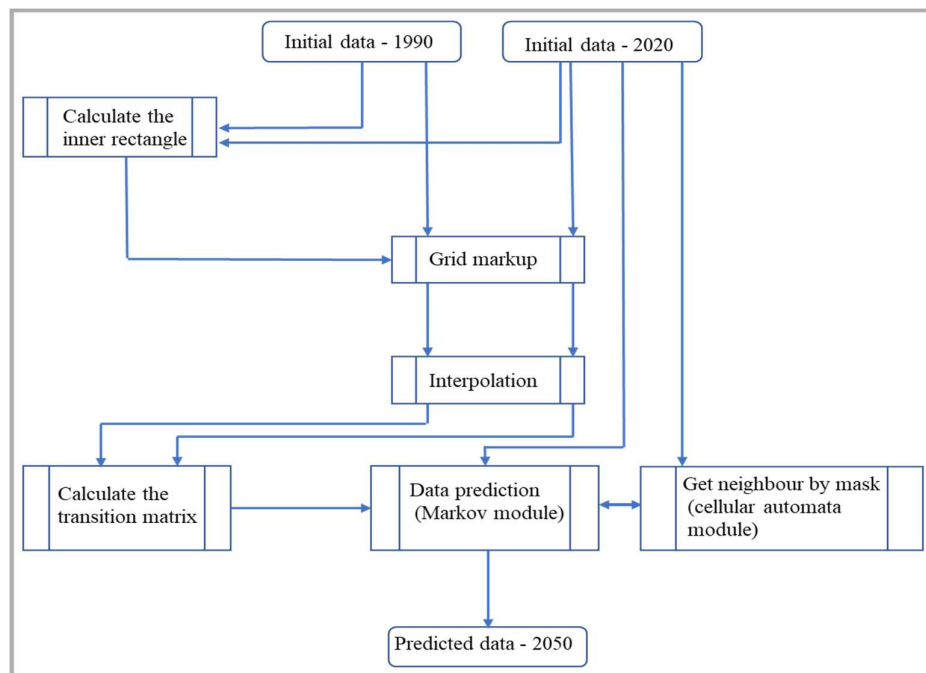


Figure 3:11 Flow diagram of the CA-Markov model for predicting future depth changes due to sediment deposits in the Kainji reservoir (Source: Research lab).

3.5.1 Initial Dataset and Preprocessing

The initial data in this study are the depths of the studied area of the Kainji reservoir, measuring approximately 24 x 83 km, measured at 2 points in time: 1990 and 2020. Unfortunately, the coordinates of the measured depths do not correspond to each other; therefore, we have to use interpolation to compare the data. For the interpolation, the inner rectangle was selected that is enclosed in all two presented datasets. Then, the rectangle was divided into grids with a step of 100 m. Such a grid step is recognized as probably optimal for spatial data prediction (Samat, 2006). Thereafter, the depth values were calculated at each point using linear interpolation of the nearest measured points. After interpolation, contour plots of the study area for each historical moment in time were built (Figure 3.12).

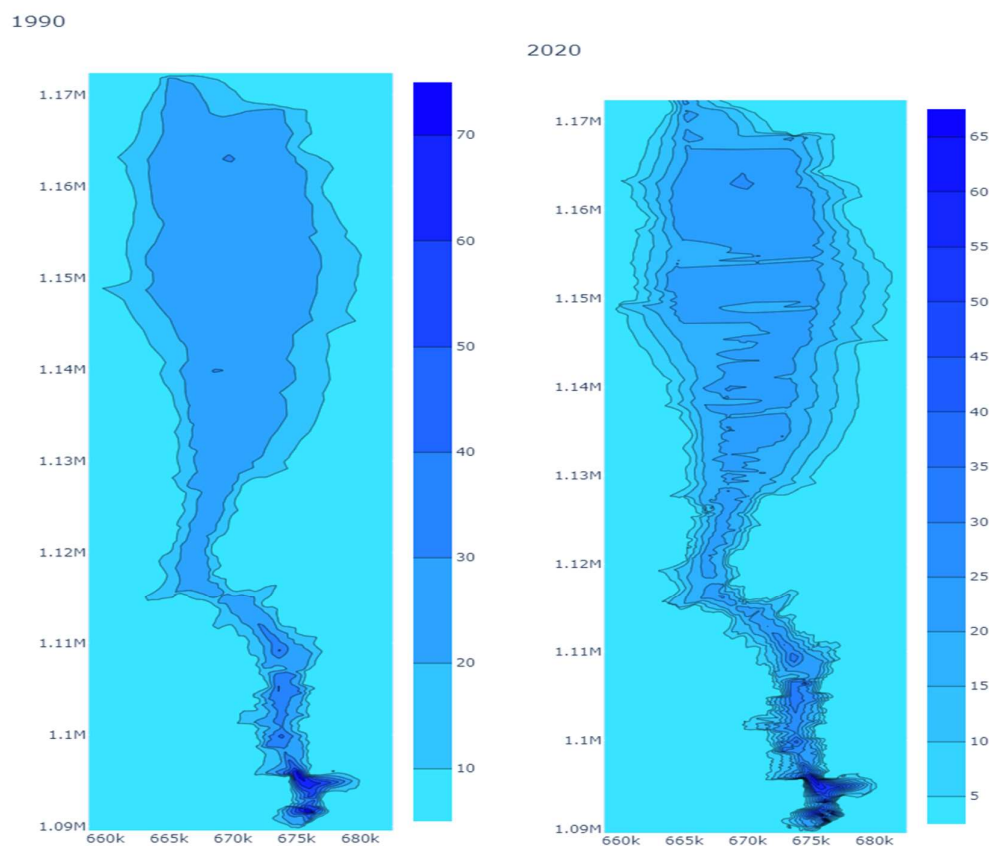


Figure 3:12 Generated contours from linear interpolation. According to these plots, it is clear that the limiting depth decreases with time due to sedimentation and siltation from

1990 to 2020. Additionally, the maximum depth at construction (1968) of 85 m was reduced to 77.3 m (1990) and 71.3 m based on 2020 HF data (Source: Research lab)

3.5.2 Cellular Automata Application

Cellular automata represent a discrete model, which is a grid of arbitrary dimensions, each cell of which at each moment can assume one of a finite set of states, and a rule for the transition of cells from one state to another is determined. The transition from one state to another is determined by the rules, which may include considering the states of the neighbourhood cells. The CA is mathematically expressed as (Hou et al., 2004):

$$S(t, t + 1) = f(S(t), N) \quad 3.11$$

where S is the set of limited and discrete cellular states, N is the cellular field, t and $t + 1$ indicate the different times, and f is the transformation rule of the cellular states in local space. Thus, according to the following template, this research defines a significant neighbourhood (Figure 3.13).

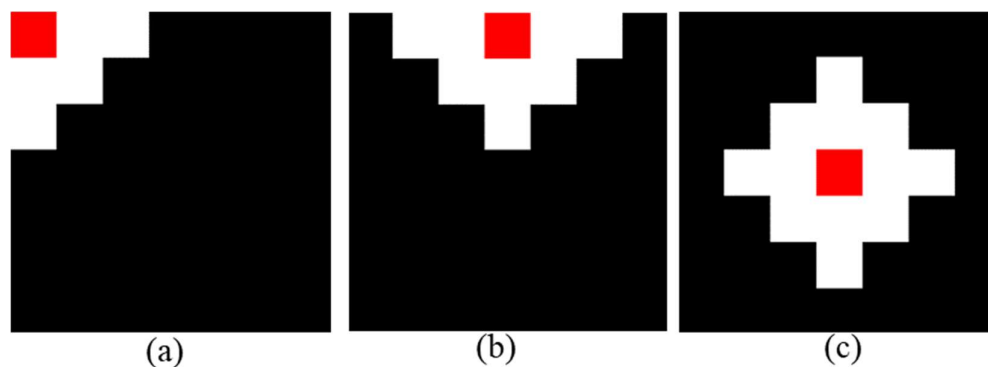


Figure 3:13 CA significant neighbourhood template. The cell to be defined is highlighted in red, significant neighbours are highlighted in white, and insignificant neighbours are black. In this case, the state of the determined cell at the previous time also affects the cell's future state. For instances where the cell is close to the edge of the study area (a, b), some of the neighbors are not considered in the calculations. Source: Research lab

However, the behaviour of CA models is affected by uncertainties arising from interactions between model elements, structures, and the quality of the data sources used as input to the model (Batty et al., 1999; Peterson et al., 2009). The CA takes into account the data trend for effective applicability.

3.5.3 Markov Chains Procedures

Markov chains imply that we have a particular graph of states and transition probabilities from one state to another. The Markov process explains the rate of changes in states between the loss in depths due to sedimentation over time and uncovers the degree of depth losses in the depth classes. Hence, to predict the surface's future state, the formula based on the conditional Bayes probability formula is also used (Hou et al., 2004; Yang et al., 2007; Jiang et al., 2009).

$$S(t + 1) = P_{ij} \times S(t) \tag{3.12}$$

where S are the system states at time t or $t + 1$ and P is the transition probability matrix in a state, which is calculated as follows (Tadese et al., 2021):

$$P_{ij} = \begin{bmatrix} p_{11} & p_{12} & \dots & p_{1n} \\ p_{21} & p_{22} & \dots & p_{2n} \\ \dots & \dots & \dots & \dots \\ p_{n1} & p_{n2} & \dots & p_{nn} \end{bmatrix} \tag{3.13}$$

$$0 \leq P_{ij} < 1 \text{ and } \sum_{j=i}^N P_{ij} = 1, (i, j = 1, 2, \dots, n)$$

Furthermore, in this research, the states are the depth intervals of the studied area ‘Kainji reservoir’. Therefore, the entire depth of the study area was divided into depth ranges of ten states from zero to nine (Table 3.9).

Table 3:10 Depth classified according to Markov states

<i>Depth span, meters</i>	<i>Markov state</i>
0.00 - 8.50	0
8.50 - 17.00	1
17.00 - 25.20	2
25.50 - 34.00	3
34.00 - 42.50	4
42.50 - 51.00	5
51.00 - 59.50	6
59.50 - 68.00	7
68.00 - 76.50	8
76.50 +	9

Consequently, the initial datasets were transformed into datasets of Markov chain states. Figure 4.14 describes the historical data's contour plots as often transformed into states.

In addition, based on the historical data of transitions, the transition probability matrix for the chain was calculated. In this case, first, each cell was considered a separate experiment. Then, the research considers its state at the next point of time as a result of the experiment. Table 4.3 presents the results generated from the calculated transition probability matrix.

3.5.4 Final CA-Markov Forecasting

The CA-Markov technique integrates the theories of Markov and CA, which are about the time series and space for an advantage of forecasting. Thus, to predict the future state of each cell, the researcher used the transition matrix for the current state of the cell and all significant neighbours determined by the mask as described above (Section 3.5.2). The majority principle determined the final state of the desired cell. The resulting maps for the estimated state of the study area in 2050 compared to historical data are shown in Figure 4.15. While appendix 1 is the attached Python programming script for the entire process.

3.6 Cellular Automata-Gradient Boosting Regression (CA-GBR)

In the same way, this section of the thesis is designed to address objective three, “*Cellular Automata and gradient boosting regression models to measure the accuracy of objective two*”. Depth changes are not discrete in nature, so the researcher decided to try a different technique to predict future changes due to sediment deposits at the surface under study. This is because of the artifacts generated on the surface of the CA-Markov chain 2050, and the research tried another approach called gradient boosting regression (GBR) to check and compare the output of both models. Thus, Figure 3.14 describes the methodology employed to execute this aspect of the research.

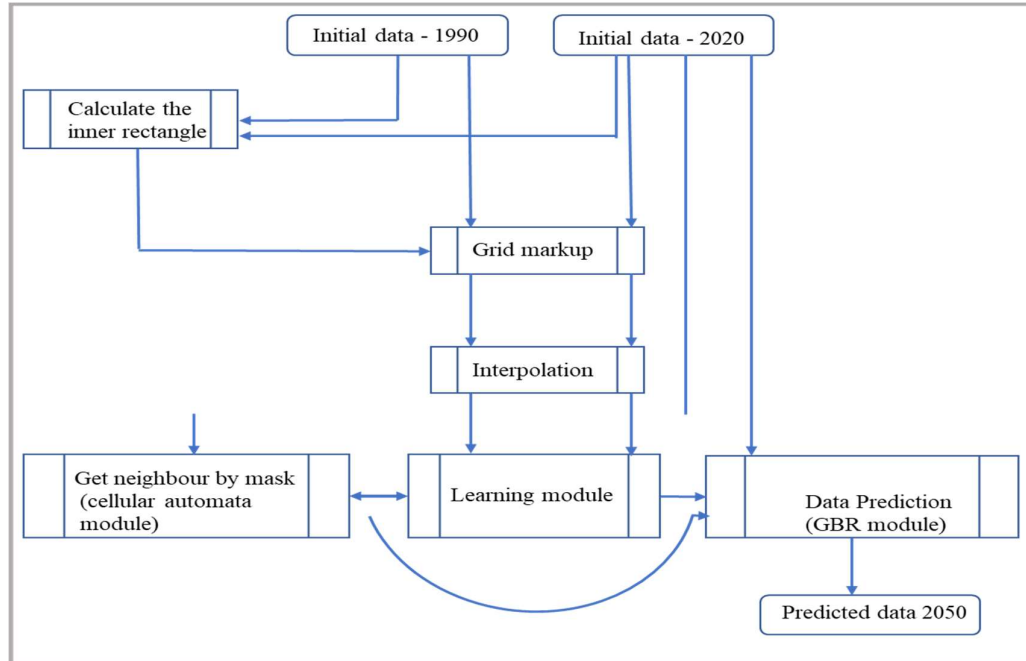


Figure 3:14 Flow chart for conducting the CA-GBR model for predicting future depth changes due to sediment deposits in the Kainji reservoir. Source: Research lab.

Furthermore, the thesis also used cellular automata, but instead of Markov chains, the research applied gradient boosting regression. Meanwhile, the grid markup and interpolation are as explained in section 3.4.1. Again, the neighbour by mask (Cellular Automata module) is described in section 3.5.2. The GBR is a model ensemble technique. In this case, the base model is a random forest. Each subsequent model in GBR is built based on the previous model to minimize its errors. The input parameters of this model are the values of significant neighbours for a particular point at the last moment in time, and the target value is the current value of the depth at this point. The optimal hyperparameters of the model were selected using a grid search algorithm. Actually, there are 16 models and the best one was adopted. The maximum depth parameter is related to the depth of each decision tree in the random forest model. Hence, the first model will have such parameters; ‘learning_rate’:0.01, ‘subsample’:0.9, ‘n_estimators’:100, ‘max_depth’:4, then another parameter is changed to build a new model. Thus, the second model will have; ‘learning_rate’:0.01, ‘subsample’:0.9, ‘n_estimators’:100, ‘max_depth’:10 and so on. Finally, the best parameters across all search parameters were obtained with (‘learning_rate’: 0.01, ‘max_depth’:4, ‘n_estimators’:1500, ‘subsample’:0.1). Thus, the final prediction accuracy was 95.7%. The complex procedures and Python scripts to

execute the CA_GBR are attached in appendix 2. Figure 4.16 shows the projected reservoir surface modeled using the CA-GBR for 2050.

In addition, the GBR mathematical model is expressed as:

The input data $\{(x_i, y_i)\}_{i=1}^n$ and a differentiable loss function $L(y_i, F(x))$ 3.14

Step (1): Initiate the model with a constant value: $F_0(x) = \underset{\gamma}{\operatorname{argmin}} \sum_{i=1}^n L(y_i, \gamma)$ 3.15

Step (2): For $m = 1$ to M :

A. Compute $r_{im} = - \left[\frac{\partial L(y_i, F(x_i))}{\partial F(x_i)} \right]_{F(x)=F_{m-1}(x)}$ 3.16

B. Fit a regression tree to the r_{im} values and create terminal regions R_{jm} , for $j = 1 \dots J_m$

C. For $j = 1 \dots J_m$ compute $\gamma_{im} = \underset{\gamma}{\operatorname{argmin}} \sum_{x_i \in R_{ij}} L(y_i, F_{m-1}(x_i)) + \gamma$ 3.17

D. Update $F_m(x) = F_{m-1}(x) + v \sum_{j=1}^{J_m} \gamma_{jm} I(x \in R_{j,m})$ 3.18

E. Step (3): Output $F_m(x)$ 3.19

However, the mathematical explanation of the GBR is discussed in detail in sections 2.8.7 and 2.8.8 of this thesis.

3.7 Quality or Accuracy evaluation of Forecasted Surfaces

The practical approach in investigating the quality and reability of projected surface is the implementation of interactive performance check or spatial coordinates matching (Ibrahim and Sternberg, 2021). Thus, spatial coordinates matching was conducted to evaluate the accuracy of the projected bathymetric surface of Kainji reservoir from CA – Markov and CA – GBR models of 2050 respectively. While the change between 1990 and 2020 measured data shows a remarkable reduction in depth in the year 2020 due to the menance of sedimentation, this also translate to decrease in depth in the projected surfaces of 2050 depending on the characteristics of existing sediment inflow pattern. Table 3:10 shows the quality and accuracy of the projected surfaces.

Table 3:11 Quality and accuracy evaluation of forecasted bathymetric surfaces. The change is the difference between CA – Markov and CA – GBR, neglecting the negative signs. The measurement is meter (m).

Matched coordinates (E, N)	1990	2020	CA-Markov 2050	CA-GBR 2050	Change
676182.42, 1093090.31	75.42	70.27	68.20	68.13	0.07
675839.24, 1091575.45	68.08	62.36	59.41	59.50	0.09
674489.16, 1106413.62	44.92	41.78	39.01	39.22	0.21
664890.56, 1150213.41	23.41	20.82	18.92	18.41	0.51
670145.08, 1162347.31	29.42	24.62	21.29	21.94	0.65
670056.56, 1113540.71	21.01	18.83	15.97	16.00	0.03
669957.34, 1159313.12	25.21	23.73	20.51	20.42	0.09

Similarly, the difference between CA – Markov 2050 and CA – GBR 2050 lies within the neighbourhood of 0.65 m and 0.03 m has shown in Table 3:10. The small change between CA – Markov and CA – GBR of 2050 forecasted bathymetric surface indicates that the depth predicted are reable depending on the measured data used.

3.8 Investigating the Scientific Contribution to Sedimentation in the Kainji Reservoir.

This section discusses the methodology employed to achieve objective four of this research: “*To investigate the scientific contribution to sediment deposits from river catchment analysis and model the flood scenario*”. Hence, the following assessment was performed to examine the high rate of sediment inflow in the Kainji reservoir. First, the land use land cover classification of the research area was conducted to examine the changes that have taken place over the years using imagery from 1990, 2005, and 2020, “i.e., epoch data of 15 years interval”. Second, the catchment area and drainage pattern and sediment concentration-time were determined using OpenDEM data for 2020. Third, the Universal Soil Loss Equation was employed to assess the sediment deposit rate in the study area. Finally, the flood impact scenario was modeled to estimate the devastating effects of possible occurrences.

3.8.1 Landuse Land Cover Classification, Catchment Area and Drainage Network of Kainji Reservoir and Environs

3.8.2 Land Use Land Cover Classification Procedure

The land use land cover classification (LULC) of the Kainji Reservoir and environs was performed to investigate the changes that have occurred within the study area over the years that might exacerbate the rate of soil erosion into the reservoir. Hence, Table 3.11 shows the data and software used for the classification model, and Figure 3.15 describes the basic methodology employed.

Table 3:12 Description of data used for classification and drainage network analysis.

Source: <https://earthexplorer.usgs.gov/>

Types of data/software	Details of data/software	Sources
Land 4 satellite imagery	1990/12/27	https://earthexplorer.usgs.gov/
Land 7 satellite imagery	2005/12/04	
Land 8 satellite imagery	2020/01/20	
	Path/row:191/53 Grid resolution: 30 m/30 m	
SRTM DEM	25 m, year 2020	https://www.opendem.info/opendem_client.html
ArcGIS	ArcGIS 10.6	https://desktop.arcgis.com

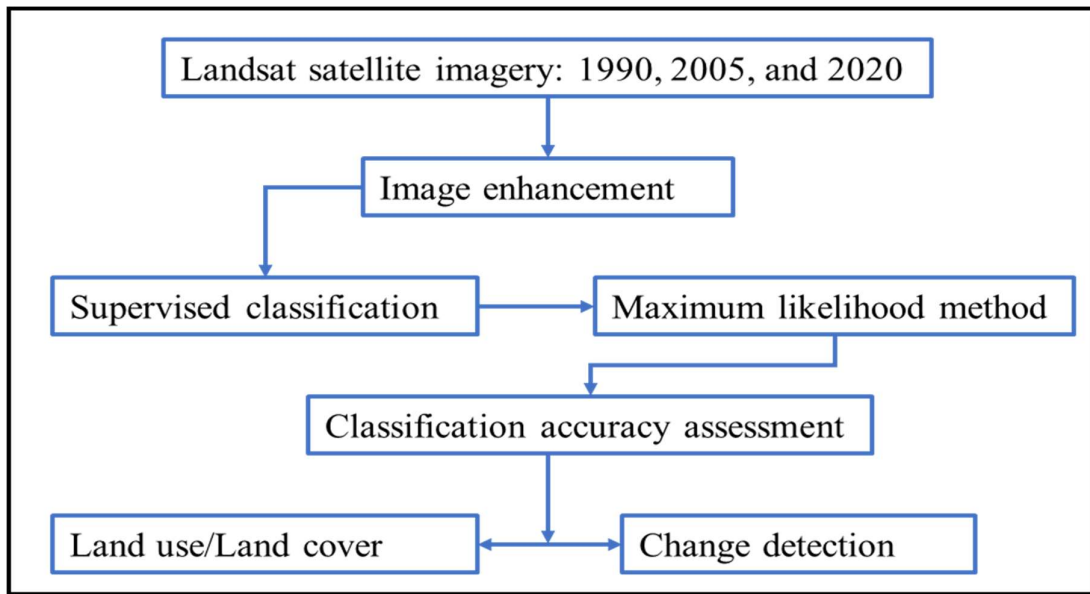


Figure 3:15 Flow diagram of land use/land cover methodology (Source: Research lab).

The Landsat imagery was downloaded from the USGS website in Tagged Image File Format (tiff) for the years 1990, 2005, and 2020, as shown in Table 3.9. Image enhancement was performed on the Landsat data to improve the quality of the data by removing errors caused by the atmospheric condition, scanline error, and radiometry effect using ArcMap 10.6. “The raster calculator tool was used to perform the atmospheric correction, and the Fix Landsat 7 scanline error tool was used to correct the scanline error of Landsat 7”. Additionally, the RGB band was obtained using the composite tool in the raster processing toolbox. These processes were performed for all the imagery of the project area. Supervised classification was employed by selecting the training samples. The images were classified based on the chosen samples by performing the following steps: selecting training areas, generating signature files, and finally classifying the data using the maximum likelihood method. The final classification accuracy assessment obtained is 89.6% by comparing the pixels and polygon of the classified image against the ground-referenced data.

Furthermore, change detection was performed by comparing the raster dataset of each epoch against another to ascertain the type, magnitude, and location of change caused by anthropogenic activity, abrupt natural disturbances, and long-term climatological or environmental trends. In general, five classes were considered for the classification, i.e., water, vegetation, bare-ground, built-up area, and forest. Figure 5.1 shows the LULC maps of the data epochs considered and their accompanying changes.

3.8.3 Drainage Network and Catchment Area Delineation

The drainage network and catchment/watershed of the Kainji reservoir and the contributing hydrological inferences were produced and discussed. The aspect, slope, drainage network showing the stream order, and catchment maps were produced. Figure 3.16 describes the methodology employed to analyse the study area's morphometric parameters. Table 3.12 shows some of the equations used to determine the morphometric parameters of the Kainji Basin.

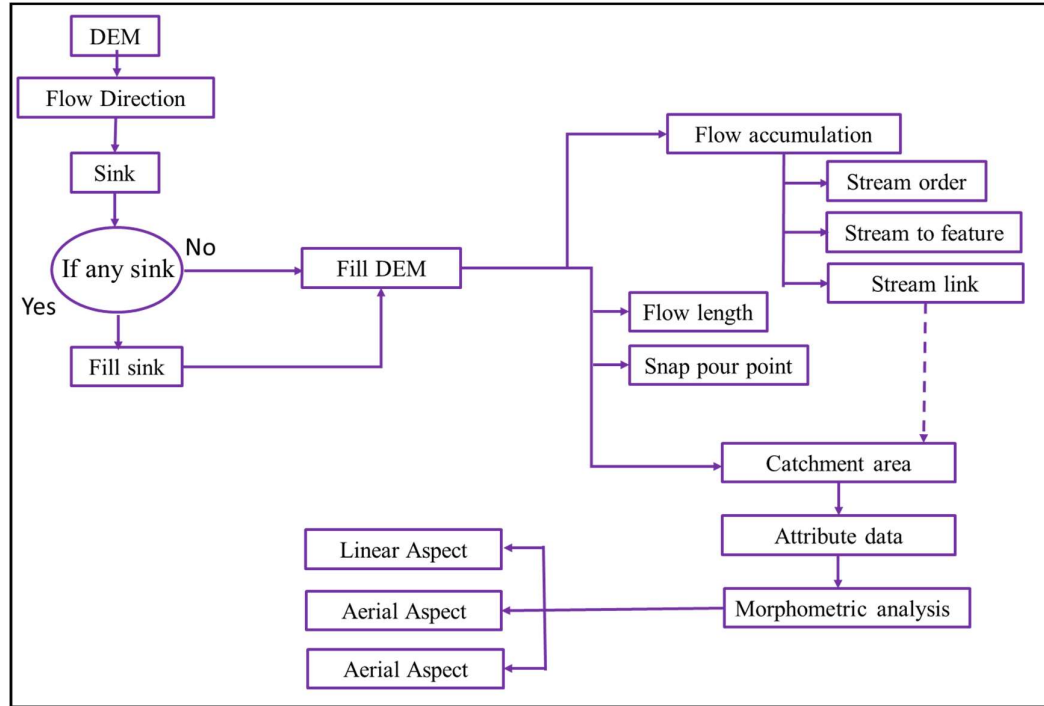


Figure 3:16 Methodology flow diagram of drainage and catchment area delineation (Source: http://webhelp.esri.com/arcgisdesktop/9.3/printBooks_topics.cfm?pid=6050 and modified in the Research lab)

Table 3:13 Some morphometric parameter determination equations from the DEM. The parameters in the equations are computed directly except for the Kirpich equation with a constant $K = 0.01947$. Source: Research lab from the literature as cited.

SN	Morphometric parameters	Formula	Citation
A	Drainage Network		
	Stream order	Hierarchical rank	Strahler (1952)
	Total stream order	Sum of stream order	
	Stream number (Nu)	$Nu = N1 + N2 + \dots + Nn$	Horton (1945a)
	Stream length (Lu) km	Length of the stream	Strahler (1964)
	Stream length ratio (Lur)	$Lur = Lu / (Lu - 1)$	Strahler (1964)
	Bifurcation ratio (Rb)	$Rb = Nu / (Nu + 1)$	Strahler (1964)
B	Concentration time (t_{ch})	$(t_{ch}) = KL^{0.770}S^{-0.385}$	Kirpich (1940)
C	Basin Geometry		
	Basin perimeter (P)	GIS software analysis	Schumm (1956)
	Basin length (Lb) (km)	GIS software analysis	Schumm (1956)
	Basin area (km ²) (A)	GIS software analysis	Schumm (1956)
	Form factor ratio (Rf)	$Ft = A/Lb^2$	Horton (1932)
	Elongation ratio (Re)	$Re = 2\sqrt{(A/\pi)}/L$	Schumm (1956)
	Shape factor ratio (Sf)	$Sf = Lb^2/A$	Horton (1945a)
	Circularity ratio (Rcn)	$Rcn = 4\sqrt{A}/P^2$	Strahler (1964)
	Relative perimeter (Pr)	$Pr = A/P$	Schumm (1956)

D Drainage Texture Analysis			
Drainage density (Dd)	Dd = Lu/A		Horton (1932)
Stream frequency (Fs)	Fs = Nu/A		Horton (1932)
Drainage intensity (Di)	Di = Fs/Dd		Faniran (1968)
Length of overland flow (Lo)	Lo = 1/DdXF _s		Horton (1945a)
E Relief characteristics			
Maximum basin height (Z) (m)	GIS software analysis		
Minimum basin height (z) (m)	GIS software analysis		
Total basin relief (H) (m)	H = Z - z		Strahler (1952)
Relief ratio (Rhl)	Rhl = H/Lb		Schumm (1956)
Relative relief ratio (Rhp)	Rhp = H * 100/P		Melton (1957)
Ruggedness number (Rn)	Rn = Dd * (H/1000)		Patton & Baker (1976)
Melton Ruggedness number (MRn)	MRn = H/A ^{0.5}		Melton (1965)

Furthermore, Figure 5.2(a) describes the stream networks superimposed on the elevation map, and Figure 5.2(b) shows the aspect in degree of Kainji reservoir. Figure 5.3(b) shows the flow accumulation superimposed on drainage basins, and Figure 5.3(b) describes the stream junctions and 2020 bathymetric map. Tables 5.3 to 5.5 present the reservoir morphometric parameter outputs computed based on Table 3.12.

3.8.4 Predicting Soil Loss Via Universal Soil Loss Equation Model (USLEM)

The Universal Soil Loss Equation Model (USLE) predicts sediment loss in the catchment by rill and interrill erosion (Mitra et al., 1998). The prediction is based on the long-term average annual rate of erosion on a field slope, which depends on the rainfall pattern, soil type, topography, crop system and management practices (Wischmeier and Smith, 1978; Forster, 2008; LaRocque, 2013). The USLE gives an estimate of soil erosion in tons/acre/year depending on catchment parameters, including rainfall index, topographical slopes, soil characteristics and land use. The USLE equation is expressed in basic component multiplication as:

$$A = R \times K \times LS \times C \times P \quad 3.20$$

Where:

A is the potential long-term average annual soil loss in tons per hectare (tons per acre) per year.

R represents the rainfall and runoff factor by geographic location. The greater the intensity and duration of the rainstorm, the higher the erosion potential.

K is the soil erodibility. K is a measure of the susceptibility of soil particles to detachment and transport by rainfall and runoff. Texture is the principal factor affecting K, but the structure, organic matter and permeability also contribute.

LS represent the slope length-gradient factor. The steeper and longer the slope, the higher the risk for erosion.

C is the vegetation/crop and management factor. Its function is to determine the relative effectiveness of soil and crop management systems to prevent soil loss. The C factor compares the soil loss from land under a specific crop and management system to the corresponding loss from continuously fallow and tilled land.

P represents the support practice. This shows the effects of practices that will reduce the amount and rate of water runoff and thus reduce the amount of erosion. The factor (P) is the ratio of soil loss by a support practice to that of straight-row farming up and down the slope.

Furthermore, the rainfall erosivity index (R) used for this research is 543.46 for the Kainji Reservoir catchment based on area annual rainfall data, as documented by [Musa et al. \(2021\)](#). The soil erodibility factor chosen is $k = 0.20$, which is for loamy sand/sandy loam clay with the highest silt/clay ratio and best fits the characteristics of the study area ([Peter et al., 2008](#); [Atat et al., 2012](#); [Babatunde et al., 2016](#)). Additionally, the land cover factor (C) and the soil support practice factor (P) were assigned a combined value of 0.40 due to the dominant soil type, which is vegetation and bare ground (Figure 5.1 of 2005 and 2020). [Robert and Hilborn \(2012\)](#) discussed the criteria for such a decision. The catchment slope lengths and steepness factors (LS) were derived from digital elevation data in the QGIS software environment using the LS equation of [Robert and Hilborn \(2000\)](#);

$$LS = [0.065 + 0.0456(\text{slope}) + 0.006541(\text{slope})^2](\text{Slope length}/\text{constant})^{NN} \quad 3.21$$

where the slope is the slope steepness in percent, slope length is the measured length of slope (m), the constant is 22.1 metric, and NN ranges from 0.2 to 0.5 depending on the slope value (Table 3.13) [Robert and Hilborn, \(2000\)](#).

Table 3:14 NN value based on terrain slope (Source: [Robert and Hilborn, 2012](#))

S	< 1	1 ≤ slope < 3	3 ≤ slope < 5	≥ 5
NN	0.2	0.3	0.4	0.5

Similarly, each slope value with a corresponding NN value was used at each instant, thus allowing an estimation of the effectiveness of individual slope steepness intervals in overall rill erosion deposition estimation into the reservoir. Figure 5.4 shows the slope in degree and percentage. Table 5.6 presents the results obtained from the USLE model.

Furthermore, handling flood risk, including hazards and potential consequences, is an imperative aspect of adapting to global change, which has gained recognition, especially in recent times due to climate change challenges rampaging the globe ([de-Moel et al., 2015](#)). Hence, the flood vulnerability map of the study area was produced to assess the area that is danger zones in case there is dam failure due to sediment load at the dam axis (embankment region). The disaster map was generated using the combination of OpenDEM data and the 2020 bathymetric data in the QGIS environment using the necessary tools, e.g., SRTM Downloader, QuickOSM, Qgis2threejs, etc. Figure 3.17 describes the conceptual framework of the general flood assessment, and Figure 3.18 shows the downloaded contour data of the study area (a) and the superimposition of the bathymetric contour data on the downloaded digital contour of the Kainji reservoir and environs.

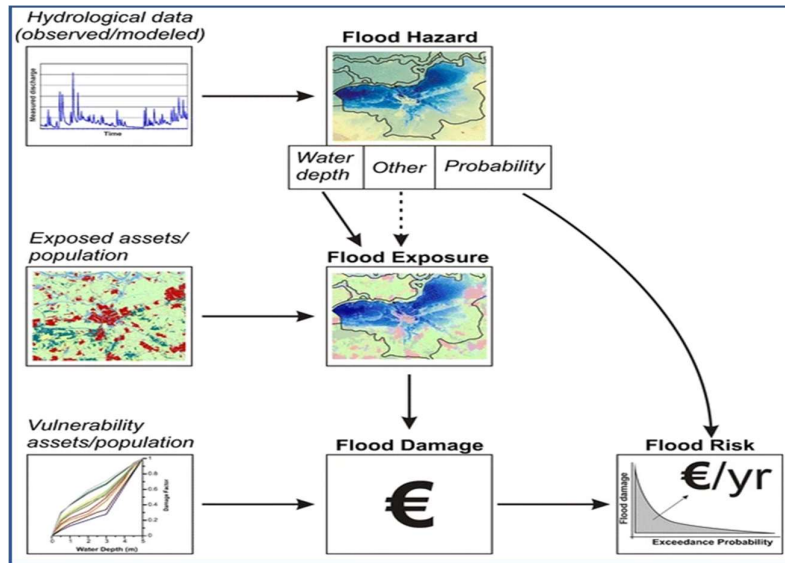


Figure 3:17 Conceptual framework of general flood assessment (Source: Merz et al., as cited by de-Moel et al., 2015)

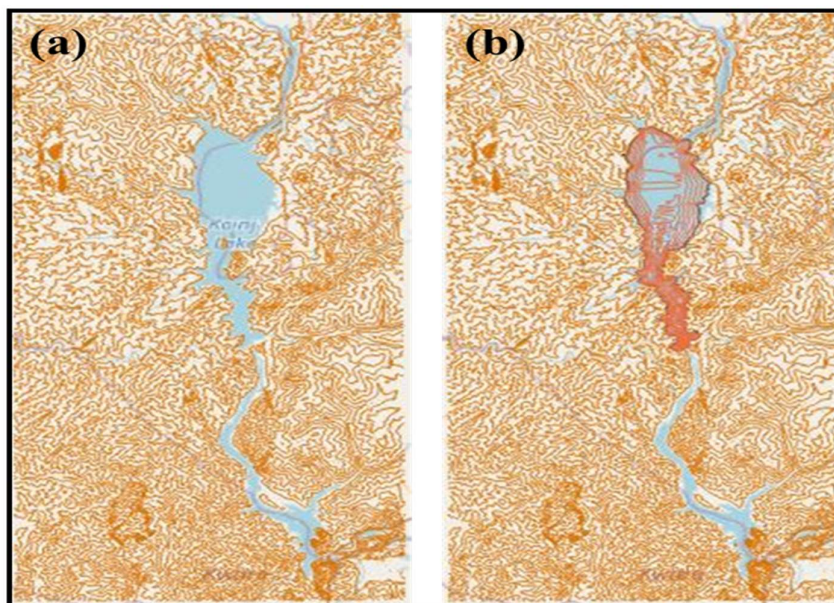


Figure 3:18 Downloaded contour data (a) and superimposed bathymetric contours on downloaded contour data (b) for interpolation to generate a digital elevation model (DEM) for flood hazard assessment.

Source: OpenDEM and field observations (sounding operations).

Meanwhile, the purpose of modelling the areas that are prone or that will be submerged in water in case of possible dam failure is to provide a holistic view of understanding and managing the scenario, i.e., prevention, preparation, mitigation, response and recovery of the disaster management cycle (Lumbruso, 2007; De-Moel and Aerts, 2008; Kreibich et al., 2014).

4 CHAPTER FOUR: Result and Analysis

4.1 Result and Analysis (Objective One):

4.1.1 Introduction

This section of the results presentation and analysis is designed to address objective one of this research. *Objective one aims to design and execute an underwater topographic profile survey and produce a bathymetric chart and 3D dam models for ease of assessment.*

Dual-frequency echo sounding profiling is an excellent method for bathymetry and sedimentation surveys (Hansen and Boss, 2000; Reid and Holcombe, 2000; El-Hattab, 2014). The bathymetric data from multifrequency acoustic surveys can be used to generate bathymetric maps, estimate the quantity of deposited sediments, and study the long-term sediment fluxes and reservoir storage capacity. By extension, the data can be used to estimate the reservoir capacity lost to sedimentation, which is an integral aspect in basin management and monitoring.

However, the echo sounding operation of 2020 shows that the maximum depth of the reservoir is 71.2 m, while the 1990 bathymetric data present a maximum depth of 77.3 m. This accounts for a 7.49% (5.8 m) loss in depth over the past 30 years. The construction highest depth of the reservoir as of 1968 is 85 m. This implies that the reservoir has lost an estimated 13.4 m within the period of 52 years due to sedimentation and siltation. This geomorphological region is located at the dam axis area. This region is termed the hydrological powerhead of the reservoir. The total area of 1990 data is 1007.780km^2 , as recorded, while as of 2020, the estimated area is 1009.110km^2 . Consequently, the next section presents and discusses the results generated from the developed reservoir bathymetric stand-alone system, cross-sections, profiles, volume determination and sediment deposits, and digital depth modelling.

4.1.2 Reservoir Bathymetric Information System (RBIS)

The reservoir bathymetric information system (RBIS) contains depth information of various locations on the map. A stand-alone RBIS is a real-time system where the digital copy is uploaded into an electronic system to become an electronic reservoir navigation system. This

system becomes effective and real-time when connected to a continuous tidal gauge for an efficient reservoir monitoring system that provides safe navigation data to navigators and presents reservoir engineers with an integrated and efficient view of the well-being and performance of the reservoir. Figure 4.1 describes the stand-alone RBIS superimposed on the Google Earth open street map (OSM) standard at a scale of 1 in 150,000. The minimum and maximum depths are 0.2 m and 71.2 m, with a minor contour interval (gray lines) of 2 m and an index contour of 4 m interval (brown lines). The blue line indicates the surveyed shoreline with a sounding datum value of 141.32 m above mean sea level. It is evident that the extent of the survey does not cover all the tributaries of the reservoir. This is due to the meandering nature of waterbody. The developed system is based on S-44 order 1b of the IHO. The general depiction of the bottom is considered adequate, and underkeel, clearance is not of major interest. This is because the bottom characteristics of the research area have the likelihood of features that will endanger the type of surface vessel navigating the lake section are absolutely low. The information on the RBIS is also a reservoir database for future reference.

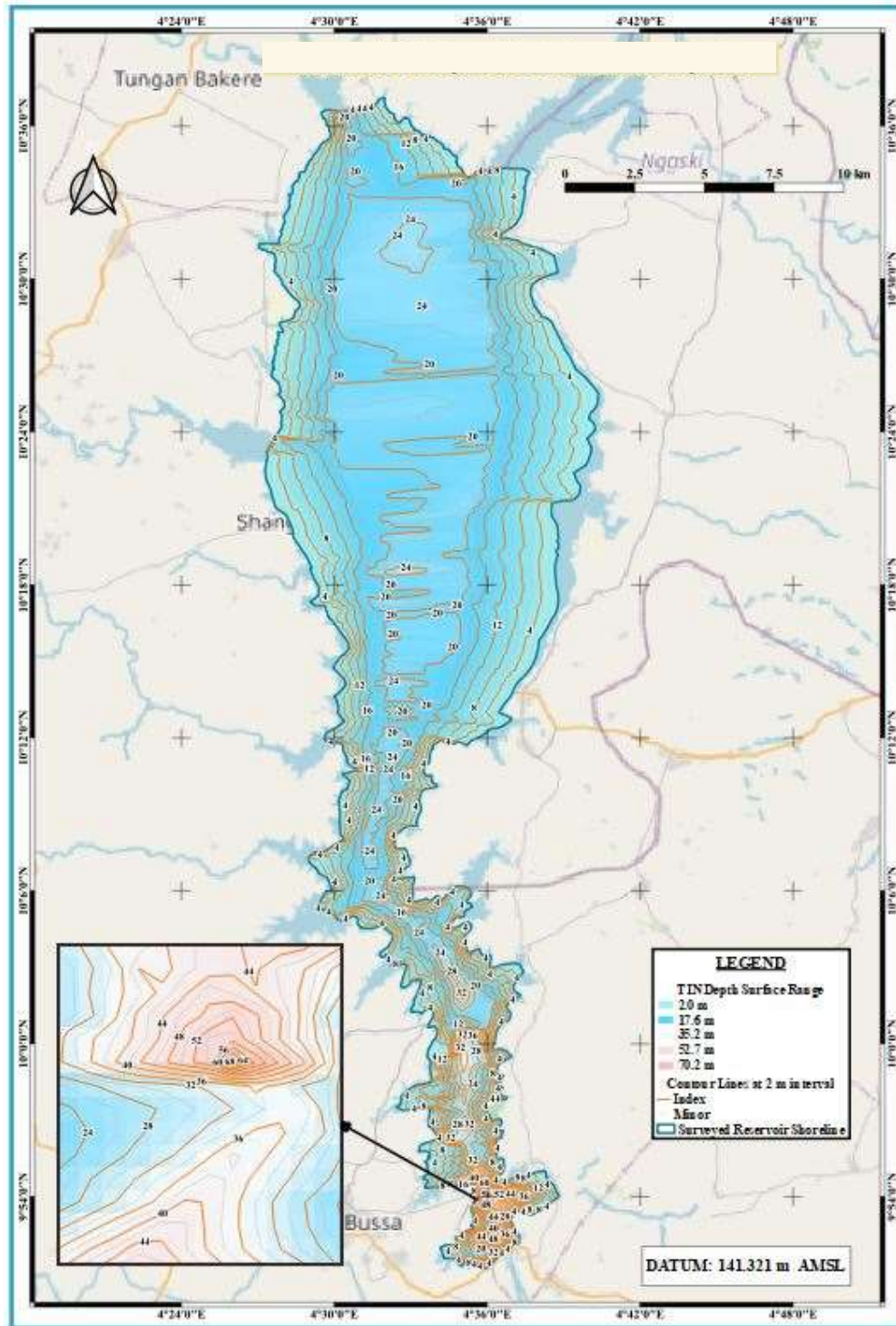


Figure 4:1 RBIS of Kainji Reservoir and Lake superimposed on the OSM standard. The map was generated at a scale of 1 in 150,000 on a paper size of A2 (Source: Research lab)

4.1.3 Cross Section and Profile

The hydrographic parameters are measured only from definite points between the surface and the bottom. These points may be more or less regularly spaced. However, to standardize the data analysis, it is suitable to interpolate the shape of each vertical profile/cross-section and then read off the data values at regularly spaced depth intervals. Some depth information may not be captured, but rather they can be traced on the profile/cross-section curve. The interpolated data can either be presented graphically or numerically. The profile represents the longer section of the point cloud data drawn longitudinally, while the cross section shows the shorter section of the line drawn perpendicularly (Cenderelli et al., 2011). The advantage of the shape of each vertical data profile is that the interpolated data are between the highest and lowest data points. Consequently, Figure 4.2 is the graphical presentation of cross-sections of the Kainji reservoir of some selected areas of the lake area. It describes the cross-sections (CS_1 to CS_4) at a scale of $0.01 m = 1 km$ or $0.02 m = 2 km$ on the horizontal axis and $0.01 m = 10 m$ on the y axis. The blue and red lines indicate the 1990 and 2020 reservoir bed relief, respectively. The cross-sectional profile is an indicator of a temporal sequence of activities as to how much the reservoir characteristics have changed over time (Syvitski et al., 2005)

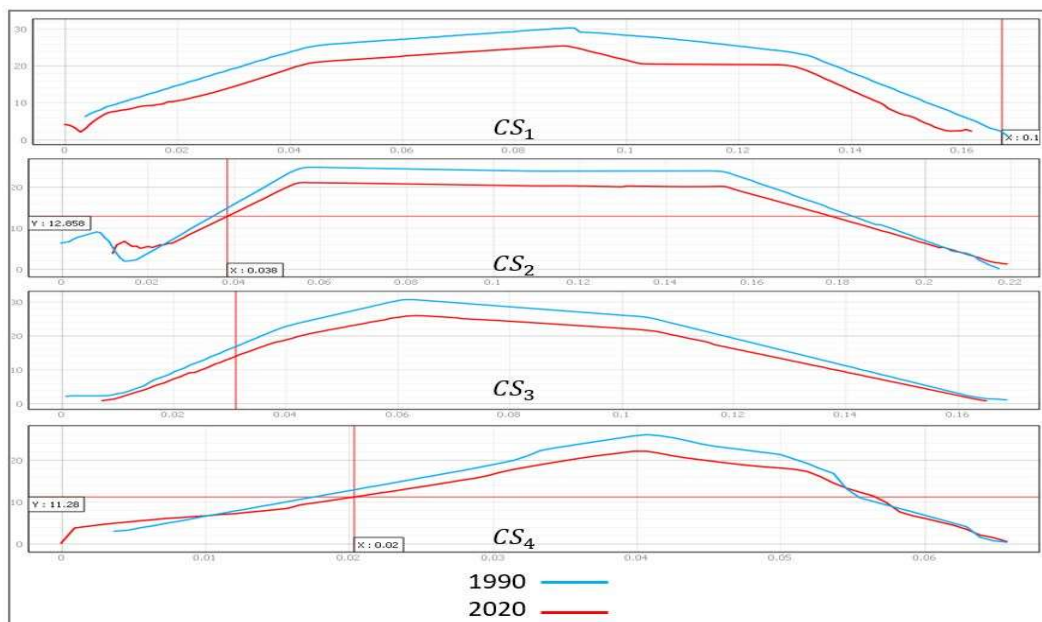


Figure 4:2 Cross sections of lines 1 to 4. The scale of the graph is $0.01 m = 1 km$ “i.e., $0.02 m = 2 km$ ” and $0.01 m = 10 m$ on the X and Y axes, respectively.

Source: Research lab

Similarly, Figures 4.3 (CS_5) to CS_8) illustrate the cross-section of the main dam area where the maximum depths are located. The vertical scale differs from Figure 4.2 by 10 m, while the y axis scale of Figure 4.3 is 0.01 m, representing 20 m. The maximum depths of 77 m and 71 m are traced on CS_7 and CS_8 these points are located at the reservoir main axis area. The cross-sections describe the channel dimensions and their characteristics from west to the east of the reservoir from embankment to embankment. The space between the 1990 and 2020 cross-sections on the graphs represents lacustrine sediment accretion within the last 30 years. The gradient pattern shows that from CS_1 to CS_3 and CS_5 , the left and right widths are symmetrically distributed with little variation from the centre. This is one basic physical characteristic of a lake or reservoir. In contrast, the remaining cross-sections show the rough and undulating nature of the dam bed within that region due to unevenly distributed depths from suspended sediment. This is evident in Figure 4.4 and Figure 4.5 of the slope percentage plot pattern of the cross-sections. Additionally, the area under the curves is the imaginary reservoir basin.

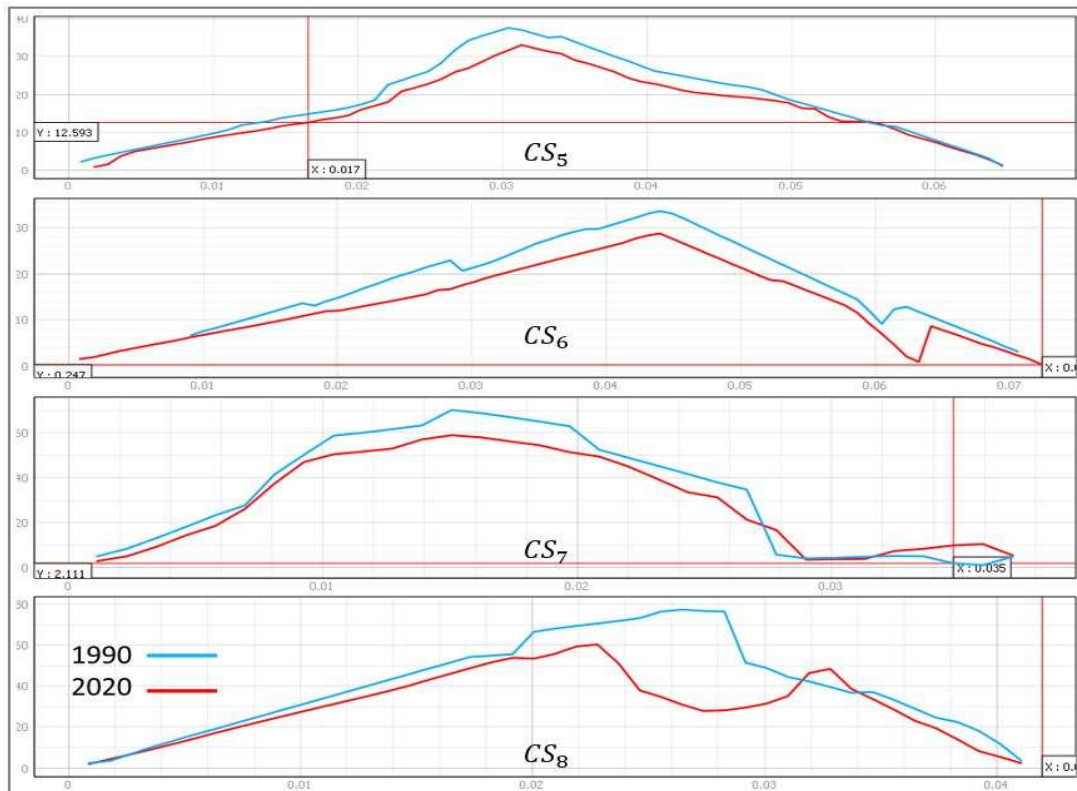


Figure 4:3 Cross-sections of lines 5 to 8. The scale of CS_5 is the same as that of Figure 4.1.

Additionally, they all have equal horizontal scales, but the vertical scale differs at some points where the depth values increase. The vertical scale of CS_6 to CS_8 is 0.01 m = 20 m.

Source: Research lab.

Figure 4.4 and Figure 4.5 describe the percentage slope of the cross-section (CS_1 to CS_8) generated from the application of equation 3.3. The slope shows the rise and fall of the waterbed. If the value is high, the graph represents a rise, and if it shows a fall or run then it is a low. The percentage can also be converted to degree slope, but working with grids, it is recommended to not use slope degree because when you zoom in or out, the value changes, affecting the angle (Choanji, 2017). However, that is not the case with slope percentage. The region with a projected crest shows sharp changes in depth. The section with a similar and continuous flow pattern describes the change in reservoir topography based on a small change in depth within the area. The slope demonstrated that there is an existing and continuous inflow of sediment from the upper eastern and western regions to the main absorbing basin.

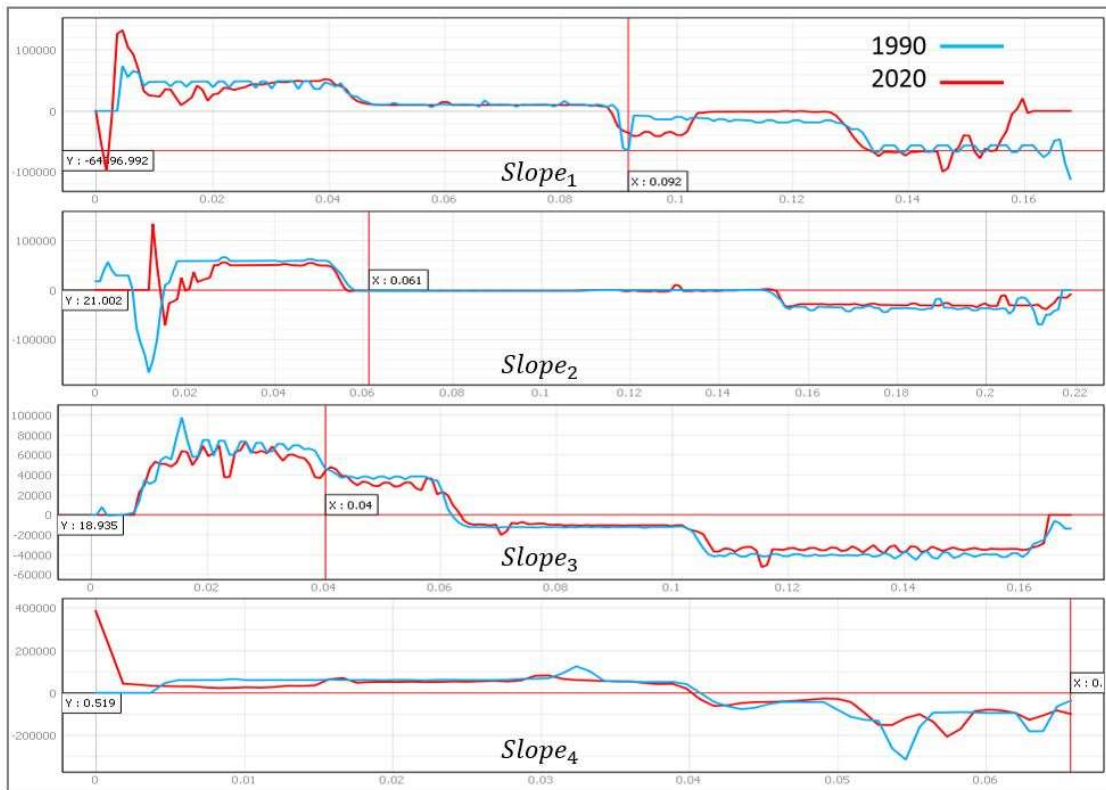


Figure 4:4 Percentage slope from CS_1 to CS_4 (Source: Research lab)

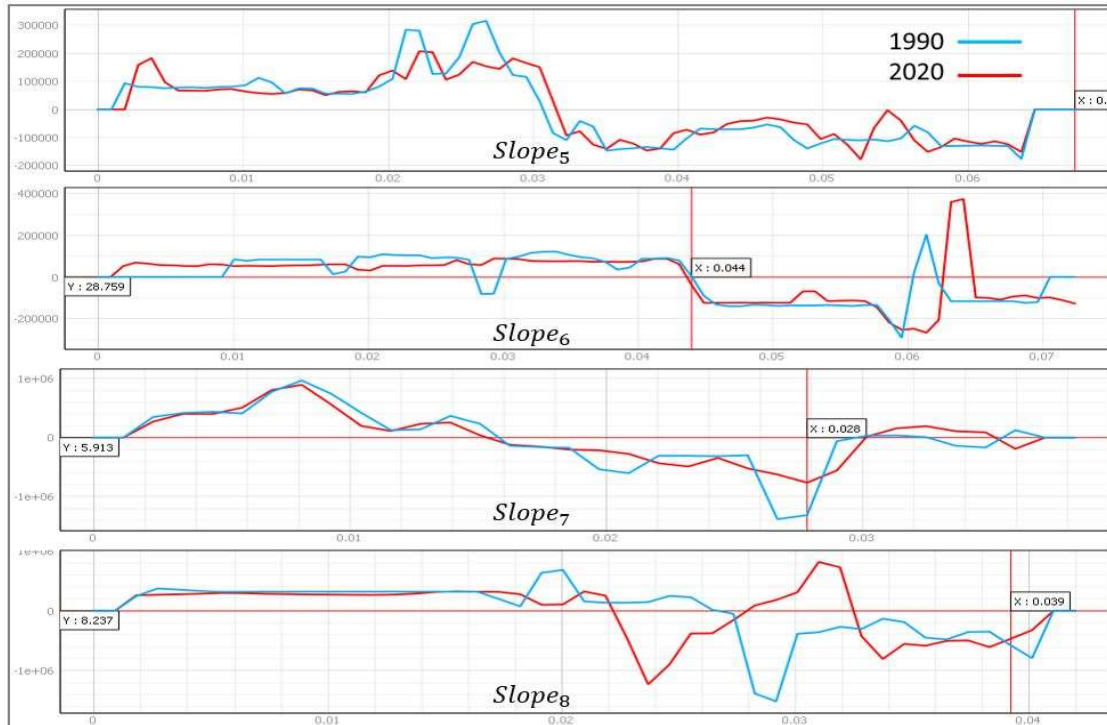


Figure 4:5 Percentage slope from CS_5 to CS_8 (Source: Research lab)

Meanwhile, the longitudinal profiles are similar to cross-sections; the major difference is that profiles assume the longest part, while cross-section is presumed the shortest line drawn perpendicular to the profile line. Figure 4.6 describes the profile lines and their corresponding slope percentages as designed in Figure 3.6. These lines were drawn to pass through the middle of the reservoir to assess the reservoir bottom characteristics within that region. P_1 to P_3 present the reservoir configuration, and it is evident from the slope lake basin pattern that the sediment deposit follows the reservoir geomorphology. The blue and red lines represent the sediment thickness between the 1990 and 2020 bathymetry datasets. However, this will be analysed in the sediment analysis section.

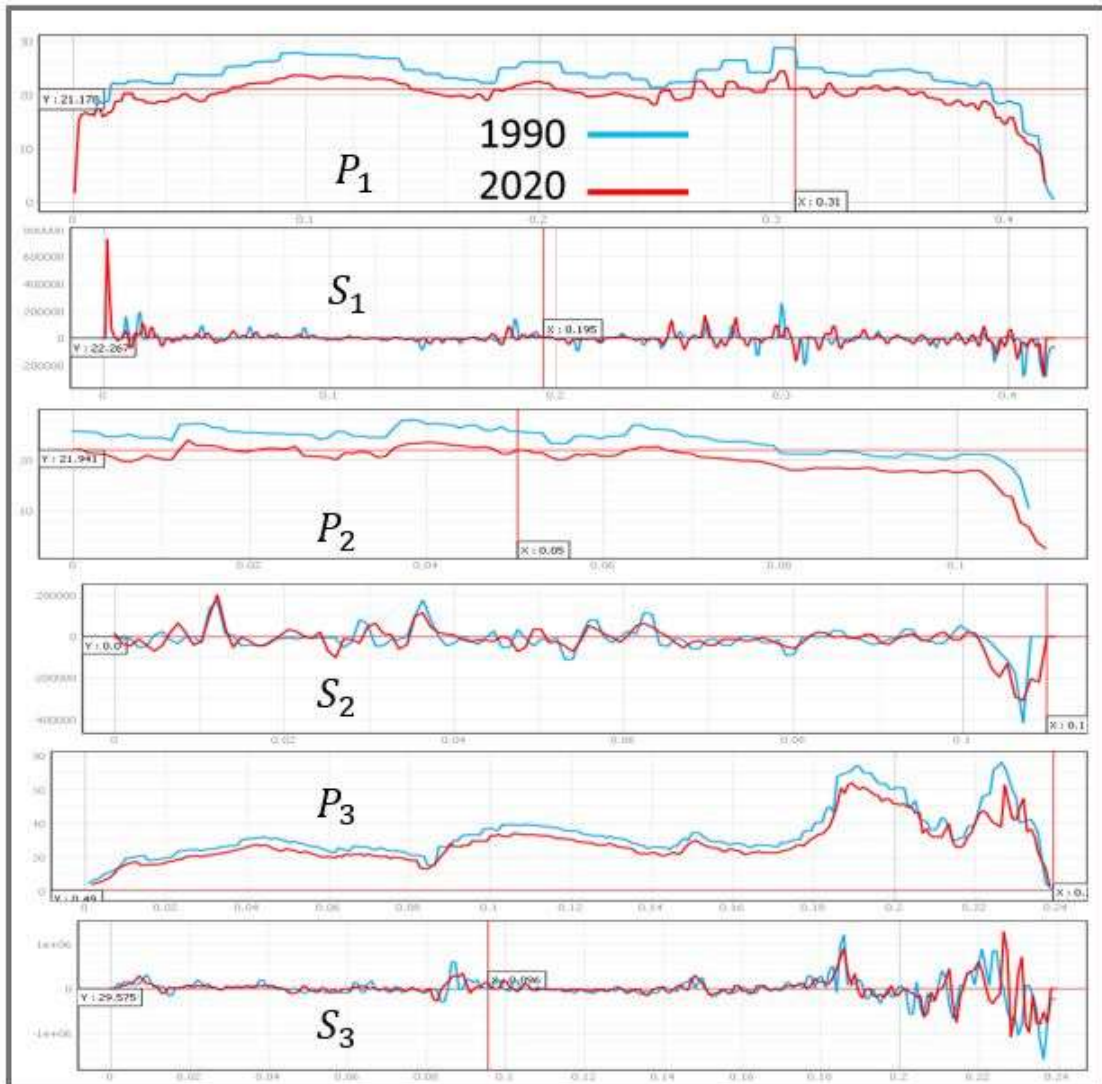


Figure 4:6 Longitudinal profile and slope from upstream to the embankment
(Source: Research Lab)

4.1.4 Sediment Deposit and Volume Determination Analysis

The Kainji reservoir sediment thickness was generated from the difference in depth measurement by 200 kHz and 20 kHz echo sounder pulses. The recorded and calculated sediment thickness of the Kainji Basin varied from 0.2 m within the basin banks to approximately 6 m around the lake (see Figure 4.7(a)). Dense sediment ($> 6\text{ m}$) was noticed around the central area of the lake and the dam embankment area. The bulky sediments represent the majority of the soil or alluvium, which were excavated to form the barrier at the northwest and northeast parts of the main lake prior to impoundment and are gradually eroded into the main dam. Additionally, the reservoir serves as a trap to erode

alluvium from upstream of the Niger River and other tributaries. Excluding the maximum sediment thickness, the average sediment thickness recorded in the Kainji dam ranges from 3.5 m to 5.5 m (Figure 4.7a). The central area of the dam has the tendency to trap a high volume of sediment because it serves as basin. Similarly, Figure 4.7b describe the the long-term average sediment accumulation rates. While the total sediment thickness computed volume for the entire reservoir was estimated as $2.67 \times 10^9 m^3$.

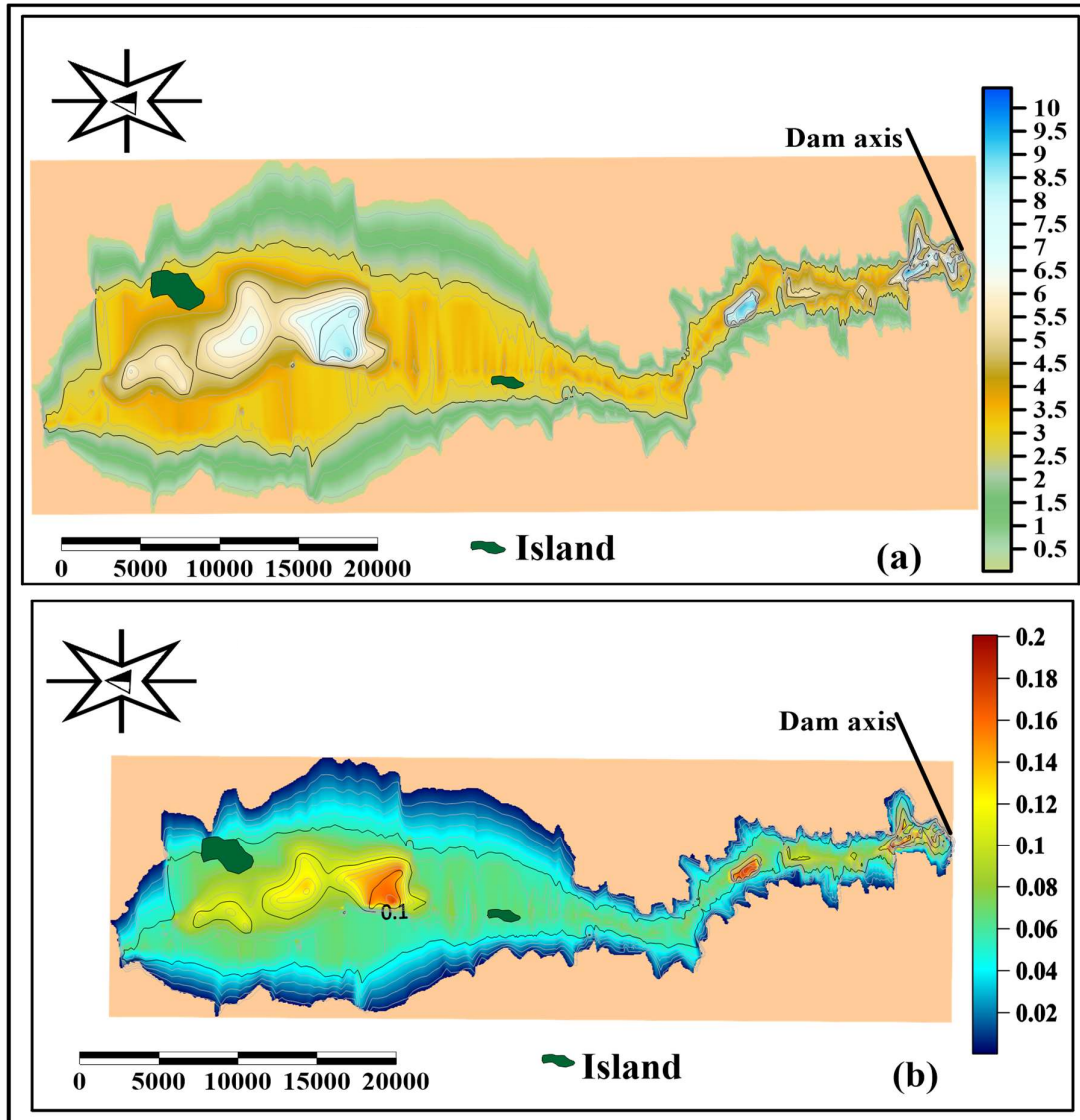


Figure 4:7 Maps of Kainji Reservoir describing (a) sediment thickness (contour intervals of 0.5 m) and (b) long-term average sediment accumulation rates (contour intervals of 0.01 m/y). Source: Research lab

Furthermore, the long-term annual average sediment accumulation rate was computed by dividing the recorded sediment thickness values by the age of the reservoir (52 years), and

the result varied from 0.01 m/y to 0.23 m/y , with a basin average of 0.051 m/y (see Figure 4.7(b)). The accumulation rates of 0.23 m/y corresponded to the output when the construction depth was subtracted from the maximum observed depth ($85 \text{ m} - 71.2 \text{ m}$), and then dividing the result by the age of the reservoir (52 years) yielded an accumulation rate of 0.26 m/y . A more categorical view of the sediment thickness and long-term accumulation rate can be seen on the colour scale of Figure 4.7.

Meanwhile, the calculated sediment volume of the Kainji dam was divided by the age of the reservoir (52 years) based on the time of sounding, producing a corresponding long-term average annual sediment flux of $5.16 \times 10^7 \text{ m}^3/\text{y}$. This suggested that the Kainji reservoir has experienced an average annual storage loss due to sedimentation of 0.5 percent. However, this value does not account for potential sediment compaction. Figure 4.8 describes the comparison of the computed volumes from the HF_1990, HF_2020 and LF_2020 data.

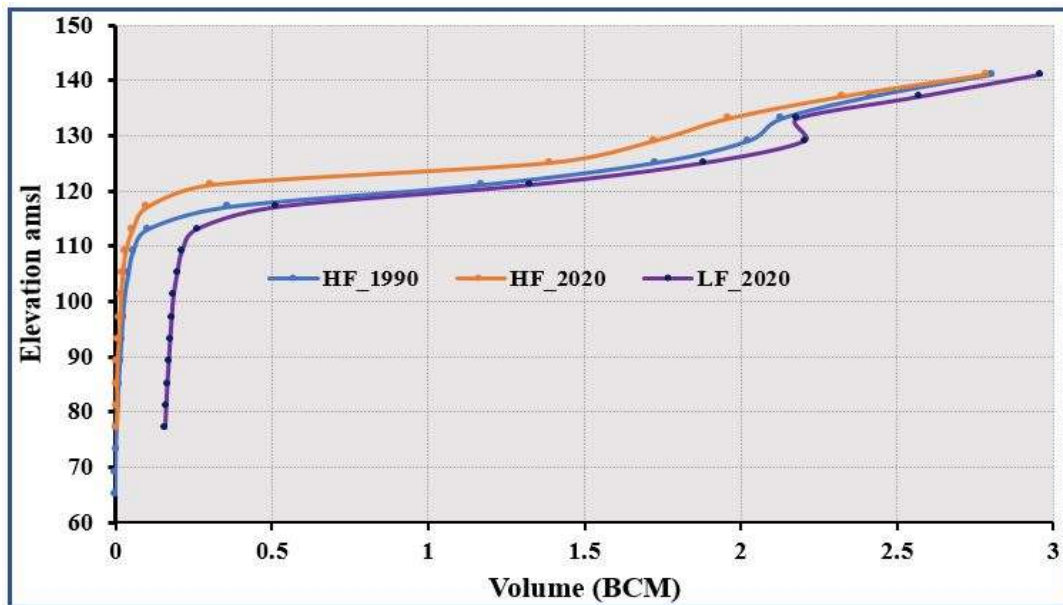


Figure 4:8 Elevation capacity curve of the Kainji reservoir. The volume presented is computed from the LF and HF of 2020 acquired bathymetric data and the received HF_1990 bathymetric data. The space between LF_2020 and HF_2020 is the region consumed by lacustrine sediment from 1968 to 2020 when the measurement was carried out. Additionally, amsl refers to elevation above mean sea level while BCM is abbreviation for billion cubic metres. Source: Research lab.

Additionally, the output of the computed volume from the 200 kHz data of 2020 shows that the volume of the reservoir at the time of the survey was $10.5 \times 10^9 \text{ m}^3$. The 1990 200

kHz data presented an estimated reservoir volume of $12.9 \times 10^9 m^3$. This implies that the reservoir has experienced an 18.6% loss in storage capacity within the period of 30 years. However, the estimated volume for 2020 does not include some of the reservoir tributaries, especially areas that are inaccessible due to the hazardous nature of the terrain. The reservoir capacity estimated at the instant of the survey also showed the maximum capacity of the basin because the dam surface was level with the spillway. Table 4.1 shows the computed reservoir capacity at 4 m range. The estimated reservoir area at the instant of the survey was $1009.110 km^2$ for 2020, and that of 1990 was determined to be $1007.780 km^2$. This again implies that the dam increased in the shoreline by 0.2%. The increase in the area suggested that some alluvium within the reservoir corridor was eroded and deposited into the basin. Hence, this points at the high rate of lacustrine sediment recorded by the low-frequency pulses and as computed and presented in Figure 4.7.

Table 4:1 Kainji Reservoir depth volume comparison. The volume is in billion cubic metres (BCM) with a contour interval of 4 m. Source: Research lab

ID	Depth Range (m)	1990 – Volume (*10 ⁹ m ³)	2020 – Volume (*10 ⁹ m ³)
D1	77.1 - 76.1	0.0000035	
D2	76.1 - 72.1	0.00001	
D3	72.1 - 68.1	0.0015	0.000014
D4	68.1 - 64.1	0.0036	0.00001
D5	64.1 - 60.1	0.0068	0.0004
D6	60.1 - 56.1	0.0106	0.0019
D7	56.1 - 52.1	0.015	0.0041
D8	52.1 - 48.1	0.0196	0.0091
D9	48.1 - 44.1	0.0243	0.014
D10	44.1 - 40.1	0.0302	0.0155
D11	40.1 - 36.1	0.0423	0.0217
D12	36.1 - 32.1	0.0575	0.0391
D13	32.1 - 28.1	0.105	0.0545
D14	28.1 - 24.1	0.3595	0.1006
D15	24.1 - 20.1	1.1711	0.3057
D16	20.1 - 16.1	1.7261	1.3896
D17	16.1 - 12.1	2.1236	1.5249
D18	12.1 - 8.1	2.0282	2.3246
D19	8.1 - 4.1	2.4153	1.8605
D20	4.1 - 0.1	2.8022	2.7876
Total		12.9428	10.4455
<i>Construction Volume = 15.0000 bcm is the estimated volume in the year 1968</i>			

Additionally, the empty rows (D1 and D2) in Table 4.1 of the column (2020 – Volume) are the loss in depth from 1990 to 2020. Figure 4.9 describes the 100% stacked column chart

showing the percentage loss in volume over time relative to the observed depths. A greater percentage has been lost to sedimentation, and it is more pronounced at the depth ranges of 76.1 m - 64.1 m, while depths of 76.1 m to 72 m are not in existence based on the survey data of 2020, suggesting that 71 m to 64 m will soon go into extinction.

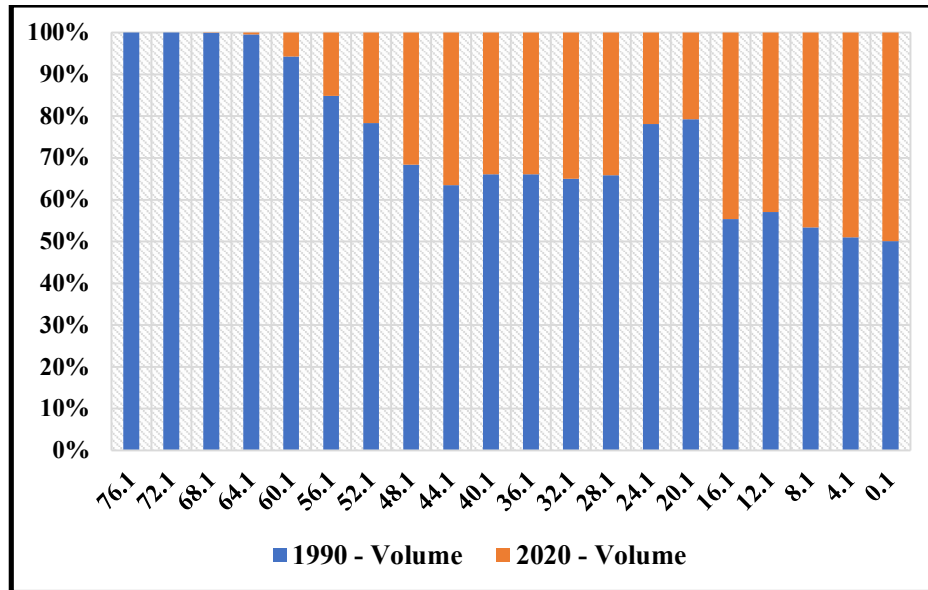


Figure 4:9 100% stacked column chart of 1990 and 2020 computed volume. The graph shows the relative loss in volume to depth between the two epochs of data. Mainly, it compares the percentage that each depth range value contributes from each dataset to the computed volume of that section. Source: Research lab.

Additionally, Table 4.2 presents some of the reservoir sediment yield computed from different models. The results show that the area increases while the storage capacity decreases relative to the depth. The per kilometre square per year ($/km^2/year$) sediment deposits yielded an estimated value of $86805.29 m^3$ based on the model of Vahid et al. (2018). The estimated annual average sediment deposit from the high-frequency datasets of 1990 and 2020 was $8.7 \times 10^7 m^3/year$ “from the model of Adediji, 2005; Timothy and Jenifer, 2017,” which is 40.7% greater than the result derived from the low-frequency long-term average annual sediment flux determined from Chapra (1997). This shows that using two different epoch high-frequency datasets to determine lacustrine sediment deposits is not an adequate approach, but it is suitable for storage capacity investigation (John et al., 1999). Thus, the precise and reliable approach to sediment yield determination from bathymetric data is through the use of high- and low-frequency pulse echosounders (John et al., 1999; Odhiambo and Stephen, 2004).

Table 4:2 Sediment yield from different models. Source: Research lab

	1968	1990 200 kHz	2020 200 kHz
Area(km^2)	1004.5	1007.780	1009.110
Volume (BCM)	15	12.943	10.446
Max depth (m)	85	77.3	71.2
Vahid et al., 2018 Equ. 2.38	86805.29 $m^3/km^2/year$	2020_20 kHz According to Chapra, (1997) equ. 3.7: 5.16 x 10 ⁷ $m^3/year$	
Adediji 2005; Timothy and Jennifer, 2017. Equ. 2.39	8.7 x 10 ⁷ $m^3/year$		
Reservoir half-life Vahid et al., 2018. Equ. 2.40	85.6 years		

Similarly, the reservoir half-life was derived based on the Vahid et al. (2018) model as 85.6 years. The computed half-life suggested that the basin's effective and economic life span was 85.6 years. However, this is a function of the rate of sediment inflow computed at a particular period (Yang, 2015). In addition, Figure 4.10 describes the relationship between reservoir area and storage capacity of the two epochs data. As the area increases, the volume is enhanced, but not in all cases. For instance, when the area is 117.42 km^2 the volume is 1.86 BCM and relating it to when the area is 119.23 km^2 the volume is 1.38 BCM, which shows a shortage in volume; Table 4.1 at D17 and D18 (1990) and D18 and D19 (2020) are representations of this scenario. The irregular shapes of both graphs in Figure 4.10 indicate the irregular nature of the reservoir bed due to lacustrine sediment and the brakes between the lake and the main dam.

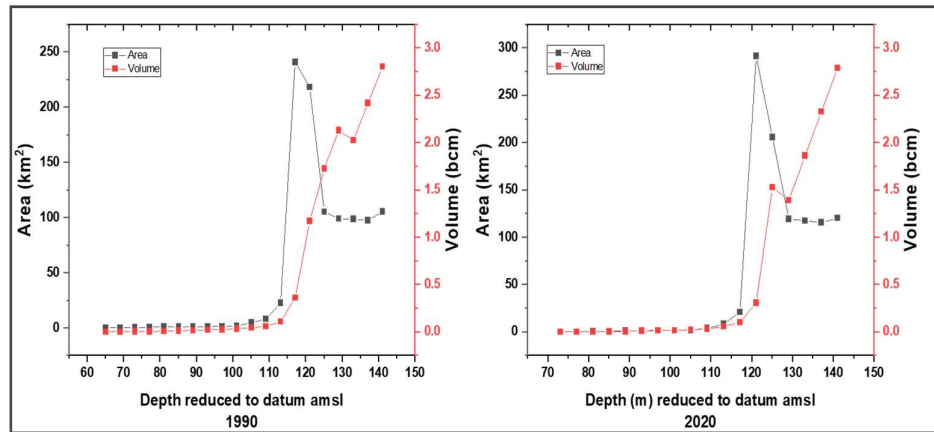


Figure 4:10 Reservoir capacity curve from 1990 and 2020_200 kHz data (Source: Research lap)

4.1.5 Digital Depth Model of Kainji Reservoir

The digital depth model of the reservoir bed is an integral part of reservoir modelling because it aids in identifying the section of the reservoir bed where dredging should be prioritized (Daryl et al., 2021; Kai et al., 2021). Figure 4.11 describes the DDM colour relief map with a colour scale that shows the complicated nature of the reservoir bed topography. This is supported by the corresponding 3-dimensional surface, as shown in Figure 4.12. The quality of DDMs generated was enhanced by ensuring that both datasets were in the same geographic coordinate system to avoid unnecessary exaggeration over rugged or steep sloping basin beds. However, the surface model generated from two different epoch bathymetric data acquired using the same equipment will still be deficient due to survey lines and other systematic errors. The setback introduced by the difference in survey line can be corrected through interpolation by maintaining uniform model parameters during surface modelling (Dorst, 2005).

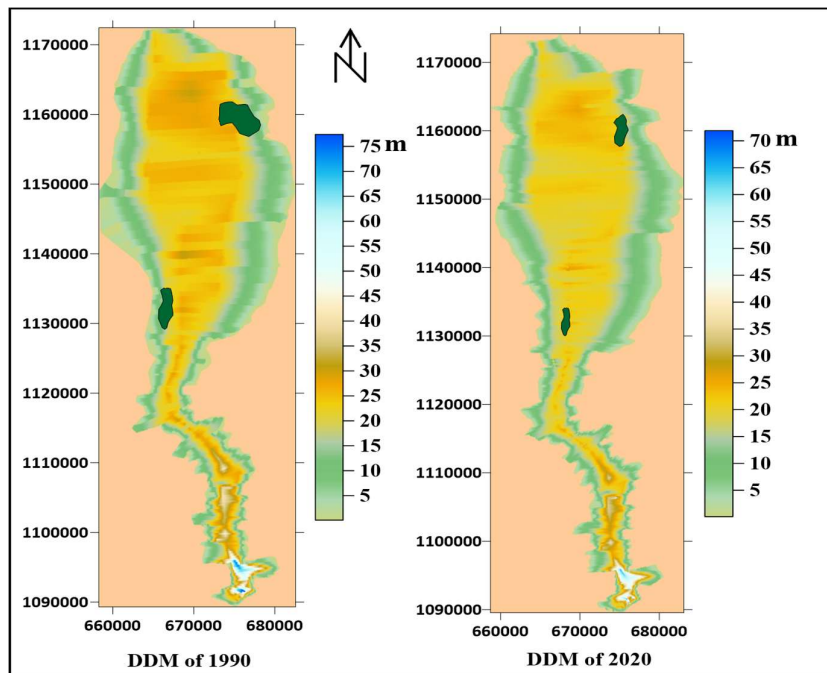


Figure 4:11 Digital depth model relief of Kainji Reservoir generated using a TIN technique from datasets of 1990 and 2020 high-frequency pulses (Source: Research lap)

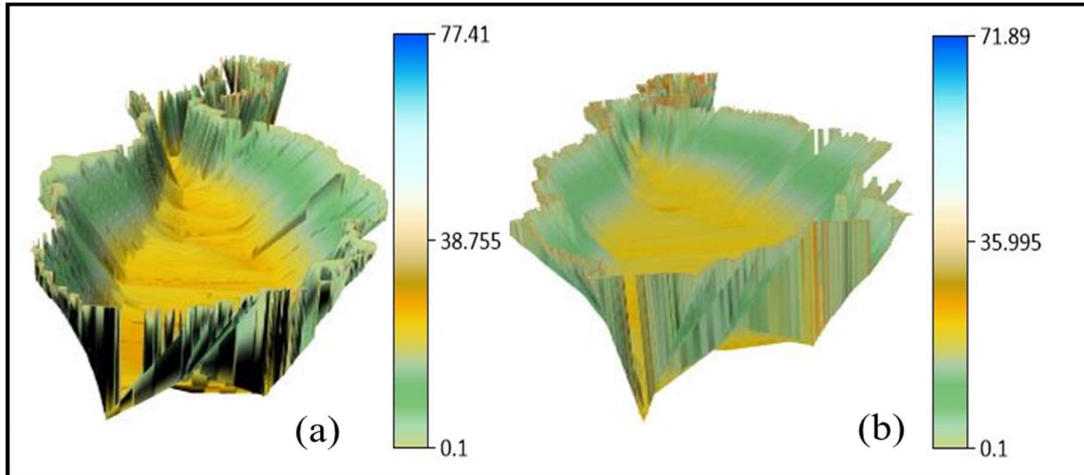


Figure 4:12 3-D display of the Kainji reservoir of 1990 (a) and 2020 (b). The 3-dimensional models describe the reservoir from the water level to the reservoir bed, and the colour scale shows the difference and loss in storage capacity. The content of the basin at each moment indicates its storage capacity and can be determined at every depth range (see Table 4.1). (Source: Research lab).

Additionally, Figure 4.13 describes the modeled interpolation errors of both datasets. The error pattern ranges from -5 m to 6 m and - 4 m to 2.5 m for the archive and measured data, respectively. Generally, the errors lie between -1 m and 1 m for the archive data and -0.5 and 0.5 for the observed data, as seen on the error maps of Figure 4.13 and collaborated by the 3-D modeled error maps of Figure 14. However, a few points of the achieved interpolated surface show a residual of -5 to 6; this is caused by the steep slope introduced by the deepest point of the reservoir depths observed. These points are not evenly distributed in the observed archived data; hence, the pikes on the error map. This does not mean that the interpolation technique is inadequate; rather, it suggests that the point is either on the observed data or on the interpolated data. Hence, when it is negative, the point is on the interpolated surface, while when it is positive, it is on the measured surface (Farrira et al., 2017; Ibrahim and Sternberg, 2021).

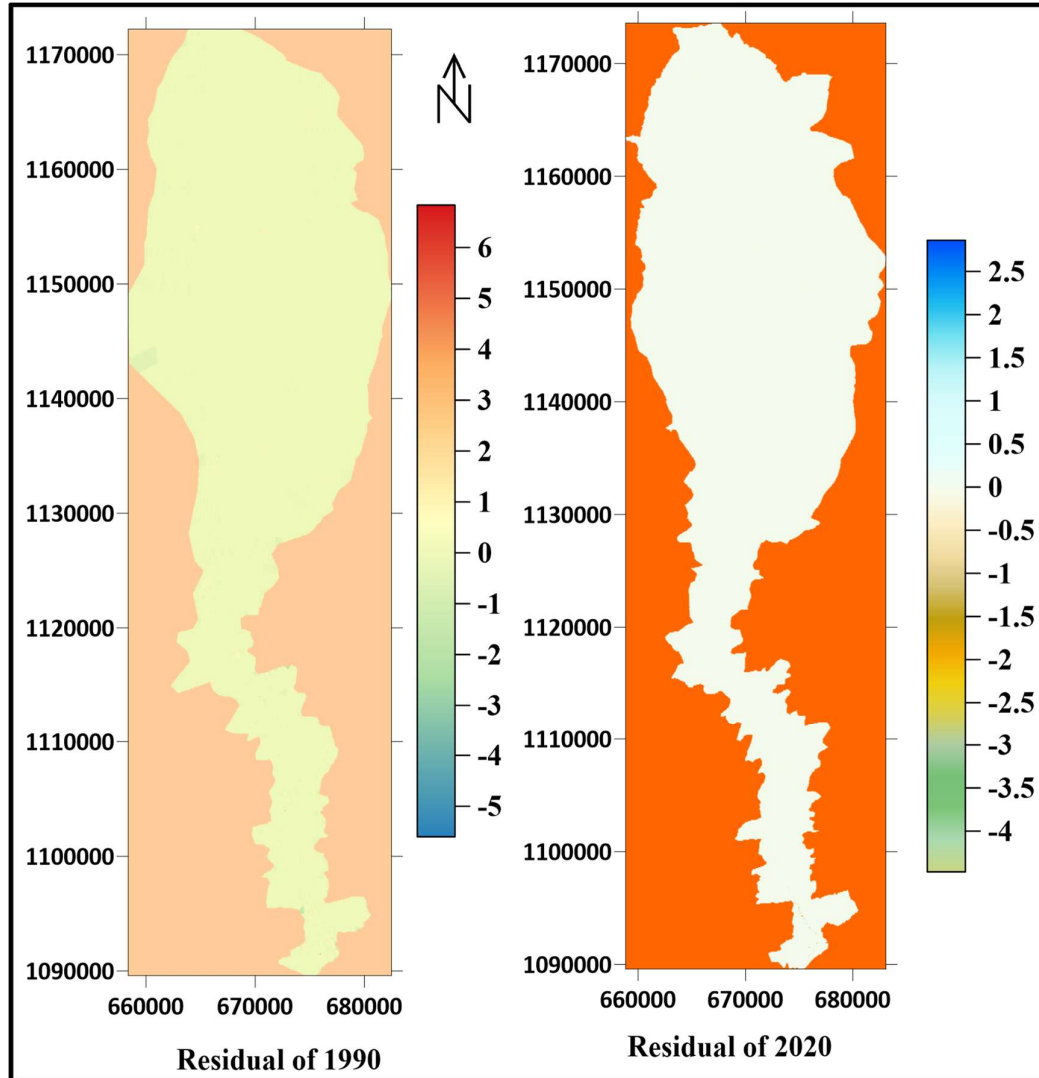


Figure 4:13 Residual plots from the split-sample evaluation method employed using TIN DD modelling. The error outcome is dominated with an error range of -1 m to 1 m on the residual of 1990 and -0.5 m to 0.5 m on the 2020 residual as computed. Hence, the residual maps are encompassed by one colour scale (source: Research lab).

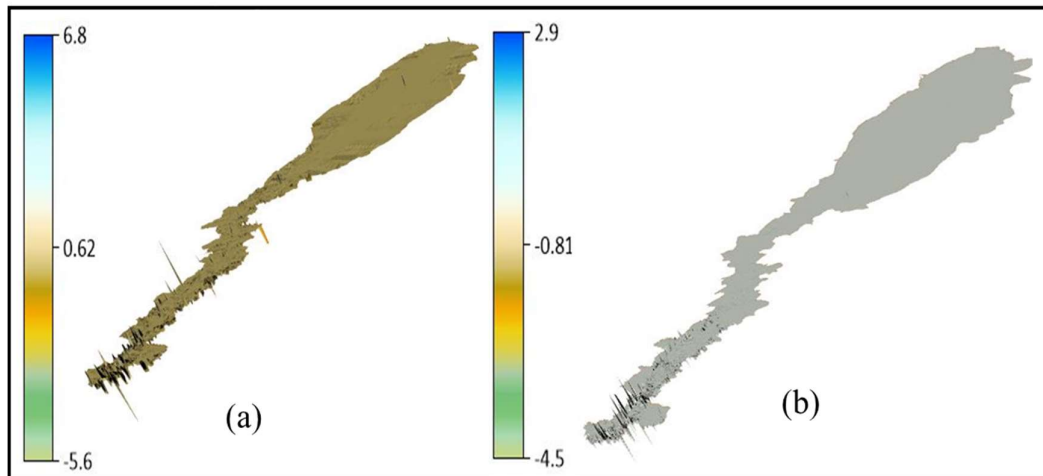


Figure 4:14 3-D model of residual 1990 data (a) and 2020 data (b). The three-dimensional model shows the maximum pecks caused by the steep slopes created by some points that are deeper than neighbouring points. The flatness of some regions is within the value of -1 m and 1 m. However, zero is the most dominant (Source: Research lab)

4.2 Result and Analysis (Objective Two): CA-Markov Sediment Effect Forecasting

This section is designed to present and discuss the results of objectives two of this research. The objectives are: “*To carry out sediment deposit analysis of the study area and forecast by the use of Cellular Automata - Markov chain and To carry out sediment deposit analysis of the study area and forecast by the use of Cellular Automata and GBR*”

Figure 4.15 below describes the Markov chain classification of depths into state contour plots prior to the application and computation of the probability matrix or confusion matrix. The vertical scale readings show the states for both the 1990 and 2020 historical data as classified, and the depth reduces gradually based on historical data.

The computation outcome of transition probabilities using Markov chain analysis is presented in Table 4.3 below; in the table, the rows reflect from which state the transition occurs and the columns to which state. For example, the probability of going from state 1 to state 0 is 13.9 percent. It is evident that the table is not symmetrical about the main diagonal. For example, the probability of going from state 0 to state 1 is much less than the probability of going back, which is 2.4 percent. The research printed the zero transition probabilities in light gray for adequate presentation. The maximum values bylines are underlined. Analysis of Table 4.3 shows that states with small ordinal numbers (shallow depths) tend to preserve the status quo. Their most significant value lies on the main diagonal. It is also evident that the values under the main diagonal are more significant

than the values above the main diagonal, which means there is a tendency for a decrease in the state number, which means, in general, there is a decrease in the depth of the investigated area. The research made the same conclusions when constructing contour diagrams from historical data.

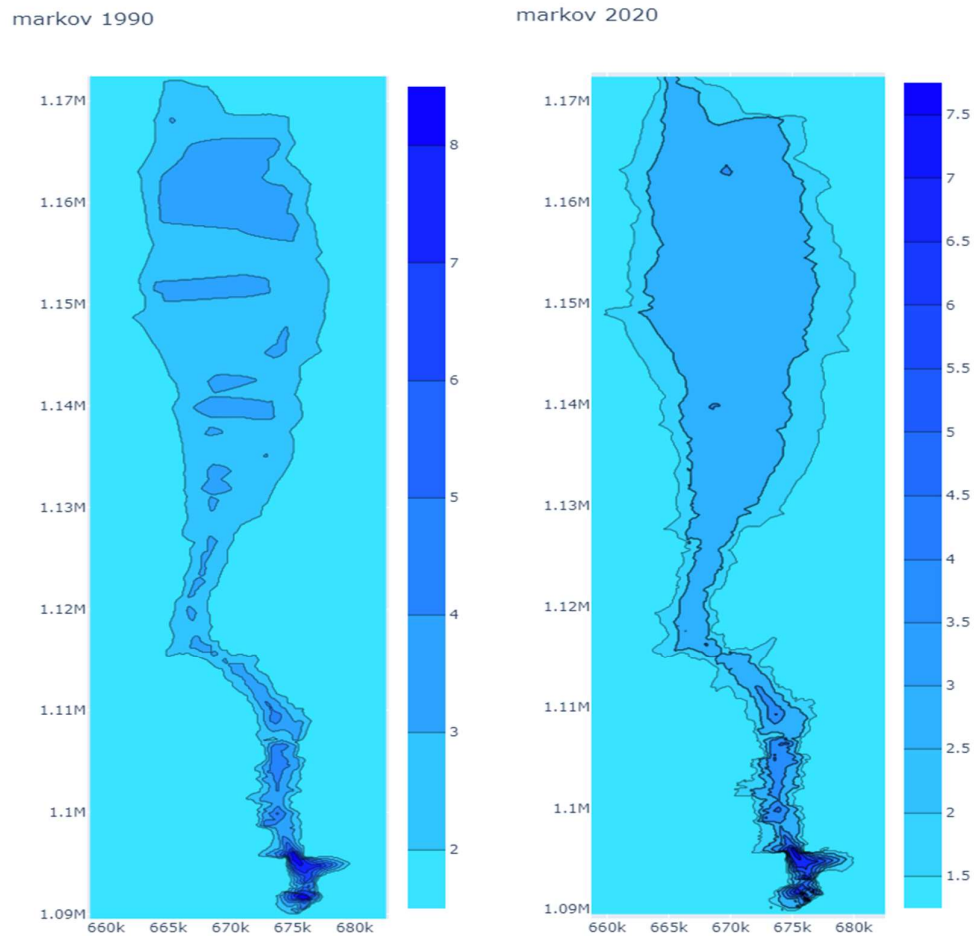


Figure 4:15 Contour plots for depth states based on historical data. Horizontal and vertical scale readings are in metres (m). The plots present the Markov chain depth states based on the transformation conducted on the historical datasets of 1990 and the measured datasets of 2020. Source: Research lab.

Table 4:3 Transition probability matrix of the Markov chain states in percentage.
Source: Research lab

	0	1	2	3	4	5	6	7	8	9
0	<u>97.543075</u>	2.360739	0.096186	0.000000	0.000000	0.000000	0.000000	0.000000	0.000000	0.000000
1	13.910420	<u>65.007047</u>	20.010129	1.070202	0.002202	0.000000	0.000000	0.000000	0.000000	0.000000
2	0.195477	16.368107	<u>76.101465</u>	7.273866	0.047342	0.013744	0.000000	0.000000	0.000000	0.000000
3	0.074890	0.773861	<u>76.920090</u>	21.695837	0.418828	0.036058	0.049926	0.030511	0.000000	0.000000
4	0.507068	0.476337	35.172096	<u>52.596804</u>	9.864782	0.645360	0.199754	0.460971	0.076829	0.000000
5	3.176471	1.529412	5.529412	23.058824	<u>41.411765</u>	15.411765	4.470588	2.352941	3.058824	0.000000
6	0.374532	0.561798	4.494382	9.176030	15.355805	<u>47.191011</u>	14.981273	5.992509	1.872659	0.000000
7	0.000000	0.000000	2.736318	4.975124	7.462687	16.915423	<u>51.741294</u>	15.174129	0.995025	0.000000
8	0.000000	0.000000	4.838710	9.139785	12.365591	11.290323	<u>33.870968</u>	24.731183	3.763441	0.000000
9	0.000000	0.000000	6.896552	<u>37.931034</u>	24.137931	6.896552	6.896552	5.172414	12.068966	0.000000

Finally, the predicted future depth distribution was modelled based on the CA-Markov chain technique, as presented in Figure 4.16. The forecast was for the period of 2050 (Markov 2050). The map contains artefacts caused by the random choice of the following state in the Markov chains. The reason is that the Markov process is a categorization process that is best applicable to spatially categorized data, e.g., imagery depicting different land uses and covers. The CA-Markov chain adequately predicted the future state depths following historical patterns except for the introduced artefacts on the map (Figure 4.16 “Markov 2050”). The future maximum depth is between 59 m and 65 m, the depth gradually decreases from upstream, and the weight is experienced at the reservoir axis region. Meanwhile, the actual cause of the artefacts is not clearly ascertained; therefore, it is subject to future investigation.

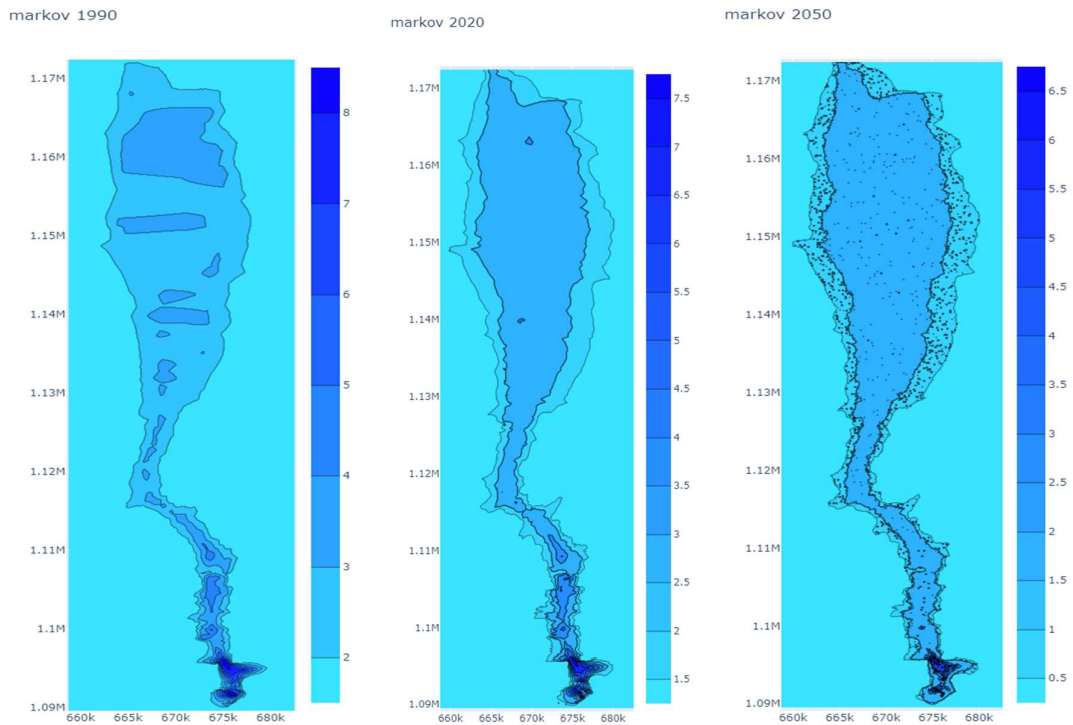


Figure 4:16 CA-Markov historical and forecasted plots. The vertical scale is the Markov states in all plots. The predicted plot (Markov 2050) contains artifacts caused by the uncertainty of the modeled Markov states. However, this assertion is subject to future investigation. Source: Research lab.

4.3 Result and Analysis (Objective Three): CA-GBR Sediment Effect Forecasting

This section is designed to present and discuss the results of objective three of this research. The objective is “to carry out sediment deposit analysis of the study area and forecast by using cellular automata and gradient boosting regression models to measure the accuracy of objective (ii) above”.

The CA-GBR method for predicting bathymetric data produced more realistic images without artifacts. Figure 4.17 describes the plots of the CA-GBR forecasted reservoir surface. The cellular automata-gradient boosting regression technique was specifically designed for this research. It effectively predicted the future bathymetric surface because each bathymetric spatial point was treated like a tree (random forest). This method can best be described as an object-oriented method. The maximum predicted depth lies between 56 m and 60 m; relating this to the maximum construction depth implies that by 2050, the reservoir will lose approximately 29.4% of its depth to sedimentation.

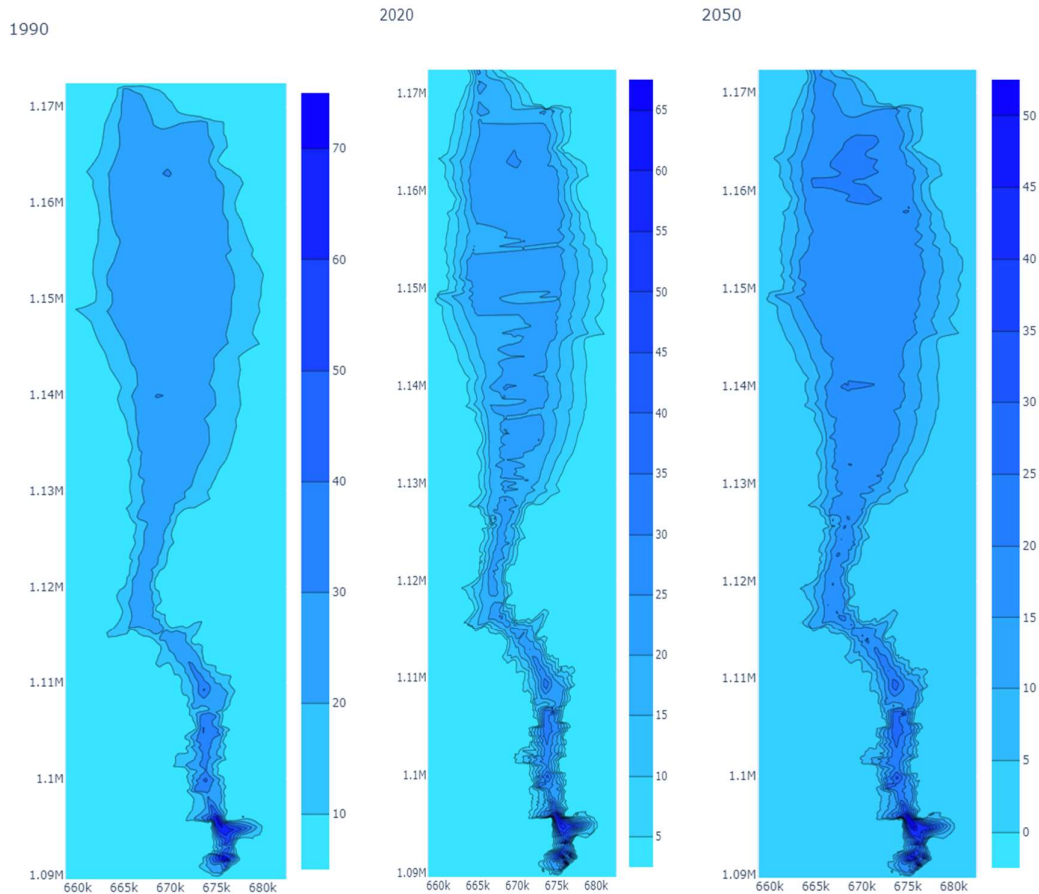


Figure 4:17 CA-GBR historical, measured and forecasted plots. The vertical scale is in meter (m). The projected surface is without artifacts, indicating that CA-GBR is most suitable for predicting future bathymetric data that are affected by sedimentation and siltation. Source: Research lab

Additionally, the CA-GBR predicted depths are in agreement with those forecasted by the CA-Markov chain, but the only challenge with the CA-Markov chain is the artifacts introduced on the surface. The anticipated loss in reservoir depths is realistic due to the multiple river systems that recharge the basin, with the major river being the Niger River. Additionally, the predicted bathymetric map of 2050 from CA-GBR is visually unique and depicts the depth loss from sedimentation. The negative impacts of sedimentation are exacerbated by global changes brought on by a rapidly growing population and increased vulnerability to severe climate conditions, which aggravates soil erosion predominantly from uphill to the reservoir basin (UNESDOC-ISI, 2009).

4.4 Summary

The results and analysis addressing objectives one to three are presented in this chapter. The results and discussion addressing objective one were first presented. The results revealed that sedimentation is exacerbating a greater danger to the reservoir functionality. The present-day reservoir bathymetric stand-alone information system of the reservoir was developed and presented. The profiles and cross-sections of selected sections were plotted from both historical and recent data (1990 and 2020) to show the change over time. The results show that the reservoir has lost a greater percentage of its volumetric capacity to sedimentation over the last 30 years. The low-frequency data revealed that the reservoir had lost 15.7% of its maximum construction depth to sedimentation over the past 52 years. The research also shows that the reservoir has depreciated in volume by 18.6% from 1990 to 2020, and 30% has been a loss from 1968 to 2020 due to sedimentation. However, the reservoir experienced an increase in area by 0.2%. The estimated sediment thickness computed was $2.67 \times 10^9 m^3$ with a long-term annual average sediment flux of $5.16 \times 10^7 m^3/y$. This suggests that the reservoir has experienced a 0.5% loss annually over the last 52 years. Additionally, the digital depth model of the study area was modelled from both datasets depicting the change in the three-dimensional surface.

Furthermore, this research predicted the bottom surface of the studied area of the Kainji reservoir by two methods, Markov chain and gradient boosting regression; both methods were used in conjunction with cellular automata, based on objectives two and three of this research. The proven techniques for analysing spatial data, such as the Markov Chain and Cellular Automata, best suited for analysing categorical transition data, show some deficiency “artifacts” in the generated map. Additionally, the research uses its model explicitly designed to analyse continuous bathymetric data, the “Cellular Automata and Gradient Boosting Regression model”. The CA-GBR model, in the research opinion, is more suitable for predicting continuous-discrete data such as depth. The results from the CA-Markov process have some artefacts, while the predicted bathymetric surface from CA-GBR is impressive. Despite the setback from the CA-Markov process, both models cope with determining the trend of surface changes with almost similar depth distributions. In addition, the research projected surface is in agreement with the [International Sediment Initiative \(2011\)](#), which says that by 2050, most reservoirs will lose more than 50% of their

designed capacity to sedimentation if left on check. The writer concluded that major dams would not adequately serve their purpose of construction within the projected period.

Furthermore, the next chapter presents and discusses the results obtained from identifying the scientific contribution to the high sedimentation rate in the study area based on objective four of this project. Additionally, assessing the possibility of flooding due to sediment aggregation at the reservoir embankment is a potential risk to people and structures along the reservoir axis and downstream. Hence, the next chapter addresses objective four of this research: *investigating the scientific contribution to sedimentation and modelling the possible flood impact to the study area.*

5 CHAPTER FIVE: Result and Analysis (Objective Four)

5.1 Introduction

This section presents the results and analysis based on objective four of this thesis. The object of the objective is to investigate the scientific contribution to sediment deposits from drainage and catchment area analysis and model the flood scenario. Hence, the result and analysis of land use and land cover classification (LULC) of 1990, 2005, and 2020 and how the changes propagate sediment erosion into the reservoir are discussed. The catchment area, drainage pattern, and sediment contribution results were presented and analysed. In addition, the universal soil loss equation (USLE) was employed to assess the rate and estimate of soil deposits in the study area. The result of the flood scenario impacts was also presented.

5.1.1 Land Use Land Cover Classification Scheme of Kainji Reservoir and Environs

The alteration of Earth's terrestrial surface by human activities, either coordinated or uncoordinated, is termed land use/land cover change (LULCC) worldwide ([Dwivedi et al., 2005](#)). The extent, intensity and degree of LULCC are advancing exponentially due to the increase in the global population and the need for human development. These changes are experienced at the local, regional and international scales, and they are the driving forces for unprecedented changes within ecosystems and environmental processes ([Hassan et al., 2016](#)). Figure 5.1 shows the land use/land cover changes of the Kainji Reservoir and the environment. Table 5.1 describes the changes that have occurred over the period of 30 years to date. Additionally, Table 5.2 presents a summary of the changes that have occurred based on Table 5.1.

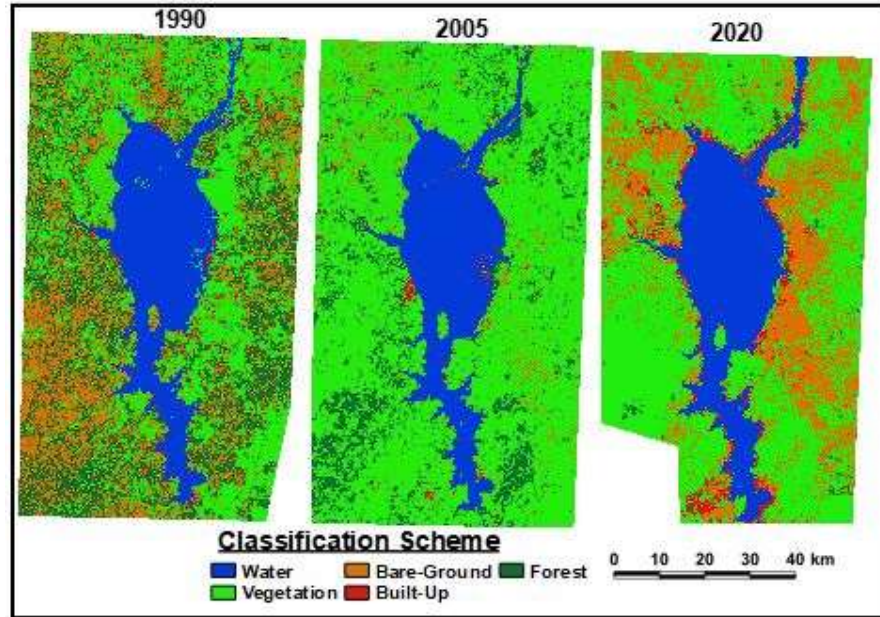


Figure 5:1 Land use land cover (LULC) maps of Kainji Reservoir and environs from three epoch datasets “1990, 2005, and 2020”. Source: Research lab

Table 5:1 Area statistics of LULCC conversions (1990 – 2005, 2005 – 2020). This shows the land use land cover area changes over the period under investigation. The dash sign (–) indicates the transition from one class to another e.g. Bare ground to built up or water to water etc. Source: Research lab

S/N	Change (1990-2005)	Area (Sq K)	S/N	Change (2005-2020)	Area (Sq K)
1	Bare ground – Bare ground	21.671	1	Bare ground – Bare ground	103.699
2	Bare ground – Built up	10.043	2	Bare ground – Built up	8.006
3	Bare ground – Forest	254.952	3	Bare ground – Forest	0.926
4	Bare ground – Vegetation	1217.305	4	Bare ground – Vegetation	33.026
5	Bare-Ground – Water	0.319	5	Bare ground – Water	0.016
6	Built up – Bare ground	8.600	6	Built up – Bare ground	31.404
7	Built up – Built up	16.785	7	Built up – Built up	23.006
8	Built up – Forest	29.586	8	Built up – Forest	1.082
9	Built up – Vegetation	135.848	9	Built up – Vegetation	29.820
10	Built up – Water	4.102	10	Built up – Water	24.847
11	Forest – Bare ground	31.681	11	Forest – Bare ground	121.825
12	Forest – Built up	23.606	12	Forest – Built up	34.988
13	Forest – Forest	382.885	13	Forest – Forest	19.981
14	Forest – Vegetation	1427.883	14	Forest – Vegetation	464.533
15	Forest – Water	0.296	15	Forest – Water	29.581
16	Vegetation – Bare ground	81.425	16	Vegetation – Bare ground	1310.304
17	Vegetation – Built up	42.240	17	Vegetation – Built up	203.636
18	Vegetation – Forest	179.403	18	Vegetation – Forest	49.544
19	Vegetation – Vegetation	1914.126	19	Vegetation – Vegetation v	2838.736
20	Vegetation – Water	15.194	20	Vegetation – Water	26.986

Table 5.1 Continue

21	Water – Bare ground	0.016	21	Water – Bare ground	0.005
22	Water – Built up	19.319	22	Water – Built up	0.426
23	Water – Forest	0.221	23	Water – Forest	0.010727
24	Water – Vegetation	2.676	24	Water – Vegetation	2.540
25	Water – Water	1038.999	25	Water – Water	1055.777

Table 5.2: Summary of LULCC area statistics and percentage units of 1990 – 2005 and 2005 – 2020. The signs (+/-) indicate loss or gain between the classification scheme of the epoch datasets. Source: Research lab

LULC classification scheme	1990		2005		1990 – 2005	
	Area (km ²)	Area (%)	Area (km ²)	Area (%)	Changed Area (%)	Annual Changed (%)
Water	1090.94	17.4	1056.29	16.7	0.7	0.05
Vegetation	2010.1	32.1	4242.86	67.2	-35.1	-2.34
Bare – ground	1332.39	21.3	135.82	2.2	19.1	1.27
Built – Up	189.17	3.1	114.48	1.8	1.3	0.09
Forest	1633.03	26.1	762.47	12.1	14	0.93
	2005		2020		2005 – 2020	
	Area (km ²)	Area (%)	Area (km ²)	Area (%)	Changed Area (%)	Annual Changed (%)
Water	1056.29	16.7	1130.24	19.3	-2.6	-0.17
Vegetation	4242.86	67.2	2967.39	50.6	16.6	1.11
Bare – ground	135.82	2.2	1430.87	24.5	-22.3	-1.49
Built – Up	114.48	1.8	260.46	4.5	-2.7	-0.18
Forest	762.47	12.1	63.18	1.1	11	0.73

The results of the land use/land cover changes plots are shown in Figure 5.1, and the total map accuracy obtained is 89.6% by using the pixel and polygon from the imagery against the ground reference data “this is the best approach for evaluating LCLCC (Lu and Weng, 2004). The computed kappa statistics/index to measure the accuracy of the results of each data point is approximately 0.92. Kappa statistics measure of the accuracy of 0.75 is adequate for further analysis and change detection (Lea and Curtis, 2010).

The average land area, including the reservoir area used for this research, is 6139.90 km²; meanwhile, the total areas for 1990, 2005, and 2020 are 6255.63, 6311.92 and 5852.14 km², respectively. The percentage area of each category shows that vegetation has the largest share of each class of the three datasets of 32.1%, 67.2% and 50.6%, i.e., 2008.06, 4241.61, 2961.18 km² respectively. The increase in vegetation from 32.1% to 67.2% from the year 1990 to 2005, is due to the period of satellite pass and when the datasets were downloaded. Also, because the Nigeria weather consist of two major seasons that is dry

and raining seasons. Hence, this class faced a 16.6% (704.32 km^2) reduction in 2020. The other class that faced a decline within the consideration period was the forest class, which decreased from 26.1% (1633.03 km^2) in 1990 to 1.1% (63.18 km^2) in 2020, which was 25% (1569.85 km^2) within the period of 31 years. The loss in forest resulted in increased vegetation and bare ground in 2020. The bare ground decreased from 21.3% in 1990 to 2.2% in 2005 and then skyrocketed in 2020 by 22.3% (1295.05 km^2). The reduction in forest and increase in bare ground is caused by the uncontrollable deforestation that is ongoing in Niger state, which made the state government enacted a law that prohibits unnecessary falling down of trees in recent years.

Furthermore, the increase in bare ground due to some anthropogenic activities exposed the land area to erosion. All soil possesses a certain resistivity to erosion, and this resistivity may be enhanced greatly by vegetable cover, especially good grass sods. The underlying soil may have a much smaller resistivity to erosion, and if the surface conditions are altered by cultivation or otherwise destroy the surface resistance, erosion will begin on land that has not hitherto been subject to erosion (Horton, 1945a). Hence, the increase in bare-ground and built-up areas propagated soil erosion rates into the adjoining river and the Kainji reservoir trapping plate. This is evident from the sediment deposit computed from bathymetric observations, as shown in Figure 4.8, Figure 4.9 and Table 4.1. Additionally, there was a significant change in water class from the three epochs of data; this class experienced a 0.7% (34.65 km^2) decline in 2005 from 1990 and faced an increase of 2.6% (73.95 km^2) in 2020.

This section of this research revealed a more significant reduction in forest and vegetation class of the study area, and there was a sporadic increase in bare-ground and built-up regions, which dramatically affected the resistivity of the soil, making the area prone to erosion. There is no doubt that bulky material is deposited in the Kainji reservoir. Karami et al. (2018), collaborated that the principal causes of sediment erosion of the topsoil to a basin are anthropogenic activities such as deforestation and overgrazing and, by extension, natural changes aggravated by the dynamic nature of climate and environmental occurrences.

5.1.2 Drainage Network and Catchment Area Analysis of Kainji Reservoir

Morphometric analysis is a mathematical approach to determining and presenting basin information to understand the aspect and characteristics of the drainage system relative to the catchment area (Strahler, 1964; Clarke, 1996; Markose et al., 2014). The major information that best describes the geomorphology of any reservoir drainage basin and its stream channel is information derived from the linear aspects of the drainage network, aerial aspects of the drainage basin and relief (topography) aspects of the stream network (Strahler, 1964). Hence, this section presents the results and discussion of morphometric analysis of Kainji Reservoir and environs conducted with parameters such as stream order, stream length, bifurcation ratio, basin perimeter, basin area and length, catchment area, form factor ratio, texture ratio, concentration-time, maximum and minimum relief, ruggedness number, etc. Consequently, Figure 5.2(a) describes the stream networks superimposed on the elevation map, and Figure 5.2(b) shows the aspect in degree of Kainji reservoir. Figure 5.3(a) shows the flow accumulation superimposed on drainage basins, and Figure 5.3(b) describes the stream junctions and 2020 bathymetric map. Table 5.3 to Table 5.5 present the reservoir morphometric parameter outputs computed based on Table 3.10.

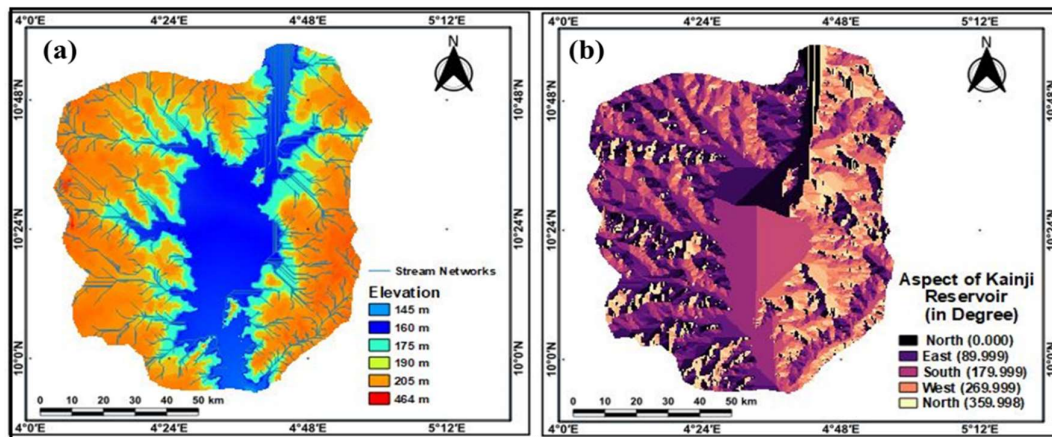


Figure 5.2 Stream network superimposed on the elevation map (a) and aspect in degree of Kainji reservoir (b). Source: Research lap

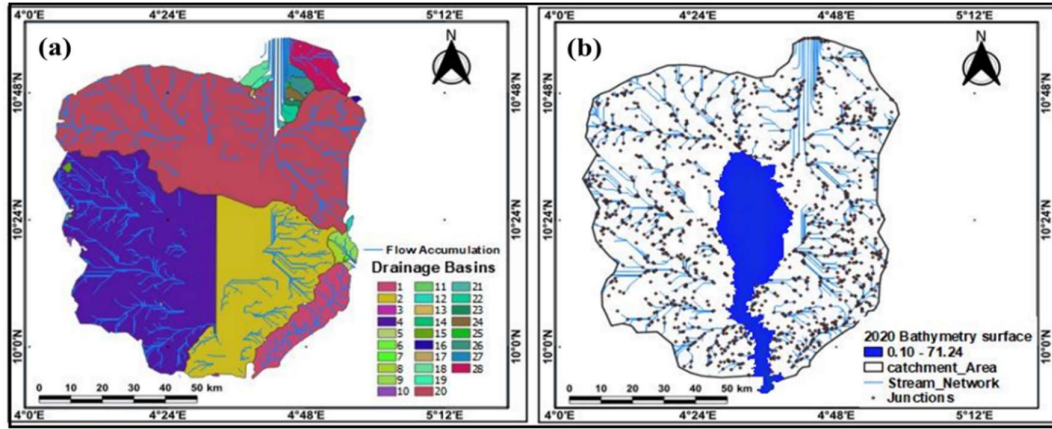


Figure 5:3 Flow accumulation superimposed on drainage basins (a), stream junctions and 2020 bathymetric map (b). Source: Research lab

Table 5:2 Linear Aspects of the Kainji Reservoir catchment (Source: Research lab)

Stream order	Stream number (Nu)	Total Stream Number	Stream length Lu (km)	Total stream Length (km)	Mean stream length (km) Lsm	Stream length ratio (Lur)	Bifurcation ratio (Rb)	Mean bifurcation ratio (Rbm)	Rho coefficient
I	670		2105.4		3.14				
II	369		1032.5		2.78	0.49	1.82		0.269
III	174	1383	444.6	4053.04	2.56	0.43	2.12	3.06	0.203
IV	142		313.1		2.20	0.70	1.23		0.569
V	22		126.4		5.75	0.40	6.46		0.062
VI	6		31.04		5.17	0.25	3.67		0.068

Table 5:3 Aerial aspect of the Kainji reservoir catchment (Source: Research lab)

P (km)	Lb km	A (km ²)	Rf	Re	Rc	Dt	Sf	Pr	Cc	Rf
3473.02	98.23	4787.71	0.50	0.80	0.01	0.40	2.02	1.38	14.16	0.03

Basin perimeter (P), Basin length (Lb), Basin area (A), Form factor ratio (Rf), Elongation ratio (Re), Circulatory ratio (Rc), Drainage Texture (Dt), Shape factor ratio (Sf), Relative perimeter (Pr), Compactness coefficient (Cc), Fitness ratio (Rf).

Table 5:4 Drainage texture of the Kainji reservoir catchment (Source: Research lab)

Drainage density (Dd) (km/km ²)	Stream frequency (Sf)	Constant of channel maintenance (C) km	Concentration time t _{ch} (minutes)	Infiltration number (If)	Length of overland flow (Lg) km
0.85	0.29	47.62	Max. = 562.6 Min. = 7.02	0.25	0.59

Table 5:5 Relief aspect of the Kainji reservoir catchment (Source: Research lab)

Z (m)	z (m)	H (m)	Rr	Rhp	Rg	Rn	MRn
464.02	145.08	318.94	3.25	0.01	3.24	0.27	4.61

Max. basin height (Z), min. basin height (z), basin relief (H), relief ratio (Rr), relative relief ratio (Rhp), gradient ratio (Rg), ruggedness number (Rn), and Melton ruggedness number (MRn).

5.1.3 Linear Aspects of Kainji Reservoir Catchment

The linear aspects of the basins relate to the channel patterns connecting the drainage network, and the topographic characteristics of the stream junctions are analysed (Strahler, 1964). Hence, the following linear aspects results are discussed based on Table 5.3:

- i) *Stream order (Nu) and stream number*: The flow accumulation and stream order of Kainji Basin were determined at a threshold of 5 using the DEM, as shown in Figure 3.3(a), employing the Strahler (1964) model. A total of 6 stream orders were identified, of which 670 are first order, 369 are second-order, 174 are third order, 142 are fourth-order, 22 are fifth-order, and 6 are sixth order (see Table 5.3). The total stream number is 1383, contributing to the Kainji Reservoir, with river Niger as the major contributor.
- ii) *Stream length (Lu)*: The stream length is a major hydrological component of any basin that describes the surface runoff characteristics from the source to the outlet. The total estimated stream length is 4053.04 km, of which 2105.04 km first order, 1032.5 km second order, 444.6 km third order, 313.1 km fourth-order, 126.4 fifth-order, and 31.4 km sixth-order (see Table 5.3). The mean stream length and the stream length ratio are also presented.
- iii) *Bifurcation ratio (Rb)*: Rb is the ratio between the number of streams in one order and the next order. It is achieved by dividing the number of streams in the low order by the number in the higher orders. Low Rb shows that drainage is affected by geological structures; in contrast, high Rb indicates that the drainage pattern is influenced by geologic structures (Rai et al., 2017). The computed Rb of the Kainji reservoir ranges between 1.23 and 6.46, with a mean Rb of 3.06 (Table 5.3). However, the Rb of natural drainage systems lies between 3.0 and 5.0 (Strahler, 1964; Verstappen 1983). The estimated Kainji reservoir catchment Rb indicates that the basin has a dual Rb pattern, which suggests that the geologic structure

- iv) obstructs some stream networks and that others do not depend on the area (Figure 5.3(a), (b)).
- v) *Rho coefficient*: is the stream length divided by the bifurcation ratio (R_b). The Rho values computed for the Kainji reservoir range from 0.062 to 0.569 (Table 5.3).

5.1.4 Aerial Aspect of Kainji Reservoir Catchment

The aerial aspects of a drainage morphology describe the arrangement of area elements such as the basin perimeter, basin shape (outline form), basin area, shape factor ratio, etc. The computed aerial aspects of the Kainji Basin and the environment are:

- i) *Basin area (A)*: The basin area is an important component of drainage basin analysis, similar to other geomorphology parameters. The total basin area estimated for the study area is 4787.71 km^2 (Table 5.4).
- ii) *Basin Perimeter (P)*: The Kainji Reservoir catchment perimeter was computed using QGIS 3.16 software; the basin perimeter was 3473.02 km.
- iii) *Basin Length (Lb)*: The basin length morphometric parameter of a drainage basin is the length in a straight line from the mouth of the stream to the farthest point of the drainage divide of its basin (Schumm, 1956). The Lb estimated is 98.23 km (Table 5.4).
- iv) *Form factor ratio (Rf)*: Horton (1932) describes the form factor as the basin area (A) divided by the square of the basin length (Lb); the estimated form factor ratio of the Kainji Reservoir catchment is 0.50, which shows the flow intensity of a basin of a defined area (Horton, 1945). The value should always be less than 0.7854, which is the value corresponding to a perfectly circular basin (Waikar and Aditya, 2014). This suggests that the form factor ratio of the Kainji drainage basin is perfect.
- v) *Elongation ratio (Re)*: the ratio of the diameter of a circle having the same area as the basin and the maximum basin length (Schumm, 1956). The elongation ratio describes the shape of the catchment and is classified based on their values, e.g., elongated (0.5 – 0.7), less elongated (0.7 – 0.8), more elongated (< 0.5), oval (0.8 – 0.9), and circular (0.9 – 1). Again, this suggests that the Re of Kainji drainage is less elongated (Table 5.4).

- vi) *Drainage texture ratio (T)*: drainage texture is the total number of streams in all stream orders divided by the perimeter of the basin (Horton, 1945a). The drainage texture of the Kainji basin falls in a very coarse category (< 2). Smith (1950) categorized drainage texture into five sections: very coarse (< 2), coarse (2 – 4), moderate (4 – 6), fine (6 – 8) and very fine (> 8).
- vii) *Circularity ratio (Rc)*: circularity ratios range from 0.4 to 0.5 (Miller, 1953). Rc is influenced by the frequency and length of streams, land use and land cover, geological structures, climate, relief and slope of the catchment. The Rc of the Kainji Reservoir basin of 0.01 shows that the basin is not circular, whereas the 28 subcatchments (Figure 5.3(a)) have values ranging from 0.04 to 0.12.
- viii) *Shape factor ratio (Sf)*: The shape factor is the ratio between the mainstream length and the basin area's square root. The computed Sf is 2.02 (Table 5.4). This factor indicates the flow intensity of a basin of a defined area (Horton, 1945a). The high form factors of the Kainji reservoir basin show high peak flows of shorter duration. An elongated subbasin with a low form of 0.25 indicates a slightly elongated shape and lower peak flows for a longer period (Nautiyal, 1994).
- ix) *Relative perimeter (Pr)*: the relative perimeter is the basin area divided by its perimeter (Schumm, 1956). The estimated Pr of the study area is 1.38.
- x) *Compactness coefficient (Cc)*: The compactness coefficient (Cc) shows the relationship between the hydrologic basin and circular basin (Iqbal et al., 2013). The computed Cc of the subcatchment ranges from 0.65 to 4.6, and the overall value of the Kainji Reservoir catchment is 14.16
- xi) *Fitness ratio (Rf)*: The fitness ratio is the ratio of the mainstream length to the length of the basin perimeter, which describes the topographic fitness (Melton, 1957). The fitness ratio of the study area is 0.03.

5.1.5 Drainage Texture of Kainji Reservoir Catchment

- i) *Drainage density (D_d)*: the drainage density (D_d) describes the closeness or spacing of streams (Horton, 1932). The importance of drainage density is that it determines the travel time of water (Schumm, 1956). The Kainji Reservoir basin drainage density is moderate (0.85 km/km²). However, it varies with climate and vegetation, rock properties, soil, relief, landscape, and evolution (Kelson and Wells, 1989; Oguchi, 1997).

-
- ii) *Stream frequency (Sf)*: the total number of stream segments within a basin per unit area (Horton, 1945a). The Sf of the whole basin is 0.29 (Table 5.4); it depends on the lithology of the basin.
 - iii) *Concentration time t_{ch}* : This describes the time needed for water to flow from the most remote area to the catchment outlet (Haan et al., 1994). This factor depends on the catchment's topography, geology, and land use. The maximum and minimum t_{ch} estimated are 562.6 and 7.02 minutes, respectively.
 - iv) *Infiltration number (If)*: infiltration number is the product of drainage density and stream frequency, and it shows the infiltration capability of a catchment (Faniran, 1968). The infiltration value of the Kainji Reservoir drainage basin is 0.25. It is mainly affected by the type of vegetation within the catchment.
 - v) *Length of overland flow (Lg)*: length of overland flow is the inverse of drainage density. It refers to the length of water flow over the ground before it becomes concentrated into the mainstream, affecting the drainage basin's hydrology and physiographic development (Horton, 1945a; Soni, 2017). When the soil can no longer hold the excess rainfall water, it flows over the land surface as overland flow (Suresh, 2017). The morphometric parameter depends on the permeability, climatic regime, rock type, vegetation cover and relief (Schumm, 1956). The Lg of the study area basin is 0.59 (Table 5.4). This means that the area is influenced by high structural disturbance, low permeability, steep to very steep slopes and high surface runoff.

5.1.6 Relief Aspect of Kainji Reservoir Catchment

The relief aspect of a basin describes the vertical spatial attributes of a drainage basin (Figure 5.3a). The following relief aspects of the study area are discussed:

- i) *Basin relief (R)* is the vertical change depicting the lowest and highest points in a basin. The relief properties of a basin determine the stream gradient and influence flood patterns and sediment volumes that can be transported (Hadley and Schumm, 1961). It describes in detail the denudation characteristics of the basin (Sreedevi et al., 2009). The maximum and minimum height values of the study area from the DEM are 464.02 and 145.08 meters, respectively (Table 5.5 and Figure 5.3a).

- ii) *Relief ratio (Rr)*: The relief ratio is a dimensionless ratio of basin relief and basin length and describes the gradient aspects of the catchment (Schumm, 1965). It points at the overall steepness of a drainage basin and is an indicator of the intensity of erosion processes operating on the slopes of the basin (Javed et al., 2009). The Rr value of the Kainji catchment is 3.25, and the value is high, suggesting a steep slope within the catchment.
- iii) *Ruggedness number (Rn)*: The dimensionless ruggedness number is the product of basin relief and drainage density (Strahler, 1952). It shows the level of surface unevenness (Selvan et al., 2011). The ruggedness number of the Kainji Reservoir catchment is 0.27, which is relatively low and suggests that it is less prone to soil erosion and has intrinsic structural complexity with relief and drainage density (Paretha and Paretha, 2011).
- iv) *Melton ruggedness (MRn)*: it is a slope index that gives a specialized representation of relief ruggedness within the catchment (Melton, 1965). The MRn of the Kainji reservoir basin is 4.61, which signifies a high flow in the mainstream with more debris flow.

5.2 Universal Soil Loss Equation Model of the Kainji Reservoir Catchment

Estimating soil loss through rainfall is vital to understanding the severity of soil loss via rill and sheet erosion within catchment areas and how the final deposited sediment is trapped in the reservoir. The result of the Universal Soil Loss Equation model shows that rill and sheet erosion are the predominant morphological operations of sediment erosion and transport within the catchment area. Figure 5.4a and Figure 5.4b describe the study area's slope steepness in degree and percent; Table 5.6 shows the computed parameters used for the USLE model and the amount of soil loss based on the input values.

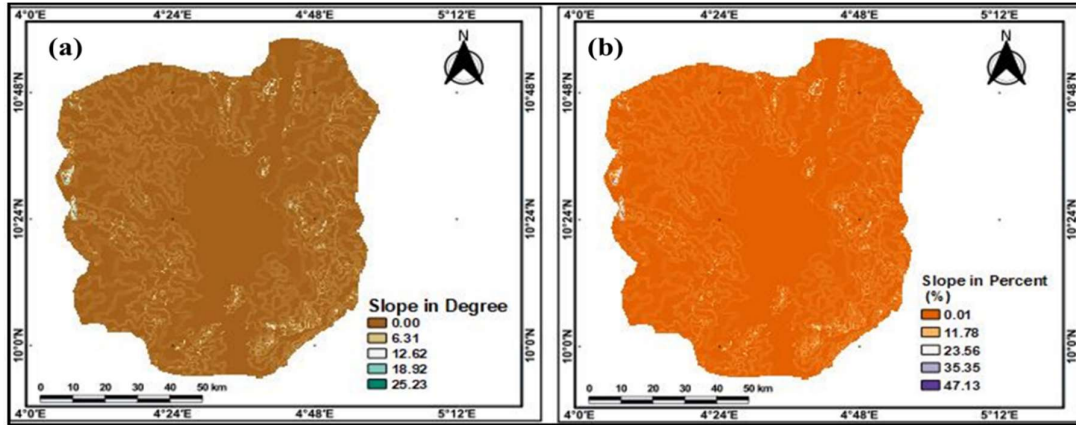


Figure 5:4 Slope steepness in degree (a) and slope steepness in percent (b).
Source: Research lab

Table 5:6 USLE model results of the Kainji reservoir and catchment

Slope interval (degrees)	>10	5 to 10	3 to 5	1 to 3	< 1
Percentage slope (percent)	47.12	18.73	11.78	4.62	0.79
Average slope length (m)	1,682	2,104	1,365	3,406	1,263
LS factor	146	31.36	5.20	4.53	2.25
Area (km^2)	136	684	676	622	1,239
Sediment estimated (tons/acre/year)	1,132.64	243.29	90.43	35.14	17.46
Annual load (tons)	38,063,839.63	41,120,875.8	15,105,698.49	5,401,018	5,345,616.46

Furthermore, the USLE predicted that slopes greater than five (5) degrees would yield approximately 90% of the sediment in the Kainji reservoir from the catchment. Slopes with values less than five (gentle slope) have the major slope lengths (Figure 5.4) but made no important contribution to the entire sediment load determined (Table 5.6). Additionally, the amount of eroded sediment depends on the value of the slope lengths and steepness factors (LS). Hence, the higher the LS, the better the computed soil deposited vis-à-vis. Another factor that shifts the amount of runoff material to the rise is the rainfall erosivity index (R) “if the intensity of R is high, the material flooded will be greater”. The annual soil loss load is 1.06 times (105037048.38 tons) the computed annual sediment flux estimated for the Kainji Reservoir (99175200 tons), assuming that the density of wet sand is 1922 kg/m^3 derived from division by the reservoir age.

Similarly, the difference between the computed annual sediment deposits of the USLE and the low-frequency echosounder of 5.6% shows that the results are reliable and that the USLE can be used to validate the amount of sediment measured in a reservoir using low-frequency pulse data. However, this does not mean that both results will be equal arithmetically, but the difference should not be too wide. Additionally, errors in the USLE model can occur because some eroded sediment may be trapped and stored within significant intervals considering the channel lengths and low gradient slopes before transporting to the reservoir. This has again shown that sedimentation is a greater menace affecting the optimization of the reservoir, which will cause a disaster at no distance. The next section addresses the flood vulnerability assessment of the study area.

5.3 Flood Vulnerability Impact Assessment

The repercussions of flooding are usually related to structural assets; however, the concept of vulnerability consists of human and capital assets exposed to the menace of flooding at any occurrence. There is no specific model for assessing flood risk; instead, each reservoir that poses a threat is estimated based on the range of environmental parameters characterizing the predicting dam failure (Danso – Amoaka et al., 2012). A holistic dam failure can be predicted when the mean flooding depth and managed maximum flood water volume can be determined or the catchment morphological variable parameters are known (Scholz and Yang, 2010; Danso – Amoako et al., 2012). Flood risk assessment contains various uncertainties; some authors have demonstrated that validation in real-life cases yields conflicting results (Jongman et al., 2012b). However, some welcoming results have been documented (Aerts et al., 2014). Consequently, Figure 5.5 shows the modeled flood impact map of the Kainji reservoir based on predicting flood level employing both DEM and bathymetric datasets, and Table 5.7 presents the towns that are projected to be in danger based on the classified classes of vulnerability.

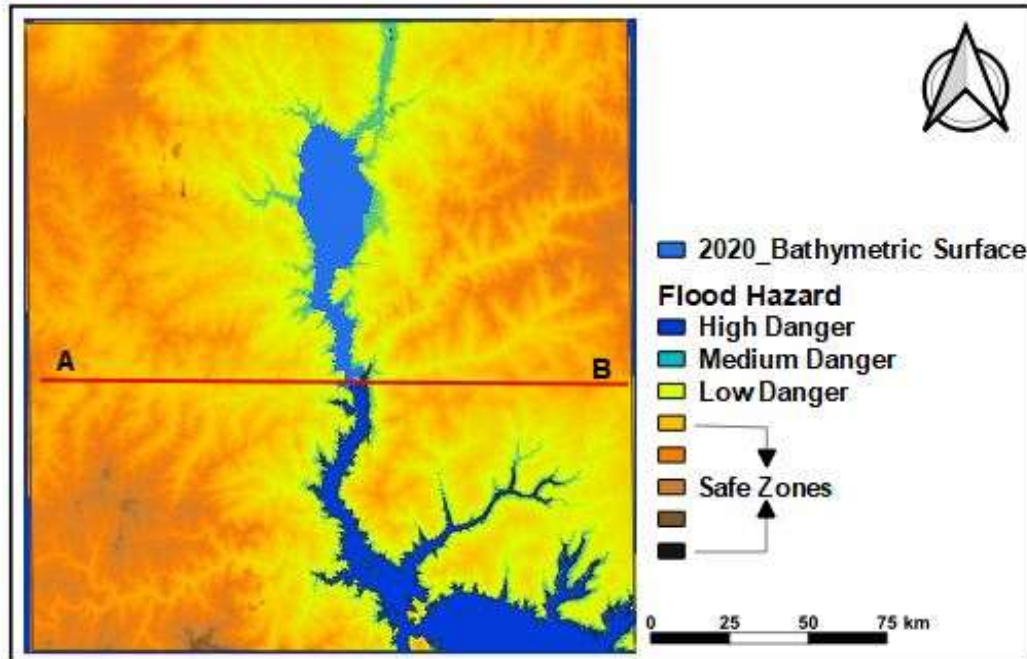


Figure 5:5 Flood impact map of potential Kainji dam failure. The broad spectrum predicted flood map indicates the spatial extents that are expected to inundate in the event of dam failure. The different hues buffer lines show the flood risk vulnerability class and extent. A to B is the line cutting across the Reservoir axis. Source: Research lap.

Table 5:7 Flood risk vulnerability class and towns. Source: Research lab.

Flood risk class	Town at risk
High danger	Kpatchi, Faku, Falla, Awuru Emigi, Awuru, Chegu, Sabon Leaba, Shankadadle, Yankade, Bajibo, Fort Goldie, Sungogi, Gungiborku, Bukah, Karo, Kalama, Mokwa, Dana, and the towns down the river bank.
Medium danger	Moro, Edu, Gbaki, Chizi, Tifi, Fellagi, Kwaroin
Low danger	Bitogi, Kwali, Efuwagi, Patiko, Kanti, Borgu, Tabioloko, Gata, Biribiri
Safe zones	Mogu, Konkon, Kudu, Eban

The A to B of Figure 5.5 upstream represents the reservoir area and catchment, while the downstream of the dam shows the region of flood risk and safe zone as modelled. The flood vulnerability region is categorized as high danger, medium danger, low danger, and safe zones. The total area in high danger is 108.4 km^2 and is highly vulnerable when flooded. The towns that fall within this region are Kpatchi to Dana (Table 5.7) and the villages along the river bank. This means that the Jeba dam downstream will be entirely submerged with water, which will be a greater loss to the people and the government in general. The prediction shows that any region below the elevation of 133 m (i.e.,

approximately 8 m below the hydraulic level of the reservoir) above mean sea level will be flooded with a water depth of approximately 3 m to 4 m. However, this water depth reduces as the water travels continuously to approximately 0.5 m farther away from the reservoir axis. Meanwhile, flood damage depends largely on the water depth, current and the type of structures and people existing within the flooding domain (Merz et al., 2004). In the event of the reservoir (Kainji reservoir) structural failure due to sediment load at the embankment, greater damage will be meted on the settlers downstream because the lower dam accommodates a greater percentage of dwellers around that region. This is because farming and fishing are their dominant occupations due to the fertile soil with vast landmasses.

Furthermore, to hint at the weight of sediment load on the Kainji reservoir embankment, it was reported on 14th September 2020 by *“THISDAY news outlet that “The collapse of the embankment of the Kainji dam followed the opening of the four spillway gates of the facility to throw out surplus water as a result of heavy rains. THISDAY learned that the incident occurred on Sunday after the management of the dam, Mainstream Energy Solution Limited, decided to open the spillway gates when it was discovered that the dam was impounding more water than it could impound. “We opened the 4 spillway gates because of the pressure of water. Now, it is hitting the embankment. If the embankment is not reinforced, it will continue to hit the ground directly”. It will continue to expand and get deeper,” a top official of the firm confided in THISDAY. “The embankment of the dam is falling, rocks are falling into the water,” the official said. THISDAY further learned that there is no immediate threat to the dam but that if the water spilling out is not checked, it could affect the safety office of the company because the facility is wrongly positioned. It was further learned that the latest development was not the first time, as a source said “it is a periodic happening, I don’t know why they have not corrected the situation.” A source at the palace of the Emir of Borgu also confirmed the incident saying “one side of the embankment of the dam broke away”.* Consequently, this shows that Kainji Reservoir present conditions are a disaster in waiting.

5.4 Summary

This chapter presents the results based on objective four of this research “To investigate the scientific contribution to sedimentation and model the flood scenario of Kainji reservoir”. In totality, the results of four investigations were presented, i.e.;

First, the land use/land cover classification scheme was used to check the land-use pattern changes over the period of 30 years (1990 to 2020). Three Landsat epoch datasets off 1990, 2005 and 2020 were used considering five classes of water, bare-ground, forest, vegetation and built-up. The results show that forest and vegetation lost a greater percentage of area to bare ground within the past 30 years due to deforestation, which further exposed the soil to erosion. The eroded sediment finds there way into the reservoir in the long run.

Second, drainage network and catchment area analyses of the study area were conducted. The outcome shows that there is a mass movement of sediment from the channel networks to the main basin; this is demonstrated from the stream network analysis. The morphological parameters of the study area suggest that the area has steep slopes, which encourage soil erosion to a greater extent.

Third, the Universal Soil Loss Equation (USLE) model was used to model and estimate the soil loss within the study area catchment. The USLE outcome indicates that there is a high rate of soil loss in the reservoir basins. The annual sediment loss from USLE is 5.6% tons greater than the estimated annual sediment flux using a low-frequency echosounder. The small change in USLE and low-frequency data approaches shows that the USLE approach is reliable and can be used to validate sediment volume deposits from low-frequency pulses.

Finally, the flood risk vulnerability map was generated, indicating the hazardous area in the case of dam failure. In the event of dam failure, all towns within the river corridor and an average of 1.5 km away from the river centreline will be submerged in water. The accurate long-run danger assessment in the case of a flood is only visible after flooding. A total extent of 108.6 km^2 will be submerged in water with a water depth ranging from 3 m to 0.5 m. However, the water current, water depth, people and structure types will determine the degree of disaster that is awaiting Kainji and environs in the event of dam failure if the necessary precaution is not taken.

In addition, this study has further exposed the menace of sedimentation and siltation on the Kainji reservoir and environs, pointing at pending danger. This is also a clarion call in support of the statement that by 2030, 50% of the world's population will be exposed to flooding, storms and tsunamis ([Antonio Guterres, UN chief: 2021](#)).

6 CHAPTER SIX: Conclusion and Future Outlook of the Research

6.1 Conclusion

Sediment deposits in reservoirs have been identified as the major challenge that limits the storage capacity of basins globally. The sedimentation process is more dynamic considering the large extent of the catchment area, and in most cases, the receiver is connected with a major river. In this study, the main river is the Niger river, which constantly contributes water to the Kainji reservoir. The transported water from upstream to the basin carries sediment along and is suspended in the main basin. Thus, quantifying the amount of sediment deposited in a reservoir is adequately determined via a bathymetry survey using a dual frequency sounder. In this case, high- and low-frequency pulses are needed; the difference between the high- and low-frequency acquired datasets gives the total deposited lacustrine sediment for the period in study. To this end, dual frequency echosounders were used to conduct sounding operations of the Kainji reservoir to estimate the amount of deposited lacustrine sediment over 52 years. A second bathymetric dataset of 1990 from a high-frequency echosounder was used to estimate the reservoir storage capacity loss due to sediment from the high-frequency dataset of 2020. Furthermore, this research was formulated to address the four objectives and approached in two phases, with each phase addressing a specific objective.

The first phase was designed to achieve objectives 1 to 3 which are; firstly, designed and executing an underwater topographic profile survey, producing a bathymetric chart and 3 – D models of the study area for ease assessments; secondly, carried out sediment deposit analysis of the study area and forecasting by the use of a cellular automata – Markov chain; thirdly, employing cellular automata and gradient boosting regression models to measure the accuracy of objective 2 (carried out sediment deposit analysis of the study area and forecasting by the use of a cellular automata – Markov chain). Based on objective 1 (To design and execute an underwater topographic profile survey, produce a bathymetric chart and 3-D models of the dam for ease of assessment), the research review shows that the reservoir has lost a greater percentage of its volumetric capacity to sedimentation over the last 30 years considering 1990 and 2020 datasets. The low-frequency datasets revealed that the reservoir had lost 15.7% of its maximum construction depth to sedimentation over the past 52 years. The study also shows that the reservoir has depreciated in volume by 18.6% from 1990 to 2020, and 30% has been a loss from 1968 to 2020 due to sedimentation.

However, the reservoir experienced an increase in area by 0.2%. The estimated sediment thickness computed was $2.67 \times 10^9 m^3$ with a long-term annual average sediment flux of $5.16 \times 10^7 m^3/y$. The digital depth model maps of the study area were generated from both datasets.

The objective 2 (carried out sediment deposit analysis of the study area and forecasting by the use of a cellular automata – Markov chain) outcome revealed that Cellular Automata – Markov chain models effectively predicted the future reservoir depth pattern for 2050. The transition matrix shows similar results. The lower diagonal has a majority of the high figure, and the upper diagonal has a lower figure, suggesting loss in depth due to sedimentation. However, the projected surface map has some artefacts on it, meaning CA-MC is not a good model for forecasting bathymetric point cloud data. Additionally, the third objective of this research shows that Cellular Automata – Gradient Boosting Regressing perfectly fits the datasets, and the predicted depth surface is without artifacts and follows the sediment regression pattern. This is because the CA – GBR treated the data points individually like a forest, and each point is a tree. CA – MC categorized the bathymetric data into ten classes, making it not fit for such a dataset.

The second phase addresses objective 4 (To investigate the scientific contribution to sediment deposits from river catchment analysis and model flood scenarios of this research) which evaluates and investigates the scientific contribution to sedimentation, conducts catchment area analysis, and models the flood risk vulnerability map in the case of dam failure. Objective 4 was achieved using four (4) stages. First, the land use/land cover classification was used to determine the changes that have taken place in the study area over the past 30 years. Five classes were considered: water, vegetation, bare ground, forest, and built-up. The results revealed that vegetation and forest have lost a greater percentage of their area to bare ground and built up, paving the way for sediment erosion with a larger portion going into the reservoir. Second, drainage network and catchment area analyses were conducted. The results show that the study area has several stream networks, which indicates a mass movement of sediment to the reservoir. Third, USLE was employed to estimate the rate of soil loss to the reservoir. The USLE results indicate that there is a high rate of soil loss from the basins to the reservoir. The annual sediment loss from USLE is 5.6% tons

greater than the estimated annual sediment flux using a low-frequency echosounder. The small change in USLE and low-frequency data approaches shows that the USLE approach is reliable and can be used to validate sediment volume deposits from low-frequency pulses. Finally, the flood risk vulnerability map of the reservoir was estimated using an elevation 133 m above mean sea level. The hazard map shows that greater proportion of the dwellers are in great danger in the event that there is dam failure.

6.2 Future Outlook of the Study

This research has developed a new methodology for forecasting future reservoir depth based on previous data trends relying on existing sediment transport patterns using the cellular automata-Markov chain model. However, the projected surface has some artefacts present on it caused by some uncertainty of the modelled Markov states. Meanwhile, this assertion is subject to future investigations.

Another milestone attained in this research is the development of the Cellular Automata – Gradient Boosting Regression (CA – GBR) model for predicting future reservoir depth loss due to sedimentation and siltation activities. This again is based on the existing sediment deposition pattern. The CA – GBR model forecasted future bathymetric depth loss effectively and adequately without any artifacts on the projected bathymetric surface map, “a factor that made CA – GBR superior over CA – MC model for reservoir bathymetric depth prediction. Consequently, applying CA – GBR to different bathymetric datasets to evaluate the robustness of the model will be a greater exercise in the future. Meanwhile, neither model accounted for the island area in the study area. Improving the models to account for the island will be excellent research in the future.

Additionally, further study is needed to show that the Universal Soil Loss Equation model is capable of evaluating the accuracy of sediment deposit estimation from the low-frequency echosounder dataset.

7 LIST OF REFERENCES

- Adediji, A. (2005). Reservoir sedimentation: the case of Opa Reservoir catchment, Southwestern Nigeria. *S Afr Geograph J* 87(2), 123–128
- Andreatos, A. & Leros, A. (2021). Contour Extraction Based on Adaptive Thresholding in Sonar Images. *Information*, 12(9), 354. <https://doi.org/10.3390/info12090354>
- Aerts J.C.J.H., Emanuel, K., Lin, N., Moel, H., Michel, E. (2014). Evaluating Flood Resilience Strategies for Coastal Megacities. *Science* 344(6183), 473-475. <https://www.science.org/doi/10.1126/science.1248222> Accessed on 15th October, 2020
- Agapie, A. Andreica, A., Chira, C., Giuclea, M. (2014). Predictability in Cellular Automata. *PLoS ONE* 9(10): e108177. <https://doi.org/10.1371/journal.pone.0108177>.
- Aguilar, F.J., Agüera, F., Aguilar, M.A., Carvajal, F. (2005). Effects of terrain morphology, sampling density, and interpolation methods on grid DEM accuracy. *Photogrammetric Engineering and Remote Sensing*, 71, 805–816. Retrieved on 12th June, 2021.
- Ajitesh, K. (2020). *Gradient Boosting Regression Python Examples*. <https://vitalflux.com/gradient-boosting-regression-python-examples/>
- Ajith, AV (2016). Bathymetric Survey to Study the Sediment Deposit in Reservoir of Peechi Dam. *IOSR Journal of Mechanical and Civil Engineering*, 12(6), 34-38. <https://doi.org/10.9790/1684-12644143>
- Alkali, N.A., Yadima, S.G. & Ibrahim, S. A. (2016). Relationship between Rainfall and Sediment Yield in Gubi Dam Reservoir, Bauchi State, Nigeria
- Alkheder, S. Wang, J., & Shan, J. (2006). Change detection - cellular automata method for urban growth modelling. <https://www.isprs.org/proceedings/xxxvi/part7/PDF/237.pdf> Accessed on 19th September, 2020.
- Allen, K., James, G.W., & Antony, J. (2000). Encyclopedia of Microcomputers (Vol. 25-Supplement 4): *Application of Doppler Effect in Navigation and Oceanography* (pp. 17-18). MerceL Dekker INC.
- Al-Shaar, W., Adjizian, G., Nehme, J.N. et al., (2021). Application of modified cellular automata Markov chain model: forecasting land use pattern in Lebanon. *Model. Earth Syst. Environ.* 7, 1321–1335. <https://doi.org/10.1007/s40808-020-00971-y> Retrieved on 4 August 2021
- Amante, C.J. & Eakins, B.W. (2016). Accuracy of interpolated bathymetry in digital elevation models. In: J.C. Brock, D.B. Gesch, C.E. Parrish, J.N. Rogers, & C.W. Wright, (eds.), *Advances in Topobathymetric Mapping, Models, and Applications*. *Journal of Coastal Research*, 76, 123–133. <https://doi.org/10.2112/SI76-011>

-
- Amir, H., Fathy, N., & Amir B.A. (2013, May). *Cellular Learning Automata and Its Applications, Emerging Applications of Cellular Automata* [Paper presentation]. Alejandro Salcido. DOI: 10.5772/52953. <https://www.intechopen.com/chapters/44535>. Retrieved on 15th October, 2020.
- Amiri-Simkooei, A., Snellen, M., Simons, D.G. (2008). *Using the MBES for classification of riverbed sediments*. www.acoustics08-paris.org Accessed on 03/09/2021
- Amiri-Simkooei, A.R., Koop, L., van der Reijden, K.J., Snellen, M., Simons, D.G. (2019). Seafloor Characterization Using Multibeam Echosounder Backscatter Data: Methodology and Results in the North Sea. *Geosciences*, 9, 292. <https://doi.org/10.3390/geosciences9070292>
- Annalisa, M., Anna, N.T., Gianna, F. (2020, October). *Uncalibrated Multibeam Echosounder capabilities for fish schools measuring and tracking: An application in the nearby of an Adriatic offshore structure* [Paper presentation]. IMEKO TC-19 International Workshop on Metrology for the Sea Naples, Italy.
- Anon, K. (1973). *Atlas of Elektronik Bremen*: Technical manual on Dolog.
- Antonio, G. (2021). *Half world's population will be exposed to flooding, storms, tsunamis by 2030*. <https://thenewsnigeria.com.ng/2021/11/05/half-worlds-population-will-be-exposed-to-flooding-storms-tsunamis-by-2030-unchief/>
- Antony, J. (2000). Applications of doppler effect in Navigation and Oceanography. In K. Allen & G.W. James (Eds), *Encyclopedia of Microcomputers* Vol. 25, 17–45). Executive Marcel Dekker Inc.
- Aqil, T. & Shu, H. (2020). CA-Markov Chain Analysis of Seasonal Land Surface Temperature and Land Use Land Cover Change Using Optical Multi-Temporal Satellite Data of Faisalabad, Pakistan. *Remote Sensing*, 12(20), 3402. <https://doi.org/10.3390/rs12203402> Retrieved on 12th January, 2021
- Atat, J.G., Akpabio, G.T., George, N.J., & Umoreu, E.B. (2012). Geophysical assessment of elastic constants of topsoil using seismic refraction compressional and shear wave velocities in the Eastern Niger Delta, Nigeria. *International Journal of Modern Applied Physics* 1(2), 7-12.
- Australian Bureau of Meteorology National Tide Centre Glossary (ABMNTCG). http://www.bom.gov.au/oceanography/projects/ntc/NTC_glossary.pdf
- Babatunde. J.F., Adeleye, Y.B., Chris, O., Olabanji, O.A., Adegoke, I.A. (2016). GIS-based estimation of soil erosion rates and identification of critical areas in Anambra Subbasin, Nigeria. *Model Earth Syst. Environ.* 2(159).
- Barman, N., Chatterjee, S., Khan, A. (2014). Trends of Shoreline Position: An Approach to Future Prediction for Balasore Shoreline, Odisha, India. *Open Journal of Marine Science*, 5, 13-25. Doi:10.4236/ojms.2015.51002. Retrieved on 10 September, 2021
- Bates, C.R., Lawrence, M., Dean, M., & Robertson, F. (2011). Geophysical methods for wreck site monitoring: the rapid archaeological site surveying and

- evaluation (RASSE) programme. *The International Journal of Nautical Archaeology*, 40(2), 404–416. <https://doi.org/10.1111/j.1095-9270.2010.00298.x>
- Batty, M. (1997). Possible urban automata. *Environment and Planning B* 24,175-192.
- Batty, M., Yichun, X., & Zhanli, S. (1999). Modelling urban dynamics through GIS-based cellular automata. *Comput., Environ. and Urban Systems*, 23, 205-233. <http://www.complexcity.info/files/2011/07/batty-ceus-1999.pdf> Retrieved on 13th February, 2021.
- Benjamin, J.W., Philippe, B., Laura, D., Williamson, B., & Scott, E. (2021). Application of a multibeam echosounder to document changes in animal movement and behaviour around a tidal turbine structure. *ICES Journal of Marine Science*, 78, 4, 1253–1266. <https://doi.org/10.1093/icesjms/fsab017>
- Bjorno, L. (2017). Sonar system. In H. N. Thomas, & B. David (Eds), *Applied Underwater Acoustic* (pp. 587-742). Elsevier.
- Buller, A.T., & McManus, J. (1979). Sediment sampling and analysis: In K.R. Dyer (Ed), *Estuarine hydrography and sedimentation* (pp.87-89). Cambridge University Press.
- Burrough, P. A., & McDonnell, R. A. (1998). *Principles of geographical information systems*. Oxford University Press.
- Carvalho, J.P., Carola, M., & Tomé, A.B. (2002). *Using Rule-Based Fuzzy Cognitive Maps to Model Dynamic Cell Behavior in Voronoi Based Cellular Automata FCT* [Paper presentation]. Portuguese Foundation for Science and Technology, Lisboa, Portugal.
- Cenderelli, D., Clarkin, K., Gubernick, R., & Weinhold, M. (2011). Stream Simulation for Aquatic Organism Passage at Road–Stream Crossings. *Transportation Research Record Journal of the Transportation Research Board*, 2203. Doi:10.3141/2203-05.
- Chapra, S.C. (1997). *Surface Water-Quality Modelling*. McGraw-Hill
- Charles, W.D. (2000). *Acoustic Applications of Phased Array Technology*. <http://casa.colorado.edu/~danforth/science/sonar/sonar1.html>
- Che Hasan R.C., Ierodionou, D., Rattray, A., Monk, J., & Laurenson, L. (2011, September). *Applications of multibeam echosounder data and video observations for biological monitoring on the south east Australian continental shelf* [Paper presentation]. ISG & ISPRS, Shah Alam, MALAYSIA.
- Chen, Y.H, Lopez, J.L., Richardson, E.V. (1978). Mathematical modelling of sediment deposition in reservoir. *J Hydrol Div*, 104, 1605–1616.
- Chiang, K-W., Huang, Y-S., Tsai, M-L., Chen, K-H. (2010). The perspective from Asia concerning the Impact of Compass/Beidou-2 on future GNSS. *Survey Review*, 42(3-19). Doi:10.1179/003962609X451654

-
- Chih-Hung, C. (2014). Some properties of topological pressure on cellular automata. *Journal of Algebra Combinatorics Discrete Structures and Applications*, 1(1), 41-51. ISSN 2148-838X. <https://dergipark.org.tr/tr/download/article-file/148543> Retrieved on 10 September, 2021.
- Choanji, T. (2017). Slope Analysis Based on SRTM Digital Elevation Model Data: Study Case on Rokan IV Koto Area And Surrounding. *Journal of Dynamics*, 1.
- Chris, F. (2010). *Technologies for Ocean Acoustic Monitoring. Revised June 09, 2010 by the NOAA Ocean Explorer Webmaster.* <https://oceanexplorer.noaa.gov/explorations/sound01/background/technology/technology.html>
- Chukwu, F.N , & Badejo, O.T. (2015). Bathymetric Survey Investigation for Lagos Lagoon Seabed Topographical Changes. *Journal of Geosciences and Geomatics*, 3(2), 37-43.
- Chun, M., Yang, X., Cao, W., & Xiaoqiao, L. (2016, June). *The Application of Multibeam Bathymetry Systems in Process Control and Quality Detection of Channel Dredging Operations* [Paper presentation]. The 26th International Ocean and Polar Engineering Conference, Rhodes, Greece.
- Clarke, J.I. (1996). *Morphometry from maps: essay in geomorphology* (pp 235–27). Elsevier Publ, Co, New York.
- Clifford, G. C., Sanjay, K. M., & Bernard, E. McT. (2001). Sonar and Radar System Applications. In S. Stergios (Ed), *Advanced Signal Processing Handbook; Theory and Implementation for Radar, Sonar and Medical Imaging Real Time system* (Chap. 10.5.2). CRC Press.
- Cui, Y. (2007). The Unified Gravel-Sand (TUGS) Model: Simulating Sediment Transport and Gravel/Sand Grain Size Distributions in Gravel-Bedded Rivers. *Water Resour. Res.*, 43. doi:10.1029/2006 WR0
- Cui, Y., Parker, G., Braudrick, C., Dietrich, W.E. & Cluer, B. (2006). Dam Removal Express Assessment Models (DREAM): Model development and validation. *Journal of Hydraulic Research*, 44, 291–307.
- Curtis, T. E. & Ward, R. J. (1980). Digital beam forming for sonar systems. IEE Proceedings F – Communications. *Radar and Signal Processing*, 127(4), 257-265. doi: 10.1049/ip-f-1.1980.0040
- Danso-Amoako, E., Miklas, S., Nickolas, K., Qinli, Y., Junming, S. (2012). Predicting dam failure risk for sustainable flood retention basins: A generic case study for the wider Greater Manchester area. *Computers, Environment and Urban Systems* 36, 423–433. <http://dx.doi.org/10.1016/j.compenvurbsys.2012.02.003>
- Dargahi, B. (2012). Reservoir Sedimentation. In L. Bengtsson, R.W. Herschy, & R.W. Fairbridge (eds), *Encyclopedia of Lakes and Reservoirs* (pp. 628 – 649). Springer. https://doi.org/10.1007/978-1-4020-4410-6_215
- Daryl, H., Stephen, B., & Geoff, P. (2021). A method to include reservoir operations in catchment hydrological models using SHETRAN. *Environmental Modelling*
-

-
- & *Software*, 138. ISSN 1364-8152.
<https://doi.org/10.1016/j.envsoft.2021.104980>.
- David, M. (2000). Interpretation of Bathymetry. In Peter J.C. and Chris M.C. (Eds), *Continental Shelf Limits: The Scientific and Legal Interface* (pp160-176). Oxford University Press.
- De Jong, C.D., Lachapelle, G., Skone, S., Elema, I.A. (2010). Hydrography 2nd edn. eBook with corrections January 2010.
- De Moel, H., Aerts, J.C.J.H. (2008). Integration of flood management and spatial planning in European research. In J.G. Timmerman, C. Pahl-Wostl, J. Moltgen (eds), *Adaptiveness of IWRM—analysing European IWRM research (EU Report series, chapter 9)*, pp 129–139. IWA Publishing.
- De Moel, H., Jongman, B., Kreibich, H. et al., (2015). Flood risk assessments at different spatial scales. *Mitig Adapt Strateg Glob Change*, 20, 865–890.
<https://doi.org/10.1007/s11027-015-9654-z>
- de Moustier, C. (June 1, 1988). Approaches to Acoustic Backscattering Measurements From the Deep Seafloor. *ASME. J. Energy Resour. Technol*, 110(2): 77–84.
<https://doi.org/10.1115/1.3231369>
- Devore, J.L. (2011). *Probability and Statistics for Engineering and the Sciences* (8th ed.). Boston, MA: Cengage Learning. ISBN 978-0-538-73352-6.
- Diego G, Martina B, Massimo R, Gordon G, Nikolai F, Ian GC, Fernando M, Tom B (2017) Linking environmental flows to sediment dynamics. *Water Policy* 19:358–375.
- Dietterich, T.G., & Eun, B.K. (1995). *Machine Learning Bias, Statistical Bias, and Statistical Variance of Decision Tree Algorithms*.
<http://citeseerx.ist.psu.edu/viewdoc/download?rep=rep1&type=pdf&doi=10.1.1.38.2702> Retrieved on 15th September, 2020.
- Donghwan, J., Jeasoo, K. & Gihoon, B. (2018). Numerical Modeling And Simulation Technique In Time-Domain For Multibeam Echo Sounder. *International Journal of Naval Architecture and Ocean Engineering*, 10(2), 225-234.
<https://doi.org/10.1016/j.ijnaoe.2017.08.004>
- Dorst, L.L. (2005). Optimization of Survey Frequency: The Netherlands Hydrographic Service. *HYDRO International*, 9(8), 6-9.
- Dutta, S. (2016). Soil erosion, sediment yield and sedimentation of reservoir: a review. *Model Earth Syst. Environ.*, 2, 123. <https://doi.org/10.1007/s40808-016-0182-y>
- Dwivedi, R.S, Sreenivas, K., Ramana K.V. (2005). Land-use/land-cover change analysis in part of Ethiopia using Landsat Thematic Mapper data. *International Journal of Remote Sensing*, 26(7),1285–1287.
- Eakins, B.W. & Grothe, P.R. (2014). Challenges in building coastal digital elevation models. *Journal of Coastal Research*, 30(5), 942–953.
-

-
- Ebrahimipour, A., Saadat, M., Farshchin, A. (2016). Prediction of Urban Growth through Cellular Automata-Markov Chain. *Bulletin de la Société Royale des Sciences de Liège*, 85, 824 – 839. <https://popups.uliege.be/0037-9565/index.php?file=1&id=5677> Retrieved on 14 August, 2021
- Edward, M.L. (2017). *The dynamics of marine craft: Manoeuvring and seakeeping; Dynamics of rid bodies*. World Scientific Publishing.
- EL-Hattab, A.I. (2014). Single beam bathymetric data modelling techniques for accurate maintenance dredging. *Egyptian Journal of Remote Sensing and Space Sciences* 17(2), 189–195. <http://dx.doi.org/10.1016/j.ejrs.2014.05.003>
- Elith, J., John, R. L., & Trevor, H. (2008). A Working Guide to Boosted Regression Trees. *Journal of Animal Ecology*, 77(4), 802-813.
- Emel'yantsev, G.I., Stepanov, A.P., Blazhnov, B.A., Radchenko, B.A., Vinokurov, I.Y. & Petrov, P.Y. (2017). *Using satellite receivers with a common clock in a small-sized GNSS compass*. Saint Petersburg International Conference on Integrated Navigation Systems (ICINS). Doi: 10.23919/ICINS.2017.7995619.
- Estigoni, M., Matos, A., & Mauad, F. (2014) Assessment of the accuracy of different standard methods for determining reservoir capacity and sedimentation. *Journal of Soils and Sediments*, 14, 1224–1234. <https://link.springer.com/article/10.1007/s11368-013-0816-x>
- Etzelmuller, B. (2000). On the quantification of surface changes using grid-base digital elevation models (DEMs). *Transactions in GIS*, 4(2), 129-143.
- Externe, A., Marco, K., & Ina, E. (2007). *Converting NL Chart Datum: Consequences of change from MLLWS to LAT*. <https://www.hydro-international.com/content/article/converting-nl-chart-datum>
- Faniran, A. (1968). The Index of Drainage Intensity: A Provisional New Drainage Factor. *Australian Journal of Science*, 31, 328-330.
- Farrira, I.O., Dalto, D.R., Géron, R.S., & Lidiane, M.F. (2017). In Bathymetric Surfaces: I.D.W. Or Kriging. *B.C.G.–Bulletin of Geodetic Sciences* 23(3), 493–508. <http://dx.doi.org/10.1590/S1982-21702017000300033>
- Flache, A., & Hegselmann, R. (2002). Do Irregular Grids make a Difference? Relaxing the Spatial Regularity Assumption in Cellular Models of Social Dynamics. *Journal of Artificial Societies and Social Simulation*, 4(4 of 26).
- Fonstad, M.A. (2013). Cellular Automata in Geomorphology. F.S. John (Ed), *Treatise on Geomorphology*. Academic Press, pp.117-134. <https://doi.org/10.1016/B978-0-12-374739-6.00035-X>.
- Foster, G. R. (2008). Draft Science Documentation: Revised Universal Soil Loss Equation Version 2. *USDA-Agriculture Research Service*, p. 349. Washington (DC). http://www.ars.usda.gov/SP2UserFiles/Place/64080530/RUSLE/RUSLE2_Science_Doc.pdf.
-

-
- Francina, D., Bieri, C. & Lawrence, D. (2021). Impacts of Large-Scale Soil Moisture Anomalies on the Hydroclimate of Southeastern South America. *Journal of Hydrometeorology*, 22. Doi:10.1175/JHM-D-20-0116.1.
- Friedman, J. (2001). Greedy boosting approximation: a gradient boosting machine. *Ann. Stat.* 29, 1189–1232. doi:10.1214/aos/1013203451
- Gagniuc, P.A. (2017). *Markov Chains: From Theory to Implementation and Experimentation*. John Wiley & Sons. ISBN 978-1-119-38755-8.
- Gesch, J.C., Parrish, D.B., Rogers, C.E., & Wright, C.W. (2016). Advances in Topobathymetric Mapping, Models, and Applications. *Journal of Coastal Research*, 76, 1–3. <https://doi.org/10.2112/SI76-001>
- Gharbia, S.S., Alfatah, S.A., Gill, L. et al., (2016). Land use scenarios and projection simulation using integrated GIS cellular automaton algorithms. *Model. Earth Syst. Environ.*, 2(151). <https://doi.org/10.1007/s40808-016-0210-y> Retrieved on 3 September, 2021.
- Ghimire, B., Chen, A., Djordjević, S., & Savic, D. (2011). Application of cellular automata approach for fast flood simulation [Paper presentation]. *Computing and Control for the Water Industry: Urban Water Management - Challenges and Opportunities*. Exeter, UK
- Girish, G., Ashitha, M.K., and Jayakumar, K.V. (2014). Sedimentation assessment in a multipurpose reservoir in Central Kerala, India. *Environmental Earth Sciences*, 72, 4441- 4449. DOI: 10.1007/s12665-014-3344-0
- Gleick, P.H. (2000). *The World's Water, 2000-2001: The Biennial Report on Freshwater*. Island Press. ISBN 978-1-55963-792-3.
- Goharian, E., Azizipour, M., Sandoval-Solis, S., & Fogg, G. (2021). Using Cellular Automata Approach to Optimize the Hydropower Reservoir Operation of Folsom Dam. *Water*. 13(13), 1851. <https://doi.org/10.3390/w13131851> Retrieved on 7th August, 2021.
- Gomez, F., Cassis-Nosthas, L., Morales-de-León, J. et al. (2004). Detection and recognition thresholds for the 4 basic tastes in Mexican patients with primary Sjögren's syndrome. *Eur J Clin Nutr.*, 58, 629–636. <https://doi.org/10.1038/sj.ejcn.1601858>
- Grant, J.A., Schreiber, R. (1990). Modern Swathe Sounding and Sub-Bottom Profiling Technology for Research Applications: The Atlas Hydrosweep and Parasound Systems. In E.A. Hailwood & R.B. Kidd (eds), *Marine Geological Surveying and Sampling*. Springer. https://doi.org/10.1007/978-94-009-0615-0_2 Accessed on 24th March 2020.
- Greg S., Richard D. C, Charles H, Rajib A. H., (2017) Dealing with sediment: effects on dams and hydropower
- Grover, P. (2018). 5 Regression Loss Functions All Machine Learners Should Know: Choosing the right loss function for fitting a model. <https://heartbeat.fritz.ai/5-regression-loss-functions-all-machine-learners-should-know-4fb140e9d4b0> Retrieved on 4 September, 2021.
-

-
- Guth, P.L. (1992). Microcomputer application of digital elevation models and other gridded data sets for geologists. In H. Kürzel & D.F. Merriamed. (Eds), *Use of Microcomputers in Geology*, pp.187-206. Computer Applications Series, Plenum.
- Guth, P.L. (2006, June). Geomorphometry from SRTM: Comparison to NED: Photogrammetric Engineering & Remote Sensing, special issue based on Shuttle Radar Topography Mission [Paper presentation]. *Data Validation and Applications Workshop* 72(3), 269-277. Reston, VA.
- Haan, C.T., Barfield, B.J. & Hayes, J.C. (1994). *Design Hydrology and Sedimentology for Small Catchments*. Academic Press.
- Hadley, R.F. & Schumm, S.A. (1961). Sediment sources and drainage basin characteristics in upper Cheyenne River basin. *US Geological Survey, USGS water supply paper*, 1531-B.
- Hamad, R., Balzter, H., & Kolo, K. (2021). Predicting Land Use/Land Cover Changes Using a CA-Markov Model under Two Different Scenarios. *Sustainability*, 10(10), 3421. <https://doi.org/10.3390/su10103421> Retrieved on 4 August, 2021
- Hamed, K.A., & Hassan, F. (2018). Passive Sonar Target Detection Using Statistical Classifier and Adaptive Threshold. *Journal of applied science*, 8(61), 01-17. <https://www.mdpi.com/2076-3417/8/1/61/pdf>
- Hansen, J.T. & Boss, S.K. (2000). Bathymetry and Empirical Modelling of Sedimentation in the Prairie Creek Sub-Basin of Beaver Lake, Northwest Arkansas. *Geological Society of America Abstracts with Programs*, 32(3), A13.
- Hansen, R. E., Saebo, T. O., Callow, H. J., Langli, B. & Hammerstad, E. O. (2007). Bathymetric Capabilities of the HISAS Interferometric Synthetic Aperture Sonar. *OCEANS 2007*. doi:10.1109/OCEANS.2007.4449357
- Hare, R., Eakins, B., and Amante, C. (2011). Modelling Bathymetric Uncertainty. *International Hydrographic Re-view*, 6, 31-42. <https://coast.noaa.gov/data/digitalcoast/pdf/topo-bathy-data-considerations.pdf>
- Harry, W. V. (2004). *Optimum array processing; detection, estimation and modulation theory*. John Wiley and Sons Ltd.
- Hassan, Z., Shabbir, R., Ahmad, S.S. et al., (2016). Dynamics of land use and land cover change (LULCC) using geospatial techniques: a case study of Islamabad Pakistan. *SpringerPlus*, 5, 812. <https://doi.org/10.1186/s40064-016-2414-z> Retrieved on 12th October, 2021.
- Hedlund, G. A. (1969). Endomorphisms and automorphisms of full shift dynamical system, *Math. Systems Theory*, 3, 320-375.
- Hell, B., Broman, B., Jakobsson, L., Jakobsson, M., Magnusson, A., & Wiberg, P. (2012). The use of bathymetric data in society and science: a review from the Baltic Sea. *Ambio*, 41(2), 138–150. doi:10.1007/s13280-011-0192-y
-

- Henry, C. (1999). Detection threshold. *The Journal of the Acoustical Society of America*, 106 (4), 2187 - 2187. <https://doi.org/10.1121/1.427411>
- Horton, R. E. (1932). Drainage basin characteristics. *Transactions of American Geophysical Union*, 13, 350–360. <https://doi.org/10.1029/TR013i001p00350> Accessed on 4th August, 2021
- Horton, R.E. (1945a). Erosional development of streams and their drainage basins: hydrophysical approach to quantitative morphology. *Bull Geol Soc Am.*, 56, pp. 275–370. <https://pdodds.w3.uvm.edu/research/papers/others/1945/horton1945a.pdf> Retrieved on 17th September, 2021.
- Hou, X.Y., Chang, B., Yu, X.F. (2004). Land use change in Hexi corridor based on CA–Markov methods. *Transactions of the CSAE*, 20(5) 286–291.
- Hu, K., Li, B., Lu, Y. & Zhang, F., (2004). Comparison of various spatial interpolation methods for non-stationary regional soil mercury content. *Environmental Science*, 25(3): 132-137.
- Hung, P., McLoone, S., & Monteys, X. (2010). *Seabed type clustering using single-beam echo sounder time series data* [Paper presentation]. 6th WSEAS International Conference on Remote Sensing (REMOT'E'10), Iwate, Japan.
- Hunzendorf, H. (1986). Marine Mineral Exploration. Elsevier Oceanography Series, 41.
- Iacono, M., Levinson, D., El-Geneidy, A., & Rania, W. (2012). Markov Chain Model of Land Use Change in the Twin Cities. *Journal of Land Use, Mobility and Environment*, 8. Doi:10.6092/1970-9870/2985
- Ibrahim, P.O. & Sternberg, H. (2021). Bathymetric Survey for Enhancing the Volumetric Capacity of Tagwai Dam in Nigeria via Leapfrogging Approach. *Geomatics*, 1, 246–257. <https://doi.org/10.3390/geomatics 1020014>
- Igor, I., Berk, G., Mucahit, C., Mustafa, G.B. (2020). *Explainable boosted linear regression for time series forecasting*. <https://arxiv.org/pdf/2009.09110.pdf> Retrieved on 6 September, 2021.
- Inger, A., Ousmane, D., Martha, J-H., & Jean-Claude, O. (2005). *The Niger River Basin: A Vision for Sustainable Management*. Washington, DC 20433, USA. DOI: 10.1596/978-0-8213-6203-7
- Ingham, A.E. (1984). *Hydrography for the Surveyor and Engineer*. John Wiley & Sons. ISBN 0-471-80535-1
- International Hydrography Organizations https://iho.int/uploads/user/pubs/cb/c-13/english/C_13_Chapter_3_December2010.pdf
- International Sediment Initiative (ISI-2011). <https://unesdoc.unesco.org/ark:/48223/pf0000212885> Accessed on 14th September, 2021.
- International Sediment Initiative, 2009 (ISI, 2009). <https://unesdoc.unesco.org/ark:/48223/pf0000183153> Retrieved on 04th August, 2020.

- Iqbal, M., Haroon, S. & Bhat, F.A. (2013). Morphometric Analysis of Shaliganga Sub Catchment, Kashmir Valley, India Using Geographical Information System. *International Journal of Engineering Trends and Technology*, 4(1), 10 – 23. <https://www.researchgate.net/publication/266383021>
- Jamal, J., Arsanjani, W.K. & Ali, J.M. (2011). Tracking dynamic land-use change using spatially explicit Markov Chain based on cellular automata: the case of Tehran. *International Journal of Image and Data Fusion*, 2(4), 329-345. <https://DOI.10.1080/19479832.2011.605397> Retrieved on 12th January, 2021
- Jamali, B., Bach, P.M., Cunningham, L., & Deletic, A. (2019). A CellularAutomata fast flood evaluation (CA-ffé) model. *Water Resources Research*, 55, 4936–4953. <https://doi.org/10.1029/2018WR023679> Retrieved on 3 September, 2021
- Javed, A., Khanday, M.Y. & Ahmaed, R. (2009). Prioritization of Subwatersheds based on morphomeric and land-use analysis using remote sensing and GIS techniques. *J Indian Soc Remote Sens* 37, 261–274.
- Jiang, G., Zhang, F., & Kong, X. (2009). Determining conversion direction of rural residential land consolidation in Beijing mountainous areas. *Nongye Gongcheng Xuebao/Transactions of the Chinese Society of Agricultural Engineering*, 25, 214-221.
- Jie, H., Tian, Z., Weidong, D., Jiajun, S., & Wanyuan, Z. (2018). Smart Ocean: A New Fast Deconvolved Beamforming Algorithm for Multibeam Sonar. *Sensors*, 18, 1-16. doi:10.3390/s18114013
- Joe B. *Markov Chains Handout for Stat 110* https://projects.iq.harvard.edu/files/stat110/files/markov_chains_handout.pdf Retrieved on 6 September, 2021
- John A. Dunbar, Peter M. Allen, Paul D. Higley; Multifrequency acoustic profiling for water reservoir sedimentation studies. *Journal of Sedimentary Research* 69(2): 518–527. <https://doi.org/10.2110/jsr.69.518> Retrieved on 17 September, 2021
- Jones, G., Abbott, V., Manning, A., & Jakt, M. (2017). Acoustic Seabed Survey Methods, Analysis and Applications. In R. Uncles, & S. Mitchell (Eds.), *Estuarine and Coastal Hydrography and Sediment Transport* (pp. 54-91). Cambridge University Press. doi:10.1017/9781139644426.004
- Jongman, B., Kreibich, H., Apel, H., Barredo, J.I., Bates, P.D., Feyen, L., Gericke, A., Neal, J., Aerts, J.C.J.H., & Ward, P.J. (2012b). Comparative flood damage model assessment: towards a European approach. *Nat Hazards Earth Syst Sci*, 12, 3733–3752.
- Jorgensen, K.V., Grose, B.L., & Crandall F.A. (1994). Doppler precision underwater navigation. *Sea technol.*, 35(3), 63-66.
- Jose, A.M-R, Cesar, C.M., Manuel-Francisco C-M., Juan, T. L-R., & Julio, B.M. (1999). New cellular automata applications on multitemporal and spatial analysis of NOAA-AVHRR images. *Proc. SPIE 3871, Image and Signal Processing*

- for Remote Sensing, V. <https://doi.org/10.1117/12.373267> Retrieved on 7 August, 2021
- Jose, D, Nicolas, R, Mehrez, Z (2016). The reflected global navigation satellite system (GNSS-R): from theory to practice. Elsevier, 303-355. <https://doi.org/10.1016/B978-1-78548-159-8.50007-4>.
- Jun, L., & Jian, L. (2011). Probing waveforms and adaptive receivers for active sonar. *The Journal of the Acoustical Society of America*, 129(6),1-6. <https://doi.org/10.1121/1.3575604>
- Jurag, C. & Podhorányi, M. (2013). Cellular Automata for the Flow Simulations on the Earth Surface, Optimization Computation Process. *Applied Mathematics & Information Sciences*, 7, 2149-2158.
- Justin, D. (2004). *Fera Vita: Pax draconis Supplement 1*, pp62-63. USA.
- Kai-Wei, C., Huang, Y-S., Tsai, M-L., Chen, K-H. (2010). The perspective from Asia concerning the Impact of Compass/Beidou-2 on future GNSS. *Survey Review*, 42, 3-19. Doi:10.1179/003962609X451654.
- Karami, E., Ghorbani Dashtaki, S., Khalilimoghadam, B. (2018). Effects of land management on soil erodibility-A case study in part of Zayandeh-Rood watershed. *Journal of Agricultural Engineering Soil Science and Agricultural Mechanization. Scientific Journal of Agriculture*, 40(2), 105-119. doi: 10.22055/agen.2018.18172.1281
- Kelson, K.I. & Wells, S.G. (1989). Geologic influences on fluvial hydrology and bed load transport in small mountainous watersheds, northern New Mexico, USA. *Earth Surface Processes Landforms*, 14, 671–690.
- Kesaulija, F.F., Marlon, I.A., Muhammad, S., Ali, S. (2021). Modelling Land Cover Change Using Markov Chain-Cellular Automata in Sorong, West Papua Province [Paper presentation]. *Proceedings of the Joint Symposium on Tropical Studies*, 157 – 162. 978-94-6239-362-2. <https://doi.org/10.2991/absr.k.210408.026> Retrieved on 12 August, 2021
- Khaba, L. & Griffiths, J.A. (2017). Calculation of reservoir capacity loss due to sediment deposition in the Muela reservoir, Northern Lesotho. *International Soil and Water Conservation Research*, 5, 130–140. <http://dx.doi.org/10.1016/j.iswcr.2017.05.005>
- Khattab, M.F.O., Abo, R.K., Al-Muqdadi, S.W., & Merkel, B.J. (2017). Generate Reservoir Depths Mapping by Using Digital Elevation Model: A Case Study of Mosul Dam Lake, Northern Iraq. *Advances in Remote Sensing* 6, (161–174). <https://doi.org/10.4236/ars.2017.63012>
- Kier, L.B., Seybold, P.G., Cheng, C-K. (2005). *Modeling Chemical Systems using Cellular Automata*. Springer. ISBN 9781402036576.
- Kinsler, L., Frey, A., Coppens, A., Sanders, J. (1982). *Fundamentals of Acoustics*, 3rd Ed. John Wiley & Sons.
- Kirpich, Z. P. (1940). Time of concentration of small agricultural watersheds. *Journal of Civil Engineering*, 10(6), 362.

-
- Klein, R., & Aurenhammer, F. (2001). Voronoi Diagrams. Doi:10.1016/B978-044482537-7/50006-1.
- Kreibich, H., Van den Bergh, J.C.J.M., Bouwer, L.M., Bubeck, P., Ciavola, P., Green, C., Hallegatte, S., Logar, I., Meyer, V., Schwarze, R., Thielen, A.H. (2014). Costing natural hazards. *Nat Clim Chang* 4, 303–306.
- Kumar, K.S. Kumari, K.P. and Bhaskar, P.U. (2016). Application of Markov chain & cellular automata based model for prediction of Urban transitions [Paper presentation]. *International Conference on Electrical, Electronics, and Optimization Techniques (ICEEOT)*, pp.4007-4012. doi:10.1109/ICEEOT.2016.7755466.
- L-3 Communications SeaBeam Instruments: Multibeam sonar theory of operation. <https://www3.mbari.org/data/mbsystem/sonarfunction/SeaBeamMultibeamTheoryOperation.pdf> Accessed 4th January, 2019
- LaRocque, A. (2013). Universal Soil Loss Equation (USLE). In P.T. Bobrowsky (eds), *Encyclopedia of Natural Hazards*. Encyclopedia of Earth Sciences Series. Springer. https://doi.org/10.1007/978-1-4020-4399-4_43
- Lea, C. & Curtis, A. (2010). Thematic accuracy assessment procedures: National Park Service Vegetation Inventory, version 2.0. *Natural resource report NPS/2010/NRR—2010/204*. Colorado
- Lekkerkerk, H-J. & Theijs, M-J. (2017). *Handbook of Offshore Surveying: Acquisition Sensors* (Vol. 3). Skilltrade BV, AC Voorschoten. ISBN: 978-90-816591-3-0
- Li, K., Feng, M., Biswas, A., Su, H., Niu, Y., & Cao, J. (2020). Driving Factors and Future Prediction of Land Use and Cover Change Based on Satellite Remote Sensing Data by the LCM Model: A Case Study from Gansu Province, China. *Sensors*, 20(10), 2757. <https://doi.org/10.3390/s20102757> Retrieved 9 August, 2021.
- Lingling, S., Chao, Z., Jianyu, Y., Dehai, Z., & Wenju, Y. (2011). Simulation of land use spatial pattern of towns and villages based on CA–Markov model. *Mathematical and Computer Modelling*, 54(3–4), 938-943. ISSN 0895-7177. <https://doi.org/10.1016/j.mcm.2010.11.019>. Retrieved on 12th January, 2021
- Lisa, M.Z & Daniel, R (2012). Striation-based beamforming for active sonar with a horizontal line array. *The Journal of the Acoustical Society of America*, 132 (4), EL264-EL270. <https://doi.org/10.1121/1.4748281>.
- Liu, K., Song, C., Wang, J., Ke, L., Zhu, Y., Zhu, J., et al. (2020). Remote sensing-based modelling of the bathymetry and water storage for channel type reservoirs worldwide. *Water Resources Research*, 56. <https://doi.org/10.1029/2020WR027147>
- Lu, D. & Weng, Q. (2007). A survey of image classification methods and techniques for improving classification performance. *International Journal of Remote Sensing*, 28(5), 823–870.
-

-
- Lubis, M. Z., & Pujiyati, S. (2016). Detection Backscatter Value of Mangrove Crab (*Scylla* Sp.) Using Cruzpro Fishfinder Pcff-80 Hydroacoustic Instrument. *J Biosens Bioelectron*, 7 (205). doi:10.4172/2155-6210.1000205
- Lubis, M.Z., & Manik, H. (2017). Acoustic systems (split beam echo sounders) to determine the abundance of fish in marine fisheries. <https://marinegyaan.com/what-is-an-echo-sounder-its-principle-errors-and-corrective-action/echo-sounder-2/> Accessed on 7th March 2020
- Lumbruso, D. (2007). Review report of operational flood management methods and models. Flood site project report: *Integrated flood risk analysis and management methodologies*. EU Sixth Framework Programme.
- Malcolm, J.C., Ira, D. et al., (1998). *Hand on Acoustic; Underwater Sound; Analytical representation of Sonar system elements*. John Welly and Sons Inc.
- Maranda, B.H. (2008). Passive Sonar. In D. Havelock, S. Kuwano, & M. Vorländer (eds), *Handbook of Signal Processing in Acoustics*. Springer. https://doi.org/10.1007/978-0-387-30441-0_97
- Marian, M., Dongsu, K. & Venkatesh, M. (2012). *Gravel Bed: Processes, Tools, Environmental; Modern Digital Instruments and Morphologic Characterization of River Channels*. John Wiley & Sons Ltd.
- Markose, V.J, Dinesh, A.C. & Jayappa, K.S. (2014). Quantitative analysis of morphometric parameters of Kali River basin, southern India, using bearing azimuth and drainage (bAd) calculator and GIS. *Environmental Earth Sciences*, 1(17).
- Markov chains. Brilliant.org. Retrieved on 6 September, 2021. <https://brilliant.org/wiki/markov-chains/>
- Martin J. T., (2015) Modeling Sediment Movement in Reservoirs. Prepared by the USSD Committee on Hydraulics of Dams, Subcommittee on Reservoir Sedimentation ISBN 978-1-884575-70-9.
- Matt Williams- <https://phys.org/news/2014-12-percent-earth.html>
- Melton, M.A. (1957). Correlation structure of morphometric properties of drainage system and their controlling agents. *J. Geol.*, 66, 442-460.
- Mentzafou, A., Varlas, G., Papadopoulos, A., Poulis, G., & Dimitriou, E. (2021). Assessment of Automatically Monitored Water Levels and Water Quality Indicators in Rivers with Different Hydromorphological Conditions and Pollution Levels in Greece. *Hydrology*, 8(2), 86. <https://doi.org/10.3390/hydrology8020086>
- Merz, B., Kreibich, H., Thielen, A. & Schmidtke, R. (2004). Estimation uncertainty of direct monetary flood damage to buildings. *Natural Hazards and Earth System Sciences*, 4, 153–163. <https://nhess.copernicus.org/articles/4/153/2004/nhess-4-153-2004.pdf>
- Michael, A.A. (2010). *Principles of Sonar Performance Modeling; Sonar signal processing*. Praxis Publishing. doi: 10.1007/978-3-540-87662-5
-

-
- Michele, G., Albert, S., Chen, B.G., Edward, C.K., Slobodan, D., & Dragan, A.S. (2016). A weighted cellular automata 2D inundation model for rapid flood analysis. *Environmental Modelling & Software*, 84, 378-394. ISSN 1364-8152. <https://doi.org/10.1016/j.envsoft.2016.07.008>. Retrieved on 7 August, 2021
- Miller, V.C (1953). A quantitative geomorphic study of drainage basin characteristics on the Clinch Mountain area, Virginia and Tennessee. *Columbia University, Department of Geology, Technical Report, Number 3*, pp 389-402, New York.
- Mitra, B., Scott, H.D., Dixon, J.C. & McKimney, J.M. (1998). Applications of fuzzy logic to the prediction of soil erosion in a large watershed. *Geoderma*, 86, 183-209.
- Mohammad, H., Assefa, M.M., & Hector, R. F. (2018). Erosion and Sediment Transport Modelling in Shallow Waters: A Review on Approaches, Models and Applications. *International Journal of Environmental Research and Public Health*. 15, 518. doi:10.3390/ijerph15030518.
- Monteale-Gavazzi, G., Marc, R., Xavier, L., Koen, D., Nathan, T., & Vera Van, L. (2018). Seafloor change detection using multibeam echosounder backscatter: case study on the Belgian part of the North Sea. *Mar Geophys Res*. 39, 229–247. <https://doi.org/10.1007/s11001-017-9323-6>
- Morris, G.L, & Fan, J. (1998). *Reservoir sedimentation handbook*. Tata McGraw-Hill Publishing Company.
- Mudashiru, R. B., Olawuyi, M. Y., Amototo, I. O., & Oyelakin, M. A. (2017). Morphometric analysis of Asa and Oyun River Basins, North Central Nigeria using geographical information system. *American Journal of Civil Engineering*, 5(6), 379–393. <https://doi.org/10.11648/j.ajce.20170506.20>.
- Musa, J. J., Otuario, E. A., Dada, P. O. Adewumi, J. K. Kuti, I. A. and Adams-Suberu, J. (2021). Validation of universal soil loss equation for selected soil locations in Northcentral Nigeria using a rainfall simulator. *Agricultural Engineering International: CIGR Journal*, 23(3), 21 – 30.
- Natekin, A. & Knoll, A. (2013). Gradient Boosting Machines, A Tutorial. *Frontiers in neurorobotics*, 7(21). 10.3389/fnbot.2013.00021. <https://www.smartem.com/blog/gradient-boosting-regression/>
- National Oceanic and Atmospheric Administration. <https://www.noaa.gov/>
- Nautiyal, M.D. (1994). Morphometric analysis of a drainage basin using aerial photographs: A case study of Khairkuli basin, district Dehradun. *J Indian Soc Remote Sens* 22, 251–261 (1994). <https://doi.org/10.1007/BF03026526>
- Nieukirk, S. (2015). Understanding Ocean Acoustics. Revised April 06, 2015 by the NOAA Ocean Explorer Webmaster. <https://oceanexplorer.noaa.gov/explorations/sound01/background/acoustics/acoustics.html>
- Norris, J. R. (1997). Continuous-time Markov chains I. <https://doi:10.1017/CBO9780511810633.004>. ISBN 9780511810633.
-

-
- Nugroho, A.A. (2013). *Model Perubahan Landuse akibat kenaikan muka air laut dan pasang maksimum di pantai utara teluk lamong (PUTL) bagian Surabaya* [Master Thesis]. Teknik Manajemen Pantai ITS, Indonesia
- Nurmiaty, A., Sumbangan, B., Samsu, A. (2014). GIS-Based Modelling of Land Use Dynamics Using Cellular Automata and Markov Chain. *Journal of Environment and Earth Science*, 4(4). <https://core.ac.uk/download/pdf/234663312.pdf> Retrieved on 15th August, 2021
- Odhiambo, B.K., Boss, S.K. (2004). Integrated echo sounder, GPS and GIS for reservoir sedimentation studies examples from two Arkansas Lakes. *J Am Water Resour Assoc Res* 40(4), 981–99.
- Oguchi, T. (1997). Drainage density and relative relief in humid steep mountains with frequent slope failure. *Earth Surf. Processes Landforms*, 22, 107–120.
- Ojigi, M. L., Mohammed, S. O., & Jeb, D. N. (2010). Pre-Dredging and Navigational Potential Analysis of the Niger-Benue Confluence Area, Lokoja, Nigeria Using Remote Sensing and GIS. *8th AARSE International Conference [AARSE2010]*, UNECA Hqtrs, Addis Ababa Ethiopia
- Pankin, M.D. (2017). *Markov chain models: Theoretical background*. Archived from the original. Retrieved 26 March 2021. <https://web.archive.org/web/20071209122054/http://www.pankin.com/markov/theory.htm>
- Paquet, R. (2010, April). *Estimation of interpolation error in DEMs using statistical methods*. FIG Congress: Facing the Challenges – Building the Capacity. Sydney, Australia. Retrieved on 4th August, 2021.
- Parente, C., Vallario, A. (2019). Interpolation of Single Beam Echo Sounder Data for 3D Bathymetric Model. *Int. J. Adv. Comput. Sci. Appl.*, 10, 6–13.
- Paretha, K. & Paretha, U. (2011). Quantitative morphometric analysis of a watershed of Yamuna Basin, India using ASTER (DEM) data and GIS. *Int J Geomat Geosci* 2(1), 248–269
- Patton, P. & Baker, V. (1976). Morphometry and Floods in Small Drainage Basis Subject of Diverse Hydrogeomorphic Controls. *Water Resources Research*, 12, 941-952. <https://doi.org/10.1029/WR012i005p00941>
- Peter, A.I., Mustapha, H. I., Musa, J. J. & Dike, J. (2008). Determination of erodibility indices of soils in Owerri West Local Government Area, Imo State, Nigeria. *AUJ.T.*, 12(2), 130-133. <https://citeseerx.ist.psu.edu/viewdoc/download?doi=10.1.1.574.6255&rep=rep1&type=pdf>
- Peterson, L. K., Bergen, K. M., Brown, D. G., Vashchuk, L., & Blam, Y. (2009). Forested land-cover patterns and trends over changing forest management eras in the Siberian Baikal region. *Forest Ecology and Management*, 257(3), 911-922. <https://DOI.10.1016/j.foreco.2008.10.037> Accessed on 18th January, 2021.
-

-
- Philippe, B. (2009). *The handbook of sidescan sonar*. Praxis publishing Ltd. ISBN 978-3-540-42641-7
- Pratomoatmojo, N.A (2018). LanduseSim Algorithm: Land use change modelling by means of Cellular Automata and Geographic Information System. *IOP Conf. Series: Earth Environ. Sci.*, 202. <https://iopscience.iop.org/article/10.1088/1755-1315/202/1/012020/pdf> Retrieved on 2 September, 2021.
- Prince, G. (2018). *5 Regression Loss Functions All Machine Learners Should Know: Choosing the right loss function for fitting a model*. <https://heartbeat.fritz.ai/5-regression-loss-functions-all-machine-learners-should-know-4fb140e9d4b0> Retrieved on 4 September, 2021.
- Psilovikos, A. & Margoni, S. (2010). An empirical model of sediment deposition processes in Lake Kerkini, Central Macedonia Greece. *Environ Monit Assess*, 164, 573–592. DOI 10.1007/s10661-009-0914-9
- Rai, P. K., Mishra, V. N., & Mohan, K. (2017). A study of morphometric evaluation of the Son basin, India using geospatial approach. *Remote Sensing Applications: Society and Environment*, 7, 9–20. <https://doi.org/10.1016/j.rsase.2017.05.001>.
- Reid, D.F. & Holcombe, T.L. (2000). *New Lake Ontario High-Resolution Bathymetry*. Great Lakes Environmental Research Laboratory Milestone Report 00-1-2. <http://www.glerl.noaa.gov/res/Milestone/2000/Q1/2000q1reid.html>
- Richard, P. H. (2010). *Underwater acoustics: Analysis, design and performance of sonar*. John Wiley and Sons Ltd. ISBN: 978070688755
- Richter, H., Hansen, R., Pohl, W., Roeser, H., & Ries, H.W. (1986). Marine Geophysical Exploration Techniques. In Kunzendorf, H. (Eds), *Marine Mineral Exploration* (pp. 86-87). Elsevier
- Robert, P. S. & Hilborn, D. (2000). Factsheet: Universal soil loss equation (USLE). Queen's printer for Ontario.
- Robert, D. C., & Robert, L. W. (2014). *The ROV Manual (Second Edition): Sonar*. Butterworth-Heinemann. <https://doi.org/10.1016/B978-0-08-098288-5.00024-5>.
- Robert, K., Pall, R., & Timothy, J. M. (2005). Definition of signal-to-noise ratio and its critical role in split-beam measurements. *ICES Journal of Marine Science*, 62(1), 123–130. <https://doi.org/10.1016/j.icesjms.2004.09.006>
- Robert, P.S. & Hilborn, D. (2012). *Universal Soil Loss Equation (USLE)*. <http://www.omafra.gov.on.ca/english/engineer/facts/12-051.htm>
- Robert, W.B. (2008). A Sonar application. In R.M. David, A.B. Robert, & M.V. Michael (Eds), *High Performance Embedded Computing Handbook 'A system perspective'* (pp. 411-416). Taylor and Francis Group.
- Rocca, J. (2019). *Introduction to Markov chains: Definitions, properties and PageRank example*. <https://towardsdatascience.com/brief-introduction-to-markov-chains-2c8cab9c98ab> Retrieved on 6 September 2021.
-

-
- Ronald, R.K. (1992). Sonar Beamforming: An Overview of its History and Status. *NUWC-NL Technical Report*, 10(003), 01-27. <https://apps.dtic.mil/dtic/tr/fulltext/u2/a250189.pdf>
- Saikat-Islam, K., Nazrul, U., Islam, J., Sifatul, N. (2021). Water Quality Prediction and Classification Based on Principal Component Regression and Gradient Boosting Classifier Approach. *Journal of King Saud University - Computer and Information Sciences*, xxx(xxxx). Doi:10.1016/j.jksuci.2021.06.003.
- Samat, N. (2009). Integrating GIS and CA-MARKOV Model In Evaluating Urban Spatial Growth. *Malaysian Journal of Environmental Management*, 10(1), 83-97. <https://core.ac.uk/download/pdf/11491356.pdf> Retrieved on 25th November, 2020
- Schmid, M., & Hothorn, T. (2008). Flexible boosting of accelerated failure time models. *BMC Bioinformatics* 9, 269. doi:10.1186/1471-2105-9-269
- Schmid, M., Hothorn, T., Maloney, K.O., Weller, D. E., & Potapov, S. (2011). Geoadditive regression modeling of stream biological condition. *Environ. Ecol. Stat.* 18, 709–733. doi: 10.1007/s10651-010-0158-4
- Schneider von, D.J., Weinrebe, W., Tóth, Z.S., Fossing, H., Endler, R., Rehder, G., & Spieß, V. (2013). A low frequency multibeam assessment: Spatial mapping of shallow gas by enhanced penetration and angular response anomaly. *Marine and Petroleum Geology*, 44, 217-222. ISSN 0264-8172 <https://doi.org/10.1016/j.marpetgeo.2013.02.013>.
- Schumm, S.A. (1956). Evolution of Drainage Systems and Slopes in Badlands at Perth Amboy, New Jersey. *Bulletin of the Geological Society of America*, 67, pp.597-646. [http://dx.doi.org/10.1130/0016-7606\(1956\)67\[597:EODSAS\]2.0.CO;2](http://dx.doi.org/10.1130/0016-7606(1956)67[597:EODSAS]2.0.CO;2) Accessed on 7th September, 2021
- Scholz, M. & Yang, Q. (2010). Guidance on variables characterising water bodies including sustainable flood retention basins. *Landscape and Urban Planning*, 98, 190-199
- Selvan, M.T., Ahmad, S. & Rashid, S.M. (2011). Analysis of the Geomorphometric parameters in high altitude Glacierised terrain using SRTM DEM data in Central Himalaya, India. *ARPJ Sci Technol* 1(1), 22–27.
- Seneta, E. (1996). Markov and the Birth of Chain Dependence Theory. *International Statistical Review/Revue Internationale de Statistique*, 64 (3), 255–257. doi:10.2307/1403785. ISSN 0306-7734. Retrieved on 23 March 2021.
- Serfozo, R. (2009). Basics of Applied Stochastic Processes: Probability and Its Applications. doi:10.1007/978-3-540-89332-5. ISBN 978-3-540-89331-8. Retrieved on 23 March, 2021.
- Sharaf, A., Jun, W., & Jie, S. (2006). Change Detection - Cellular Automata Method For Urban Growth Modeling. *ISPRS Archives*, XXXVI (7). <https://www.isprs.org/proceedings/xxxvi/part7/pdf/237.pdf> Retrieved on 28 August, 2021.
-

-
- Shenfeng, Y., & Yuanliang, M. (2004). High-resolution broadband beamforming and detection methods with real data. *Acoust. Sci. & Tech.*, 25(1), 73-76. doi: 10.1250/ast.25.73
- Shu-Qing, Y. (2015). Coastal Reservoir-a Technology That May Dominate Future Water Supply. *Journal of Water Resource and Hydraulic Engineering*, 4(4), 388-397. DOI: 10.5963/JWRHE0404010
- Silvia, P. (2015). *High Intensity Focused Ultrasound (HIFU): computing tools for medical applications* [Master Thesis, Sapienza University Roma]. DOI: 10.13140/RG.2.1.5098.2166
- Simmonds, J., & MacLennan, D. (2005). *Fisheries acoustics: Theory and practice* (Second edition). Blackwell.
- Smith, K.G. (1950). Standards for grading textures of erosional topography. *Am. Jour. Sci.* 248, 655-668.
- Smith, W.H F. & Marks, K.M. (2014). Seafloor in the Malaysia Airlines Flight MH370 Search Area. *Transactions American Geophysical Union*, 95(21), 173–174.
- Soares, E.F., Unny, T.E., Lennox, W.C. (1982). Conjunctive of deterministic and stochastic models for predicting sediment storage in large reservoirs. *J Hydrol*, 59, 83–105.
- Soni, S. (2017). Assessment of morphometric characteristics of Chakrar watershed in Madhya Pradesh India using geospatial technique. *Appl Water Sci*, 7, 2089–2102. <https://doi.org/10.1007/s13201-016-0395-2>
- Sreedevi, P.D., Owais, S., Khan, H.H., Ahmed, S. (2009). Morphometric analysis of a watershed of South India using SRTM data and GIS. *J. Geol. Soc. India* 73, 543–552.
- Stefan W. (2017). The Base-platform project: Deriving the bathymetry from combined satellite data. *Hydrographische Nachrichten*, HN 108 – 10/2017, 20 – 23.
- Strahler, A.N (1964). Quantitative geomorphology of drainage basins and channel networks. In Chow Ven Te (Ed), *Handbook of applied hydro*. McGraw Hill Book Company.
- Strahler, A.N. (1952). Dynamic Basis of Geomorphology. *Geological Society of America Bulletin*, 63, 923-938. [http://dx.doi.org/10.1130/0016-7606\(1952\)63\[923:DBOG\]2.0.CO;2](http://dx.doi.org/10.1130/0016-7606(1952)63[923:DBOG]2.0.CO;2) Retrieved on 4th November, 2021
- Strahler, A.N. (1957). Quantitative analysis of watershed geomorphology. *Trans Am Geophys Union*, 38, pp. 913–920.
- Suresh, K. & Surya, G. (2017). Simulating climate change impact on soil erosion using RUSLE model – A case study in a watershed of mid-Himalayan landscape. *J. Earth Syst. Sci.* 126(43). DOI: 10.1007/s12040-017-0823-1
- Syvitski, J. P. M., Vörösmarty, C., Kettner, A. J. & Green, P. (2005). Impact of humans on the flux of terrestrial sediment to the global coastal ocean. *Science*, 308, 376–380.
-

-
- Tadese, S., Soromessa, T., Bekele, T (2021). Analysis of the Current and Future Prediction of Land Use/Land Cover Change Using Remote Sensing and the CA-Markov Model in Majang Forest Biosphere Reserves of Gambella, Southwestern Ethiopia. *The Scientific World Journal*, 2021. <https://doi.org/10.1155/2021/6685045>
- Tellez, O.L.L., Borghgraef, A., Mersch, E. (2017). The Special Case of Sea Mines, Mine Action. The Research Experience of the Royal Military Academy of Belgium. *InTech*, 251-279 <http://dx.doi.org/10.5772/66994>
- Temitope, B. O., and Kehinde, A. G. (2019). Bathymetric Survey and Topography Changes Investigation of Part of Badagry Creek and Yewa River, Lagos State, Southwest Nigeria. *Journal of Geography, Environment and Earth Science International*, 22(4), 1-16. <https://doi.org/10.9734/jgeesi/2019/v22i430153>
- Terence, P. & Jeremy, H. (2021). *Gradient boosting: Distance to target*. <https://explained.ai/gradient-boosting/L2-loss.html#sec:2.4>
- Thomas, H., & Laurence, H-M. (2006). Modeling and projecting land-use and land-cover changes with Cellular Automaton in considering landscape trajectories: An improvement for simulation of plausible future states. *European Association of Remote Sensing Laboratories*, 5(1), pp.63-76. fffhalshs-00195847f. <https://halshs.archives-ouvertes.fr/halshs-00195847/document> Retrieved on 16 July, 2021.
- Timothy, J. R. & Jennifer, B. (2017). Dam removal analysis guidelines for sediment-version 1 technical report SRH-2016-38 prepared for subcommittee on sedimentation Federal Advisory Committee on Water Information Bureau of Reclamation Technical Service Center, Denver, Colorado
- Tobler, W. (1970). A computer movie simulating urban growth in the Detroit region. *Economic Geography*, 46(2), 234-240. <https://doi.org/10.2307/143141> Retrieved on 28 of August, 2021
- Torrens, P.M. (2007). Cellular automata. In N. Thrift, & R. Kitchin (Eds.), *Encyclopedia of Human Geography*. Elsevier. <http://www.geosimulation.org/papers/2007-encyclopedia-cellular-automata.pdf> Retrieved on 4 September, 2021
- Trung, K.N. (2017). Seafloor classification with a multiswath multibeam echo sounder. Signal and Image processing. *Ecole nationale supérieure Mines-Télécom Atlantique*. English. NNT:2017IMTA0035ff. fftel-01825173f. <https://tel.archives-ouvertes.fr/tel-01825173/document> Retrieved on 14th September, 2020.
- Urlick, R.J. (2013). *Principles of Underwater Sound* (3rd Ed.). McGraw-Hill.
- USACE (2002). <https://www.publications.usace.army.mil/USACE-Publications/EngineerManuals/u43544q/487964726F67726170686963/> Retrieved on 14 January, 2021
- Vahid, R., Jude H. K., Frank deN., Mark E. J., Edward A. M., Donald H. H., Christian G., Paul M. L., Scott W. C., Ryan A. C. and Adam J. B., (2018). Examining

- Storage Capacity Loss and Sedimentation Rate of Large Reservoirs in the Central U.S. Great Plains. *Water* 2018, 10, 190; doi:10.3390/w10020190 www.mdpi.com/journal/water.
- Veli, I., Ibrahim, M. O., Reha, M. A., Serdar, E., Murat, U., Yunus, K. and Serdar, D. Z. S. (2019). Determination of Reservoir Sedimentation with Bathymetric Survey: A Case Study of Obruk dam Lake. *Fresenius Environmental Bulletin*, 28,(3), 2305-2313.
- Verstappen, H. (1983). The applied geomorphology. Ensched: *In International Institute for aerial survey and earth science (ITC)*.
- Volberg, B., & Meurling, T. (2007). Evolution and Future of Multibeam Echosounder Technology. *Symposium on Underwater Technology and Workshop on Scientific Use of Submarine Cables and Related Technologies, Tokyo, 2007* (pp. 147-155). doi: 10.1109/UT.2007.370844
- von Neumann, J. (1966). *Theory of self-reproducing automata*. Univ. of Illinois Press.
- von Neumann, J. (2010). Cellular Automata. *Embryo Project Encyclopedia*. ISSN: 1940-5030 <http://embryo.asu.edu/handle/10776/2009>. Retrieved on 11 September, 2021
- Von Ramm, O. T., & Smith, S. W. (1983). Beam Steering with Linear Arrays. *IEEE Transactions on Biomedical Engineering, BME-30* (8), 438-452. doi:10.1109/TBME.1983.325149
- Vulegbo A.A., Schoeneich K. and Alagbe S.A., (2014) Assessment of sediment generation from Tagwai drainage basin. *Am Int J Contemp Res* 4(8).
- Waikar, M.L. & Aditya, P. N. (2014). Morphometric analysis of a drainage basin using Geographical Information System: A case study. *International journal of multidisciplinary and current research*, 2, 179 – 184. <http://ijmcr.com/wp-content/uploads/2014/02/Paper32179-184.pdf> Retrieved on 14th August 2020.
- Wang, A., Church, I., Gou, J., & Zhao, J. (2020). Sea bottom line tracking in side-scan sonar image through the combination of points density clustering and chains seeking. *J Mar Sci Technol* 25, 849–865. <https://doi.org/10.1007/s00773-019-00685-6>
- Welcomme, R.L. (1986). The Niger River System. In B. R. Davies, & K.F. Walker (Eds), *The Ecology of River Systems*. Springer. ISBN 9061935407
- Wentzell, H.F., & Ziese, R. (1998). New echo sounding Methods for shallow water and deep sea surveying. Paper presented at the Oceanology '88: Proceedings of an international conference, Brighton.
- Wenzhong, S., Matthew, Y., & Cheung, P. (2000) Development of Voronoi-based cellular automata -an integrated dynamic model for Geographical Information Systems. *International Journal of Geographical Information Science*, 14(5), 455-474, DOI: 10.1080/13658810050057597

-
- White, W. R. (2000). Contributing paper flushing of sediments from reservoirs. *Thematic review, (IV)5: operation, monitoring and decommissioning of dams*. World Commission on Dams, Cape Town.
- Whitlow, W.L. & Mardi, C.H. (2008). *Principles of Marine Acoustic*. Springer
- Wilbers, A.W.E. & Ten Brinke, W.B.M. (2003). The response of subaqueous dunes to floods in sand and gravel bed reaches of the Dutch Rhine. *Sedimentology*, 50, 1013-1034. <https://doi.org/10.1046/j.1365-3091.2003.00585.x>
- William, J.A. (2012, December). Continuous-Time Markov Chains: An Applications-Oriented Approach. Springer Science & Business Media. ISBN 978-1-4612-3038-0. Retrieved on 23 March 2021.
- Wischmeier, W. H. & Smith, D. D. (1978). Predicting rainfall erosion losses: a guide to conservation planning. *U.S. Department of Agriculture, Agriculture Handbook number 537*. U.S. Government Printing Office, p.58. http://www.ars.usda.gov/SP2UserFiles/ad_hoc/36021500USLEDatabase/AH_537.pdf
- Wohlleben, R., Mattes, H & Krichbaum, T.H. (1991). Interferometry in Radioastronomy and Radar Techniques (pp. 43). Springer Science Business Media.
- Wolfram, S. (1994). Cellular Automata and Complexity: Collected Papers by Stephen Wolfram. <https://www.stephenwolfram.com/publications/cellular-automata-complexity/> Accessed on 14 June, 2020
- Woon, S.G. (2012). *Acoustical Image: Techniques and Applications for Engineers; Signal Processing*. John Wiley & Sons Ltd.
- Wu, H., Chen, X., & Zhang, X. (2006). A cellular automata based distributed model for simulating runoff in LeAnhe watershed [Paper presentation]. *International Geoscience and Remote Sensing Symposium (IGARSS)*. IEEE International Geo-science and Remote Sensing Symposium. Denver, CO; pp.1040–1043.
- Xavier, L. (2010). *An Introduction to Underwater Acoustics: Principles and Applications* Second edition. Springer
- Yan, Z.L., Qin, L.L., Wang, R., Li, J., Wang, X.M., & Tang, X.L. (2018). The Application of a Multi-Beam Echo-Sounder in the Analysis of the Sedimentation Situation of a Large Reservoir after an Earthquake. *Water*, 10, 557. <https://doi.org/10.3390/w10050557>
- Yang, G., Liu, Y., & Wu, Z. (2007). Analysis and simulation of land-use temporal and spatial pattern based on CA-Markov model. *Geomatics and Information Science of Wuhan University*, 32, 414-418.
- Ying, Y., Li, H., Xiangtao, R., Min, L. & Yang, Y. Z. (2018). Application of Sonar Equation in the Design Of Ocean Instruments. *Advances in Computer Science Research*, 86, 186-192. <https://dx.doi.org/10.2991/cccs-18.2018.34>
- Yoav, F., & Robert, E. S. (1997). A Decision-Theoretic Generalization of On-Line Learning and an Application to Boosting. *Journal of computer and system sciences*, 55, 119-139. <https://www.face-rec.org/algorithms/Boosting->
-

- [Ensemble/decision-theoretic_generalization.pdf](#) Retrieved on 4 September, 2021.
- Yong, B., & Qiang, B. (2019). *Subsea Engineering Handbook* (Second Edition). Gulf Professional Publishing. <https://doi.org/10.1016/B978-0-12-812622-6.00031-2>
- Yongjiu, F. (2017). Modelling dynamic urban land-use change with geographical cellular automata and generalized pattern search-optimized rules. *International Journal of Geographical Information Science*. <http://dx.doi.org/10.1080/13658816.2017.1287368> Retrieved on 4 August, 2021
- Zakariya, R., Abdullah, M.A., Che Hasan, R., & Khalil, I. (2018). Automatic classification techniques for type of sediment map from multibeam sonar data. IOP Conf. Series. *Earth Environ. Sci.*, 117. doi:10.1088/1755-1315/117/1/012047
- Zouiten, M., Jamal, C., & Ibtissam, N. (2021). Predicting Land Use Changes within the Tazekka Park and its Borders via A Cellular Automata-Markov modelling of satellite images. *Journal of Southwest Jiaotong University*, 56(2). <https://DOI:10.35741/issn.0258-2724.56.2.43> Retrieved on 04 August, 2021
- <https://www.thisdaylive.com/index.php/2020/09/14/kainji-dams-embarkment-collapses/>
Accessed on 21/02/2021
- <https://www.opendem.info/> Accessed on 18/03/2021
- <https://iho.int/en/importance-of-hydrography> Accessed on 20/07/2019
- https://handwiki.org/wiki/File:Principle_of_SBES.svg Accessed on 13/04/2019
- <https://www.open.edu/openlearn/science-maths-technology/analytical-science-secrets-the-mary-rose/content-section-2.1> Accessed on 13/04/2019
- <https://hytrade.en.made-in-china.com/product/iCAmFvWYlyVB/China-Sound-Velocity-Profiler.html> Accessed on 13/04/2019
- <https://www.comet.ucar.edu/> Accessed on 13/04/2019
- http://linux.geodatapub.com/shipwebpages/survey%20gear/Multibeam/EM1002%20-%20Powell/SIS/EM1002%20with%20SIS%20complete/doc/English/sis_tec_h_vessel_coordinate_system.html Accessed on 01/03/2020
- <https://www.sailingissues.com/navcourse6.html> Accessed on 17/04/2021
- <https://www.fugro.com/our-services/marine-asset-integrity/satellite-positioning>
Accessed on 10/02/2020
- <https://www.gps.gov/applications/marine/> Accessed on 10/02/2021
- <https://owaysonline.com/global-positioning-system-on-ships/> Accessed on 10/02/2020
- <https://tstarmet.com/navigation/gps/> Accessed on 10/02/2020
- https://en.wikipedia.org/wiki/Markov_chain#cite_note-norris1-49 Accessed on 10/05/2021
- https://iho.int/uploads/user/pubs/cb/c-13/english/C_13_Chapter_3_December2010.pdf
Accessed on 15/03/2021

8 Appendix 1: Python script of CA – MC

```
[ ] import pandas as pd
    import os
    import pickle
    import numpy as np
    from numpy.random import choice
    from scipy.interpolate import griddata
    from sklearn.ensemble import GradientBoostingRegressor
    from sklearn.model_selection import GridSearchCV

    import plotly.graph_objs as go
[ ] from google.colab import drive
    drive.mount('/content/drive')

Load dataframes from csv raw data files

[ ] df1 = pd.read_csv("/content/drive/MyDrive/data/geo/1990_data_
area.csv")
    df2 = pd.read_csv("/content/drive/MyDrive/data/geo/2020_data_
depth_area.csv")

Define function to interpolate data and make a grid dataframe

[ ] def grid_interpolation(df, grid_step,
                          x_min=None, x_max=None, y_min=None, y_max=None,
                          method='linear'):
    """
    df - data frame with bathimetric data to interpolate
    grid_step - step of the grid in meters
    x_min, x_max, y_min, y_max - borders of the interpolated area
    method - interpolation method (linear, cubic, nearest)
    """
    # Calculate borders if they are not assigned
    if not x_min:
        x_min = df['x'].min()
    if not x_max:
        x_max = x_min + (df['x'].max() - x_min) // grid_step * grid_
step
    else:
        x_max = x_min + (x_max - x_min) // grid_step * grid_step
    if not y_min:
        y_min = df['y'].min()
    if not y_max:
        y_max = y_min + (df['y'].max() - y_min) // grid_step * grid_
step
    else:
        y_max = y_min + (y_max - y_min) // grid_step * grid_step
    # Numbers of steps by x and y
    n_x = int((x_max - x_min) // grid_step)
    n_y = int((y_max - y_min) // grid_step)
    # Make a linear space of x and y with grid_step
    x1 = np.linspace(x_min, x_max, n_x)
    y1 = np.linspace(y_min, y_max, n_y)
    # Make a grid
    x2, y2 = np.meshgrid(x1, y1)
    # Interpolate the depth
    z2 = griddata((df['x'], df['y']), df['depth'], (x2, y2),
                  method= method)
    z2 = np.nan to_num(z2)
    # Return tuple of x, y, z variables
    return x1, y1, z2
```

Define function to plot contours. You can change colorscale, possible built-in colorscales:

```

aggrnyl  agsunset  blackbody  bluered  blues      blugrn    bluy1     brwnyl
bugn     bupu       burg       burgyl   cividis    darkmint  electric  emrld
gnbu     greens     greys      hot       inferno    jet       magenta   magma
mint     orrd       oranges    oryel    peach      pinkyl    plasma    plotly3
pubu     pubugn     purd       purp     purples    purpor    rainbow   rdbu
rdpu     redor      reds       sunset   sunsetdark teal       tealgrn   turbo
viridis  ylgm       ylgmbu    ylorbr   ylorrd    algae     amp       deep
dense    gray       haline     ice       matter     solar     speed     tempo
thermal  turbid     armyrose   brbg     earth      fall      geyser    prgn
piyg     picnic     portland   puor     rdgy       rdy1bu   rdy1gn   spectral
tealrose temps      tropic     balance  curl       delta     oxy       edge
hsv      icefire    phase      twilight  mrybm     mygbm

```

Also you can use any colorscale in reversed mode by adding "_r". For example, "colorscale=earth_r".

```

[ ] def plot_contours(res, title):
    """
    Plot contours of res tuple (x, y, z) with title
    """
    fig = go.Figure(data=
        go.Contour(
            z=res[2], x = res[0], y=res[1],
            line_smoothing=0.85,
            colorscale=[(0, "rgb(56, 228, 255)"), (1, "rgb(13, 5, 255)")]
        ))

    layout = go.Layout(yaxis=dict(scaleanchor="x", scaleratio=1))
    fig.update_yaxes(
        scaleanchor = "x",
        scaleratio = 1,
    )
    fig.update_layout(title=title,
        width=400,
        height=1000
    )
    fig.show()

```

Define the function to clear datasets

```

[ ] def clear_dataset(df, threshold = 0.4):
    """Delete values of depth lower than threshold and replace NaN values by 0"""
    df['depth'].loc[df.depth < threshold] = 0
    df = df.fillna(0)
    return df

```

Clear all three datasets

```

[ ] df1 = clear_dataset(df1)
    df2 = clear_dataset(df2)

```

Find the inner square of all three datasets

```
[ ] x_min = max(df1.x.min(), df2.x.min())
    x_max = min(df1.x.max(), df2.x.max())

    y_min = max(df1.y.min(), df2.y.min())
    y_max = min(df1.y.max(), df2.y.max())

    z_min = min(df1.depth.min(), df2.depth.min())
    z_max = max(df1.depth.max(), df2.depth.max())
```

Interpolate datasets according to a grid with a step of 100 meters.

```
[ ] GRID_STEP = 100
    res1 = grid_interpolation(df1, GRID_STEP, x_min, x_max, y_min,
                              y_max)
    res2 = grid_interpolation(df2, GRID_STEP, x_min, x_max, y_min,
                              y_max)

[ ] plot_contours(res3, "1990")
[ ] plot_contours(res3, "2020")
```

Define functions for processing the data as a Markov Chain

```
def convert_to_markov_states(arr, number_of_states, min_val, max_val):
    """Convert the array of depths into an array of the markov states of depths"""
    bins = np.linspace(min_val, max_val, number_of_states + 1)
    d = dict(enumerate(range(1, len(bins) + 1), 1))
    arr = np.vectorize(d.get)(np.digitize(arr, bins))
    return arr

def calculate_transition_matrix(arr1, arr2, arr3, number_of_states):
    """Takes 3 arrays and calculate transition matrix for particular number_of_states"""
    assert arr1.shape == arr2.shape == arr3.shape, "Matrixes of the states should be the same shape"
    res = np.zeros((number_of_states, number_of_states))

    for line1, line2, line3 in zip(arr1, arr2, arr3):
        for e11, e12, e13 in zip(line1, line2, line3):
            res[e11 - 1, e12 - 1] += 1
            res[e12 - 1, e13 - 1] += 1
    for i, line in enumerate(res):
        if line.sum() != 0:
            res[i] = line / line.sum()
    return res
```

Convert depths into the MC states and calculate the transition matrix

```

[ ] NUMBER_OF_STATES = 10
    res_m_1 = convert_to_markov_states(res1[2], NUMBER_OF_STATES,
    z_min, z_max)
    res_m_2 = convert_to_markov_states(res2[2], NUMBER_OF_STATES,
    z_min, z_max)

```

The transition matrix in percents

```

[ ] bins = np.linspace(z_min, z_max, NUMBER_OF_STATES + 1)
    pd.DataFrame(transition_matrix * 100, index=bins
   [:-1], columns=bins[:-1])

[ ] plot_contours((res1[0], res1[1], res_m_2), "markov 1990")
[ ] plot_contours((res1[0], res1[1], res_m_3), "markov 2020")

```

Define the functions to predict next state of the dataframe

```

def get_filter_matrix(n):
    """
    Get matrix to set up the CA algorithm.
    During processing, only neighbors that fall under the filter
    matrix
    will be taken into account.
    Returns an array n by n
    """
    n = (n // 2) * 2 + 1
    res = np.ones((n, n))
    for i in range(n):
        for j in range(n):
            if ((i < n//2 and ((j < n //2 and (i + j < n // 2))
                or (j > n // 2 and ((i + (n - 1 - j)) < n // 2))))
            or (i > n//2 and ((j < n //2 and (j + (n - 1 - i) < n // 2) )
                or (j > n // 2 and ((n - 1 - i) + (n - 1 - j)) < n
                // 2))))):
                res[i, j] = 0
    return res

def get_neighbours_states(arr, x, y, n=5):
    """
    Get the neighbours values according to a filter matrix n by n.
    Returns list of neighbours states.
    """
    filt = get_filter_matrix(n)
    neighbours = []
    for dx in range(-(n // 2), n // 2 + 1):
        for dy in range(-(n // 2), n // 2 + 1):
            if filt[n // 2 + dx, n // 2 + dy] == 1:
                if (0 <= (x + dx) < (arr.shape[0] - 1)) and (0 <=

```

```

        (y + dy) < (arr.shape[0] - 1)):
    try:
        neighbours.append(arr[x + dx, y + dy])
    except IndexError:
        continue

    return neighbours

def predict_mc_depth(arr, tr_m):
    """
    Predict the next step states of array, having the transition
    matrix of the MC
    """
    res = np.zeros(arr.shape)
    for i in range(arr.shape[0] - 1):
        for j in range(arr.shape[1] - 1):
            neighbours = get_neighbours_states(arr, i, j)
            temp_res_lst = [choice(range(tr_m.shape[0]), p=tr_m
                [state - 1]) for state in neighbours]
            res[i, j] = max(temp_res_lst, key=temp_res_lst.count)
    return res

```

Calculate the state of the dataframe for 2050 year

```

[ ] res_m_4 = predict_mc_depth(res_m_3, transition_matrix)

[ ] plot_contours((res1[0], res1[1], res_m_4), "markov 2050")

```

9 Appendix 2: Python script of CA – GBR

Using Cellular Automata and Gradient Boosting Regression model

Define the function to get cellular automata dataset from two datasets.

```

[ ] def get_ca_df(arr, target_arr):
    """
    Make a dataset for cellular automata method.
    Every cell of target array is considered depending on its value
    in the previous time moment and on the values of its neighbours
    """
    # radius of neighbours
    radius = 1
    # Make columns for the output dataframe
    columns = [f"neighbour_{i}{j}" for i in range(radius, radius+1)
                for j in range(-radius, radius+1)]
    # Make a target column - value of the depth in a current grid
    point
    columns.append("target")

```

```

# Make an empty output dataframe
ca = pd.DataFrame(columns=columns)
# Iterate through all the points except the points on border
for i in range(1, arr.shape[0] - 1):
    for j in range(1, arr.shape[1] - 1):
        row = {}
        # Iterate through the neighbours in the defined radius
        for k in range(-radius, radius + 1):
            for l in range(-radius, radius + 1):
                # Make a row of features
                row[f"neighbour_{k}{l}"] = arr[i+k][j+l]
        # Add target to the row
        row["target"] = target_arr[i][j]
        # Add row in the output df
        ca = ca.append(row, ignore_index = True)
return ca

```

Get the cellular automata dataset from the datasets of 1990 and 2020 years.

```
[ ] cel = get_ca_df(res1[1], res2[1])
```

Find optimal parameters of the GBR prediction model for the dataset.

```

[ ] # Find optimal parameters of the Gradient boosting r
    egression with
    X = cel.loc[:, cel.columns != 'target']
    Y = cel.target
    GBR = GradientBoostingRegressor()
    parameters = {'learning_rate': [0.01, 0.05],
                  'subsample' : [0.9, 0.1],
                  'n_estimators' : [100, 1500],
                  'max_depth' : [4, 10]
                  }
    grid_GBR = GridSearchCV(estimator=GBR, param_grid =
    parameter s, cv = 2, n_jobs=-1)
    grid_GBR.fit(X, Y)
    print(" Results from Grid Search ")
    print("\n The best estimator across ALL searched params:\n",
    grid_GBR.best_estimator_)
    print("\n The best score across ALL searched params:\n",
    grid_GBR.best_score_)
    print("\n The best parameters across ALL searched params:\n",
    grid_GBR.best_params_)

```

Results from Grid Search

```

The best estimator across ALL searched params:
GradientBoostingRegressor(alpha=0.9, ccp_alpha=0.0, criterion='friedman_mse',
                           init=None, learning_rate=0.01, loss='ls', max_depth=4,
                           max_features=None, max_leaf_nodes=None,
                           min_impurity_decrease=0.0, min_impurity_split=None,
                           min_samples_leaf=1, min_samples_split=2,
                           min_weight_fraction_leaf=0.0,
                           n_estimators=1500,
                           n_iter_no_change=None,

```

```

presort='deprecated',
random_state=None, subsample=0.1,
tol=0.0001,
validation_fraction=0.1, verbose=0,
warm_start=False)

```

The best score across ALL searched params:
0.9566955857474481

The best parameters across ALL searched params:

```
{'learning_rate': 0.01, 'max_depth': 4, 'n_estimators': 1500, 'subsample': 0}
```

Save the results

Results from Grid Search

```

The best estimator across ALL searched params: GradientBoostingRegressor(alpha=0.9,
ccp_alpha=0.0, criterion='friedman_mse', init=None, learning_rate=0.01, loss='ls',
max_depth=4, max_features=None, max_leaf_nodes=None, min_impurity_decrease=0.0,
min_impurity_split=None, min_samples_leaf=1, min_samples_split=2,
min_weight_fraction_leaf=0.0, n_estimators=1500, n_iter_no_change=None,
presort='deprecated', random_state=None, subsample=0.1, tol=0.0001,
validation_fraction=0.1, verbose=0, warm_start=False)

```

The best score across ALL searched params: 0.9566955857474481

The best parameters across ALL searched params: {'learning_rate': 0.01, 'max_depth': 4, 'n_estimators': 1500, 'subsample': 0.1}

Define the functions to load and save Python objects as a pickle file. Also define the function to get the model from file, if there is such a file or fit the model and save it to the file.

```

[ ] def load_pickle(filename):
    with open(filename, "rb") as f:
        return pickle.load(f)

def save_pickle(obj, filename):
    with open(filename, "wb+") as f:
        pickle.dump(obj, f)

def get_the_model(X, Y, params, filename=""):
    """Build and return the GBR model with params"""
    if os.path.exists(filename):
        return load_pickle(filename)
    model = GradientBoostingRegressor(**params)
    model.fit(X, Y)
    save_pickle(model, filename)
    return model

```

Prepare data and build a model with optimal parameters found by GridSearch algorithm.

```

[ ] X = cel.loc[:, cel.columns != 'target']
    Y = cel.target
    model = get_the_model(X, Y, grid_GBR.best_params_, "/content/
drive/MyDrive/data/geo/model.pickle")

```

Prepare new cellular automata dataset to predict the bathymetric data in 2050 year. Use the model we got in a previous step to predict these data and reshape the data. Note that the dimension of the predicted data is less than the dimension of the original data by 2 in x and y, since we don't use the cells which don't have all the neighbours.

```

cel_predict = get_ca_df(res2[1], res2[1])
z_pred = model.predict(cel_predict.loc[:, cel.columns !=
'target'])
z_pred = z_pred.reshape((res1[2].shape[0] - 2, res1[2].shape
[1] - 2))
Plot the contour-plot for the predicted data of 2050 year.
[ ] plot_contours([res1[0][1:-1], res1[1][1:-1], z_pred], "2050")

Save all the data in the pickle files, so we can use it without long calculations.
[ ] save_pickle(res1, "/content/drive/MyDrive/data/geo/1990_prep_
data.pickle")
save_pickle(res2, "/content/drive/MyDrive/data/geo/2020_prep_
data.pickle")

save_pickle([res1[0][1:-1], res1[1]
[1:1], z_pred], "/content/drive/MyDrive/data/geo/2050_prep_
data.pickle")
save_pickle([res1[0][2:-2], res1[1]
[2:-2], z_pred_2080], "/content/drive/MyDrive/data/geo/

```

We can load and plot the saved data like this:

```

[ ] data_2050 = load_pickle("/content/drive/MyDrive/data/geo/2050
_prep_data.pickle")
plot_contours(data_2050, "2050")

```

10 Appendix 3: Journal Publications

- 1) Ibrahim, P.O, Sternberg, H. (2021). Bathymetric Survey for Enhancing the Volumetric Capacity of Tagwai Dam in Nigeria via Leapfrogging Approach. *Journal of Geomatics*, 1(2), 246-257. <https://doi.org/10.3390/geomatics1020014>
- 2) Ibrahim, P.O., Sternberg, H. (2020). Evaluation of Exponential Factor on Boundary Value Problem of Inverse Distance Weighting Method of Interpolation (10401), *FIG Working Week 2020*, May 2020, Amsterdam, The Netherlands www.fig.net/fig2020/technical_program.htm
- 3) Ibrahim, P.O, Sternberg, H., Samaila-ija, H.A., Donald, A., Nwadiolor, J.I. Modelling Topo-Bathymetric Surface Using a Triangulation Irregular Network (TIN) of Tunga Dam in Nigeria, has been accepted for publication in the Springer Journal of Applied Geomatics on 19th April 2022.